# Development of Iron Nanoparticles for Medical Imaging and Therapeutic Treatments of Glioblastoma Multiforme

**A Dissertation Presented for the**
**Doctor of Philosophy**
**Degree**
**The University of Tennessee, Knoxville**

**Julie Elizabeth King**
**May 2019**

Copyright © 2019 by Julie King. All rights reserved.

# ACKNOWLEDGEMENTS

I would like to thank my major advisor, Dr. Jackie Johnson, and my committee members: Dr. Zhang, Dr. Silke Hecht, and Dr. David Anderson. Their advice and guidance was invaluable.

UTSI: Research Group, Interns, Staff

I am profoundly grateful for my family and friends who have supported be along this journey. My parents, Danny and Sandy King, my brother, Jason King, and my aunt, Ann Stanley provided guidance and nurturing throughout my life got me here. I am especially grateful for Cherish Hughes (nee Bowman) and Elizabeth Bennett (nee Shipley); their continuous support and encouragement throughout undergraduate and graduate studies have been essential.

Others involved in supporting my research include Dr. Adam Rondinone and Michelle Pawell at Oak Ridge National Laboratory Center for Nanophase Material Science; Dr. Todd Giorgio, Dr. Kelly Kirkbride, and Dr. Dan Colvin at Vanderbilt University, and Dr. Ecran Alp and Philipp Wissell at Argonne National Laboratory.

# ABSTRACT

The goal of the research presented in this dissertation is to develop iron nanoparticles suitable for use as Magnetic Resonance Imaging (MRI) contrast agents, for enhancement of Laser Induced Thermal Therapy (LITT), and to combine these capabilities for Magnetic Resonance guided Laser Induced Thermal Therapy (MRgLITT). In order to accomplish this, small metallic iron nanoparticles were to be produced with a biocompatible coating. Synthesis methods employed are reduction and thermal decomposition of iron (ii) chloride, iron pentacarbonyl, and iron sulfate. Several biocompatible coatings were investigated to determine their performance as a protective layer. Characterization techniques used include DLS, TEM, Mössbauer Spectroscopy, NMR, and cytotoxicity.

Reduction of iron (ii) chloride resulted in metal iron and iron oxide nanoparticles. Iron metal nanoparticles had not oxidized completely after three years of storage in air. Thermal decomposition of iron pentacarbonyl in organics produced iron oxide nanoparticles with an iron metal core. The reaction proved to be very reproducible. Iron sulfate reductions created metal and amorphous iron nanoparticles.

# TABLE OF CONTENTS


CHAPTER I Introduction ..... 1
Magnetic Resonance Imaging ..... 2
Laser Induced Thermal Therapy ..... 3
Magnetic Resonance guided Laser Induced Thermal Therapy ..... 5
CHAPTER II Reduction of Iron Chloride ..... 8
Introduction ..... 9
Methods ..... 9
Iron Nanoparticle Syntheses ..... 9
Synthesis I ..... 9
Synthesis II ..... 11
Synthesis III ..... 12
Characterization ..... 13
Transmission Electron Microscopy ..... 13
Dynamic Light Scattering ..... 13
Cytotoxicity ..... 13
Mössbauer Spectroscopy ..... 14
Results ..... 15
Characterization ..... 15
Transmission electron microscopy ..... 15
Dynamic Light Scattering ..... 18
Cytotoxicity ..... 20
Mössbauer Spectroscopy ..... 21
Discussion ..... 22
Future Work ..... 30
Chapter II Appendix ..... 32
CHAPTER III Thermal Decomposition of Iron Pentacarbonyl ..... 71
Introduction ..... 72
Methods ..... 72
Iron Oleate Synthesis ..... 72
Iron Nanoparticle Synthesis ..... 72
Iron Oleate Shell ..... 73
Sample Washing and Coating ..... 73
Transmission Electron Microscopy (TEM) ..... 76
Dynamic Light Scattering ..... 76
Mössbauer Spectroscopy ..... 76
Transmission Electron Microscopy (TEM) ..... 77
Dynamic Light Scattering (DLS) ..... 80
Mössbauer Spectroscopy ..... 82
Discussion ..... 86
Future Work ..... 88
Chapter III Appendix ..... 89
CHAPTER IV Reduction of Iron Sulfate ..... 126

Introduction ..... 127
Methods ..... 127
Iron Nanoparticle Synthesis ..... 127
Transmission Electron Microscopy (TEM) ..... 129
Magnetic Resonance (NMR) Relaxometry ..... 129
Mössbauer Spectroscopy ..... 129
Results ..... 130
Transmission Electron Microscopy (TEM) ..... 130
Magnetic Resonance Relaxometry ..... 131
Mössbauer Spectroscopy ..... 133
Discussion ..... 136
Chapter IV Appendix ..... 137
CHAPTER V Conclusions ..... 169
Iron Chloride Reduction ..... 170
Iron Pentacarbonyl Thermal Decomposition ..... 170
Iron Sulfate Reduction ..... 170
Outlook ..... 170
References ..... 172
Appendix ..... 176
VITA ..... 179

# LIST OF TABLES

Table 1 Summary of synthesis conditions for iron chloride reduction samples ..... 10
Table 2 TEM size analysis of iron chloride reduction samples ..... 17
Table 3 DLS cumulant results compared to TEM results (particle size, agglomerate size) ..... 19
Table 4 Mössbauer results of iron chloride reduction samples ..... 29
Table 5 Thermal decomposition synthesis conditions ..... 74
Table 6 TEM results of thermal decomposition samples ..... 79
Table 7 DLS cumulants results with TEM results (core + shell, agglomerates) ..... 83
Table 8 Mössbauer Results of Iron Pentacarbonyl Thermal Decomposition Samples ..... 87
Table 9 Summary of TEM Results ..... 132
Table 10 Relaxometry Results of Concentrated Samples ..... 133
Table 11 Relaxometry Value of Varying Concentrations ..... 133
Table 12 Mossbauer Results of Iron Sulfate Reduction Samples ..... 135
Table 13 Synthesis Method and Coating of All Samples ..... 177

# LIST OF FIGURES

Figure 1 Synthesis of JK001, JK003, JK006, and JK007 ..... 32
Figure 2 Synthesis of JK002, JK004, JK005 ..... 33
Figure 3 Magnetic separation of JK002 ..... 33
Figure 4 Synthesis of JK009 ..... 34
Figure 5 Synthesis of JK018-JK019 ..... 35
Figure 6 JK001 prepared for TEM characterization ..... 36
Figure 7 DLS sample of A) JK001 and B) JK007 ..... 36
Figure 8 Cell concentration and viability assessed using a hematocytometer ..... 37
Figure 9 Mössbauer apparatus setup ..... 37
Figure 10 Preparation of Mössbauer sample ..... 38
Figure 11 TEM of JK001 ..... 39
Figure 12 TEM of JK002 ..... 41
Figure 13 TEM of JK003 ..... 43
Figure 14 TEM of JK004 ..... 44
Figure 15 TEM of JK005 ..... 45
Figure 16 TEM of JK006 ..... 45
Figure 17 TEM of JK007 ..... 46
Figure 18 TEM of JK018 ..... 47
Figure 19 DLS results of JK001 ..... 49
Figure 20 DLS of JK002 ..... 50
Figure 21 DLS results of JK007 ..... 51
Figure 22 DLS results of JK011 ..... 52
Figure 23 DLS results of JK012 ..... 53
Figure 24 Plate one at 17, 24, and 48 hour timepoints ..... 54
Figure 25 Plate one and two cytotoxicity results ..... 55
Figure 26 Summary of cytotoxicity results ..... 57
Figure 27 Mössbauer Spectrum of JK002 at 6 K ..... 57
Figure 28 Mössbauer Spectrum of JK002 at 293 K ..... 58
Figure 29 Mössbauer Spectrum of JK002 at 6 K Two Months Post Synthesis ..... 58
Figure 30 Mössbauer Spectrum of Sample JK003 at 6 K ..... 59
Figure 31 Mössbauer Spectrum of JK003 at 6 K Four Years and 4 Months Post Synthesis ..... 59
Figure 32 Mössbauer Spectrum of JK003 at 6 K Four Years and 9 Months Post Synthesis ..... 60
Figure 33 Mössbauer Spectrum of JK003 at 293 K Four Years and 9 Months Post Synthesis ..... 60
Figure 34 Mössbauer Spectrum of JK003 at 293 K with a 10 kG Field Four Years and 9 Months Post Synthesis ..... 61
Figure 35 Mössbauer Spectrum of JK004 at 6 K ..... 61
Figure 36 Mössbauer Spectrum of JK007 at 6K ..... 62
Figure 37 Mössbauer Spectrum of JK011 at 6K ..... 62
Figure 38 Mössbauer Spectrum of JK011 at 293 K ..... 63
Figure 39 Mössbauer Spectrum of JK011 at 293 K with a 10 kG Field ..... 63
Figure 40 Mössbauer Spectrum of JK012 at 6 K ..... 64
Figure 41 Mössbauer Spectrum of JK012 at 180 K ..... 64

Figure 42 Mössbauer Spectrum of JK012 at 293 K ..... 65
Figure 43 Mössbauer Spectrum of JK012 at 293 K with a 10 kG Field ..... 65
Figure 44 Mössbauer Spectrum of Anhydrous $FeCl_2$ ..... 66
Figure 45 Mössbauer Spectrum of JK018 at 6 K ..... 66
Figure 46 Mössbauer Spectrum of JK018 at 293 K ..... 67
Figure 47 Mössbauer Spectrum of JK019 at 6 K ..... 67
Figure 48 Mössbauer Spectrum of JK019 at 6 K with a 0.073 T Parallel Field ..... 68
Figure 49 Mössbauer Spectrum of JK019 at 6 K with a 0.073 T Perpendicular Field ..... 68
Figure 50 Mössbauer Spectrum of JK019 at 270 K ..... 69
Figure 51 Mössbauer Spectrum of JK019 at 293 K ..... 69
Figure 52 Mössbauer Spectrum of JK019 at 293 K with a 10 kG Field ..... 70
Figure 53 Iron Oleate/Salt Mixture ..... 90
Figure 54 Iron Oleate with Added DI Water ..... 90
Figure 55 Iron Oleate with Sodium Chloride Removed ..... 91
Figure 56 Distillation of Iron Oleate Complex ..... 92
Figure 57 Thermal Decomposition Synthesis ..... 92
Figure 58 Smoke Emitted After Iron Pentacarbonyl Injection ..... 93
Figure 59 Residue on Flask Post Synthesis ..... 94
Figure 60 Magnetic Separation of Sample JK022 ..... 94
Figure 61 TEM of JK020 ..... 95
Figure 62 TEM of JK023 ..... 96
Figure 63 TEM of JK026 ..... 97
Figure 64 TEM of JK027 ..... 98
Figure 65 TEM of JK028 ..... 99
Figure 66 TEM of JK029 ..... 99
Figure 67 TEM of JK30 ..... 100
Figure 68 TEM of JK038 ..... 100
Figure 69 TEM of JK039 ..... 101
Figure 70 TEM of JK041 ..... 101
Figure 71 TEM of JK042 ..... 102
Figure 72 TEM of A) JK040 and B) JK043 ..... 103
Figure 73 TEM of A) JK040 B) JK043 ..... 103
Figure 74 DLS Distribution Results for JK020 ..... 104
Figure 75 DLS Distribution Results for JK021 ..... 105
Figure 76 DLS Distribution Results for JK022 ..... 106
Figure 77 DLS Distribution Results for JK023 ..... 107
Figure 78 DLS Distribution Results for JK024 ..... 108
Figure 79 DLS Distribution Results for JK025 ..... 109
Figure 80 DLS Distribution Results for JK026 ..... 110
Figure 81 DLS Distribution Results for JK027 ..... 111
Figure 82 DLS Distribution Results for JK028 ..... 112
Figure 83 DLS Distribution Results for JK029 ..... 113
Figure 84 DLS Distribution Results for JK030 ..... 114
Figure 85 DLS Distribution Results for JK031 ..... 115

Figure 86 Mössbauer Spectrum of JK020 at 6 K ..... 116
Figure 87 Mössbauer Spectrum of JK021 at 6 K ..... 116
Figure 88 Mössbauer Spectrum of JK023 at 6 K ..... 117
Figure 89 Mössbauer Spectrum of JK025 at 6 K ..... 117
Figure 90 Mössbauer Spectrum of JK026 at 6 K ..... 118
Figure 91 Mössbauer Spectrum of JK027 at 6 K ..... 118
Figure 92 Mössbauer Spectrum of JK028 at 6 K ..... 119
Figure 93 Mössbauer Spectrum of JK029 at 6 K ..... 119
Figure 94 Mössbauer Spectrum of JK029 at 290 K ..... 120
Figure 95 Mössbauer Spectrum of JK030 at 6 K ..... 120
Figure 96 Mössbauer Spectrum of JK031 at 6 K ..... 121
Figure 97 Mössbauer Spectrum of JK032 at 290 K ..... 121
Figure 98 Mössbauer Spectrum of JK033 at 6 K ..... 122
Figure 99 Mössbauer Spectrum of JK033 at 290 K ..... 122
Figure 100 Mössbauer Spectrum of JK034 at 6 K ..... 123
Figure 101 Mössbauer Spectrum of JK034 at 293 K with a 10 kG Field ..... 123
Figure 102 Mössbauer Spectrum of JK034 at 300 K ..... 124
Figure 103 Mössbauer Spectrum of JK034 at 300 K with a 0.078 T Field ..... 124
Figure 104 Mössbauer spectrum of JK036 at 6 K ..... 125
Figure 105 Synthesis of iron nanoparticles with separatory funnel ..... 137
Figure 106 Synthesis of iron nanoparticles with distillation column ..... 138
Figure 107 FEI Tecnai Osiris TEM at VINSE ..... 139
Figure 108 TEM single tilt sample holder ..... 139
Figure 109 Varian MR Imaging System ..... 140
Figure 110 Concentrated samples in NMR tubes ..... 141
Figure 111 Placement of NMR tubes ..... 141
Figure 112 Probe Sonicator at Vanderbilt University ..... 142
Figure 113 Prepared NMR Tubes of Varying Concentrations ..... 142
Figure 114 A) Before and B) After Probe Sonication of Sample JK048 ..... 143
Figure 115 Mössbauer Spectrometer Setup ..... 143
Figure 116 TEM of JK044 ..... 144
Figure 117 TEM of JK045 ..... 145
Figure 118 TEM of JK046 ..... 146
Figure 119 TEM of JK046B ..... 147
Figure 120 TEM of JK047 ..... 148
Figure 121 TEM of JK047B ..... 149
Figure 122 TEM of JK048 ..... 150
Figure 123 TEM of JK049 ..... 151
Figure 124 TEM of JK049B ..... 152
Figure 125 TEM of JK050 ..... 153
Figure 126 TEM of JK051 ..... 154
Figure 127 Original T2 and T1 Map ..... 155
Figure 128 T2 and T1 Map of Varying Concentrations ..... 155
Figure 129 Mössbauer Spectrum of JK044 at 5K ..... 156

Figure 130 Mössbauer Spectrum of JK044 at 293K ..... 156
Figure 131 Mössbauer Spectrum of JK045 at 5K ..... 157
Figure 132 Mössbauer Spectrum of JK045 at 293K ..... 157
Figure 133 Mössbauer Spectrum of JK046 at 5 K ..... 158
Figure 134 Mössbauer Spectrum of JK046 at 293 K ..... 158
Figure 135 Mössbauer Spectrum of JK046 at 293 K in 10 kG Field ..... 159
Figure 136 Mössbauer Spectrum of JK047 at 5K ..... 159
Figure 137 Mössbauer Spectrum of JK047 at 293K ..... 160
Figure 138 Mössbauer Spectrum of JK047B at 5K ..... 160
Figure 139 Mössbauer Spectrum of JK047B at 293K ..... 161
Figure 140 Mössbauer Spectrum of JK047B at 5K after One Week in Air ..... 161
Figure 141 Mössbauer Spectrum of JK047B after Two Weeks in Air ..... 162
Figure 142 Mössbauer Spectrum of JK047B at 6K after Three Weeks in Air ..... 162
Figure 143 Mössbauer Spectrum of JK047B at 6K after Four Weeks in Air ..... 163
Figure 144 Mössbauer Spectrum of JK047B at 6K after Five Weeks in Air ..... 163
Figure 145 Mössbauer Spectrum of JK047B at 293K after Five Weeks in Air ..... 164
Figure 146 Mössbauer Spectrum of JK048 at 5K ..... 164
Figure 147 Mössbauer Spectrum of JK048 at 293K ..... 165
Figure 148 Mössbauer Spectrum of JK049 at 6K ..... 165
Figure 149 Mössbauer Spectrum of JK049 at 293K ..... 166
Figure 150 Mössbauer Spectrum of JK049B at 6K ..... 166
Figure 151 Mössbauer Spectrum of JK049B at 293K ..... 167
Figure 152 Mössbauer Spectrum of JK050 at 6K ..... 167
Figure 153 Mössbauer Spectrum of JK050 at 293K ..... 168
Figure 154 Mössbauer Spectrum of JK051 at 6K ..... 168

# CHAPTER I
# INTRODUCTION

The aim of this research is to develop iron nanoparticles suitable for use as MRI contrast agents, for enhancement of LITT, and to combine these capabilities for MRgLITT. Synthesis methods employed are reduction and thermal decomposition of various iron reactants. Several biocompatible coatings were investigated to determine their performance as a protective layer. Characterization techniques used include DLS, TEM, Mössbauer Spectroscopy, NMR, and cytotoxicity. The main target of this biomedical application is to further the diagnosis and treatment of brain cancer, specifically glioblastoma multiforme.

## Magnetic Resonance Imaging

Nanoparticles containing iron, including metallic iron (Fe), maghemite ($\gamma$-$Fe_3O_4$) and magnetite ($Fe_3O_4$), are being heavily researched for their applications in medicine, including magnetic hyperthermia and Magnetic Resonance Imaging (MRI) (Pinsanic). Iron nanoparticle contrast agents offer improvement to current MRI technologies and can be used in combination with hyperthermia therapies to precisely treat tumors. Image-guided hyperthermia treatments have been shown to be an efficient diagnostic and therapeutic tool in recent oncology clinical trials (Lewin).

MRI contrast agents are fast-relaxing superparamagnets which shorten the relaxation time of surrounding protons. They typically reduce T2 and T2*-weighted relaxation times resulting in a negative contrast. This spin-spin relaxation is due to induced local field inhomogeneities and is described by relaxivity R2 (1/T2). The relaxivity of the particles is associated with their magnetic susceptibility as a function of particle size and composition (Qiao). Metallic iron has the highest room-temperature magnetic susceptibility of any element, giving it the strongest response to an applied field (Huber). Along with a low magneto-crystalline anisotropy, metallic iron has more magnetism per unit volume than nickel, cobalt or its oxide counterpart. It also exhibits a greater magnetic moment than any other metal (Huber).

Induced hyperthermia for cancer treatment is another significant contribution magnetic nanoparticles can make to medicine. They are introduced directly at the tumor or through systemic injection. The high magnetic saturation of the nanoparticles would allow them to absorb energy from an alternating magnetic field and convert it to heat through hysteresis losses or Néel relaxation (Laurent). The hypoxic environment of tumor cells cause them to be more sensitive to

heat than normal cells (Rahmathulla). This allows the tumor to be eliminated with minimal collateral damage to surrounding tissue (Hafeli).

Since nanophase toxicity is widely disputed, it is extremely important to test the iron nanoparticles thoroughly before putting them into use (Yu). The nanoparticle medium must be biocompatible to serve as a viable hyperthermia or MRI contrast agent. Producing metallic iron nanoparticles in a form that can be used in biomedical applications is challenging due to the risk of oxidation in biocompatible solvents (Reddy).

Previous researchers have successfully made metallic iron nanoparticles, but they were embedded in layers, such as graphene oxide sheets (Tucek) and polymer layers (Mørup) or onto surfaces (Christensen). For clinical use, it is necessary to make free, metallic iron particles which can be made into a suspension for injection into a patient's blood stream.

To achieve MRI contrast, materials must have high saturation magnetization (Hofmann). Metallic iron has a much greater saturation magnetization ($\mu_0 M_s$ = 2.16 T) than iron oxide (0.54 T) and would allow for less contrast medium to be used while achieving better resolution (Coey). Hence iron is a highly attractive option of nanoparticles for medical applications and is the subject of this dissertation.

Another important characteristic is size as size affects magnetic moment and the response magnetic nanoparticles have to external magnetic fields. A decreased MNP size will cause a faster relaxation time, which will increase their heating rate. This increased heating rate will make smaller sized nanoparticles more efficient as an MRI contrast agent and hyperthermia therapy (Reddy).

## Laser Induced Thermal Therapy

In recent years, development of nanomaterials for medical applications has been a major focus amongst scientists. Magnetic nanoparticles (MNPs) are a subset of nanoparticles (particulate material of size < 100 nm) able to be directed under the influence of a magnetic field. These magnetic properties are desirable for their potential applications in magnetic resonance imaging (MRI), hyperthermia therapies, and drug delivery (Shubayev, Wu).

In using Laser-induced Thermal Therapy (LITT) as a hyperthermia treatment of cancer, localized photo-thermal heating will cause tumor tissue to reach coagulation temperatures while sparing healthy tissue (Carpentier). Superparamagnetic MNPs will absorb energy from a near-infrared laser and convert it to heat. Because tumor tissue is more susceptible to heat than healthy tissue, this can be used to destroy the tumor (Laurent).

Size affects the magnetic moment and response MNPs have to external magnetic fields. A decrease in size of MNPs will result in a faster relaxation time, which would increase their heating rate and make them more efficient as hyperthermia therapies or MRI contrast agents. Particle size has been known to influence the signal (T2/T1) in MRI (Reddy).

Size also affects the biocompatibility of MNPs. Clearance of MNPs through the reticuloendothelial system is much slower with smaller particles. MNPs > 200 nm may become trapped in the spleen. In addition, uptake by the liver increases with size. MNPs larger than 10 nm have great difficulty penetrating cell walls (Reddy). For ideal heating properties and biocompatibility, it is important to synthesize iron nanoparticles < 10 nm.

Monometallic nanoparticles suffer from increased reactivity due to their large surface-to-volume ratio (Huber). If left in air, MNPs quickly oxidize, causing an undesirable decrease in magnetic susceptibility. Uncoated MNPs are prone to agglomeration attributed to their van der Waals and magnetic forces (Gupta).

Reactivity and agglomeration can be mitigated through the application of a hydrophilic coating to the nanoparticle surface. A polymeric material stabilizes the fluid by providing steric repulsion that acts as a barrier between individual particles, preventing aggregation. Polyethylene glycol (PEG) is the most popular nanoparticle coating in medicine due to its steric and nontoxic properties (Reddy). A hydrophilic PEG coating increases resistance to protein adsorption in the blood, allowing MNPs to experience a longer lifetime in the circulatory system (Illes). Circulation half-life can be amplified from several minutes to hours, sometimes even days, depending on the hydrophilic coating (Reddy).

A possible drawback to coating monometallic MNPs is reduced magnetization attributed to non-magnetic coatings or purposefully oxidized shells (Yoon). An optimal ferrofluid consisting of monometallic iron nanoparticles must achieve a balance between the desirable magnetic properties of pure iron and the biocompatibility of a coated MNP. The main goal of this work is to compare the effect different coatings have on chemical composition, size, and stability of iron nanoparticles prepared using a thermal decomposition synthesis. Transmission Electron Microscopy (TEM) and Mössbauer Spectroscopy will be employed to characterize these effects.

## Magnetic Resonance guided Laser Induced Thermal Therapy

The aim of this research is to develop a biocompatible nanoparticle that can be safely injected into humans to improve contrast imaging of T2 weighed MRI, to offer laser induced thermal treatments for those unable to undergo surgery or as palliative care, and to combine the two techniques to offer precision in targeting deep seated, hard to reach brain tumors and destroy them via hyperthermia. This combined technique is Magnetic Resonance guided Laser Induced Thermal Therapy (MRgLITT).

Magnetic Resonance guided Laser Induced Thermal Therapy (MRgLITT) is a hyperthermia therapy that uses real time magnetic resonance imaging to plan treatments preoperatively and monitor ablative therapy intraoperatively. Laser Induced Thermal Therapy (LITT) was discovered in the 1980s when tissue coagulation of brain tumor models were noted after exposure to a neodymium-doped yttrium aluminum garnet (Nd:YAG) laser. Other studies established the feasibility of LITT during this period, but the treatment was shelved due to the inability to monitor tissue heating rates in real time that lead to tissue vaporization. Progression of imaging technology has now made intraoperative thermal monitoring possible. In recent years MRgLITT has resurfaced as an option for treatment of difficult to access and recurrent glioblastomas (Rahmathulla 2014).

Adding MRgLITT to traditional and current therapies could improve patient survival in an area that needs improvement. The survival rate of glioblastoma is very low: 5 months for recurrent GBM and 14 to 16 months for newly diagnosed GBM following resection surgery, radiation

treatments, and chemotherapy. When progression occurs, there is a 6-month survival rate of just 5-15% (Lee 2016).

At least ten notable clinical trials have been performed using MRgLITT on patients with glioblastoma multiforme (King Book chapter). A majority of patients evaluated in the clinical trials had recurrent tumors, chose not to undergo radiation and/or chemotherapy treatments or were ineligible for traditional surgery. These clinical studies determined MRgLITT to be a feasible treatment, but suggested clinical trials need to be improved (i.e. larger sample sizes and randomized studies) in order to validate the efficacy of MRgLITT as a treatment for glioblastomas. Many of these clinical studies also resulted in suggestions for standard treatment procedures that could improve MRgLITT's effectiveness. One consensus among all authors of the clinical trials was the need to define the optimal role of MRgLITT moving forward as a treatment.

There are currently two commercially available systems suitable for MRgLITT: NeuroBlate (Monteris Medical Inc.) and Visualase (Medtronic Inc.). NeuroBlate uses a Nd:YAG laser with a sapphire, $CO_2$ gas-cooled laser probe. Both a side-firing and diffuse-tip probe are available. The NeuroBlate system connects to existing MRI systems and uses a thermocouple to provide real-time thermographic data seen in the figure below (Missios 2015, Lee 2016).

Visualase uses a diode laser with a quartz, saline cooled diffusion probe tip. Although Visualase's probe is omnidirectional and may not provide as much control as the side-emitting probe of NeuroBlate's system, Visualase provides a faster heating rate and can reduce a patient's time under anesthesia. The Visualase system estimates then displays damage based on the Arrhenius model of tissue damage and has the ability to set temperature limits to prevent tissue vaporization (Lee 2016).

Challenges currently facing MRgLITT include post-treatment edemas and the lack of response to focal therapies. Edemas and neurological deficits following treatments can affect patient quality of life. Many of these complications were proven temporary in clinical trials and patients were restored to pre-treatment or improved neurological function. Glioblastomas are an invasive

disease that traditional focal therapies do not adequately address, but due to its aggressive tentacle nature many therapies have not successfully treated this disease. In some cases, there may be no other treatment options available (Elder 2013).

The development of magnetic nanoparticles to improve the efficacy of MRgLITT treatments was suggested in several clinical studies (Norred 2014, Missios 2015). Nanoparticles would increase the definition of thermal gradients between healthy and tumor tissue (Missios, 2015). This would aid in sparing critical eloquent structures or tissue that might be damaged due to laser probe limitations (Rahmathulla, 2014).

Iron containing nanoparticles specifically have been shown to function as both an MR contrast agent and a heat transducer for LITT. The bi-functionality of these nanoparticles could make planning MRgLITT treatments more accurate. The exact distribution of the therapeutic agent could be imaged preoperatively and allow surgeons to adjust trajectories or time as needed to optimize treatment. This would result in increased ablation accuracy and less thermal damage to healthy tissue (Ding 2011).

# CHAPTER II
# REDUCTION OF IRON CHLORIDE

A version of this chapter was originally published by J.E. King et al.:

King JE, Hah HY, Johnson CE, Johnson JA, Pawel MD, et al. (2018) Synthesis of Iron Nanoparticles for Enhanced MRI Contrast Agents. J Nanosci Adv Tech 2(3): 14-19.

J.E. King wrote the article and performed most of the research. Dr. Gorgio and Dr. Kirkbride assisted in Cytotoxicity measurements at Vanderbilt University. Dr. Rondinone and M.D. Pawel provided guidance during synthesis at Oak Ridge National Laboratory. Dr. Hah and Dr. C. Johnson assisted with Mössbauer spectroscopy. Dr. J. Johnson supervised the work. Changes have been made to this article for inclusion in this dissertation. The synthesis and characterization of nine more samples were added. DLS results were added for previously mentioned and newly added samples. Additional TEM results and Mössbauer Spectroscopy results were included for all samples.

## Introduction

In this chapter, iron metal nanoparticles and superparamagnetic iron oxide nanoparticles were successfully synthesized. Thirteen samples were created using a reduction method with various coatings and synthesis techniques. These results were confirmed by Mössbauer Spectroscopy, Transmission Electron Microscopy (TEM), and Dynamic Light Scattering (DLS). Cell toxicity was evaluated on one sample to ensure the biocompatibility required for medical applications.

## Methods

### *Iron Nanoparticle Syntheses*

A summary of synthesis conditions including type, coating, and solvent can been seen in Table 1.

### *Synthesis I*

Samples JK001-JK007 were synthesized at the Center for Nanophase Materials at Oak Ridge National Laboratory, Oak Ridge, TN by reacting 2.4 g iron (II) chloride (Sigma Aldrich) and 30 mL pure ethanol (Decon Labs) with 1.2 g sodium borohydride (Sigma Aldrich) and 30 mL deionized water. The two mixtures were collected into 30 mL syringes and placed in a dual syringe pump; the pump was set to a rate of 5 mL per minute. The nanoparticles were formed when the borohydride solution interacted with the chloride solution by reducing it in a nitrogen atmosphere. For samples JK001, JK003, JK006 and JK007 the reduction reaction continued down the

**Table 1 Summary of synthesis conditions for iron chloride reduction samples**

| Sample | Synthesis Type | Coating | Solvent |
|---|---|---|---|
| JK001 | Reduction with syringe pump and separatory funnel into flask | Brij 30 | Ethanol |
| JK002 | Reduction with syringe pump into flask | Brij 30 | Ethanol |
| JK003 | Reduction with syringe pump and separatory funnel into flask | Brij 30 | Ethanol |
| JK004 | Reduction with syringe pump into flask | Brij 30 | Ethanol |
| JK005 | Reduction with syringe pump into flask | Brij 30 | Ethanol |
| JK006 | Reduction with syringe pump and separatory funnel into flask | Brij 30 | Ethanol |
| JK007 | Reduction with syringe pump and separatory funnel into flask | PEG 600 diacid | Ethanol |
| JK009 | Reduction with syringe pump and separatory funnel into flask | none | Ethanol |
| JK010 | Reduction without funnels and syringe pump | Brij 30 | Ethanol |
| JK011 | Reduction with syringe pump and separatory funnel into flask | PEG 600 diacid | Ethanol |
| JK012 | Reduction with syringe pump and separatory funnel into flask | PEG 600 diacid | Ethanol |
| JK018 | Reduction with funnels into flask | Brij 30 | Ethanol |
| JK019 | Reduction with funnels into flask | Brij 30 | Ethanol |

separatory funnel then the side of a round bottom flask and into a stirring coating mixture as seen in Figure 1 (all figures can be found in the chapter's Appendix). Samples JK002, JK004, and JK005 did not utilize the separatory funnel and instead the tubing from the syringe pump fed directly onto the neck of a round bottom flask, down the side of the flask and into a stirring coating mixture as seen in Figure 2. The coating mixtures for samples JK001-JK006 consisted of 10 mL Brij 30 (Sigma Aldrich) and 50 mL ethanol. The coating mixture for sample JK007 consisted of 10 mL polyethylene glycol diacid 600 (Sigma Aldrich) in 50 mL of ethanol. The particles were stirred at 250 rpm for 30 minutes to break up the agglomerations and sufficiently coat the particles.

*Washing and Sample Work-Up*

The coated particles were centrifuged at 9000 rpm for 10 minutes and washed with ethanol twice then transferred to a sample jar and sonicated for 45 minutes to break up agglomerates. After sonication the particles were magnetically separated using a neodymium magnet below the sample jar and pipetting off the liquid remaining above the particles.

***Synthesis II***

Samples JK009-JK012 were synthesized at the University of Tennessee Space Institute in Tullahoma, TN. Sample JK009 replicated the procedure for Synthesis I with a separatory funnel using 4.8 g iron (ii) chloride (Sigma Aldrich) in 60 mL of ethanol and 1.2 g sodium borohydride (Sigma Aldrich) in 30 mL ultrapure water into the Brij 30 (Sigma Aldrich) coating mixture.

Sample JK010 was prepared by slowly pouring 1.2 g sodium borohydride in 30 mL ultrapure water into 1.2 g iron (ii) chloride in 30 mL ethanol. The reaction was extremely exothermic and released a lot of gas. The reaction mixture was swirled for 30 seconds to aid mixing then stirred for 5 minutes.

For samples JK011 and JK012 iron reactant and sodium borohydride solutions were prepared by sonicating 2.4 g iron (ii) chloride with 60 mL ethanol and 2.4 g sodium borohydride with 60 mL deionized water. 25 mL of each solution was taken up into 30 mL syringes through tubing and placed in a dual syringe pump; the pump was set to a rate of 8 mL per minute. The nanoparticles formed by reacting down the side of a separatory funnel and neck of a round bottom flask into 50 mL of a coating mixture as seen in Figure 3. The coating mixture was prepared by stirring 40 mL

PEG diacid 600 and 200 mL ethanol. Sample JK011 was stopped after 20 mL of the reactant solutions were dispensed; the sodium borohydride mixture outgassed before the entirety could be used. For the same reason and due to the pump stalling on five occasions, JK012 was stopped after 17 mL of iron chloride solution had been dispensed. 50 mL and 15 mL of coating solution was used to rinse the stir bar of particles for JK011 and JK012 respectively.

*Washing and Sample Work-Up*

Samples JK011 and JK012 were magnetically separated from the reaction solution. Ethanol was added to rinse the particles followed by magnetic separation of particles from solution; this was repeated three times. (DLS samples were diluted with ethanol and sonicated. Mössbauer samples were taken as is after washing).

***Synthesis III***

Samples JK018 and JK019 were synthesized at the Center for Nanophase Materials at Oak Ridge National Laboratory, Oak Ridge, TN by reacting 2.4 g iron (II) chloride (Sigma Aldrich) and 30 mL pure ethanol (Decon Labs) with 1.2 g sodium borohydride (Sigma Aldrich) and 30 mL deionized water. The two mixtures were added to two different separatory funnels. The funnels were placed so that the ends of the funnels met together on the side of a funnel above a flask as seen in Figure 4. This was done to provide maximum reaction time and decrease particle size. The nanoparticles were formed when the borohydride solution interacted with the chloride solution by reducing it down the sides of the glassware into a coating mixture under argon gas flow. The coating mixture consisted of 10 mL Brij 30 (Sigma Aldrich) and 50 mL ethanol. The reaction rate was controlled by adjusting the stoppers of the separatory funnels for each solution. The separatory funnel containing iron chloride was closed off when the sodium borohydride had outgassed; this was done to prevent unreacted iron chloride in the product. The particles were stirred at 250 rpm for 30 minutes to break up the agglomerations and sufficiently coat the particles.

*Washing and Sample Work-Up*

The coated particles were magnetically separated from the reaction solution. Ethanol was added to rinse the particles followed by magnetic separation of particles from solution. Samples were magnetically separated using a neodymium magnet below the sample jar and pipetting off the liquid remaining above the particles; this was repeated three times. For Sample JK019, 10 mL of

toluene was added to aid particle suspension in storage.

## Characterization

***Transmission Electron Microscopy***

Transmission electron microscopy (TEM) was performed at the Center for Nanophase Materials at Oak Ridge National Laboratory, Oak Ridge, TN using a Zeiss Libra 120. Samples were prepared by diluting the nanoparticles with ethanol until the solution was barely tinted as in Figure 5. A copper TEM grid was dipped into the solution and dried in air. Samples JK001, JK002, JK003, JK004, JK005, JK006, JK007, and JK018 were characterized using this technique.

***Dynamic Light Scattering***

Dynamic Light Scattering (DLS) analysis was performed at the University of Tennessee Space Institute, Tullahoma, TN using a Particulate Systems NanoPlus Zeta/Nano Particle Analyzer. Samples were prepared by diluting the nanoparticles with ethanol until the solution was barely tinted as seen in Figure 6. The diluted solution was pipetted into a quartz cuvette. Analysis was performed using the NanoPlus software program. Samples JK001, JK002, JK007, JK011 and JK012 were characterized using this technique.

***Cytotoxicity***

Cytotoxicity studies were performed at Vanderbilt University, Nashville, TN using varying concentrations of JK003. Sample JK003 was selected for this experiment because it appeared the most promising with respect to size from TEM results; ideal diameters are 3-7 nm. Mössbauer spectroscopy had not been completed at this time but JK003 was later determined to possess metallic iron.

Luc-231 cells, human breast cancer MDA-MB-231 cells that are stably transfected to constitutively expressed firefly luciferase, were cultured in DMEM (Gibco, Carlsbad, CV) with 10% FBS (Gibco, Carlsbad, CA) and 50 µg/mL gentamicin (Gibco, Carlsbad, CA). Cells were isolated by incubation for 5 minutes in 0.05% trypsin. Isolated cells were centrifuged at 1000 rpm for 5 minutes in conical tubes to separate the cells from the media. The supernatant was discarded and cells were re-suspended in DMEM. The concentration and viability of cells were assessed using trypan blue and measured in a hematocytometer shown in Figure 7. Cells were cultured in

96 well plates with an initial seeding density of 50,000 cells per $cm^2$.

Iron nanoparticles were added to the cells at various dilutions and untreated wells served as controls. Nanoparticle concentrations were estimated by volume. Nanoparticles were in contact with cells for 17, 24 or 48 hours prior to the replacement of cell culture medium with DMEM containing 1:200 luciferin. Plates were imaged using a Xenogen IVIS 200 imaging system and the luminescence was measured in radiance (photons). Cell growth suppressed by iron nanoparticles are detected by a reduced luminescence intensity relative to untreated controls in direct proportion to cell number and metabolism.

***Mössbauer Spectroscopy***

The Mössbauer Spectroscopy experiments were performed at The University of Tennessee Space Institute (UTSI), Tullahoma, TN using a $^{57}Co$ source, a Janis SHI-850-5 cryogen-free cryostat, Lakeshore 325 Temperature Controller (seen in Figure 8) and Mössbauer GenFit Software (R.S. Preston and D.E. Brown) for analysis. Samples were prepared by pipetting concentrated nanoparticle solutions into Mössbauer sample cups made at UTSI. The samples were dried by allowing the ethanol to evaporate in air; this can be seen in Figure 9. Once dry, a plug was used to seal the sample cup. Samples JK002, JK003, JK004, JK007, JK011, JK012, JK018, and JK019 were characterized using this technique.

Sample JK002 was characterized at 6 Kelvin (K), 293 K (room temperature), 293 K with a 10 kilogauss (kG) field, and at 6 K two months post synthesis. Sample JK003 was characterized at 6K, 6K with a 0.073 Tesla (T) perpendicular field, 293 K, 293 K with a 10 kG field, 6 K two years post synthesis, and again at 6 K, 293 K, 293 K with a 10kG and 20 kG field four years post synthesis. Samples JK004 and JK007 were characterized at 6 K. Sample JK011 was characterized at 6 K, 293 K, and 293 K with a 10 kG field. Sample JK012 was characterized at 6 K, 180 K, 250 K, 293 K, and 293 K with a 10 kG field. Sample JK018 was characterized at 6 K, 293 K, and 300 K. Sample JK019 was characterized at 6 K, 6 K with a 0.073 T perpendicular and parallel fields, 260 K, 270 K, 293 K, and 293 K with a 10 kG perpendicular field. A summary of these samples and their experimental conditions can be seen in Table Q alongside their results.

Anhydrous iron (II) chloride reactant used in nanoparticle syntheses was characterized with

Mössbauer Spectroscopy to compare with sample results, specifically JK011 and JK012. An iron calibration spectrum was obtained from the Mössbauer Spectrometer to compare with our synthesized samples. A $^{57}$Co source was used for the calibration and sample runs. The chemical isomer shift of metallic iron is 0 mm/s. The hyperfine field is shown by the distance between the first and last lines.

Hyperfine fields are the measure of the internal field in the nucleus of a particular iron atom. A metallic iron atom has a hyperfine field of 330 kG, which will Zeeman split and span the spectrum between ± 5.1 mm/s. However, the oxides have a much larger field (anywhere from 490 kG upwards), which will span the spectrum over a range larger than 5.1 mm/s.

Samples were run at 6 K to avoid potential relaxation effects. Nanoparticles below a critical size are superparamagnetic at room temperature and can yield a non-Zeeman split spectrum; samples were run at room temperature (293 K) to determine this characteristic. Samples were run between 6 K and 300 K to find their blocking temperature.

# Results

### *Characterization*

#### *Transmission Electron Microscopy*

TEM results show that the diameter of nanoparticles for Sample JK001 are 4-7 nm with 20-70 nm agglomerates (Figure 10). TEM results also revealed excess coating that had not been removed by sample washing (Figure 10D, 10F). Sample JK001 demonstrates an excellent core and shell structure (Figures 10A, 10C, 10G, and 10D). However, some particles seemed to have completely oxidized and no longer retain their iron core as evident in Figures 10E and 10H. Other notable characteristics include rod shaped figures visible in Figure 10G.

Sample JK002 are 4-12 nm (Figures 11A and 11B) with 60-150 nm agglomerates (Figures 11E and 11D). Residual coating appears to remain in this sample as well (Figure 11F). Sample JK002 demonstrated a greater size distribution than Sample JK001 (Figure 11C compared to Figure 10E). As in Sample JK001, some particles seem to have completely oxidized at the time of characterization (Figures 11A and 11B). TEM was performed on Samples JK001 and JK002 four

and three days after synthesis respectively, so smaller particles may have oxidized from the shell inward before characterization.

Sample JK003 are 3-7 nm (Figures 12A and 12B) with 25-40 nm agglomerates (Figure 12C). Sample JK003 demonstrates excellent size distribution overall. Similarly to JK001, there are rod-like structures present (Figure 12D) and some particles seem to have completely oxidized (Figures 12A and 12D).

Sample JK004 is 4-11 nm (Figures 13A, 13B, and 13C) with 45-150 nm agglomerates (Figures 13B and 13D), and there appears to be lots of residual coating (Figures 13D and 13C). Sample JK005 is 11-33 nm with agglomerates >330 nm (Figures 14A and 14B). This sample has notable core and shell structures ranging from 11-18 nm cores and 20-33 nm with a shell (Figures 14A and 14B). Sample JK006 is 13-48 nm (Figure 15A) with agglomerates >340 nm (Figure 15B). Like JK005, Sample JK006 also has a notable core and shell structure. Sample JK007 is 32-52 nm with agglomerates >440 nm (Figure 16) and has a thicker coating than previous samples. It is difficult to discern individual particle sizes in this sample.

Sample JK018 is 8-35 nm (Figure 17C) with agglomerates >230 nm (Figures 17A and 17B). JK018 had several extremely large particles (Figures 17D and 17E). Figures 17A and 17B appear to show remnants of coating, poor workup and/or coated agglomerates. Sample JK018 demonstrated the largest size distribution in TEM while Sample JK003 had the smallest visible size distribution. A summary of these results can be seen in Table 2.

TEM indicates all the nanoparticles are coated and agglomerated. The results infer a larger reaction distance created by using the separatory funnel produced a smaller iron core; the sodium borohydride was able to reduce the iron (ii) chloride more with the greater distance allowed. The Brij 30 appeared to be a superior coating over the polyethylene glycol 600 diacid. The sample coated in polyethylene glycol 600 diacid (JK007) was ≥50 nm in diameter, and the thickness of its coating was greater than that of Brij 30 coated samples. The result is a product too large for contrast agent applications.

**Table 2 TEM size analysis of iron chloride reduction samples**

| Sample | Smallest Diameter | Largest Diameter | Agglomerates |
|---|---|---|---|
| JK001 | 3.8 nm | 6 nm core, 7 nm total | 20-70 nm |
| JK002 | 4 nm | 12 nm | 60-150 nm |
| JK003 | 3 nm | 6.5 nm | 25-40 nm |
| JK004 | 4 nm | 11 nm | 45-150 nm |
| JK005 | 11 nm | 11 nm core, 33 nm total | 330 nm, >400 nm |
| JK006 | 8 nm core, 13 nm total | 25 nm core, 48 nm total | >340 nm |
| JK007 | 17 nm core, 32 nm total | 32 nm core, 52 nm total | >440 nm |
| JK011 | n/a | n/a | n/a |
| JK012 | n/a | n/a | n/a |
| JK018 | 8 nm | 35 nm | >230 nm |
| JK019 | n/a | n/a | n/a |

***Dynamic Light Scattering***

DLS cumulants results of Sample JK001 indicated a particle size of 1421.7 nm with a polydispersion index (PDI) of 0.772. Sample JK002 yielded a particle size of 383.2 nm with PDI of 0.226. Sample JK007 results gave a particle size of 11,368.9 nm with a pdi of 5.035. Sample JK011 exhibited particle size of 959.1 nm with a pdi of 0.572. Sample JK012 cumulant results gave a particle diameter of 818.9 nm with a pdi of 0.485.

DLS cumulants results contradicted TEM images and characterized particles as up to 11,000 nm in size. Polydispersion indexes (PDI) for samples ranged from 0.226 to 5.065. An ideal PDI, meaning particles are monodispersed, is a value of 0.0. Sample JK007's PDI was especially off indicating a very broad size distribution. Sample JK002 was closest to an ideal PDI. Intensity, number, and volume distribution analysis were performed to discern agglomerate groups and provide an explanation for the high particle size results. The cumulants results of samples and their PDI are compared to TEM results in Table 3.

Sample JK001 yielded three distribution peaks. Intensity results show particle sizes of 90.2 nm ± 9.5 nm, 598.6 nm ± 109.3 nm, and 20,908.7 nm ± 4,657.2 nm. Number distribution values for JK001 are 84.8 nm ± 1.0 nm, 497.7 nm ± 82.1 nm, and 16,198.4 ±3,011.1 nm. Volume distribution values for JK001 are 87.3 nm ± 9.0 nm, 542.6 nm ± 97.9 nm, and 18,151.9 nm ± 3, 9010.8 nm... Sample JK001 distribution results are presented in Figure 18.

Sample JK002 yielded one distribution peak. Intensity results for JK002 are 520.7 nm ± 306.5 nm. Number distribution values for JK002 are 160.6 nm ± 45.9 nm. Volume distribution values for JK002 are 227.4 nm ± 113.3 nm. Sample JK002 distribution results are presented in Figure 19.

Sample JK007 yielded two distribution peaks. Intensity results for JK007 are 253.9 nm ± 24.0 nm and 34,006.6 nm ± 6,609.9 nm. Number distribution values for JK007 are 241.6 nm ± 20.9 nm and 27,720.3 nm ± 4,761.9 nm. Volume distribution values for JK007 are 247.3 nm ± 22.8 nm and 30,466.9 nm ± 5,804.3 nm. Sample JK007 distribution results are presented in Figure 20.

Sample JK011 yielded two distribution peaks. Intensity results for JK011 are 462.4 nm ± 53.5 nm and 19,244.6 nm ± 3,153.0 nm. Number distribution values for JK011 are 444.2 nm ± 51.3 nm and

**Table 3 DLS cumulant results compared to TEM results (particle size, agglomerate size)**

| Sample | DLS Diameter | PDI | TEM Diameter |
|---|---|---|---|
| JK001 | 1421.7 nm | 0.772 | 3-7 nm, 20-70 nm |
| JK002 | 383.2 nm | 0.226 | 4-12 nm, 60-120 nm |
| JK003 | n/a | n/a | 3-7 nm, 25-40 nm |
| JK004 | n/a | n/a | 4-11 nm, 45-145 nm |
| JK005 | n/a | n/a | 11-33 nm, >330 nm |
| JK006 | n/a | n/a | 13-48 nm, >340 nm |
| JK007 | 11368.9 nm | 5.035 | 32-52 nm, >440 nm |
| JK011 | 959.1 nm | 0.572 | n/a |
| JK012 | 818.9 nm | 0.485 | n/a |
| JK018 | n/a | n/a | 8-35 nm, >230 nm |
| JK019 | n/a | n/a | n/a |

17,733.3 nm ± 2,942.9 nm. Volume distribution values for JK011 are 427.7 nm ± 47.5 nm and 16,439.8 nm ± 2,558.9 nm. Sample JK011 distribution results are presented in Figure 21.

Sample JK012 yielded two distribution peaks. Intensity results for JK012 are 480.2 nm ± 54.5 nm and 16,694.0 nm ± 2,096.0 nm. Number distribution values for JK012 are 462.1 nm ± 52.4 nm and 15,892.9 nm ± 2,055.9 nm. Volume distribution values for JK012 are 445.5 nm ± 48.6 nm and 15,135.0 nm ± 1,919.0 nm. Sample JK012 distribution results are presented in Figure 22. A summary of DLS results for each distribution can be seen in Tables 4, 5, and 6.

***Cytotoxicity***

Cytotoxicity studies of Sample JK003 were carried out and analyzed at Vanderbilt University. The two cell plates used were imaged using an *in vivo* optical imaging system. It measured the luminescence of the wells in radiance (photons). The higher radiance in the wells represents more surviving cells. As seen in Figure 23, the brightly colored cells (red, yellow, and green) had excellent survival rates and the dark wells (dark blue and black) represent cell death. The process was repeated for the 24 hour and 48 hour time points for both plates (Figure 24). A summary of these results can be seen in Figure 25 with the luminescence of untreated control samples normalized to 100.

Cell proliferation and viability was comparable to untreated and ethanol controls for the 1:640,000 iron nanoparticle dilution and all incubation durations, suggesting the lack of acute or chronic toxicity at this dose. Toxicity was broadly proportional to iron nanoparticle dose with significant cell death at elevated concentrations of iron nanoparticles, which was especially evident for dilutions less than approximately 1:10,000. Toxicity was not consistently different as a function of incubation duration, suggesting a rapid suppression of cell metabolism at high iron nanoparticle doses.

With a dilution rate of 1:640,000 by volume, the cells had a good survival rate compared to the ethanol control. At 24 hours, the average radiance of cells diluted to 1:640,000 was 90; by comparison, the ethanol control had an average radiance of 68 at the same time point. The 1:400,000 dilution rate represented a median amount of cell survival. These results indicate that the sample is not toxic to cells at a diluted rate and can intentionally kill cells (if desired) at higher

concentrations.

Toxicity of concentrated iron nanoparticles could also serve as a treatment for inoperable brain tumors. In this treatment, uncoated iron nanoparticles would be directly injected into the tumor. Toxicity of the uncoated nanoparticles would cause cell death to the tumor and not to the surrounding healthy cells (Yu).

***Mössbauer Spectroscopy***

In a paramagnetic material, spins are oriented when an external magnetic field is applied. This is reversible, i.e. the spins are disoriented when the magnetic field is removed. Magnetically ordered materials (ferromagnets, ferrimagnets) are composed of domains consisting of interacting spins, which are oriented when an external magnetic field is applied. But when the magnetic field is removed the domains are not completely disoriented (Hysteresis). MNPs that are the size of a single magnetic domain respond to an external magnetic field but do not become permanently magnetized, i.e. they are superparamagnetic (Huang). The domain magnetic moments fluctuate with a relaxation time. Magnetite, or $Fe_3O_4$, has a domain size of 15-80 nm (Huang).

The detection of $Fe^{3+}$ in Mössbauer would represent oxidation. Any particles smaller than 10 nm could be superparamagnetic and would therefore present as a broad line. This could split into 6 lines at low temperatures when the relaxation has slowed down.

Sample JK002 dried in air and run at room temperature was depicted as a broad singlet (Figure 27), and confirms the particles are small but unlikely  less than 5 nm in diameter as the peak would appear more narrow; this was confirmed by TEM. Sample JK002 at 6 K initially presented as iron metal (Figure 26); however, two months after synthesis, the samples presented as an oxide, specifically $\gamma$-$Fe_2O_3$ in the spectra seen in Figure 28.

The spectra of Sample JK003, run at 9 K in the cryostat (Figure 29) closely matches the iron calibration spectra (±5.2mm/sec or 330 kG) but with broader lines. Sample JK003 was run again three and a half years after synthesis at 6 K (Figure 30); this revealed the sample had become 81% oxide. The sample was stored in a sealed vial and kept in air over this period. The sample was run again four years after synthesis at 6 K, 293 K, and 293 K with a 10 kG field. The results can be

seen in Figures 31, 32, and 33. Four years post-synthesis the sample had maintained 15% metallic iron. This is an increase in oxidation of 4% over six months. 85% of the sample had mostly oxidized to $\gamma$-$Fe_2O_3$ resembling Sample JK002. We believe the smaller iron metal nanoparticles fully oxidized to $\gamma$-$Fe_2O_3$ and the larger iron metal nanoparticles maintained a metallic core with a $\gamma$-$Fe_2O_3$ shell. The preservation of metallic iron could be attributed to Sample JK003's longer reaction time and/or the efficiency of the coating. The 10 kG spectra (Figure 33) at room temperature confirms Sample JK003 contains nanoparticles due to its large susceptibility.

Sample JK004 ran at 6 K revealed the sample was completely oxidized (Figure 34). Sample JK007 was determined to be a mix of iron metal (59%) and iron oxide (41%) according to Mössbauer spectroscopy (Figure 35).

Sample JK011 at room temperature (Figure 37) closely resembles the Mössbauer spectrum of $FeCl_2$ reactant used in the synthesis (Figure 43). This indicates much of the sample, if any, did not reduce to form iron nanoparticles. Sample JK012 revealed quadrupole splitting similar to its iron chloride reactant but not matching it (Figures 39-42). Samples JK018 and JK019 both contained a mix of iron metal and iron oxides (Figures 44-51). A summary of these results can be seen in Table 4.

## Discussion

The characterization results show that small nanoparticles (3-20 nm) were successfully synthesized, most likely due to a longer reaction length. Synthesis utilizing the separatory funnel resulted in smaller particles than those synthesized without the funnel, which could be due to a longer reaction length or faster synthesis rate. The polyethylene glycol 600 diacid coating led to more cross linkage and larger particles. Samples synthesized without a syringe pump resulted in high size distributions.

DLS cumulants results were artificially high compared to TEM characterization. The conflicting DLS results suggests the samples were not correctly prepared. If the samples were not completely suspended, the movement of the particles settling would yield artificial results since the software uses Brownian motion in its algorithm to determine particle size. Another contributing factor to these results could be the failure to adequately sonicate the sample. As-made samples were

**Table 4 Mössbauer results of iron chloride reduction samples**

| Sample | Temp | Field | Site 1 | Site 1 Hyperfine | Site 1 I/S | Site 2 | Site 2 Hyperfine | Site 2 I/S |
|---|---|---|---|---|---|---|---|---|
| JK002 | 6K | | 100.00% | 341.30 | 0.12 | | | |
| JK002 | 6K | | 100.00% | 463.48 | 0.47 | | | |
| JK002 | 293K | | 100.00% | 000.00 | 0.33 | | | |
| JK003 | 6K | | 100.00% | 511.20 | 0.46 | | | |
| JK003 | 5.4K | | 81.45% | 512.45 | 0.46 | 18.55% | 342.39 | 0.11 |
| JK003 | 5K | | 85.17% | 512.34 | 0.45 | 14.83% | 341.48 | 0.12 |
| JK003 | 293K | | 57.94% | 0.0 (0.78 quad) | 0.33 | 42.06% | 330.00 | 0.02 |
| JK003 | 293K | 10 kG | 12.87% | 323.54 | 0.00 | 8.64% | 0.0 (0.86 quad) | 0.32 |
| JK004 | 6K | | 100.00% | 518.52 | 0.46 | | | |
| JK007 | 6K | | 40.77% | 475.96 | 0.46 | 59.23% | 338.03 | 0.15 |
| JK011 | 293K | | 100.00% | 0.0 (0.75 quad) | 0.36 | | | |
| JK011 | 293K | 10 kG | 100.00% | 0 (0.74 quad) | 0.37 | | | |
| JK011 | 6K | | 100.00% | 0.0 (2.98 quad) | 1.35 | | | |
| JK012 | 293K | 10 kG | 100.00% | 0.0 (2.23 quad) | 1.25 | | | |
| JK012 | 293K | | 100.00% | 0.0 (2.21 quad) | 1.29 | | | |
| JK012 | 180K | | 41.23% | 0.0 (2.64 quad) | 1.33 | 58.77% | 520.0 (5.55 quad) | 2.91 |
| JK012 | 6K | | 27.71% | 0.0 (3.25 quad) | 1.34 | 72.29% | 520.0 (5.34 quad) | 2.93 |
| $FeCl_2$ | 293K | | 73.62% | 0.0 (0.78 quad) | 1.08 | 26.38% | 0.0 (2.00 quad) | 1.15 |
| JK018 | 6K | | 99.01% | 0.0 (5.64 quad) | 0.00 | 0.09% | 0.0 (2.79 quad) | -1.67 |
| JK018 | 293K | | 47.57% | 344.39 | 0.17 | 52.43% | 274.17 | 0.22 |
| JK018 | 300K | | 100.00% | 407.30 (0.64 quad) | 0.20 | | | |
| JK019 | 6K | | 22.38% | 347.72 | 0.12 | 77.62% | 293.93 | 0.19 |
| JK019 | 6K | 0.073T parallel | 18.88% | 246.09 | 0.11 | 81.12% | 299.96 | 0.23 |
| JK019 | 6K | 0.073T perpendicular | 17.85% | 343.99 | 0.11 | 82.15% | 294.44 | 0.23 |
| JK019 | 270K | | 7.59% | 330.0 | 0.00 | 92.41% | 251.83 | 0.07 |
| JK019 | 293K | 10 kG perpendicular | 6.07% | 330.0 | 0.00 | 93.93% | 242.63 | 0.00 |
| JK019 | 293K | | 3.19% | 330.0 | 0.00 | 96.80% | 405.78 (0.71 quad) | 0.20 |

concentrated after synthesis and washed from their reaction solvents for storage. When re-suspending these particles, it is possible agglomerates were never fully broken up. A longer sonication time or alternate sonication method may alleviate this issue.

Agglomeration can also be attributed to the nature of the synthesis – the particles form as agglomerates during the reaction due to the synthesis rate in both uncontrolled and controlled by a syringe pump. The coatings utilized to ensure biocompatibility and prevent oxidation bind the agglomerates together as evident in TEM. When the agglomerates are broken up via sonication, the coating may be disrupted and the particles could be left vulnerable to oxidation.

Cytotoxicity results show that cells are able to survive when introduced to the iron nanoparticles at low concentrations. At higher, intense concentrations, the cells did not survive; this is advantageous if the nanoparticles are intended for direct injection into diseased cells.

Mössbauer Spectroscopy shows that Sample JK002, synthesized with a short reaction length, contains superparamagnetic $\gamma$-$Fe_2O_3$ and metallic iron was produced in Sample JK003 with a longer reaction length. The most encouraging results are the discovery of metallic iron nanoparticles and the presence of metallic iron after four years of storage in air. Mössbauer Spectroscopy also shows that samples JK011 was not reduced to form iron nanoparticles. This might be attributed to initial inconsistency with the syringe pump used. Sample JK018 and JK019 appeared to be a mix of iron and oxides as synthesized. This could be to the lack of inert reaction environment.

***Future Work***

Future work should include the exploration of different reaction rates and coatings, sonication before coating, and/or a different source of iron. Solving the agglomeration issue is necessary for biomedical applications as the agglomerated clumps of iron act as one large particle; this affects the magnetic properties of the product and clearance from the body. Both the magnetic properties and size distribution of the nanoparticles are important for use as MRI contrast agents; the nanoparticles should be small (less than 10 nm) and monodispersed. We will also study the causes of oxidation and reasons for different oxidation rates over time between the samples (months versus years). An entirely different synthesis procedure may be required to prevent any

agglomeration and oxidation such as thermal decompositions

# Chapter II Appendix

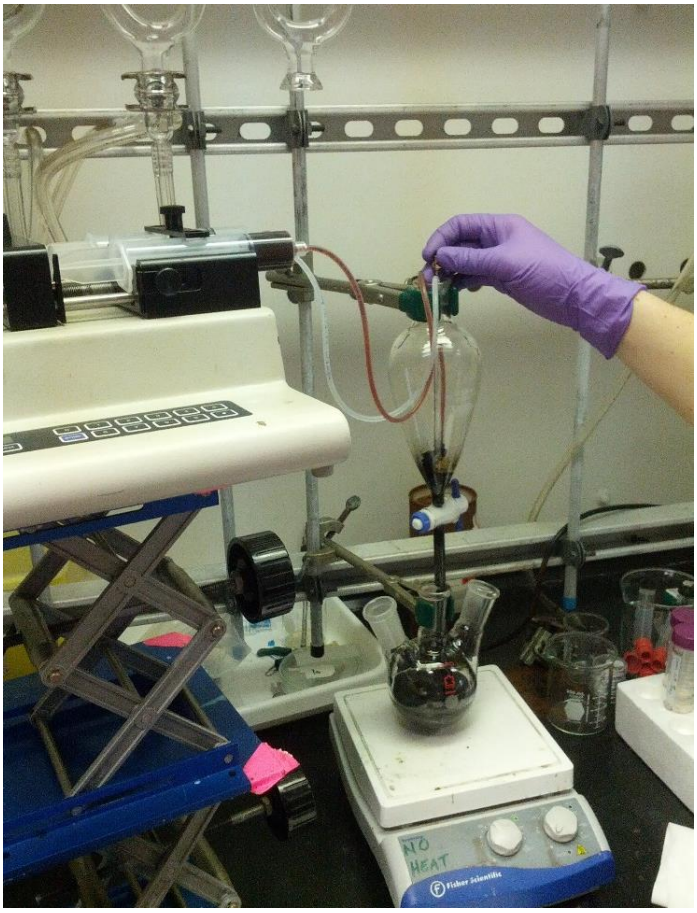



**Figure 1 Synthesis of JK001, JK003, JK006, and JK007**

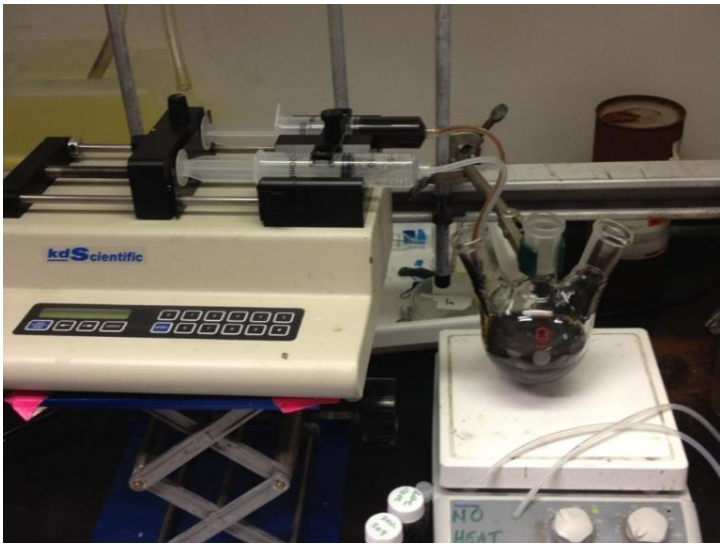



**Figure 2 Synthesis of JK002, JK004, JK005**



**Figure 3 Magnetic separation of JK002**




**Figure 4 Synthesis of JK009**



**Figure 5 Synthesis of JK018-JK019**




**Figure 6 JK001 prepared for TEM characterization**

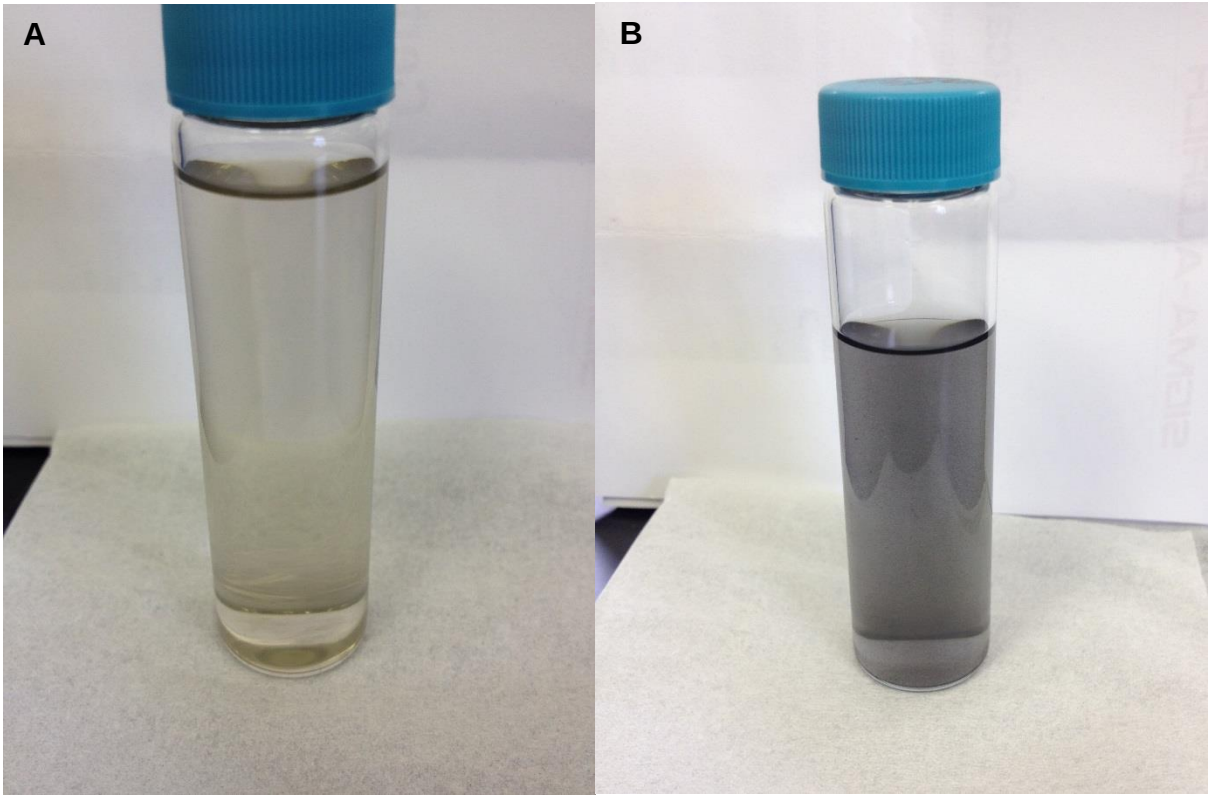



**Figure 7 DLS sample of A) JK001 and B) JK007**

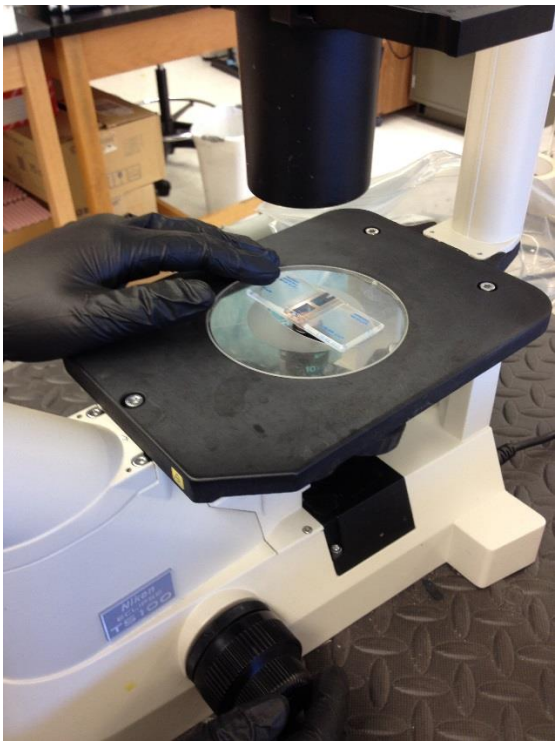


**Figure 8 Cell concentration and viability assessed using a hematocytometer**



**Figure 9 Mössbauer apparatus setup**



**Figure 10 Preparation of Mössbauer sample**

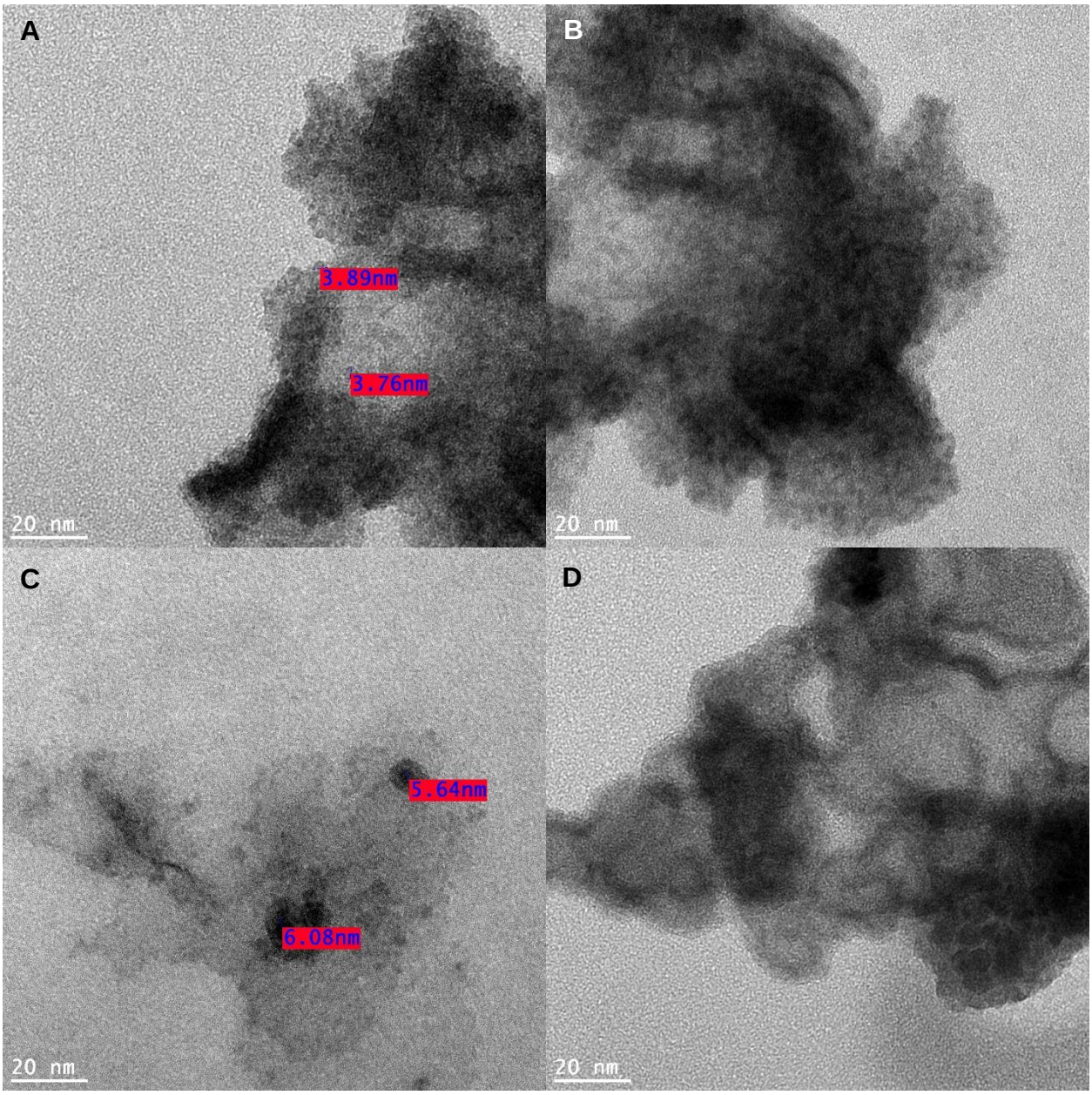



**Figure 11 TEM of JK001**

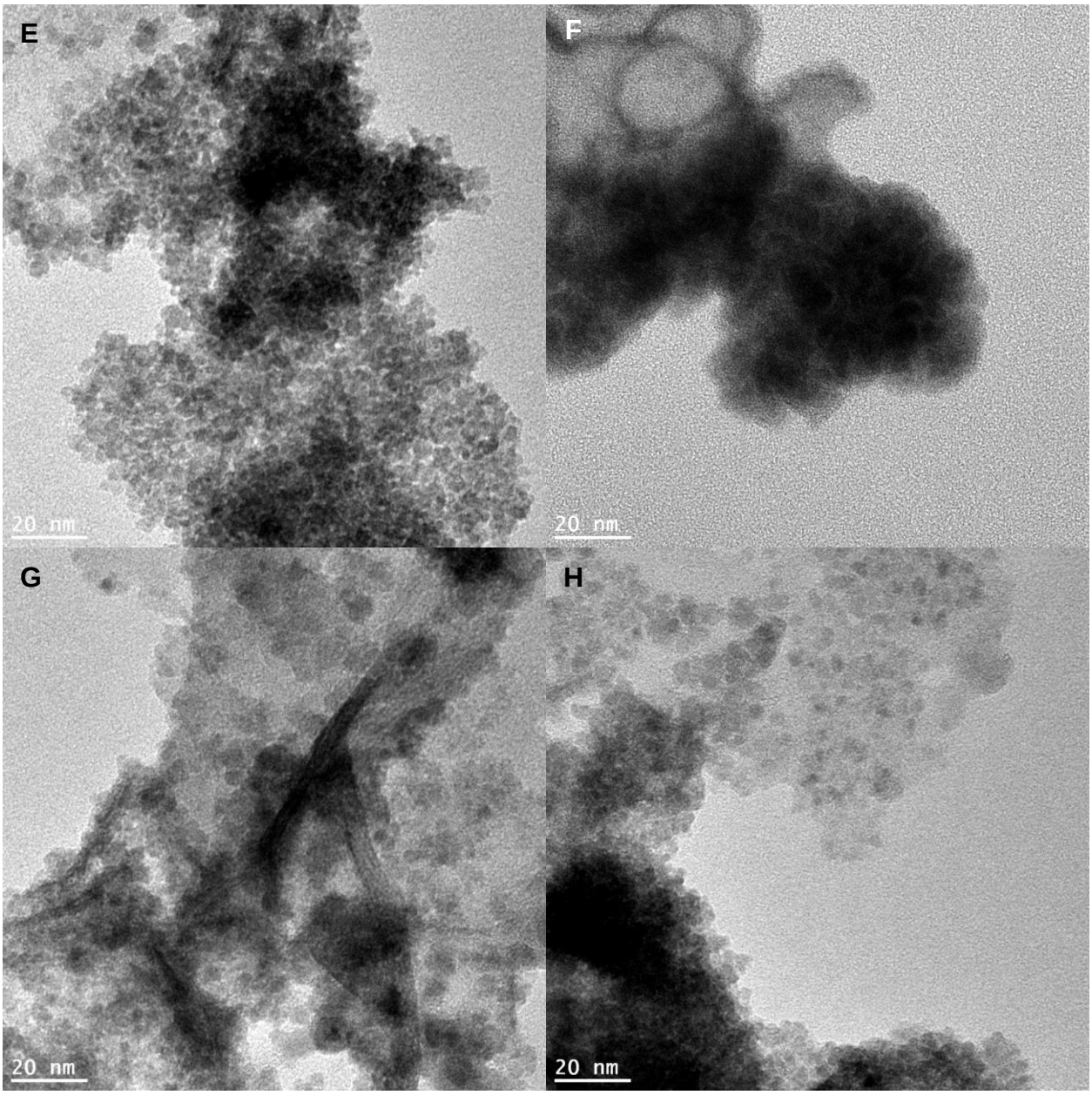



**Figure 11 continued**

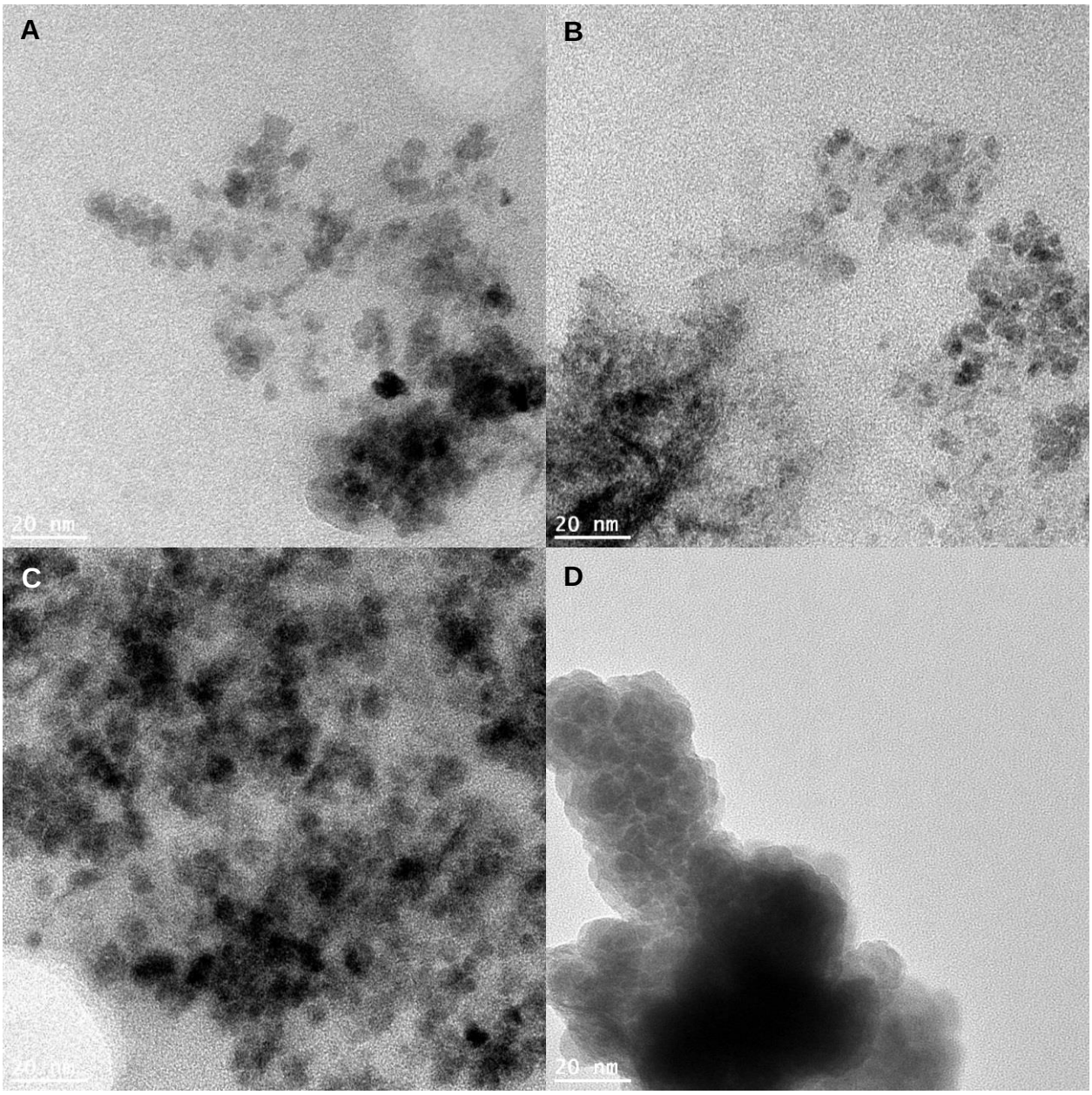



**Figure 12 TEM of JK002**

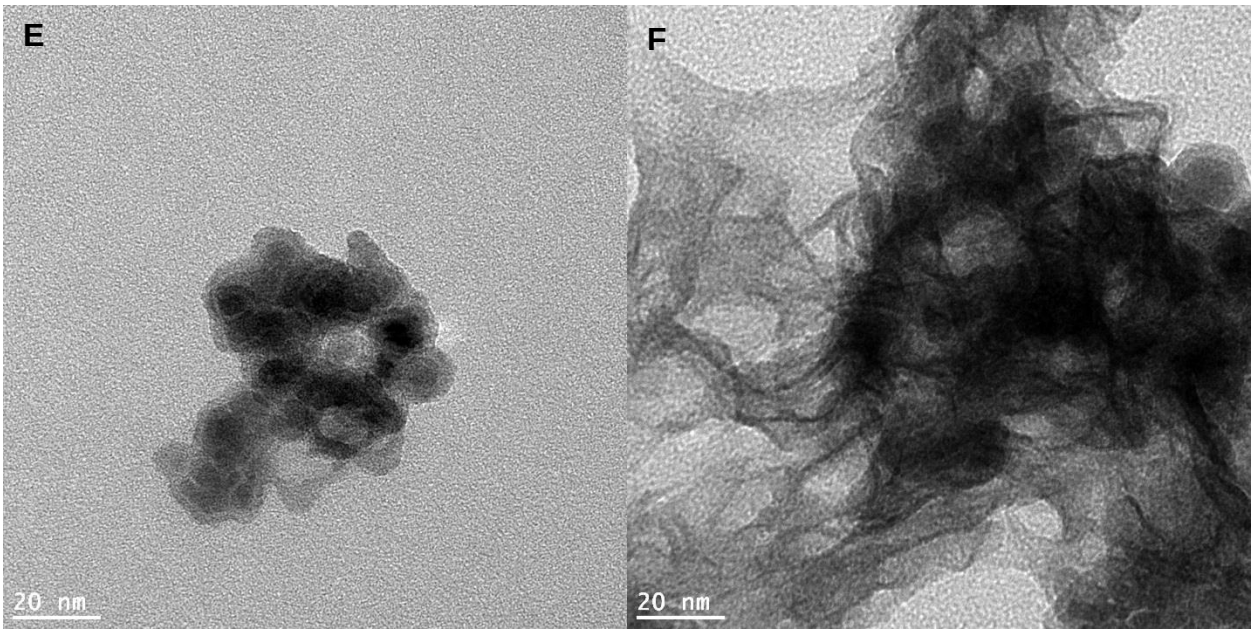



**Figure 12 continued**

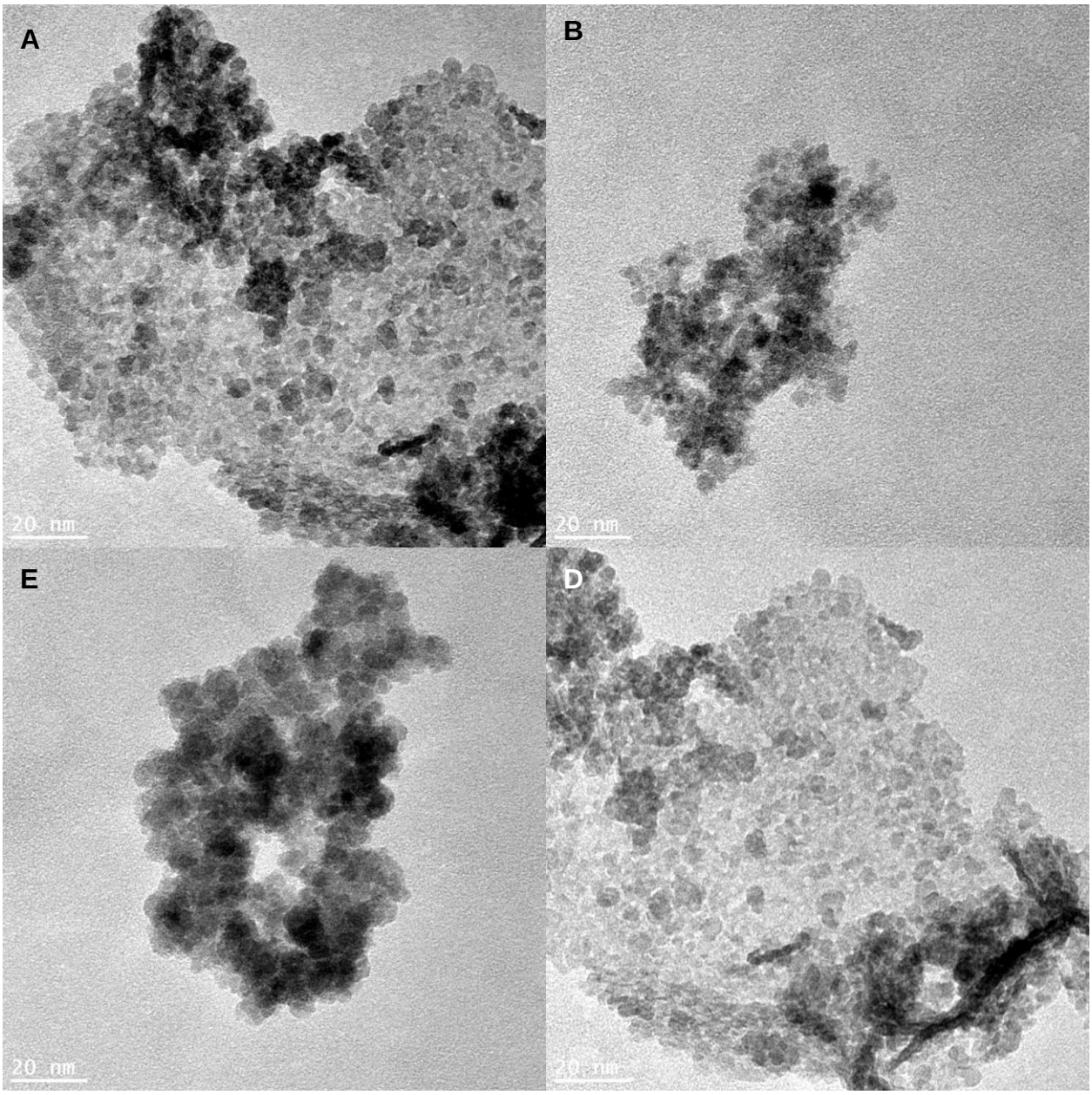



**Figure 13 TEM of JK003**

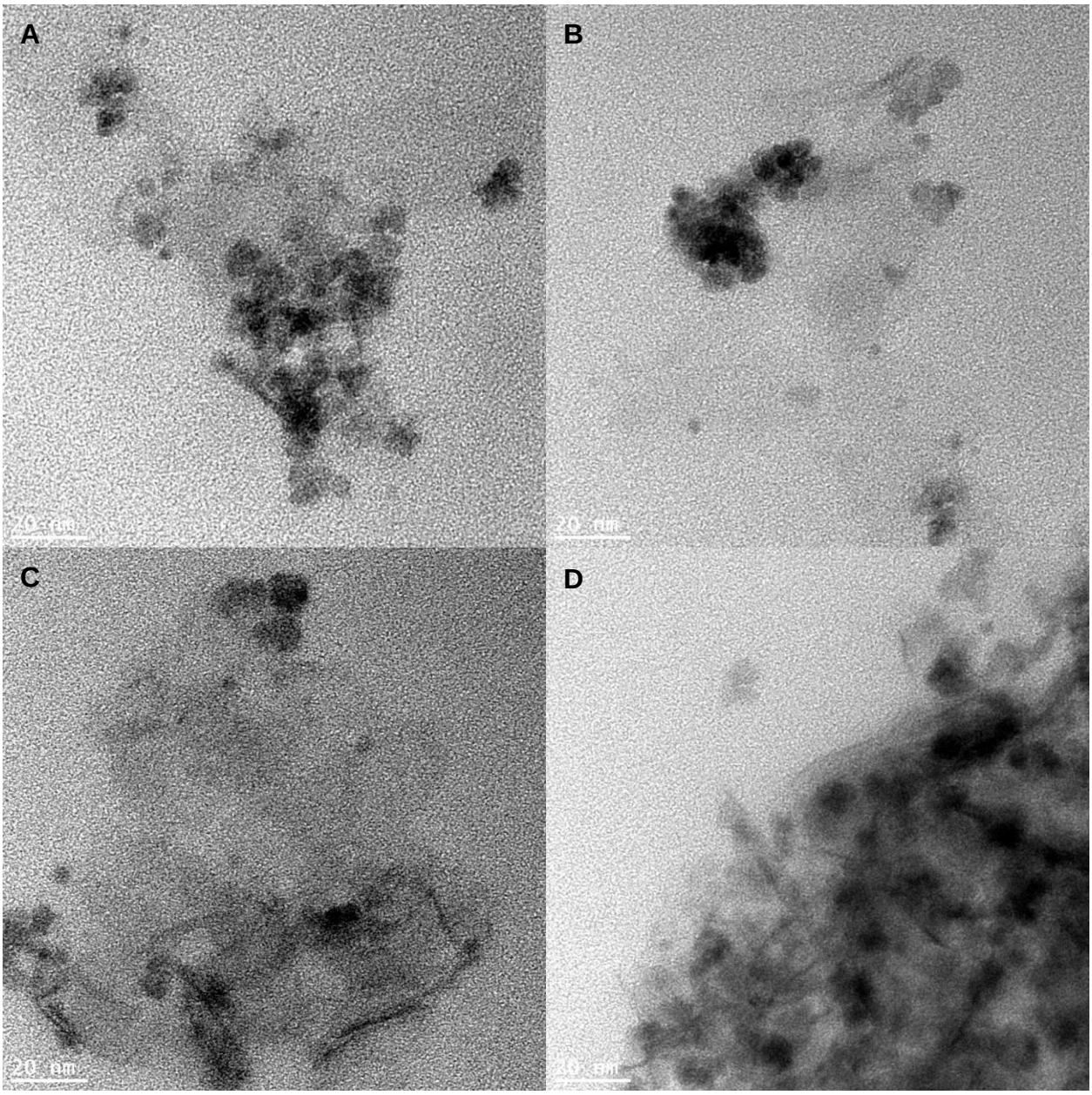



**Figure 14 TEM of JK004**

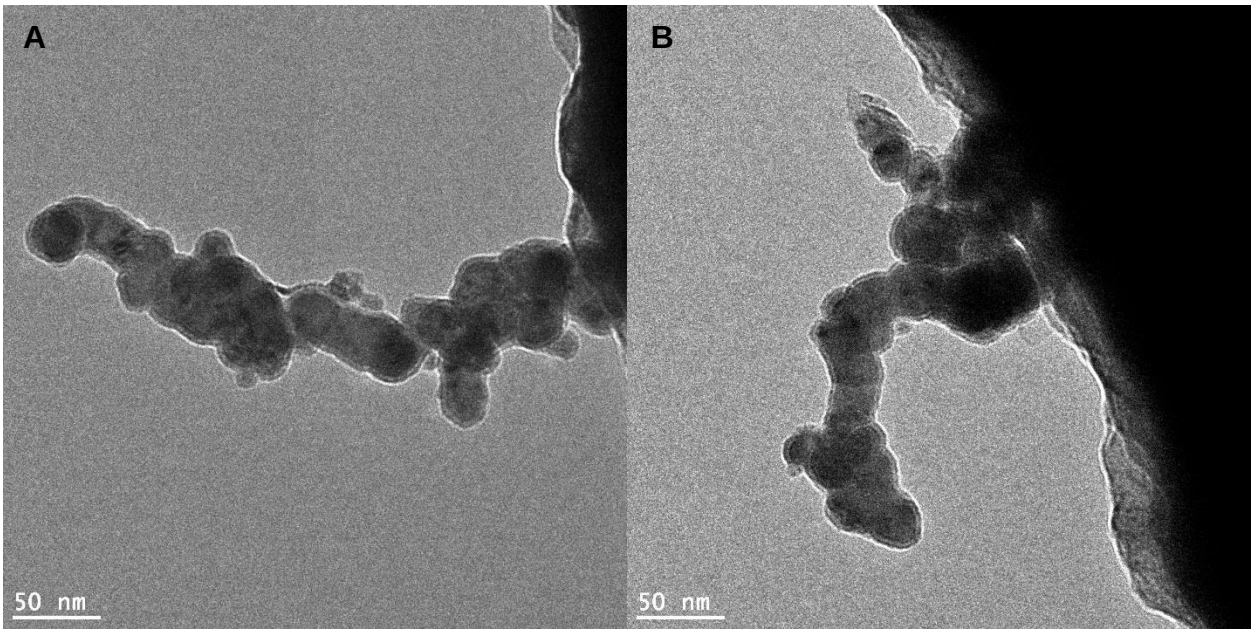



**Figure 15 TEM of JK005**

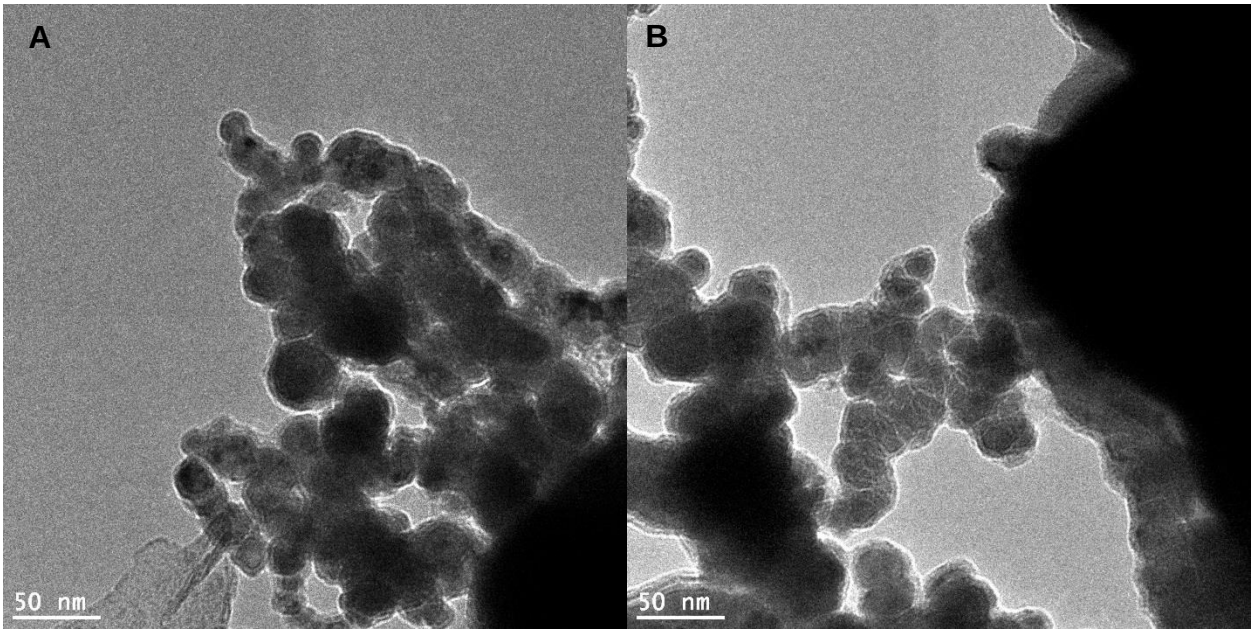



**Figure 16 TEM of JK006**

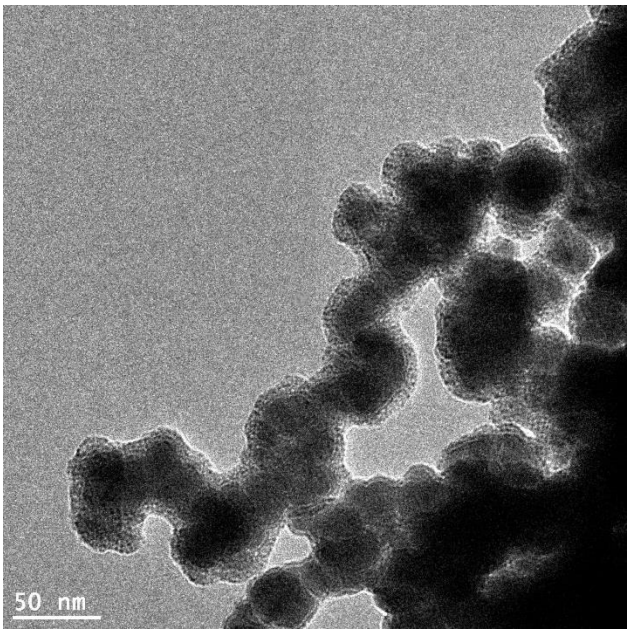



**Figure 17 TEM of JK007**

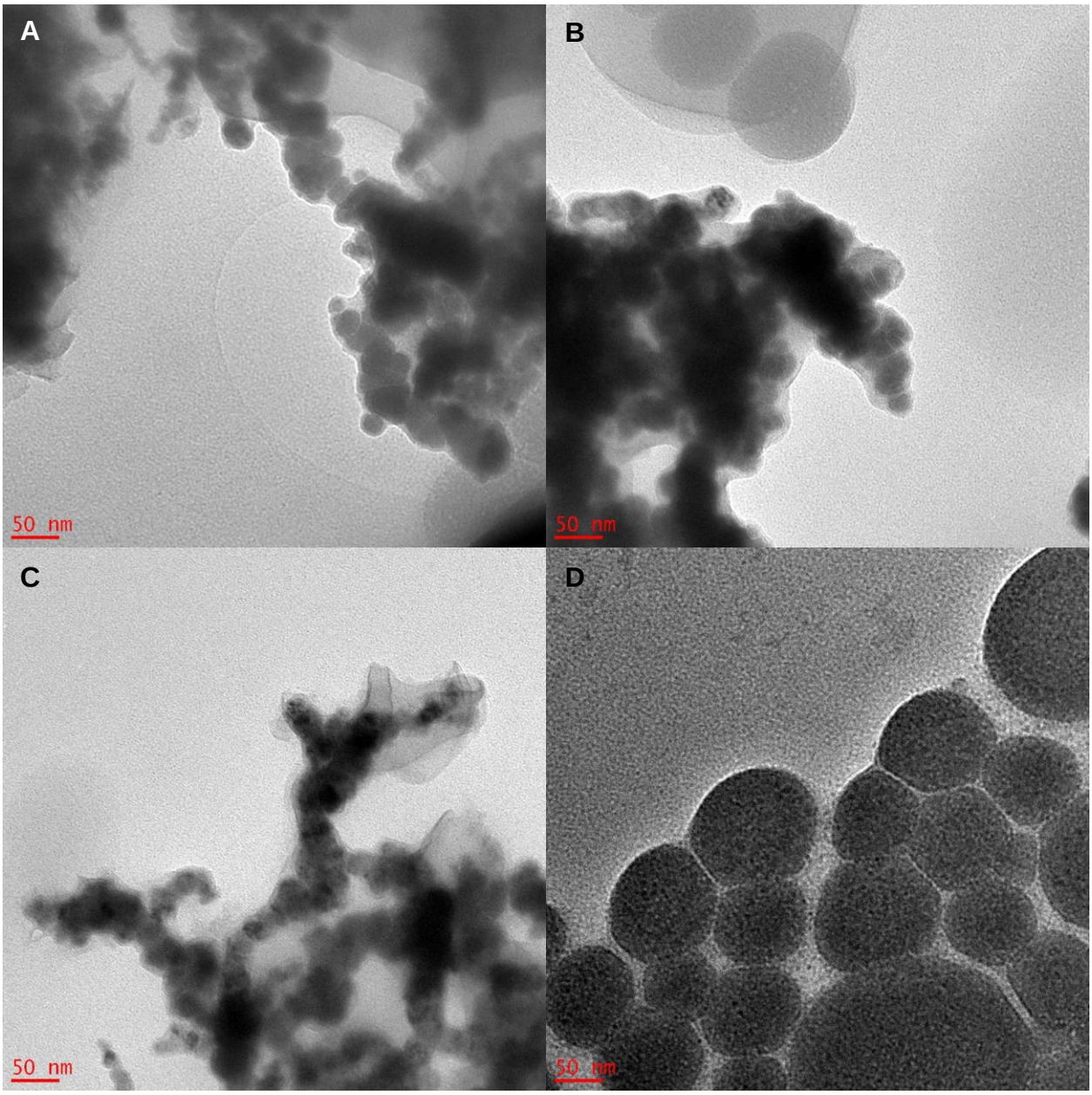



**Figure 18 TEM of JK018**

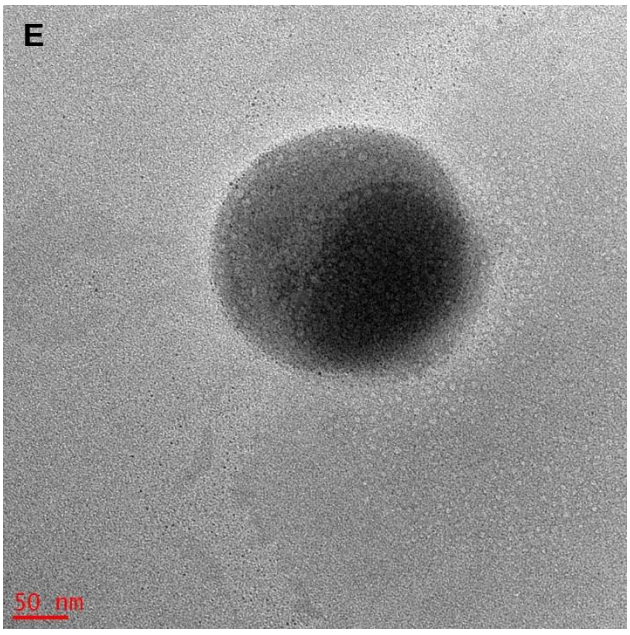



**Figure 18 continued**

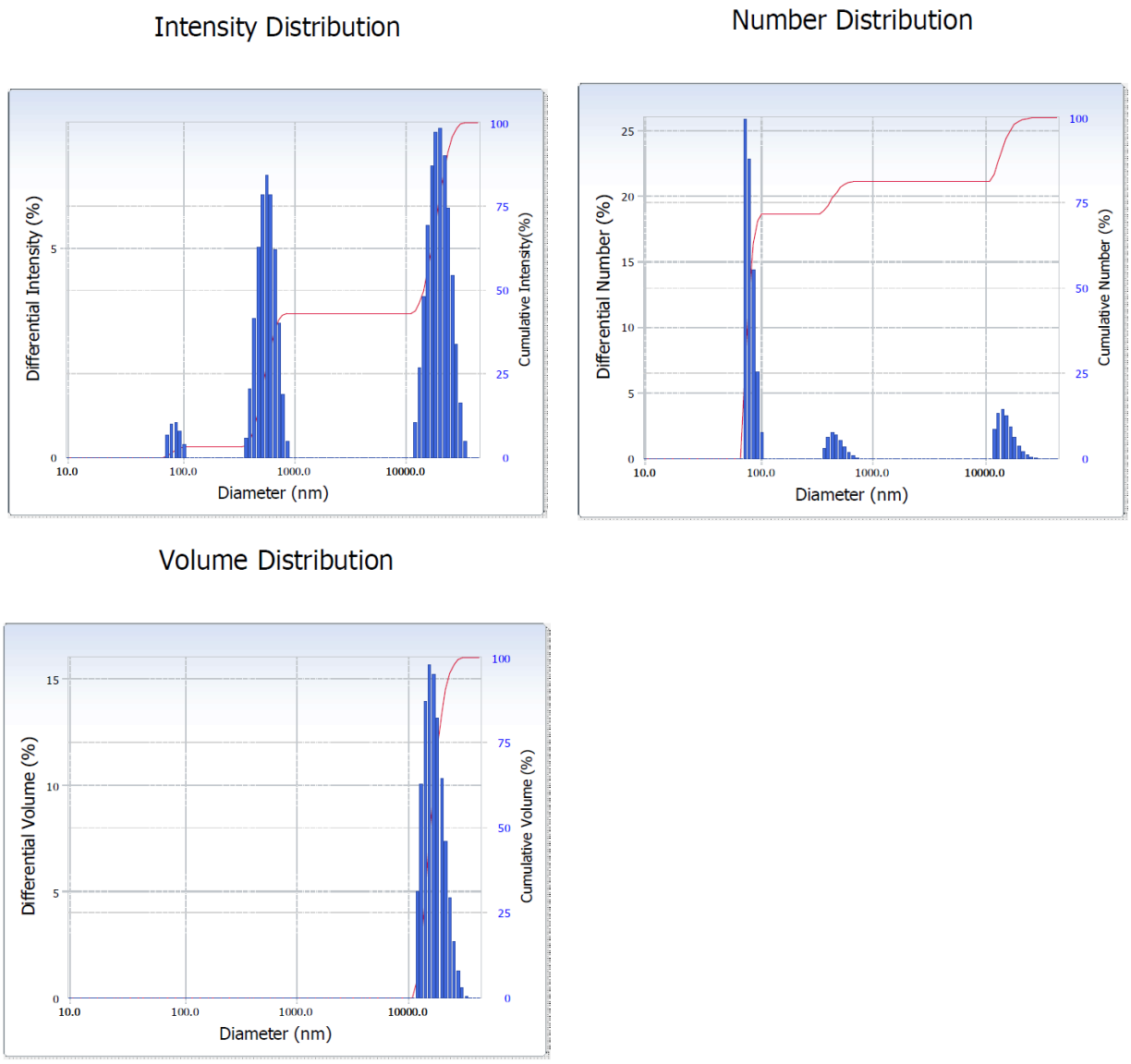



**Figure 19 DLS results of JK001**

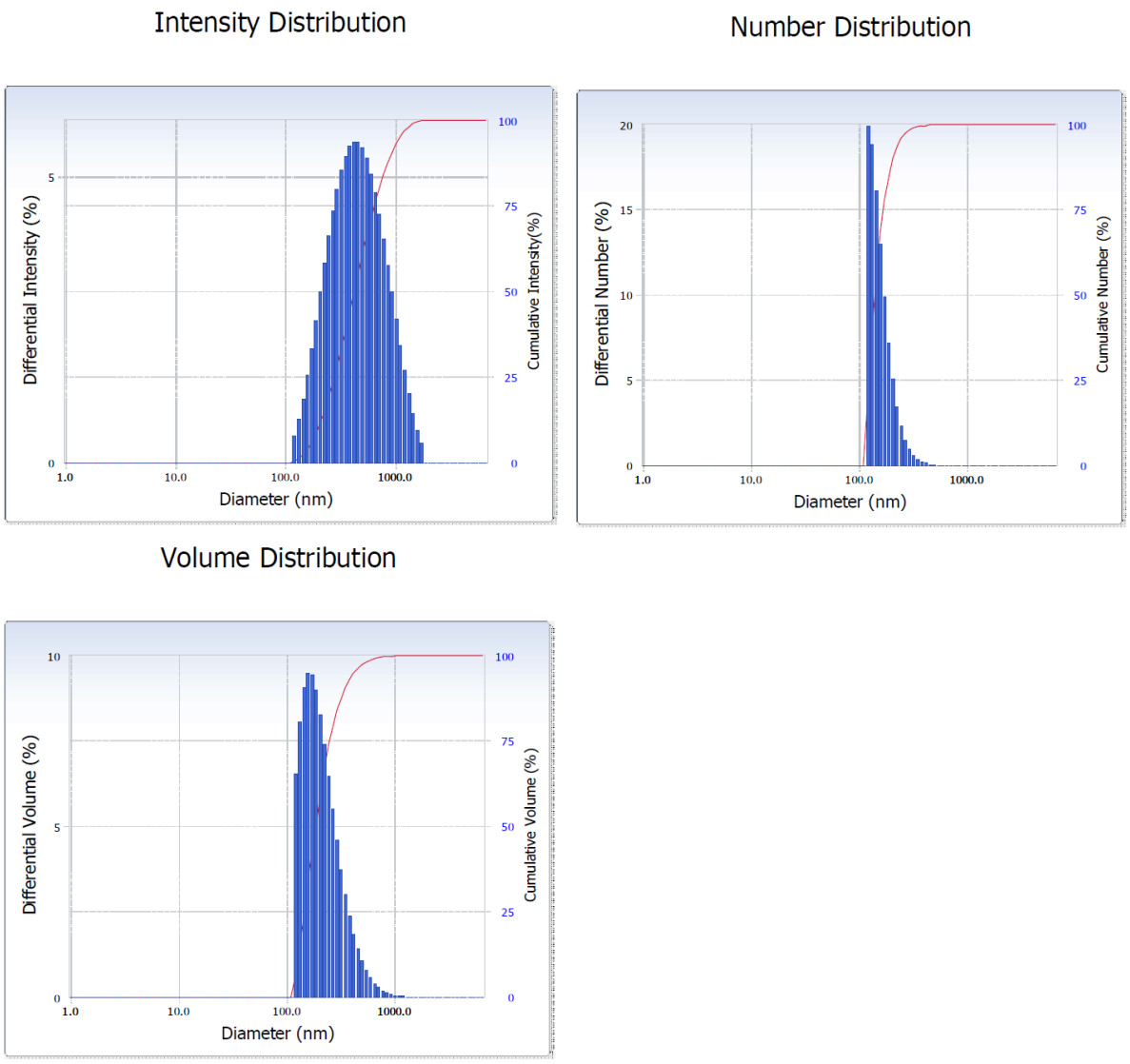



**Figure 20 DLS of JK002**

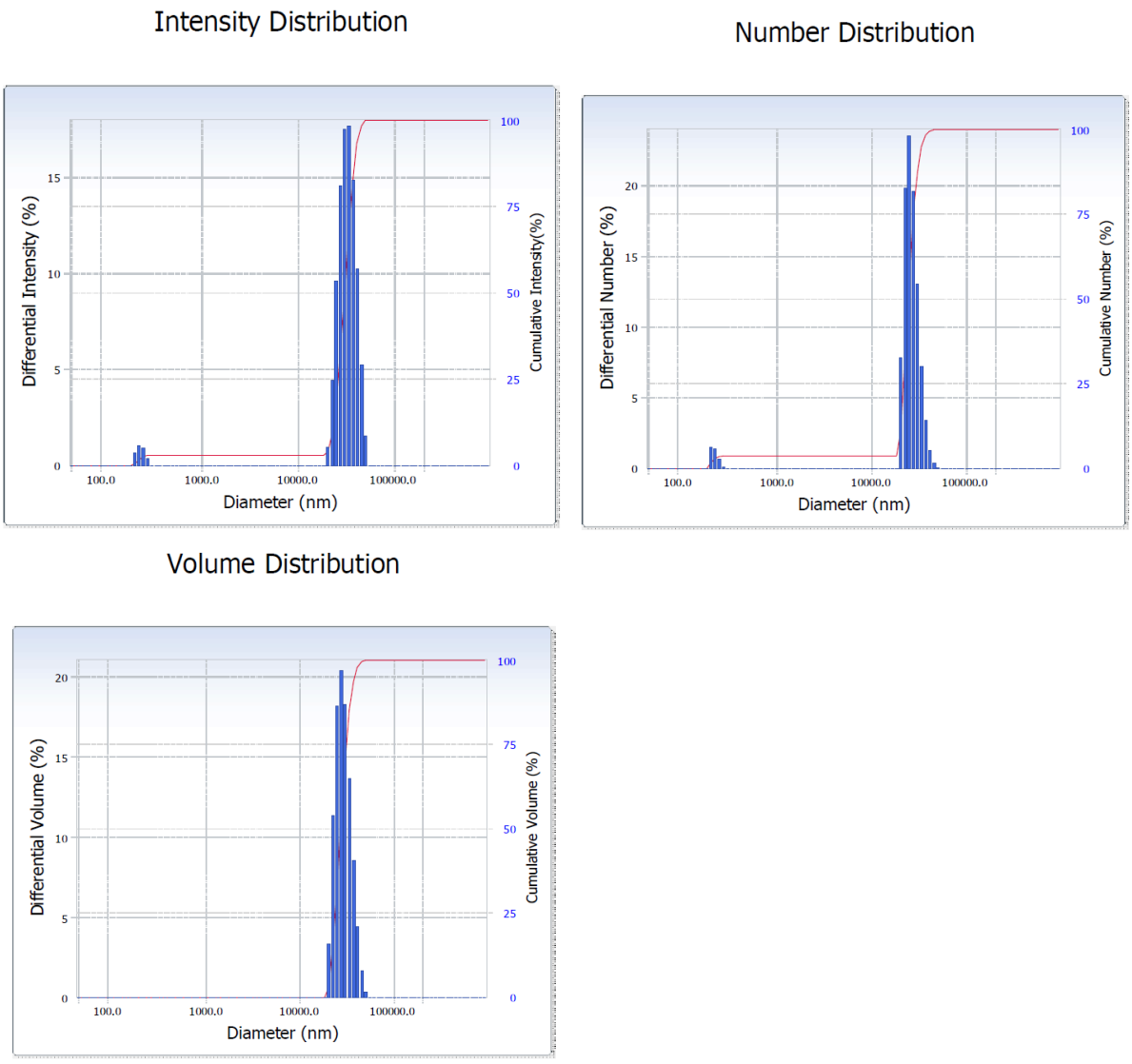



**Figure 21 DLS results of JK007**

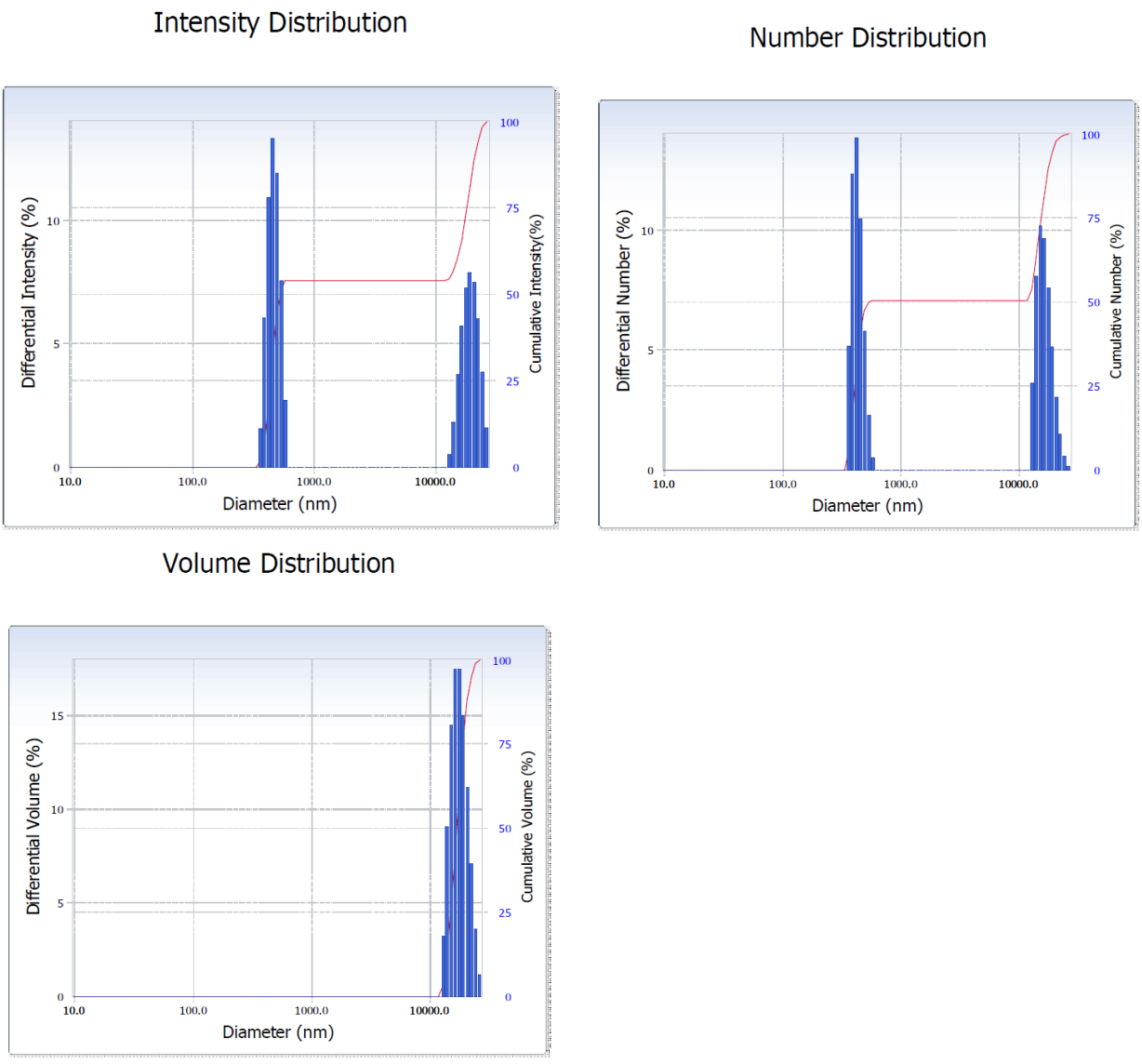



**Figure 22 DLS results of JK011**

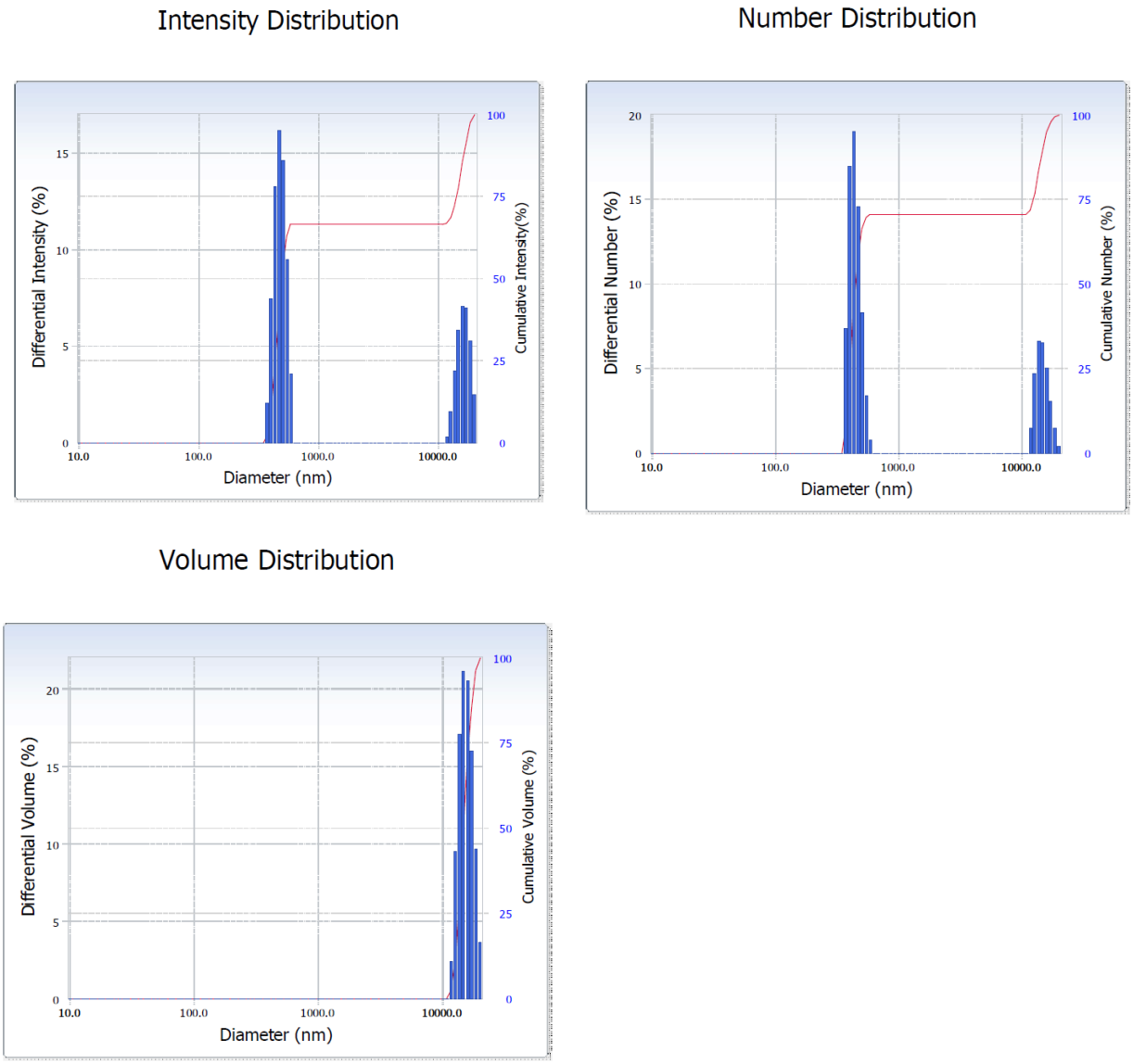



**Figure 23 DLS results of JK012**

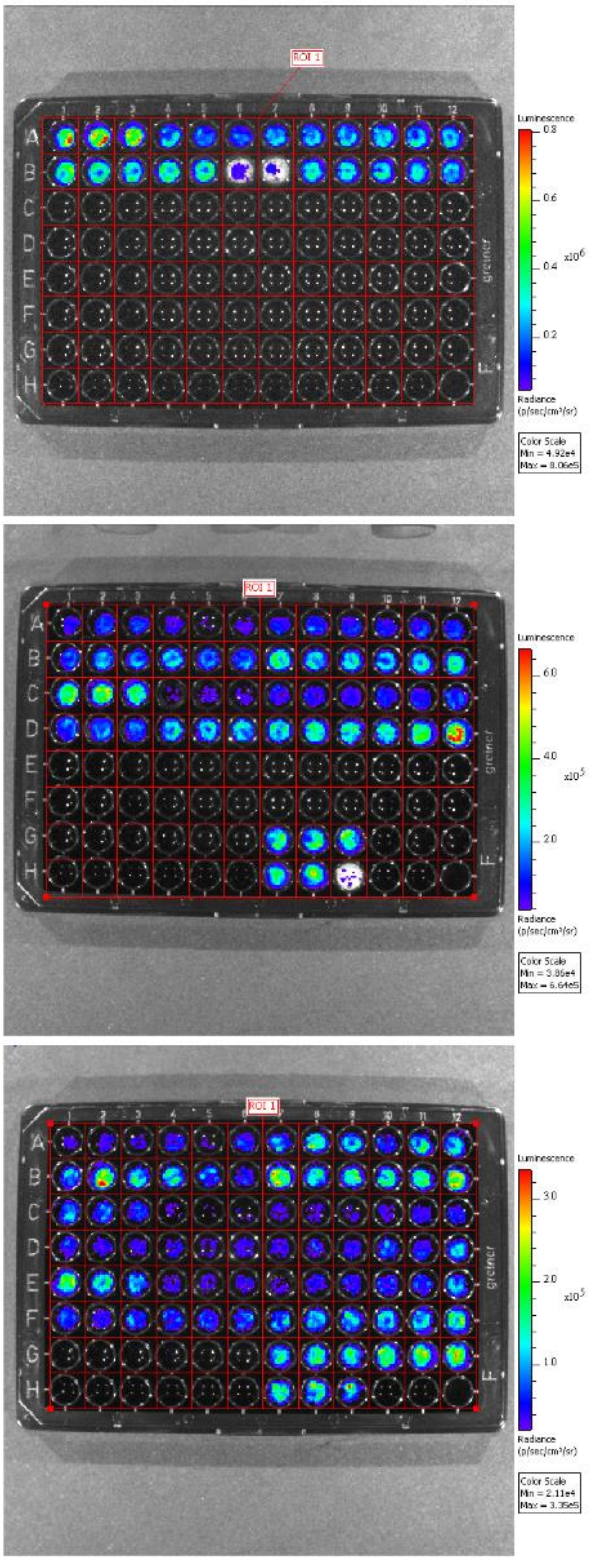



**Figure 24 Plate one at 17, 24, and 48 hour timepoints**

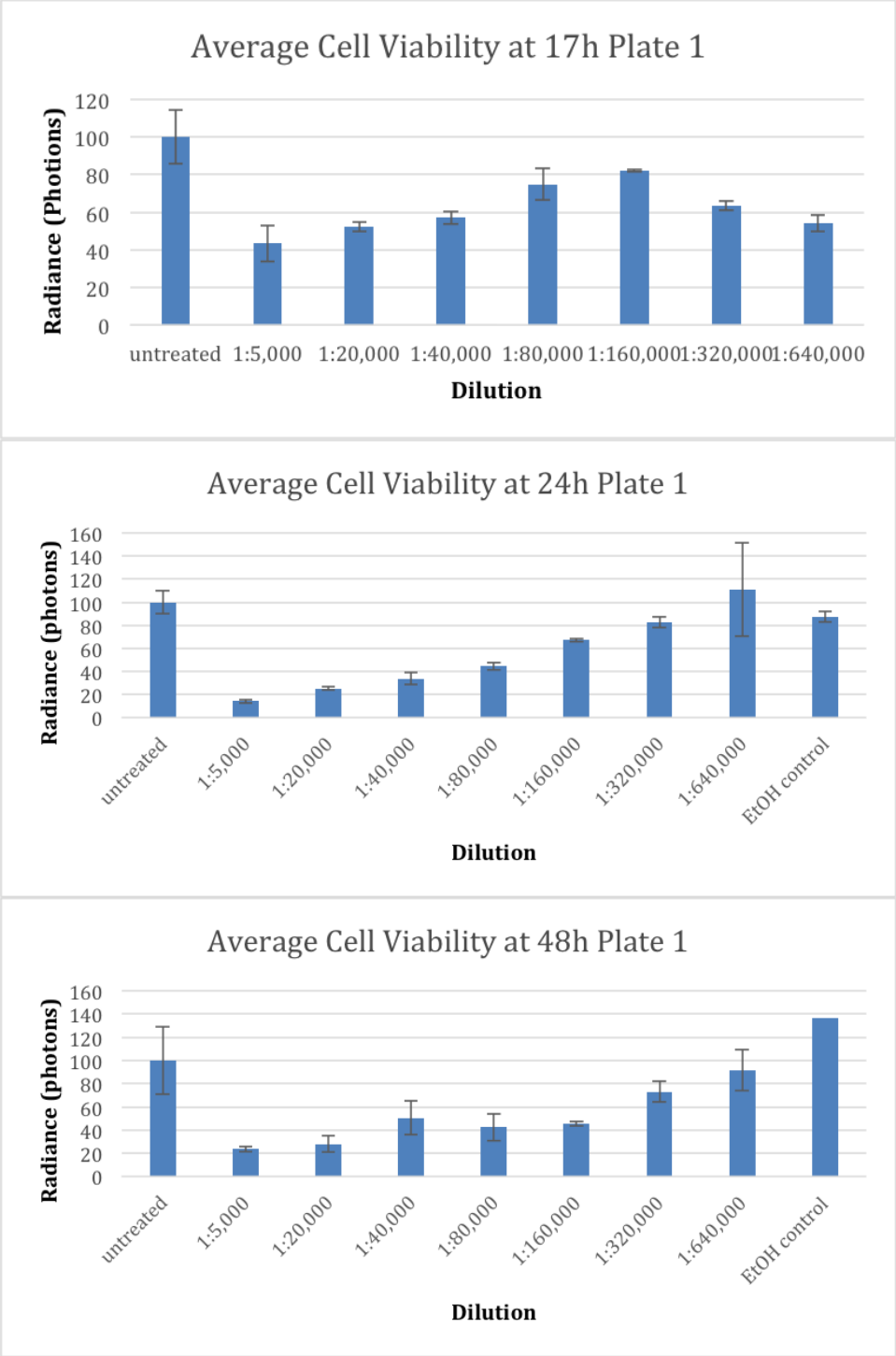
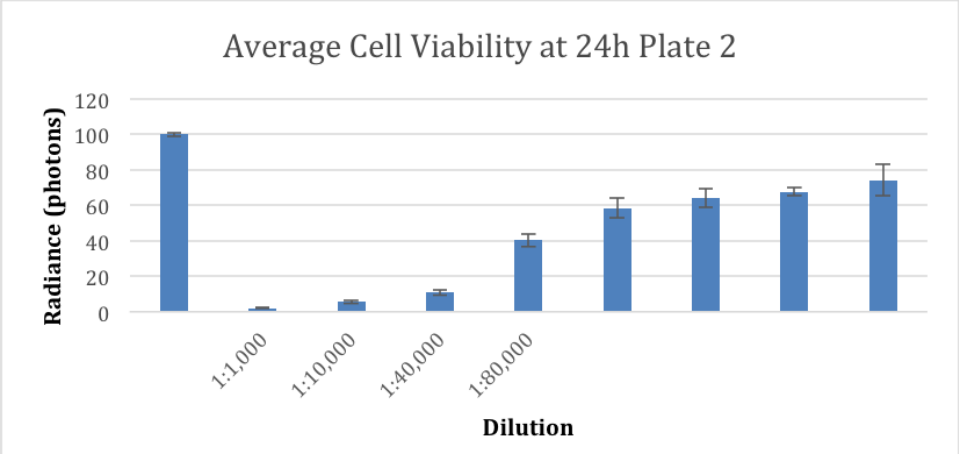



**Figure 25 Plate one and two cytotoxicity results**



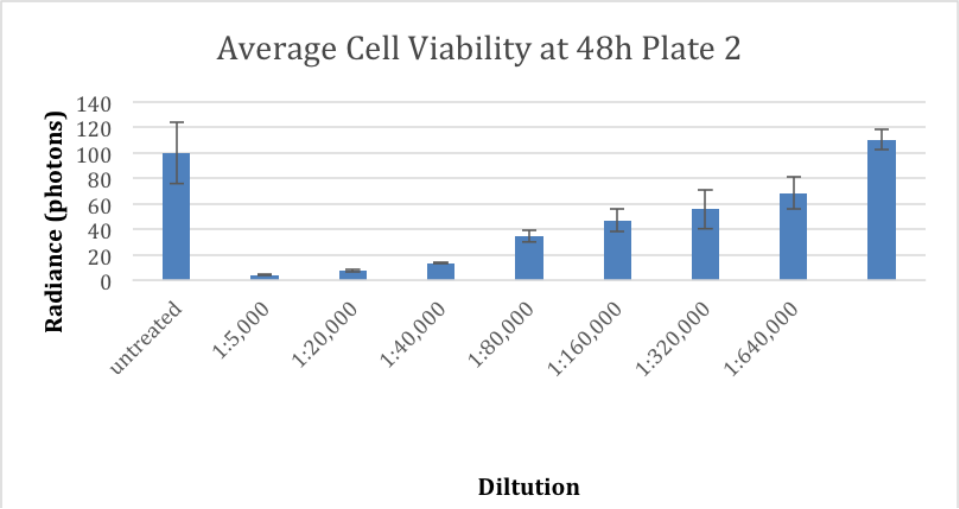




**Figure 25 continued**

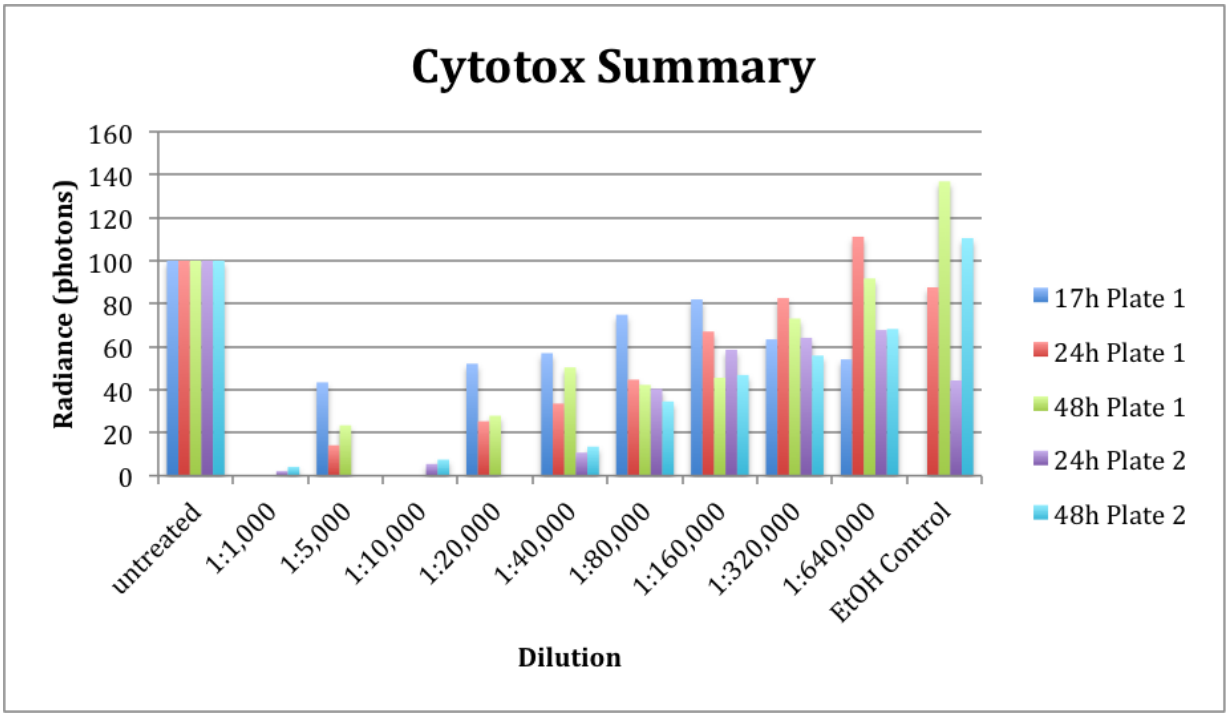



**Figure 26 Summary of cytotoxicity results**

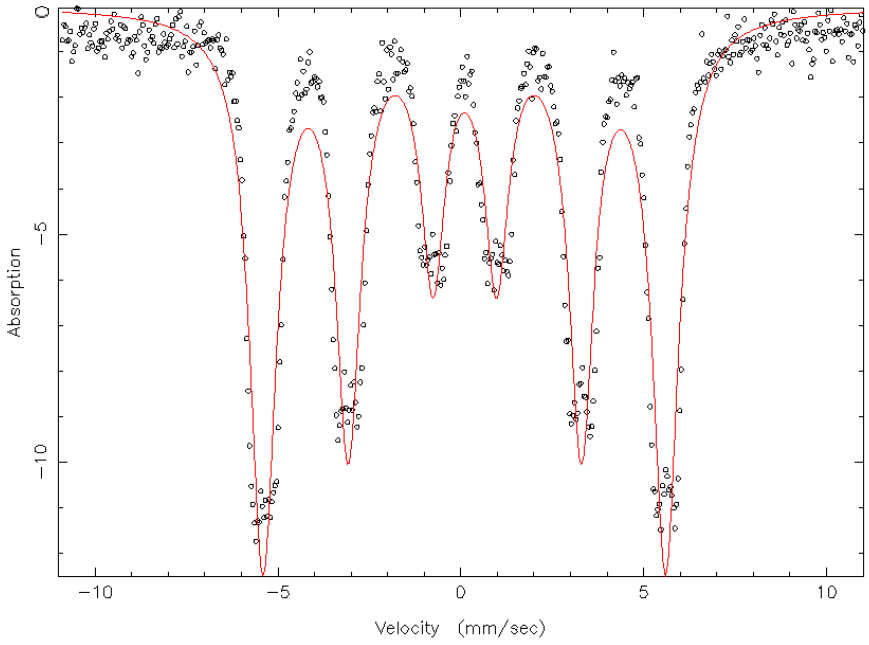



**Figure 27 Mössbauer Spectrum of JK002 at 6 K**

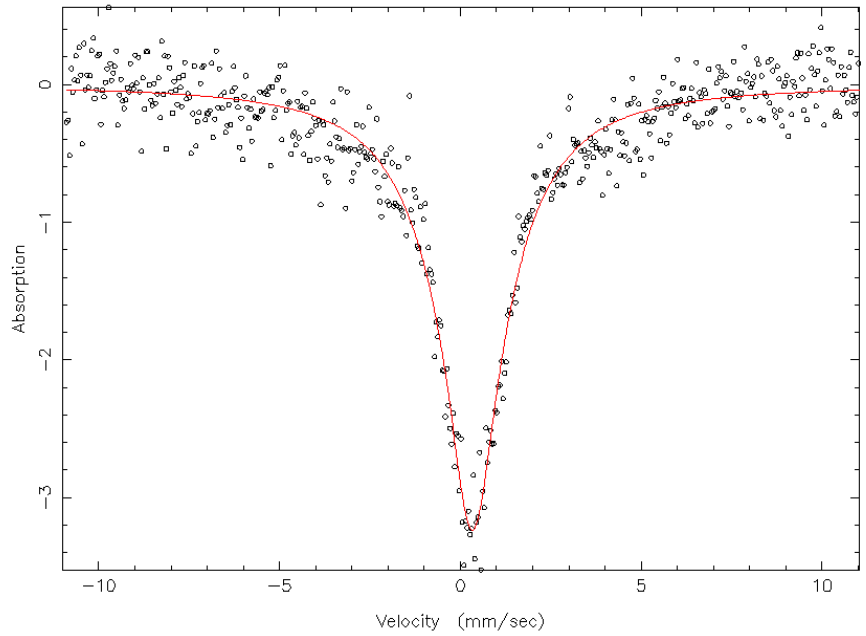



**Figure 28 Mössbauer Spectrum of JK002 at 293 K**

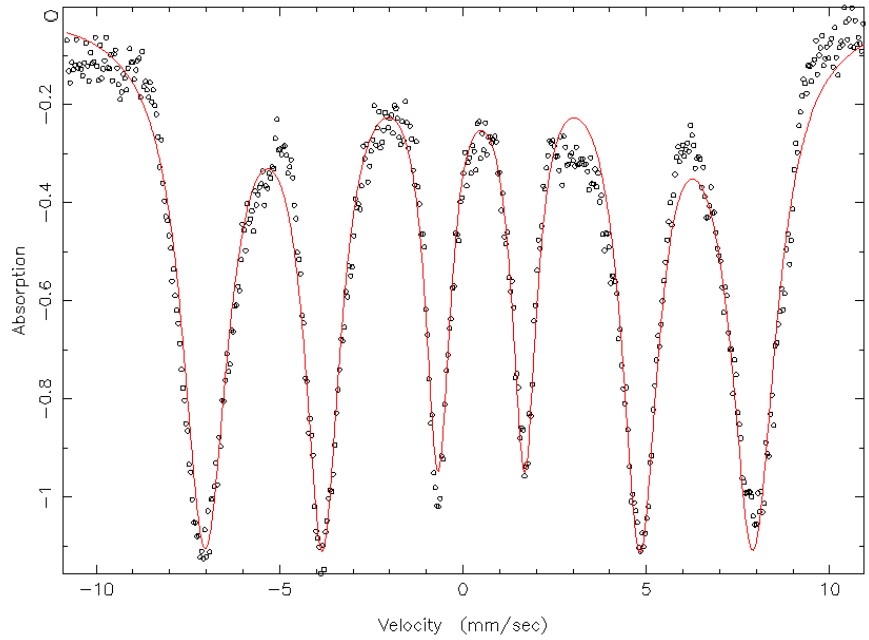



**Figure 29 Mössbauer Spectrum of JK002 at 6 K Two Months Post Synthesis**

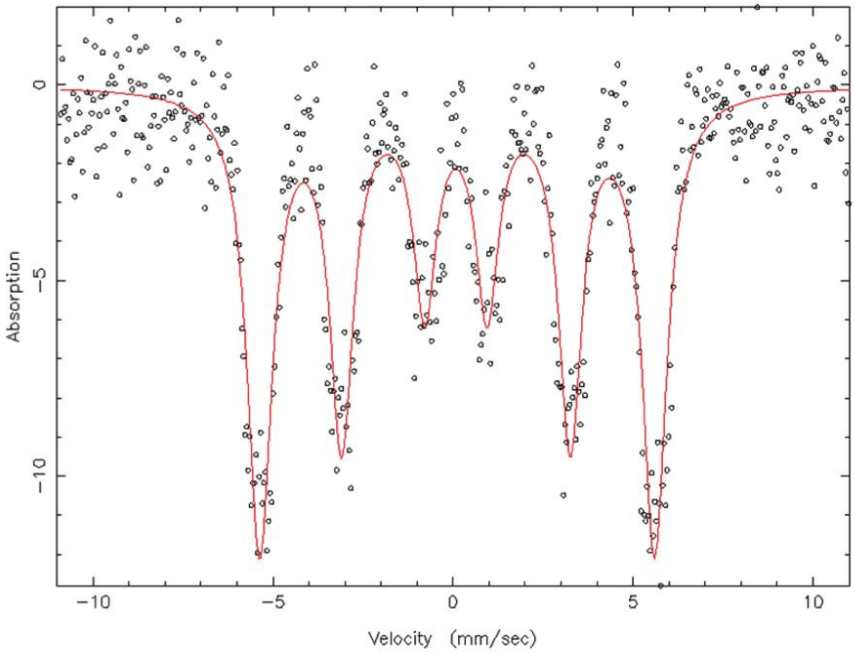



**Figure 30 Mössbauer Spectrum of Sample JK003 at 6 K**

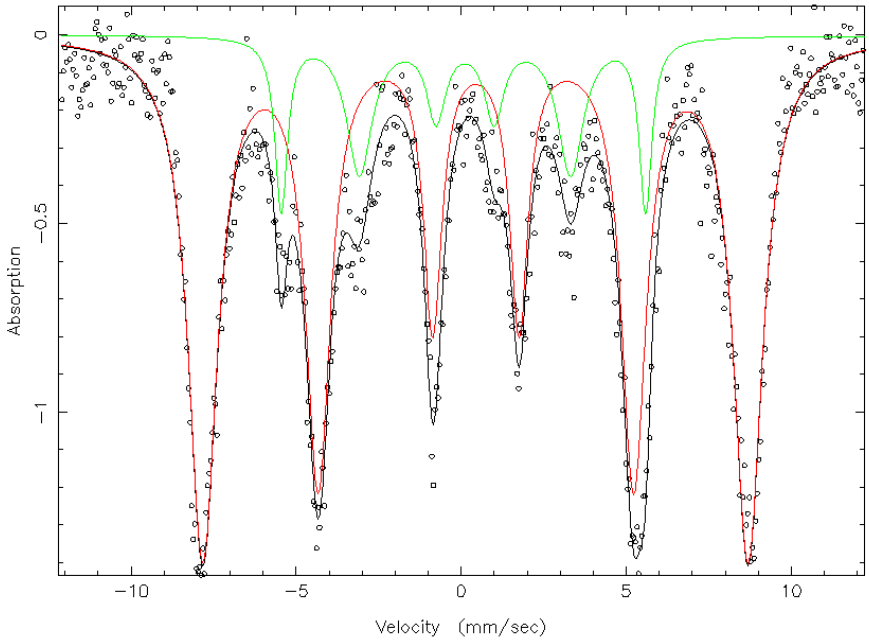



**Figure 31 Mössbauer Spectrum of JK003 at 6 K Four Years and 4 Months Post Synthesis**

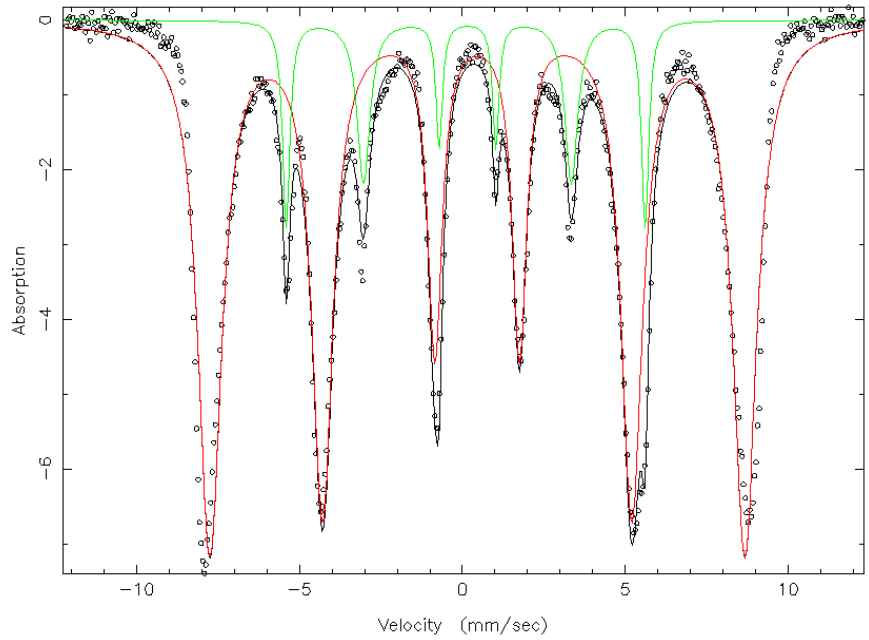



**Figure 32 Mössbauer Spectrum of JK003 at 6 K Four Years and 9 Months Post Synthesis**

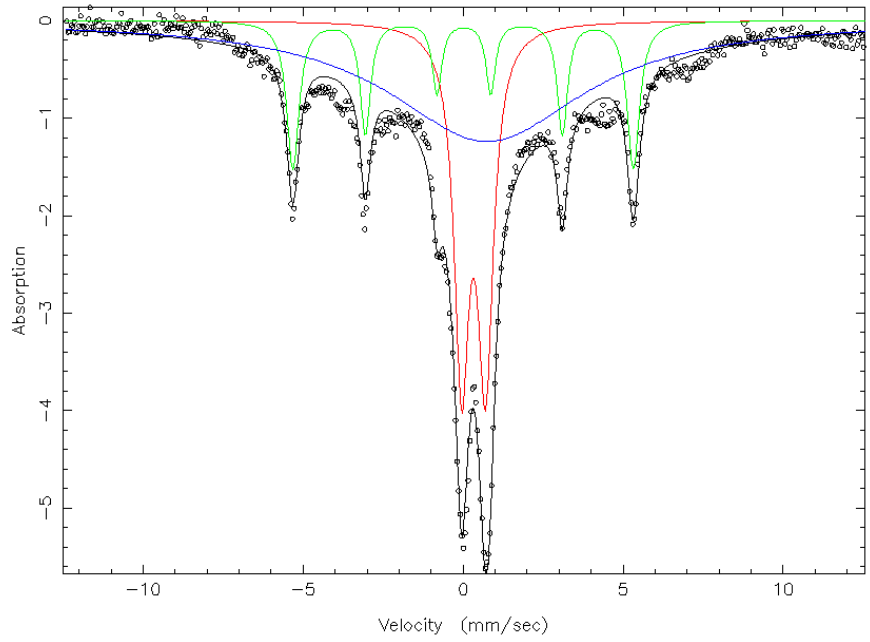



**Figure 33 Mössbauer Spectrum of JK003 at 293 K Four Years and 9 Months Post Synthesis**

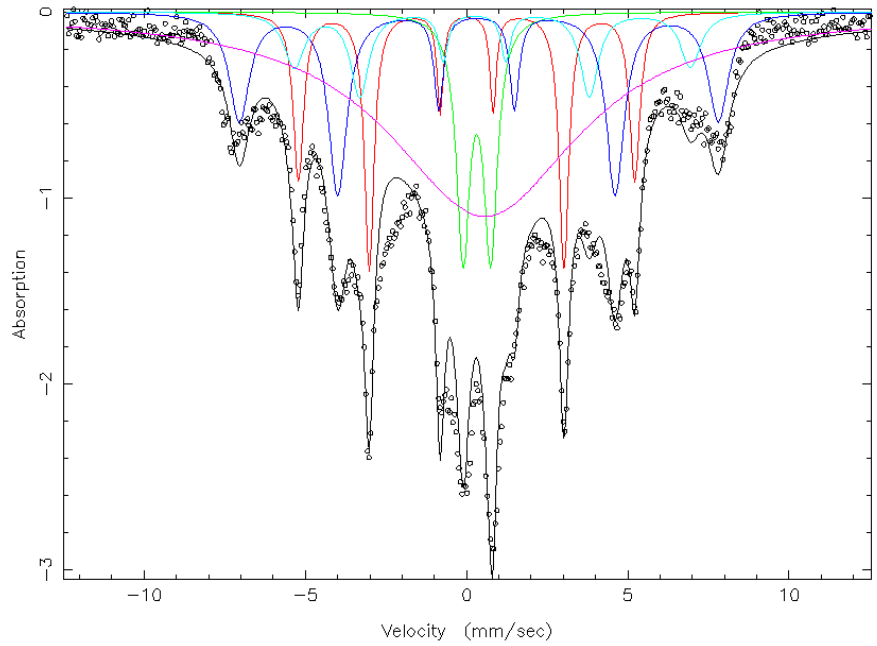



**Figure 34 Mössbauer Spectrum of JK003 at 293 K with a 10 kG Field Four Years and 9 Months Post Synthesis**

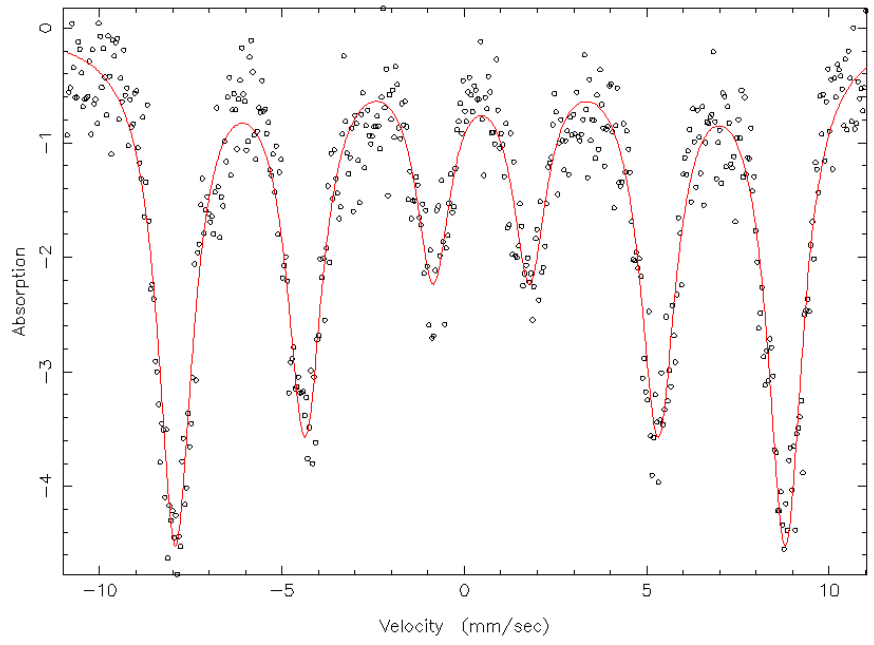



**Figure 35 Mössbauer Spectrum of JK004 at 6 K**

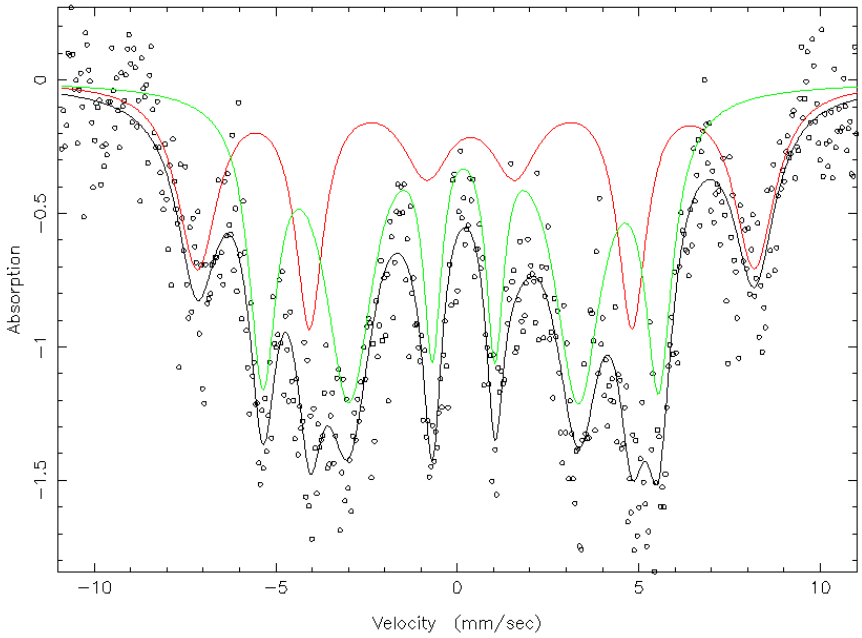



**Figure 36 Mössbauer Spectrum of JK007 at 6K**

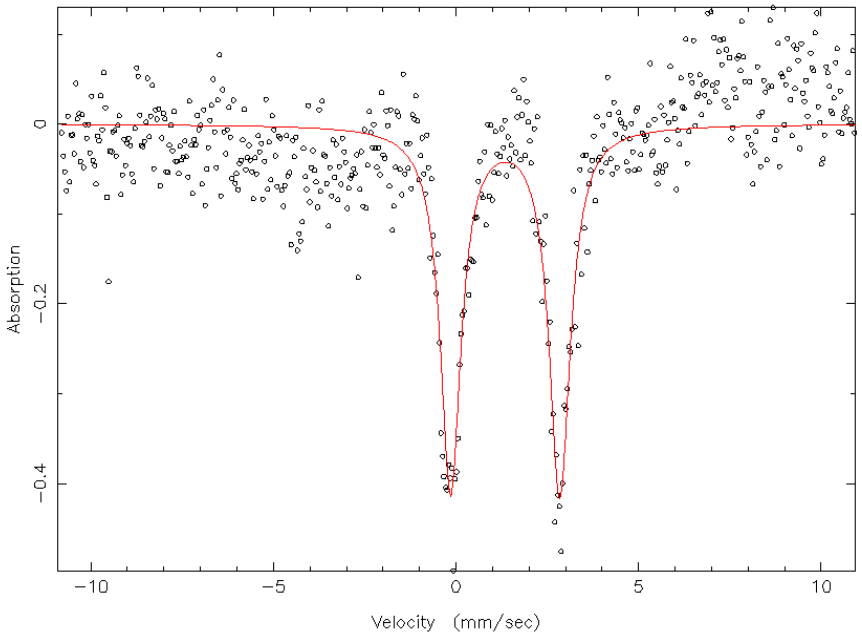



**Figure 37 Mössbauer Spectrum of JK011 at 6K**

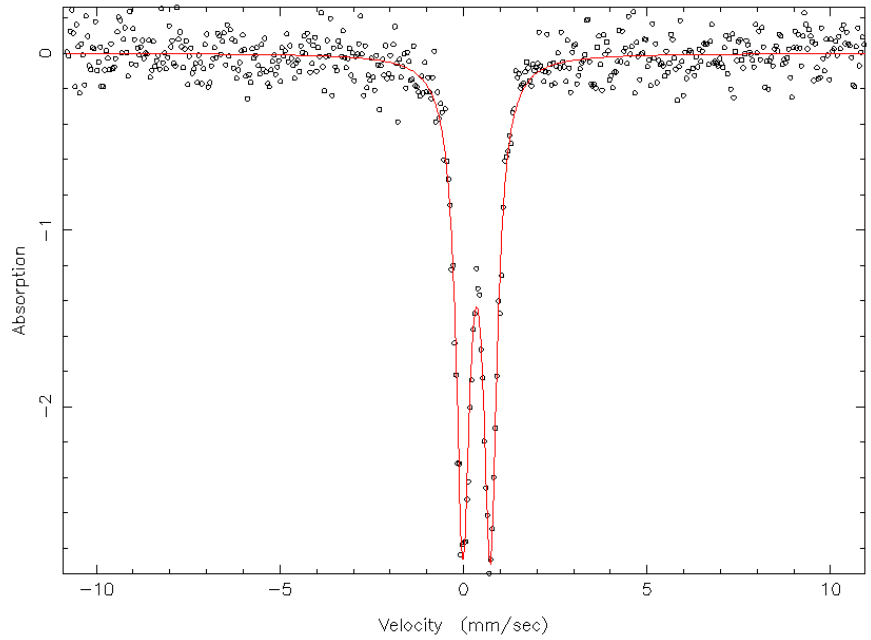



**Figure 38 Mössbauer Spectrum of JK011 at 293 K**

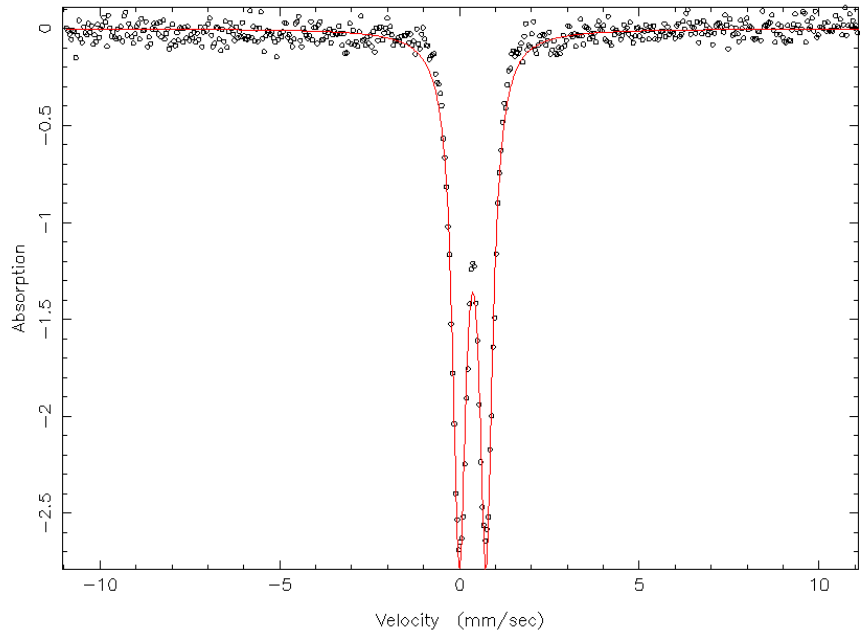



**Figure 39 Mössbauer Spectrum of JK011 at 293 K with a 10 kG Field**

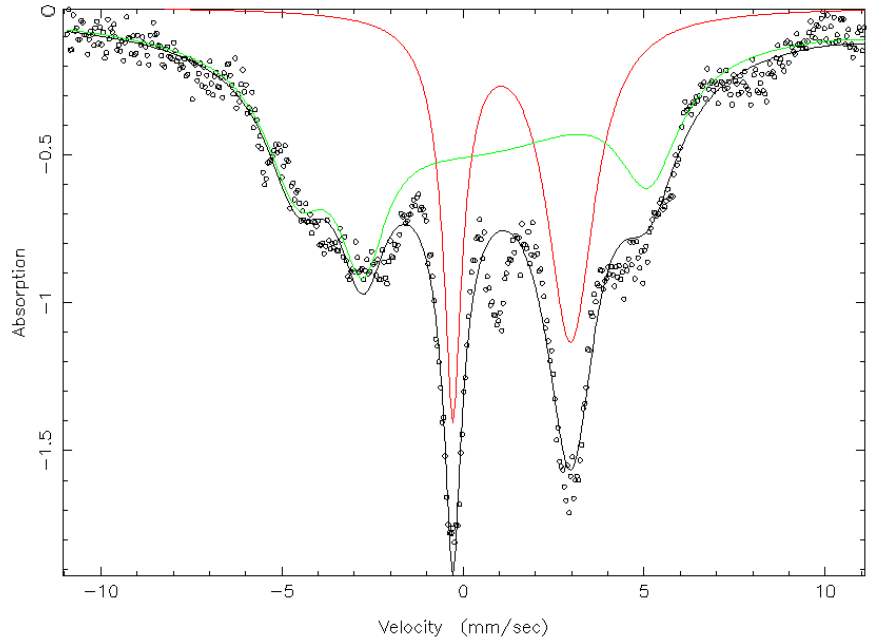



**Figure 40 Mössbauer Spectrum of JK012 at 6 K**

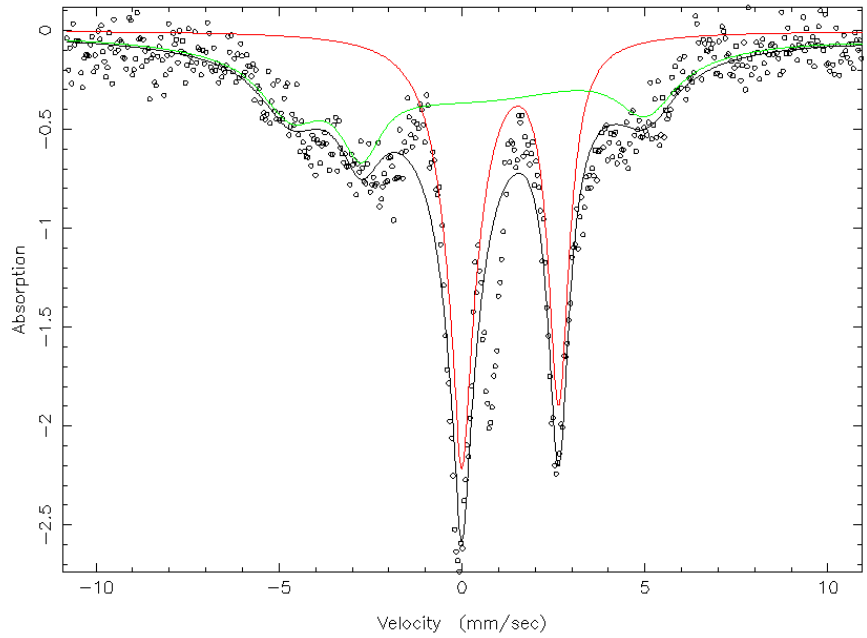



**Figure 41 Mössbauer Spectrum of JK012 at 180 K**

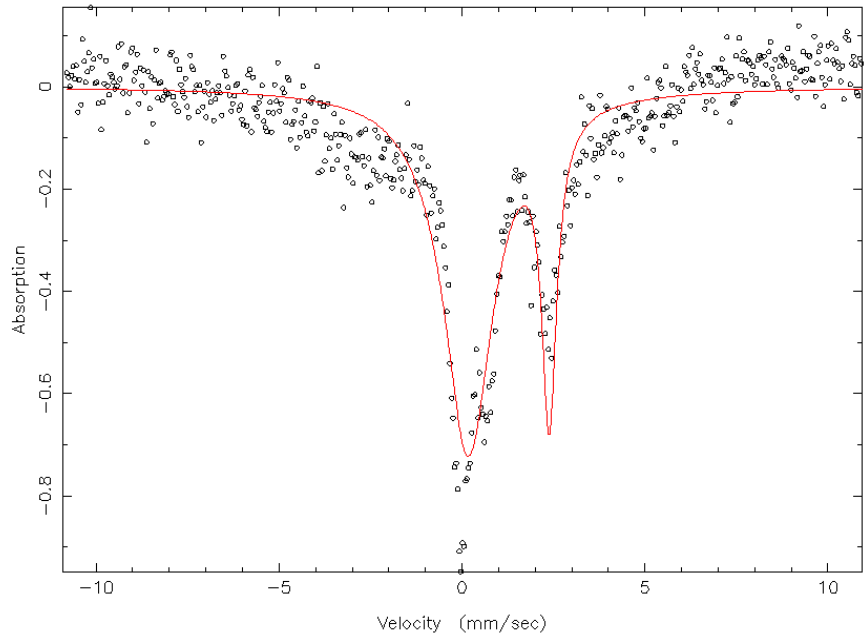



**Figure 42 Mössbauer Spectrum of JK012 at 293 K**

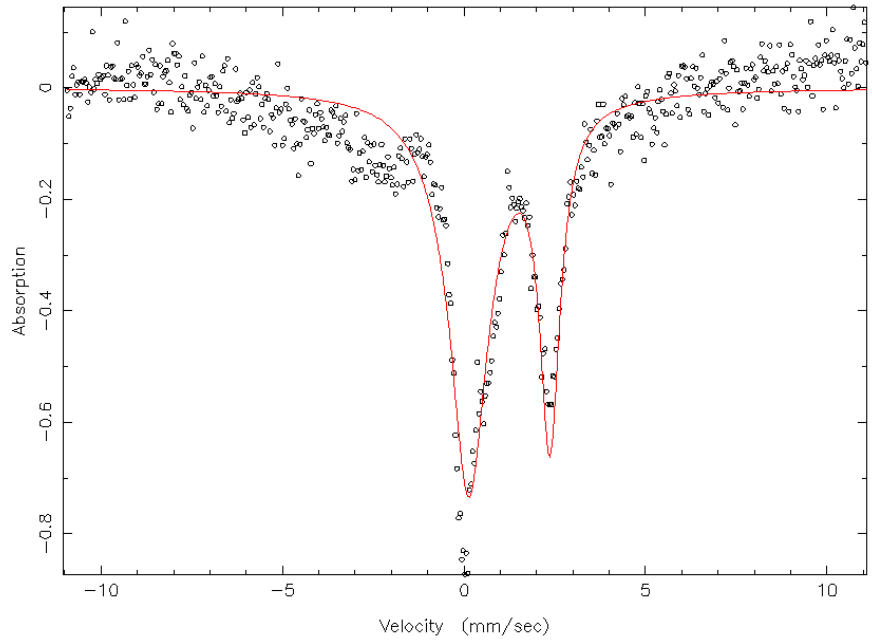



**Figure 43 Mössbauer Spectrum of JK012 at 293 K with a 10 kG Field**

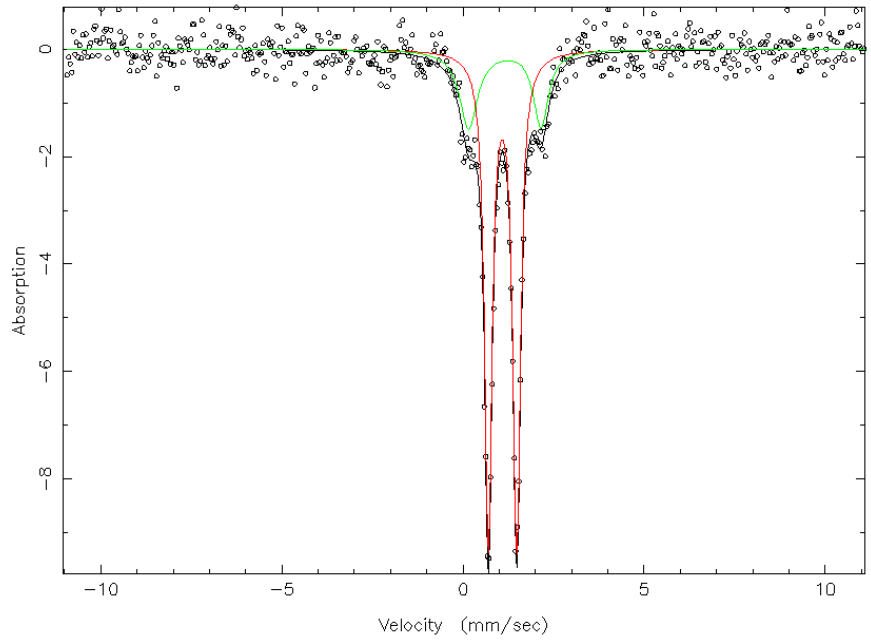



**Figure 44 Mössbauer Spectrum of Anhydrous $FeCl_2$**

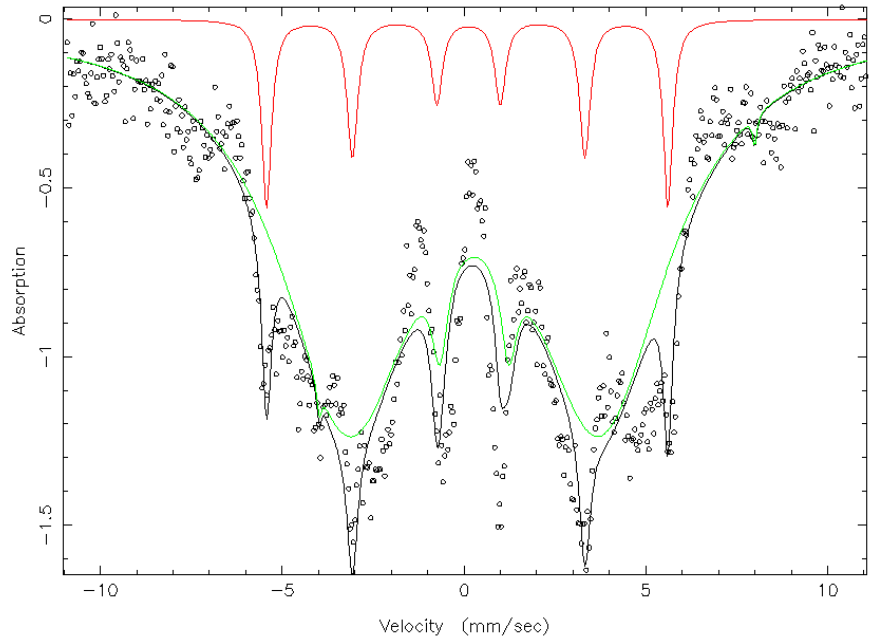



**Figure 45 Mössbauer Spectrum of JK018 at 6 K**

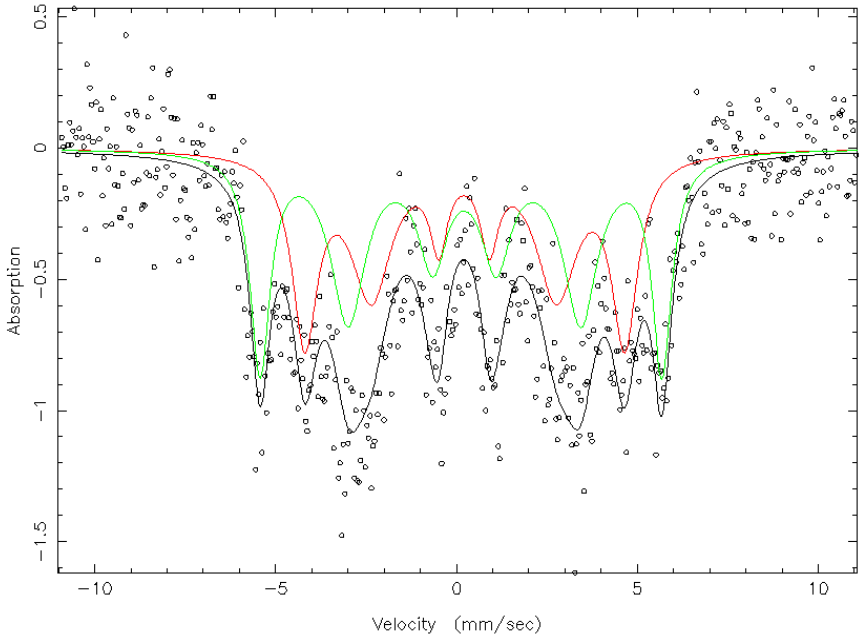



**Figure 46 Mössbauer Spectrum of JK018 at 293 K**

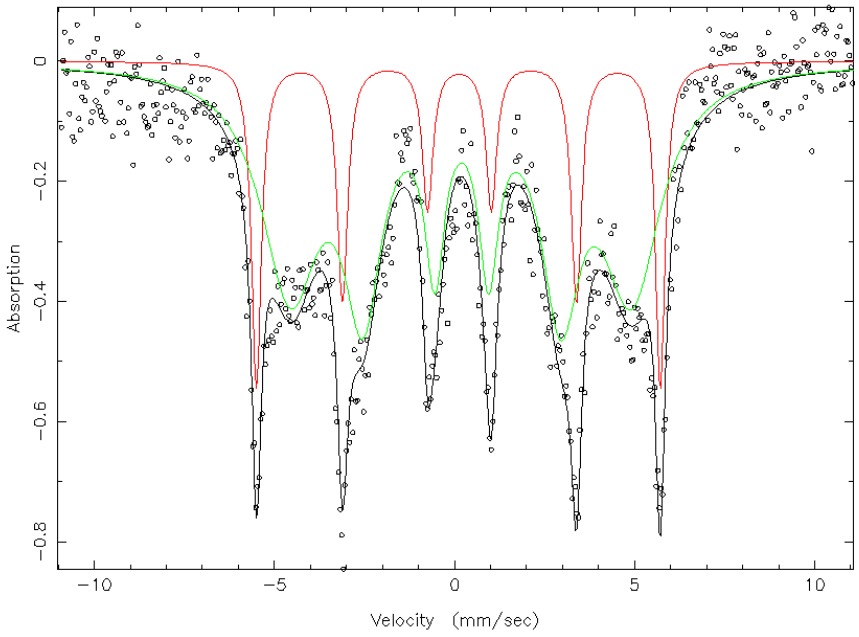



**Figure 47 Mössbauer Spectrum of JK019 at 6 K**

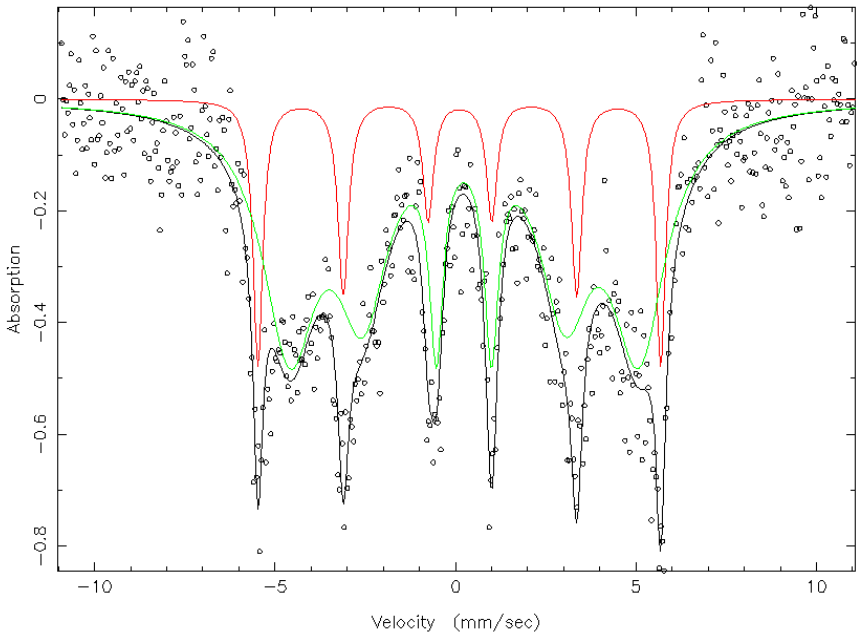



**Figure 48 Mössbauer Spectrum of JK019 at 6 K with a 0.073 T Parallel Field**

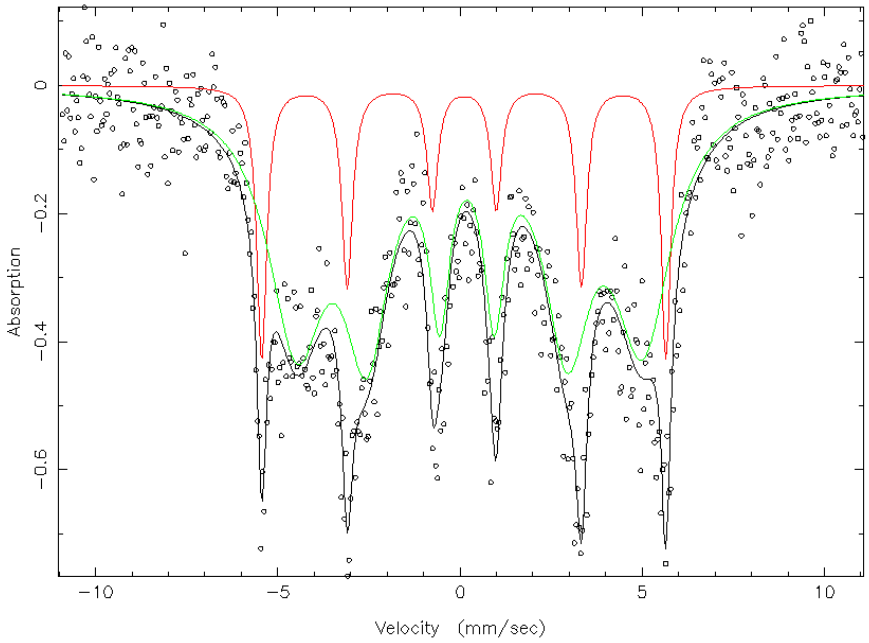



**Figure 49 Mössbauer Spectrum of JK019 at 6 K with a 0.073 T Perpendicular Field**

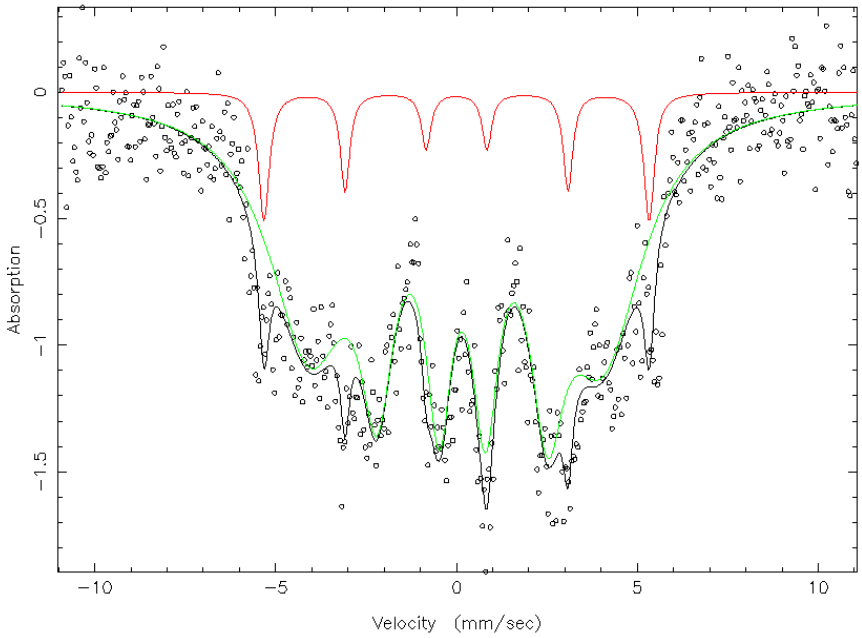



**Figure 50 Mössbauer Spectrum of JK019 at 270 K**

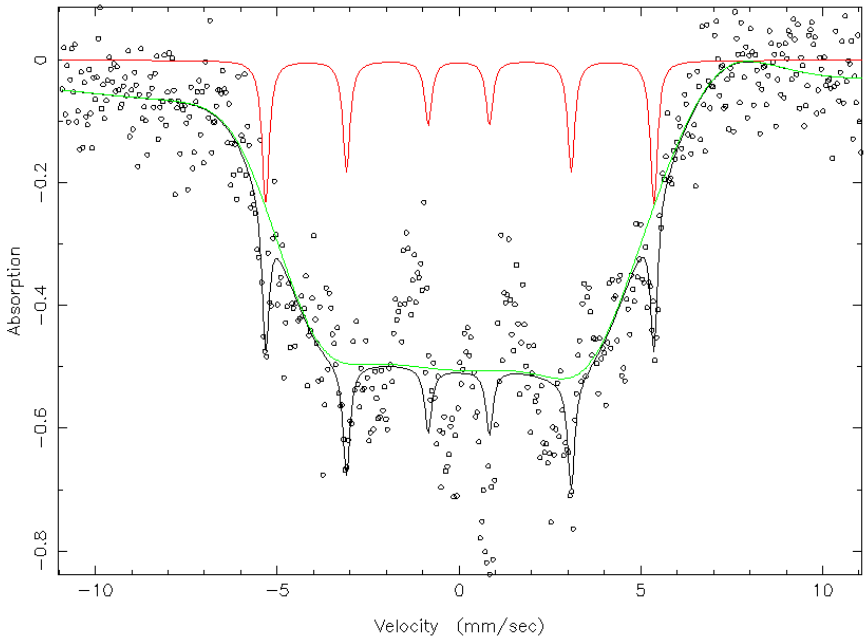



**Figure 51 Mössbauer Spectrum of JK019 at 293 K**

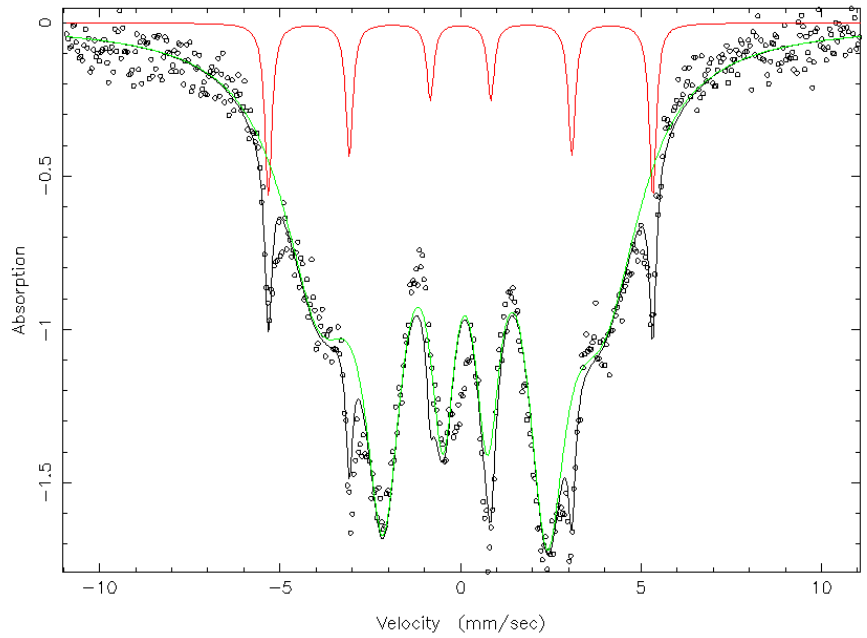



**Figure 52 Mössbauer Spectrum of JK019 at 293 K with a 10 kG Field**

# CHAPTER III
# THERMAL DECOMPOSITION OF IRON PENTACARBONYL

# Introduction

The goal of the work presented in this chapter was to synthesize spherical iron nanoparticles less than 10 nm in diameter by thermal decomposition. The ability of various biocompatible coatings to protect the metallic iron nanoparticles from oxidation was investigated. Coatings studied included Brij, polyethylene glycol and iron oxide. Transmission electron microscopy and Mössbauer spectroscopy were utilized to characterize the coated and uncoated iron nanoparticles' size and oxidation state to evaluate the effectiveness of the coatings and the procedures in which the coatings were applied. A ferrite shell was found to provide the best stabilization; however, its longer synthesis time increased particle size distribution. Polymer coatings provided biocompatibility but did not prevent oxidation.

# Methods

### *Iron Oleate Synthesis*

Iron oleate was synthesized for the iron nanoparticle ferrite shell using a modified synthesis of nanocrystals reported in Park 2004 (Park). Sodium hydroxide, ethanol, deionized water, and oleic acid were mixed together in a round bottom flask for 1 hour. Hexane and iron (III) chloride were added to the flask, and the mixture was stirred for 15 minutes. The resulting mixture can be seen in Figure 53. The iron oleate/salt mixture was transferred to a separatory funnel where the sodium chloride was washed from the iron oleate. DI water was added to the separatory funnel, mixed by swirling and the sodium chloride was funneled out (Figure 54) until the sodium chloride was completely removed (Figure 55). The hexane was distilled off leaving behind the iron oleate complex seen in Figure 56.

### *Iron Nanoparticle Synthesis*

The iron nanoparticle samples were synthesized by thermal decomposition in a nitrogen environment. Similar to Peng 2006, octadecene, oleylamine, and hexane were used in the synthesis. Peng's synthesis method was modified to produce zero-valent iron nanoparticles as opposed to iron oxide nanoparticles reported in the paper (Peng). Octadecene was dried with NaK then filtered through a 0.45 µm filter using a 30 mL disposable syringe. Dried, filtered octadecene and degassed hexane were deposited into a three-neck round bottom flask. Continuous nitrogen

flowed through a bent stopcock adapter. The remaining flask necks were fitted with a condenser tube and sealed with a septum (Figure 57). The octadecene and oleylamine were heated at 120ºC and stirred at 200 rpm for 30 minutes. The temperature was raised to 250ºC or 230ºC and $Fe(CO)_5$ was injected into the flask through a septum. A violent burst of black/green/yellow/grey smoke blew from the top of the condenser- this can be seen in Figure 58. The reaction was left to stir for 20 or 40 minutes at 250ºC or 230ºC and then allowed to cool to room temperature. A summary of synthesis conditions can be found in Table 5.

***Iron Oleate Shell***

Annealing the ferrite shell was carried out in a separate reaction after the synthesis. This was done to ensure the particle size would remain less than 10 nm (Bronstein). Once cool 0.1-0.4 mL of iron oleate complex was injected into the reaction flask of the samples. The mixture was stirred at room temperature for 30 minutes and then placed in a preheated oil bath. The temperature was raised to 250ºC/230ºC and held there for one hour to anneal the iron oleate to the nanoparticle core. Once cool, the flask was flushed with nitrogen and sealed until sample washing and further coating.

***Sample Washing and Coating***

*Sample Washing*

Samples were poured from the reaction flask into glass jars; the samples often left metallic flake residue on the flask walls (Figure 59). Ethanol (Deacon Labs) was added to each jar to precipitate the nanoparticles from their solution. The jars were shaken to mix the ethanol and particles. The jar was placed on a neodymium magnet to separate the nanoparticles from the reaction solvents (Figure 60). An oily liquid was pulled off the top with a pipet. This process was repeated until the reaction solvents had been removed. Once washed, degassed hexane was added to re-suspend the particles.

*Sample Coating*

Table 5 summarizes the samples and their corresponding coating. Samples JK026 and JK027 were coated with a Brij solution. 5 mL Brij 30 and 25 mL of ethanol were added to a round bottom flask and mixed well. The washed sample, JK026, was added dropwise into the Brij solution. The mixture was stirred in the flask for 30 minutes, and then sonicated for 1 hour. Sample JK027 was

**Table 5 Thermal decomposition synthesis conditions**

| Sample | Synthesis Type | Coating | Reaction Temp. | Reaction Time | Anneal Temp. | Anneal Time | Injection Time | Smoke Color |
|---|---|---|---|---|---|---|---|---|
| JK020 | Thermal decomposition 1.4 mL $Fe(CO)_5$ in ODE/OY | none | 250°C | 20 min. | n/a | n/a | - | - |
| JK021 | Thermal decomposition 1.4 mL $Fe(CO)_5$ in ODE/OY | 0.4 mL iron oleate | 250°C | 20 min. | 250°C | 1 hour | - | - |
| JK022 | Thermal decomposition 1.4 mL $Fe(CO)_5$ in ODE/OY | 0.4 mL iron oleate | 250°C | 20 min. | 250°C | 1 hour | - | - |
| JK023 | Thermal decomposition 1.4 mL $Fe(CO)_5$ in ODE/OY | none | 250°C | 40 min. | n/a | n/a | - | - |
| JK024 | Thermal decomposition 1.4 mL $Fe(CO)_5$ in ODE/OY | none | 250°C | 20 min. | n/a | n/a | - | - |
| JK025 | Thermal decomposition 2.8 mL $Fe(CO)_5$ in ODE/OY | 0.4 mL iron oleate | 250°C | 20 min. | 250°C | 1 hour | - | - |
| JK026 | Thermal decomposition 2.8 mL $Fe(CO)_5$ in ODE/OY | 0.4 mL iron oleate + Brij 30 | 250°C | 20 min. | 250°C | 1 hour | - | - |
| JK027 | Thermal decomposition 2.4 mL $Fe(CO)_5$ in ODE/OY | Brij 30 | 250°C | 20 min. | n/a | n/a | - | - |
| JK028 | Thermal decomposition 2.4 mL $Fe(CO)_5$ in ODE/OY | 0.1 mL iron oleate + PEG 300 | 250°C | 20 min. | 250°C | 1 hour | - | - |
| JK029 | Thermal decomposition 2.4 mL $Fe(CO)_5$ in ODE/OY | 0.1 mL iron oleate | 250°C | 20 min. | 250°C | 1 hour | - | - |
| JK030 | Thermal decomposition 2.4 mL $Fe(CO)_5$ in ODE/OY | none | 250°C | 20 min. | n/a | n/a | - | - |
| JK031 | Thermal decomposition 2.4 mL $Fe(CO)_5$ in ODE/OY | PEG 300 | 250°C | 20 min. | n/a | n/a | - | - |
| JK032 | Thermal decomposition 7.2 mL $Fe(CO)_5$ in ODE/OY | 0.6 mL iron oleate | 250°C | 10 min. | 250°C | 1 hour | 15 min | grey |
| JK033 | Thermal decomposition 7.2 mL $Fe(CO)_5$ in ODE/OY | 0.3 mL iron oleate | 250°C | 10 min. | 250°C | 1 hour | 1.5 min | black/yellow |
| JK034 | Thermal decomposition 2.4 mL $Fe(CO)_5$ in ODE/OY | 0.1 mL iron oleate | 250°C | 20 min. | 250°C | 1 hour | 0.5 min | white/grey |

**Table 5 continued**

| Sample | Synthesis Type | Coating | Reaction Temp. | Reaction Time | Anneal Temp. | Anneal Time | Injection Time | Smoke Color |
|---|---|---|---|---|---|---|---|---|
| JK034 | Thermal decomposition 2.4 mL $Fe(CO)_5$ in ODE/OY | 0.1 mL iron oleate | 250°C | 20 min. | 250°C | 1 hour | 0.5 min | white/grey |
| JK035 | Thermal decomposition 2.4 mL $Fe(CO)_5$ in ODE/OY | 0.1 mL iron oleate | 250°C | 20 min. | 230°C | 1 hour | 0.5 min | black/yellow |
| JK036 | Thermal decomposition 2.4 mL $Fe(CO)_5$ in ODE/OY | 0.1 mL iron oleate | 230°C | 20 min. | 230°C | 1 hour | 0.8 min | white |
| JK038 | Thermal decomposition 2.4 mL $Fe(CO)_5$ in ODE/OY | 0.1 mL iron oleate | 230°C | 20 min. | 230°C | 1 hour | 2 min | yellow |
| JK039 | Thermal decomposition 2.4 mL $Fe(CO)_5$ in ODE/OY | 0.1 mL iron oleate | 230°C | 20 min. | 230°C | 1 hour | 1.5 min | grey |
| JK040 | Thermal decomposition 2.4 mL $Fe(CO)_5$ in ODE/OY | 0.1 mL iron oleate | 230°C | 20 min. | 230°C | 1 hour | 2 min | yellow |
| JK041 | Thermal decomposition 2.4 mL $Fe(CO)_5$ in ODE/OY | 0.1 mL iron oleate | 230°C | 20 min. | 230°C | 30 min | - | - |
| JK042 | Thermal decomposition 2.4 mL $Fe(CO)_5$ in ODE/OY | 0.1 mL iron oleate | 230°C | 20 min. | 230°C | 1 hour | 15 sec. | black/yellow |
| JK043 | Thermal decomposition 2.3 mL $Fe(CO)_5$ in ODE/OY | 0.1 mL iron oleate | 230°C | 20 min. | 230°C | 1 hour | 2 min | - |

coated with a ferrite shell prior to washing. 60 mL of Brij 30 suspended in ethanol was added to a round bottom flask. The ferrite-coated sample JK027, was poured into the flask containing the Brij solution. The solution was stirred at 200 rpm for 1 hour. The sample mixture was poured into sample jars and sonicated for 1 hour.

Samples JK028 and JK031 were coated with a PEG 300. Sample JK028 had a ferrite shell annealed before washing while Sample JK030 had no ferrite shell added. Sample JK028 was coated by injecting 0.3 mL of PEG 300 and stirred for 30 minutes at 1200 rpm under nitrogen flow. Sample JK031 had 0.25 mL PEG 300 added after washing and was stirred at 300 rpm for 20 minutes. Both samples were coated while in a nitrogen gas flow.

***Transmission Electron Microscopy (TEM)***

Transmission electron microscopy (TEM) was performed using a Zeiss Libra 120 at Oak Ridge National Laboratory (ORNL). Samples were prepared by diluting the nanoparticles with hexane until the solution was barely tinted. A copper TEM grid was dipped into the solution and dried in air. Samples JK020, JK021, JK022, JK023, JK026, JK027, JK028, JK029, JK030, JK038, JK039, JK040, JK041, JK042 and JK043 were characterized using this technique.

***Dynamic Light Scattering***

Dynamic Light Scattering (DLS) analysis was performed at the University of Tennessee Space Institute, Tullahoma, TN using a Particulate Systems NanoPlus Zeta/Nano Particle Analyzer. Samples were prepared by diluting the nanoparticles with ethanol until the solution was barely tinted. The diluted solution was pipetted into a quartz cuvette. Analysis was performed using the NanoPlus software program. Samples JK017, JK020, JK021, JK022, JK023, JK024, JK025, JK026, JK027, JK028, JK029, JK030, and JK031 were characterized using this technique.

***Mössbauer Spectroscopy***

Mössbauer Spectroscopy and analysis was performed at the University of Tennessee Space Institute, Tullahoma, TN. A $^{57}$Co source was used for the calibration and sample measurements. The iron nanoparticle samples were dried in an inert atmosphere then frozen prior to characterization. Samples JK020, JK021, JK023, JK025, JK026, JK027, JK028, JK029, JK030, JK031, JK032, JK033, JK034, and JK036 were characterized using this technique

## Results

### *Transmission Electron Microscopy (TEM)*

TEM was performed on samples JK020, JK021, JK022, JK023, JK026, JK027, JK028, JK029, JK030, JK038, JK039, JK040, JK041, JK042 and JK043. A summary of their results can be seen in Table 6. Samples JK021 and JK022 still had reaction solvent present and was therefore too oily to image particles with TEM.

JK020 was imaged several days after synthesis and had no protective shell or additional coating. TEM showed monodispersed particles with an apparent metallic core surrounded by an oxide shell. The particles were 10 nm in diameter and can be seen in Figure 61.

Sample JK023 had aggregates of 130 nm present (Figure 62). Individual particles had a discernable core-shell structure (Figure 62). The smallest core appeared to be 2 nm (Figure 62) and the largest total diameter (core and shell) was measured at 13 nm (Figure 62).

Sample JK026, see Figure 63, exemplified particle sizes of 2 to 13 nm with cores of 2 to 6 nm. JK027, which was only coated with Brij 30, had slightly smaller measurements than JK026, which had a ferrite shell and Brij 30 coating. JK027 had cores measured at 2-5 nm and total diameters of 3-10 nm. Despite the coating, JK027 still appears to have particles that oxidized completely (Figure 64). The small particle size and possible exposure to air during sample washing and coating are both contributing factors to this result. Samples JK026 and JK027 were both agglomerated with measured agglomerates of 72 and 90 nm, respectively.

JK028, seen in Figure 65, had core structures which measured 3-10 nm and total particle diameters of 4-14 nm. While agglomerates were imaged for JK028 at 280 nm, no agglomerates were recorded in JK029. It is unlikely there are no agglomerates, but agglomerates were just not imaged (Figure 66). Sample JK029 exhibited metallic cores ranging from 1 to 9 nm in diameter and total diameters of 4 to 12 nm. This can be seen in Figure 66. Upon visual inspection, samples JK029 and JK026 had a greater size distribution than samples JK020 and JK030. During annealing, the nanoparticles were subjected to a longer duration of high temperatures causing the particles to grow. This explains the greater distribution in size.

Sample JK030 was imaged four hours after synthesis and had no protective shell or coating. Sample JK030 exhibited almost complete oxidation of the metallic iron core within 4 hours of synthesis. The smallest core size was 3 nm with the largest core of 11 nm. The total particle size varied from 4-13 nm (Figure 67). Agglomerates were measured at greater than 190 nm. The remaining core shells that had not yet fully oxidized were 5 nm in diameter and can be seen in Figure 67. This emphasizes the importance of a protective coating; both the ferrite shell and PEG 300 coatings protect the iron core enough to mostly prevent complete oxidation.

Samples JK020 and JK030 had similar syntheses but showed very different stages of oxidation. It could be that JK020 formed its own protective shell by oxidizing inward. JK030 was similar to JK029 in that they have approximately the same diameters and the size distributions were not as large as coated samples. This proved the annealing process grows the nanoparticles.

The particle size of JK038 is seen as 4-10 nm cores, 7-15 nm total diameters with agglomerates greater than 100 nm (Figure 68). JK039 had cores measured at 3-9 nm and total diameters at 7-14 nm with agglomerates of 18-250 nm (Figure 69). JK041 was measured with cores of 4-8 nm, total particles sizes of 7-13 nm and 26-87 nm agglomerates (Figure 70). JK042 total particle sizes varied from 6-11 nm with cores of 3-6 nm. The sample had agglomerates up to 1545 nm (Figure 71). Samples JK040 and JK043 appeared to have not been washed thoroughly (Figure 72); however it can be noted there are large agglomerates present in both samples (Figure 73). A summary of these TEM results can be found in Table 6.

JK038, JK039, JK041, and JK042 all appeared similar under TEM. This is expected as the sample synthesis conditions are largely the same. Noted differences in synthesis conditions are minimal: JK041's annealing time of 30 minutes as opposed to one hour and JK042's quick injection time of 15 seconds compared to 1.5-2 minutes. This indicates the designed reaction can be successfully duplicated. If iron oxide nanoparticles of less than 10 nm in diameter are desired, this would be a suitable reaction to utilize.

Another factor investigated in these samples are the correlation to iron pentacarbonyl injection time. JK042 had the quickest injection time at 15 seconds while JK038 had the longest injection

**Table 6 TEM results of thermal decomposition samples**

| Sample | Core Diameter | Total Diameter | Agglomerates |
|---|---|---|---|
| JK020 | 2-5 nm | 6-11 nm | n/a |
| JK021 | n/a | n/a | n/a |
| JK022 | n/a | n/a | n/a |
| JK023 | 2 to 7 nm | 7 to 13 nm | 130 nm |
| JK024 | n/a | n/a | n/a |
| JK025 | n/a | n/a | n/a |
| JK026 | 2 to 6 nm | 2 to 13 nm | 72 nm |
| JK027 | 2-5 nm | 3-10 nm | 90 nm |
| JK028 | 3-10 nm | 4-14 nm | 280 nm |
| JK029 | 1-9 nm | 4-12 nm | n/a |
| JK030 | 3-11 nm | 4-13 nm | >190 nm |
| JK031 | n/a | n/a | n/a |
| JK032 | n/a | n/a | n/a |
| JK033 | n/a | n/a | n/a |
| JK034 | n/a | n/a | n/a |
| JK035 | n/a | n/a | n/a |
| JK036 | n/a | n/a | n/a |
| JK038 | 4-10 nm | 7-15 nm | >100 nm |
| JK039 | 3-9 nm | 7-14 nm | 18 - 250 nm |
| JK040 | 6-13 nm | 9-16 nm | 735 nm |
| JK041 | 4-8 nm | 7-13 nm | 26-87 nm |
| JK042 | 3-6 nm | 6-11 nm | 1545 nm |
| JK043 | n/a | n/a | >450 nm |

time studied at 2 minutes. There is only a slight difference in size distribution (within nm) in TEM results. This rejects the hypothesis that particles beginning to form initially upon injection are notably larger than those beginning to form at the end of the injection.

***Dynamic Light Scattering (DLS)***

Dynamic Light Scattering (DLS) yields cumulants results, polydispersion index and distribution results for number, volume, and intensity. Cumulants results are the average particle size determined by analysis software. Polydispersion index (pdi) yields a number correlated to the particle size distribution. A perfectly monodispersed sample would yield a 0.0 pdi. All cumulants results evaluated for these samples fall between the smallest and largest dispersion measurements. This indicates groups of particle sizes that are smaller and larger than the average measurement.

The cumulants results for JK020 are 6,580.1 nm with a pdi of 1.227. JK020 had two distribution peaks. The intensity distribution of JK020 was 61.4 ± 2.3 nm and 31,088.2 ± 5,193.9 nm. Volume distribution was 61.1 ± 2.2 nm and 28,641.4 ± 4,719.2 nm. Number distribution was 60.9 ± 2.0 nm and 26,623.2 ± 4,052.5 nm. The distribution results are graphed in Figure 74.

The cumulants results for JK021 are 27,644.1 nm with a pdi of 3.133. JK021 had three distribution peaks. The intensity distribution of JK021 was 177.8 ± 8.3 nm, 3,036.9 ± 437.0 nm, and 130,290.0 ± 27,252.8 nm. Volume distribution was 176.6 ± 8.2 nm, 2,859.9 ± 401.3 nm, and 114,878.0 ± 23,347.6 nm. Number distribution was 175.6 ± 7.9 nm, 2,713.0 ± 349.4, and 103,528.0 ± 18,492.4 nm. The distribution results are graphed in Figure 75.

The cumulants results for JK022 are 6,712.9 nm with a pdi of 1.118. JK022 had two distribution peaks. The intensity distribution of JK022 was 72.1 ± 2.9 nm and 24,075.7 ± 4,071.7 nm. Volume distribution was 71.8 ± 2.7 nm and 22,159.6 ± 3,659.4 nm. Number distribution was 71.5 ± 2.6 nm and 20,616.9 ± 3,103.1 nm. The distribution results are graphed in Figure 76.

The cumulants results for JK023 are 6,580.1 nm with a pdi of 1.227. JK020 had four distribution peaks. The intensity distribution of JK023 was 52.2 ± 2.1 nm 244.5 ± 20.9 nm, 787.2 ± 146.8, and 40,102.6 ± 7,662.3 nm. Volume distribution was 51.9 ± 2.1 nm, 239.2 ± 20.5 nm, 710.3 ± 131.1

nm, and 36,073.5 ± 6,738.4 nm. Number distribution was 51.7 ± 2.1 nm, 234.2 ± 19.3 nm, 650.1 ± 107.9 nm, and 32,944.0 ± 5,542.4 nm. The distribution results are graphed in Figure 77.

The cumulants results for JK024 are 4,576.7 nm with a pdi of 0.909. JK024 had two distribution peaks. The intensity distribution of JK024 was 51.5 ± 2.0 nm and 34,813.0 ± 6,571.4 nm. Volume distribution was 51.3 ± 1.9 nm and 31,412.2 ± 5,774.4 nm. Number distribution was 51.0 ± 1.8 nm and 28,768.3 ± 4,764.8 nm. The distribution results are graphed in Figure 78.

The cumulants results for JK025 are 1,446.7 nm with a pdi of 0.335. JK025 had two distribution peaks. The intensity distribution of JK025 was 20.6 ± 0.8 nm and 26,597.1 ± 2,282.1 nm. Volume distribution was 20.5 ± 0.7 nm and 26,002.7 ± 2,269.1 nm. Number distribution was 20.5 ± 0.7 nm and 25,424.6 ± 2,191.2 nm. The distribution results are graphed in Figure 79.

The cumulants results for JK026 are 9,463.3 nm with a pdi of 1.298. JK026 had three distribution peaks. The intensity distribution of JK026 was 92.3 ± 3.6 nm, 1,136.8 ± 0.2 nm, and 21,375.7 ± 3,805.6 nm. Volume distribution was 91.9 ± 3.4 nm, 1.136 ± 0.3 nm and 19,484.3 ± 3,406.7 nm. Number distribution was 91.5 ± 3.1 nm, 1,136.8 ± 0.2 nm, and 17,981.7 ± 2,848.1 nm. The distribution results are graphed in Figure 80.

The cumulants results for JK027 are 1,230.9 nm with a pdi of 0.289. JK027 had three distribution peaks. The intensity distribution of JK027 was 23.6 ± 2.5 nm, 124.1 ± 8.9 nm, and 19,992.4 ± 2,175.9 nm. Volume distribution was 22.7 ± 2.3 nm, 122.1 ± 8.9nm, and 19,272.6 ± 2,147.8 nm. Number distribution was 22.1 ± 2.1 nm, 120.3 ± 8.5 nm, and 18,583.0 ± 2,036.6 nm. The distribution results are graphed in Figure 81.

The cumulants results for JK028 are 5, 080.1 nm with a pdi of 0.948. JK028 had two distribution peaks. The intensity distribution of JK028 was 51.6 ± 2.1 nm and 24,277.0 ± 4,095.6 nm. Volume distribution was 51.3 ± 2.0 nm and 22,320.2 ± 3,726.9 nm. Number distribution was 51.1 ± 1.9 nm and 20,709.6 ± 3,188.9 nm. The distribution results are graphed in Figure 82.

The cumulants results for JK029 are 5,218.2 nm with a pdi of 0.962. JK029 had two distribution peaks. The intensity distribution of JK029 was 51.3 ± 2.0 nm and 22,813.8 ± 3,613.5 nm. Volume

distribution was 51.1 ± 1.9 nm and 21,200.6 ± 3,299.7 nm. Number distribution was 50.9 ± 1.8 nm and 19,855.0 ± 2,866.7 nm. The distribution results are graphed in Figure 83.

The cumulants results for JK030 are 5,295.8 nm with a pdi of 0.959. JK030 had two distribution peaks. The intensity distribution of JK030 was 61.8 ± 2.4 nm and 22,458.6 ± 3,633.5 nm. Volume distribution was 61.5 ± 2.3 nm and 20,786.4 ± 34331.8 nm. Number distribution was 61.3 ± 2.2 nm and 19,385.9 ± 2,888.8 nm. The distribution results are graphed in Figure 84.

The cumulants results for JK031 are 1,971.6 nm with a pdi of 0.429. JK031 had three distribution peaks. The intensity distribution of JK031 was 30.8 ± 2.3 nm, 440.0 ± 53.0 nm, and 35,235.9 ± 5,292.0 nm. Volume distribution was 30.7 ± 1.0 nm, 421.7 ± 49.9 nm, and 32,874.4 ± 5,036.0 nm. Number distribution was 30.6 ± 1.0 nm, 405.6 ± 45.3 nm, and 30,771.0 ± 4,502.4 nm. The distribution results are graphed in Figure 85.

All measurements are greater than any diameter recorded in TEM. This is likely due to agglomerates not broken up by sonication. Sample JK021 had the greatest pdi of 3.133 while Sample JK027 had the smallest pdi at 0.289. This result indicates JK027 likely has the largest size distribution while JK020 is closer to monodispersed. A summary of DLS cumulants results compared to TEM measurements can be found in Table 7.

***Mössbauer Spectroscopy***

Mössbauer spectroscopy is a useful technique that allows for the determination of different atomic valencies in materials. For this study, it is important to distinguish between metallic iron atoms, which have a 0 mm/s isomer shift, from the $Fe^{3+}$ and $Fe^{2+}$ iron oxides which have isomer shifts of 0.5 mm/s and 1.5 mm/s respectively. Variances between spectra are the result of different coatings and washing methods.

JK020 was a monodispersed sample with no coating. Mössbauer spectroscopy, seen in Figure 86, revealed it to be a mix of oxides and possibly metallic iron. Forty percent of the sample had a hyperfine field of 548 kG while the remaining sixty percent had a hyperfine field of 273 kG.

**Table 7 DLS cumulants results with TEM results (core + shell, agglomerates)**

| Sample | DLS Diameter (nm) | PDI | TEM Diameter (nm) |
|---|---|---|---|
| JK020 | 6580.1 | 1.227 | 6-11 nm |
| JK021 | 27644.1 | 3.133 | n/a |
| JK022 | 6712.9 | 1.118 | n/a |
| JK023 | 4531.9 | 0.858 | 7-13 nm, 130 nm |
| JK024 | 4576.7 | 0.909 | n/a |
| JK025 | 1446.7 | 0.335 | n/a |
| JK026 | 9463.3 | 1.298 | 2-13 nm, 72 nm |
| JK027 | 1230.9 | 0.289 | 3-10 nm, 90 nm |
| JK028 | 5080.1 | 0.948 | 4-14 nm, 280 nm |
| JK029 | 5218.2 | 0.962 | 4-12 nm |
| JK030 | 5295.8 | 0.959 | 4-13 nm, >190 nm |
| JK031 | 1971.6 | 0.429 | n/a |
| JK038 | n/a | n/a | 7-15 nm, >100 nm |
| JK039 | n/a | n/a | 7-14 nm, 250 nm |
| JK040 | n/a | n/a | 9-16 nm, 735 nm |
| JK041 | n/a | n/a | 7-13 nm, 87 nm |
| JK042 | n/a | n/a | 6-11 nm, 1545 nm |
| JK043 | n/a | n/a | n/a, >450 nm |

Mössbauer spectroscopy of JK021 (Figure 87) had very low absorption, but the hyperfine field of 481 kG closely resembles $Fe_2O_3$. JK023 Mössbauer spectroscopy (Figure 77) portrayed relaxation not present in other samples with a hyper fine field of 392 kG. It had the longest reaction time and the largest amount of iron oleate coating which may have contributed to the relaxation.

Mössbauer spectroscopy of JK025 at 6 K, seen in Figure 89, shows a very characteristic $Fe_2O_3$ spectrum with a hyperfine field of 494 kG. The sample was coated in only a ferrite shell. It appears very similar to JK026 and JK027.

Figure 90 shows the fitted Mössbauer spectrum of sample JK026 at 6 K. The spectrum yields a single $Fe^{3+}$ site, which implies the sample is composed of $Fe_2O_3$. Sample JK026 was coated in a ferrite shell and the surfactant Brij 30. These results confirm a ferrite shell, but oxidation could also indicate the failure of the surfactant to protect the nanoparticle.

The Mössbauer spectrum of sample JK027, at 6 K, can be seen in Figure 91. Like sample JK026, the fitting of this spectra determined the composition to be $Fe_2O_3$. This sample did not have a ferrite coating added post synthesis, so sample JK027 could have oxidized before the Brij 30 surfactant was added. This could also indicate that the surfactant was not a suitable coating to protect the metallic iron nanoparticles from oxidation. JK028 has very low absorption in Mössbauer spectroscopy (Figure 92) but still seems to replicate JK025, JK026 and JK027 as it is all oxide.

Figure 93 is the Mössbauer spectrum of sample JK029 at 6 K. The low absorption and broadening of the lines hindered a good fit. However, we can confirm that the sample is not metallic iron based on the hyperfine field. The distance between the peaks seen in Figure 93 is less than the 330 kG characteristic of metallic iron.

Figure 94 depicts the Mössbauer spectrum of sample JK029 at room temperature. Like Figure 93, the absorption was very low; however, we can discern further broadening of the lines. This indicates the sample has a size distribution that includes particles extremely small in size (2.5nm) (Christensen). This agrees with TEM results of sample JK029.

Sample JK030 had no coating. Its Mössbauer spectrum (seen in Figure 95) shows a mix of oxides, where $Fe_2O_3$ is the main chemical component. Similar to sample JK029, sample JK030 had very low absorption. A definite fit of this sample cannot be made due to the absorption and mix of oxides. Again, this confirms the oxidation of the nanoparticles without coating. The lack of a ferrite shell resulted in a mix of $Fe^{2+}$ and $Fe^{3+}$ oxides. This oxidation mechanism is further described in Costa 2014 (Costa).

Figure 96 is the Mössbauer spectrum of sample JK031 at 6 K. Sample JK031 was coated only in the PEG 300 polymer after synthesis and washing of the iron nanoparticles. The spectrum shows sample JK031 to be a mix of oxides. From this result, it is determined that either oxidation occurred prior to coating the sample or PEG 300 is not an ideal coating for protecting the nanoparticle from oxidation.

JK032 had the longest injection time of the $Fe(CO)_5$ and the most iron oleate used for a coating. Figure 97 is the Mössbauer spectrum for JK032 and has a hyperfine field of 195 kG. This may be similar to $FeC_3$ which has a hyperfine field of 211 kG. It also has quadrupole splitting not characteristic of the other thermal decomposition samples.

Figure 98 is the Mössbauer spectrum of JK033 at 6 K. Figure 99 is the Mössbauer spectrum of JK033 at 293 K. At low temperature the sample resembles the other $Fe_2O_3$ spectra with a hyperfine field of 496 kG. At room temperature the spectrum narrows indicating paramagnetism.

Mössbauer spectroscopy of JK034 was performed at 6 K, 300 K, 300 K with a 0.078 T field and 293 K with a 20 kG field. At low temperature (Figure 100) JK034 was composed of twenty-eight percent $Fe_2O_3$ with a hyperfine field of 495 kG and seventy-two percent with a hyperfine field of 225 kG. There is also relaxation present at low temperature. At higher temperature the field narrows (Figure 102, Figure 103) indicating paramagnetism. With a 10 kG field applied, seen in Figure 101, the spectrum sharpens.

The Mössbauer spectrum JK036 at 6 K, seen in Figure 104, resembled JK025, JK026 and other $Fe_2O_3$ samples made using this synthesis method. The sample produced white smoke after the $Fe(CO)_5$ injection, while other $Fe_2O_3$ samples made in synthesis had black, yellow and grey smoke.

This indicates the smoke produced at synthesis is not correlated to sample composition. A summary of these findings can be found in Table 8.

## Discussion

Small iron nanoparticles <10 nm in size were synthesized by thermal decomposition and encased with various coatings. The nanoparticles appeared monodispersed under transmission electron microscopy (TEM). Upon later characterization it was found that all samples were some form of iron oxide. This could be a result of inadequate protection from oxidation by the coatings, cleaning methods or annealing and coating application procedures.

A ferrite shell was annealed to the iron nanoparticles and increased stabilization. While the PEG 300 and Brij 30 coatings seemingly did not prevent oxidation, they do provide a biocompatible surface. Uncoated nanoparticles that were washed to remove the reaction solvents almost fully oxidized within 4 hours. Storing the iron nanoparticles in their reaction solvent after synthesis appeared to extend the time before complete oxidation.

The reaction appears incredibly reliable for producing $Fe_2O_3$ nanoparticles. Nearly all of the samples were composed of only $Fe_2O_3$ or had some percentage of $Fe_2O_3$ present. This is regardless of size or coatings. It is likely then that the iron core oxidizes completely or partially into $Fe_2O_3$. The annealing process may also anneal $Fe_2O_3$ to the cores; the proportion of oxide shell may be so great that only the $Fe_2O_3$ shell is seen in Mössbauer spectroscopy.

Samples with ferrite shells had the largest size distribution. The annealing process of the ferrite shell caused the iron nanoparticles to grow which increased size distribution. The longer reaction time of JK023 (double of all other samples) also increased size distribution. From this it can be concluded that the heating of the particles past twenty minutes, whether during the synthesis or coating process, causes particles to grow and varying rates leading to larger size distributions. The smallest size distribution was seen in the two uncoated samples, JK020 and JK030.

**Table 8 Mössbauer Results of Iron Pentacarbonyl Thermal Decomposition Samples**

| Sample | Temp | Field | Site 1 Percentage | Site 1 Hyperfine | Site 1 Isomer Shift | Site 1 Quadrupole Splitting | Site 2 Percentage | Site 2 Hyperfine | Site 2 Isomer Shift | Site 2 Quadrupole Splitting |
|---|---|---|---|---|---|---|---|---|---|---|
| JK036 | 6 K | | 100.00% | 485.52 | 0.49 | | | | | |
| JK034 | 6 K | | 28.26% | 494.81 | 0.48 | | 71.74% | 224.52 | 0.42 | |
| JK034 | 293 K | 10 kG | 100.00% | 0 | 0.27 | | | | | |
| JK034 | 300 K | | 100.00% | 0 | 0.39 | | | | | |
| JK034 | 300 K | 0.078 T | 100.00% | 0 | 0.4 | | | | | |
| JK033 | 6 K | | 100.00% | 495.69 | 0.46 | | | | | |
| JK033 | 290 K | | 100.00% | 0.00 | 0.37 | 0.78 | | | | |
| JK032 | 290 K | | 78.27% | 195.02 | 0.12 | | 21.73% | | 0.32 | -1.09 |
| JK031 | 6 K | | 100.00% | 469.69 | 0.29 | | | | | |
| JK030 | 6 K | | 100.00% | 466.92 | 0.42 | 0.12 | | | | |
| JK029 | 6 K | | 100.00% | 377.22 | 0.29 | 0.31 | | | | |
| JK029 | 290 K | | 100.00% | 329.17 | 0.88 | 1.27 | | | | |
| JK028 | 6 K | | 100.00% | 445.76 | 0.38 | 0.16 | | | | |
| JK027 | 6 K | | 100.00% | 475.96 | 0.44 | | | | | |
| JK026 | 6 K | | 100.00% | 491.07 | 0.44 | | | | | |
| JK025 | 6 K | | 100.00% | 493.61 | 0.44 | | | | | |
| JK023 | 6 K | | 100.00% | 392.00 | 0.25 | | | | | |
| JK021 | 6 K | | 100.00% | 481.19 | 0.52 | 0.20 | | | | |
| JK020 | 6 K | | 39.73% | 547.87 | 0.50 | | 60.27% | 273.29 | 0.40 | |

***Future Work***

The surface area of the ferrite and naturally oxidized shell may mask a result of monometallic iron in Mössbauer spectroscopy. A reduction in size of the ferrite shell may aid the Mössbauer characterization while still preventing further oxidation. Washing techniques need to be improved to prevent oxidation while completely removing reaction solvents. An investigation into the ideal anneal time of the ferrite shell should be performed in attempt to control size distribution of the nanoparticles.

This type of reaction repeatedly produced oxide results. While this was reliable, it is not the desired product for the applications targeted in this dissertation. In order to produce iron metal, another synthesis method will likely need to be utilized. A reduction reaction with a different source of iron than Chapter II may be ideal.

# Chapter III Appendix



**Figure 53 Iron Oleate/Salt Mixture**

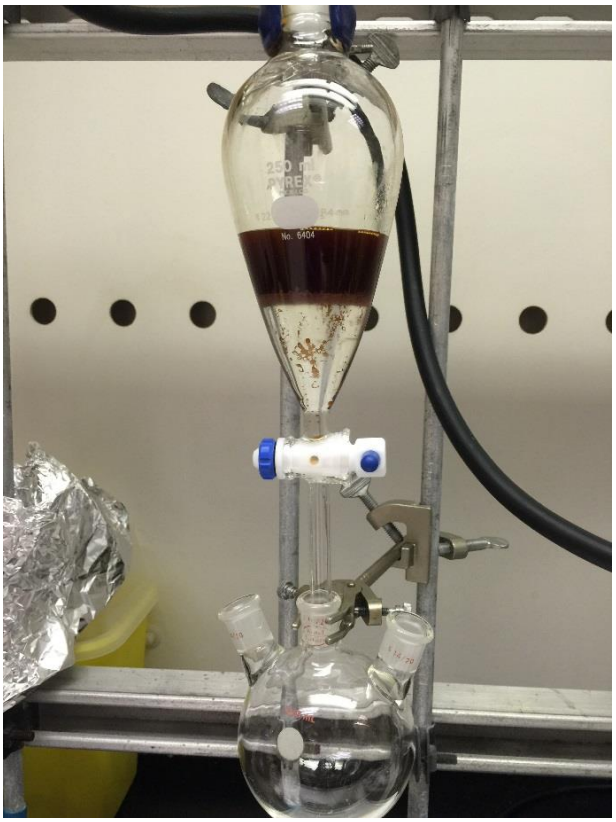


**Figure 54 Iron Oleate with Added DI Water**




**Figure 55 Iron Oleate with Sodium Chloride Removed**

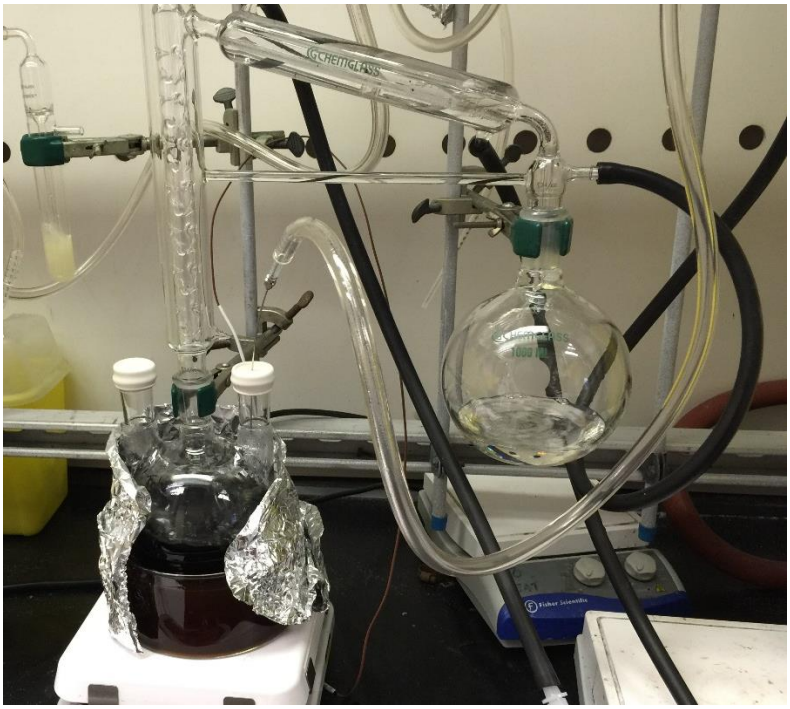


**Figure 56 Distillation of Iron Oleate Complex**

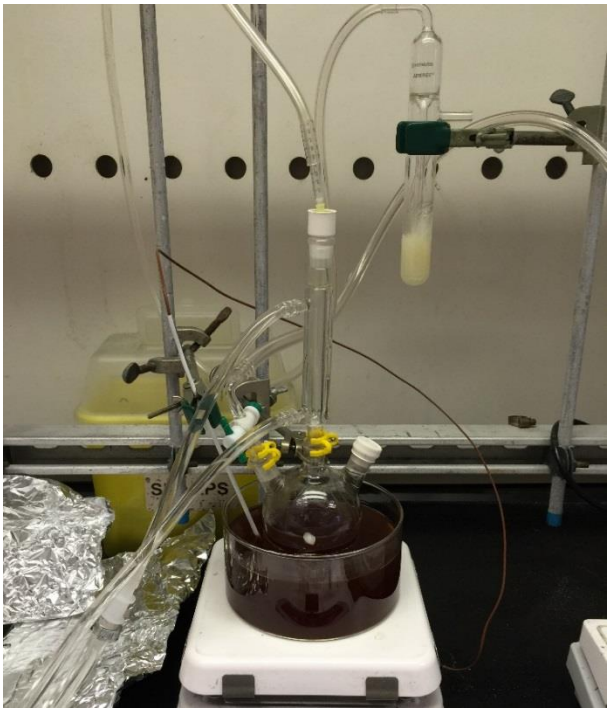


**Figure 57 Thermal Decomposition Synthesis**



**Figure 58 Smoke Emitted After Iron Pentacarbonyl Injection**




**Figure 59 Residue on Flask Post Synthesis**

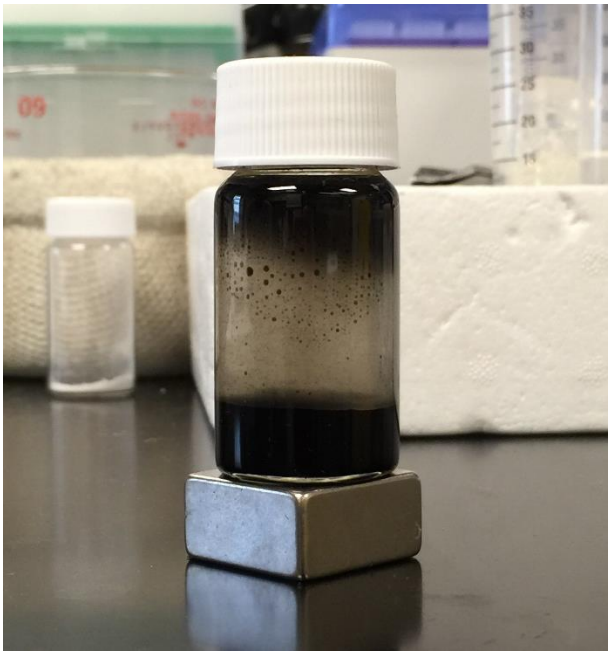


**Figure 60 Magnetic Separation of Sample JK022**

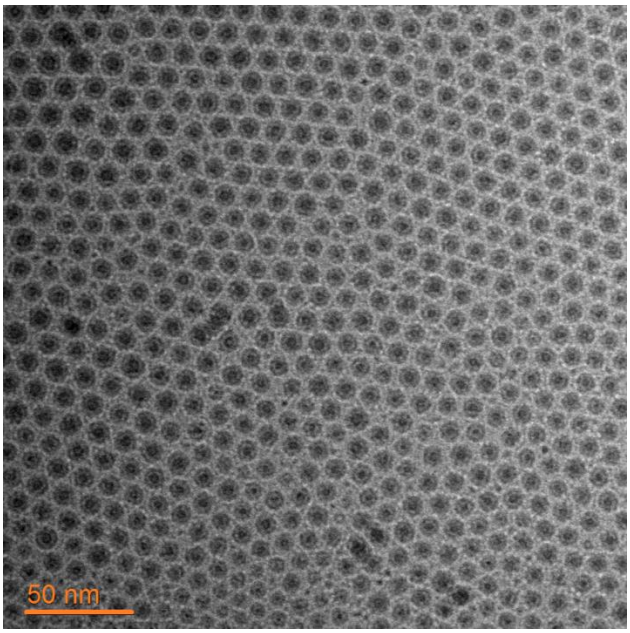



**Figure 61 TEM of JK020**

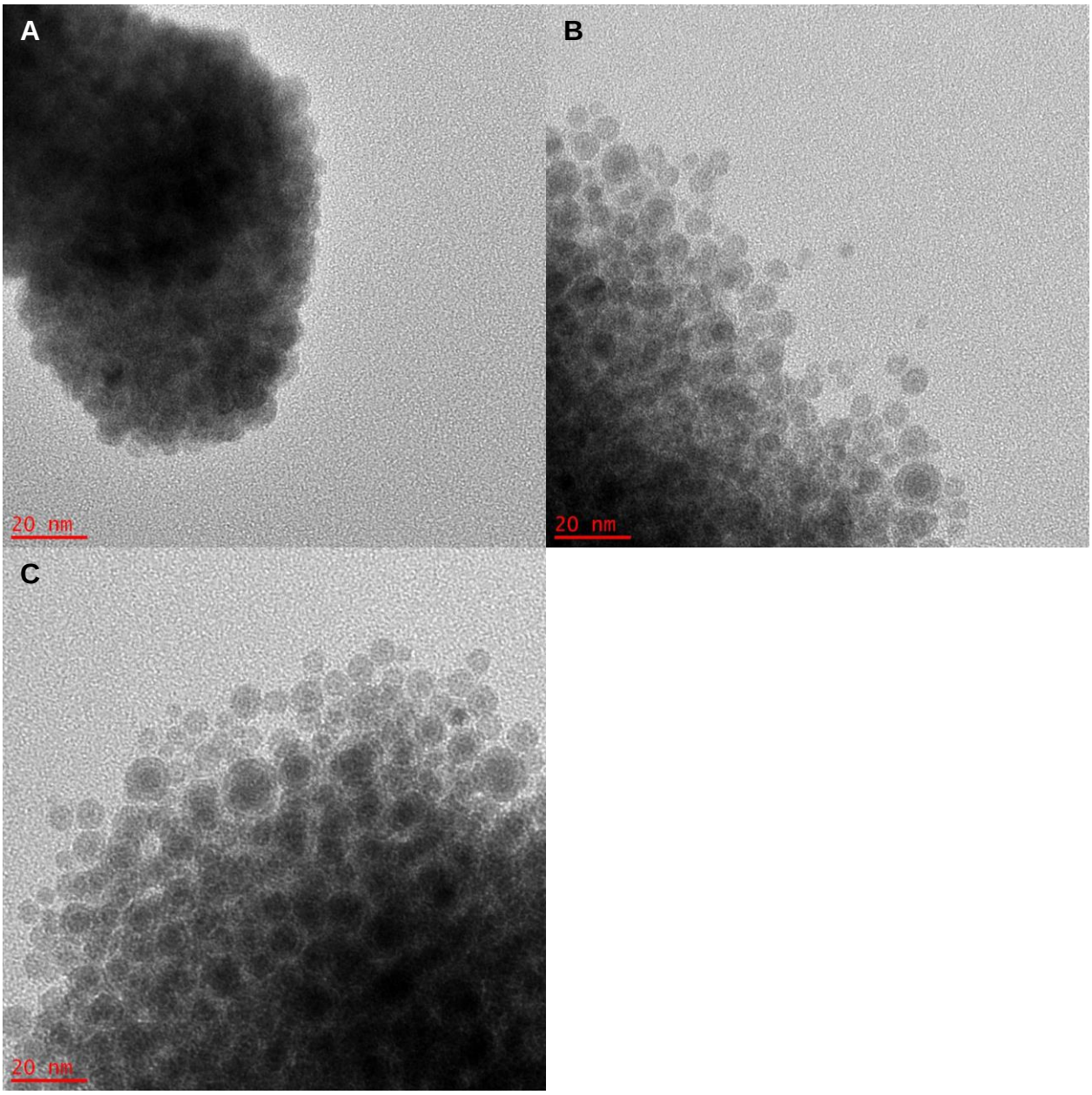



**Figure 62 TEM of JK023**

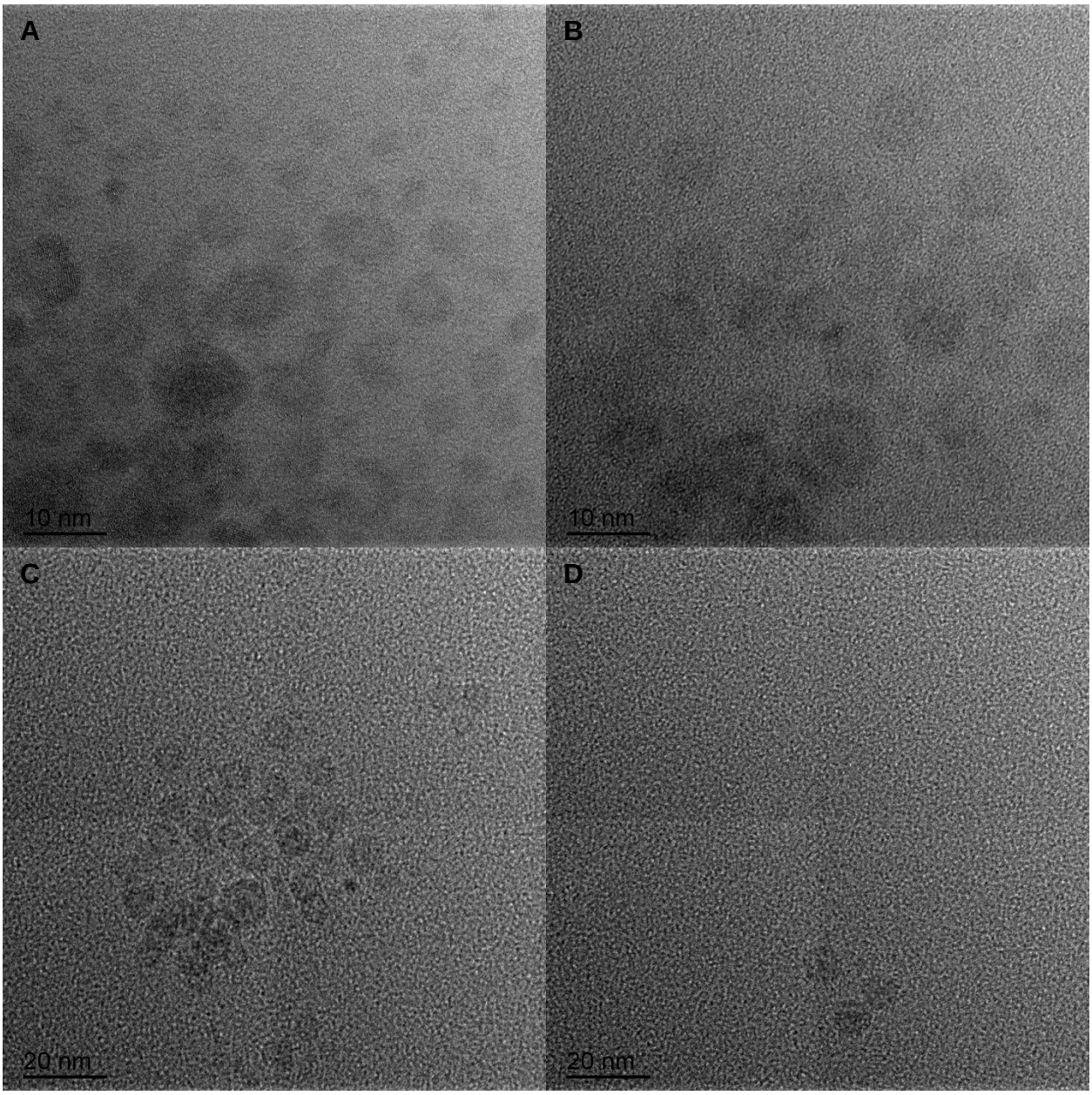



**Figure 63 TEM of JK026**

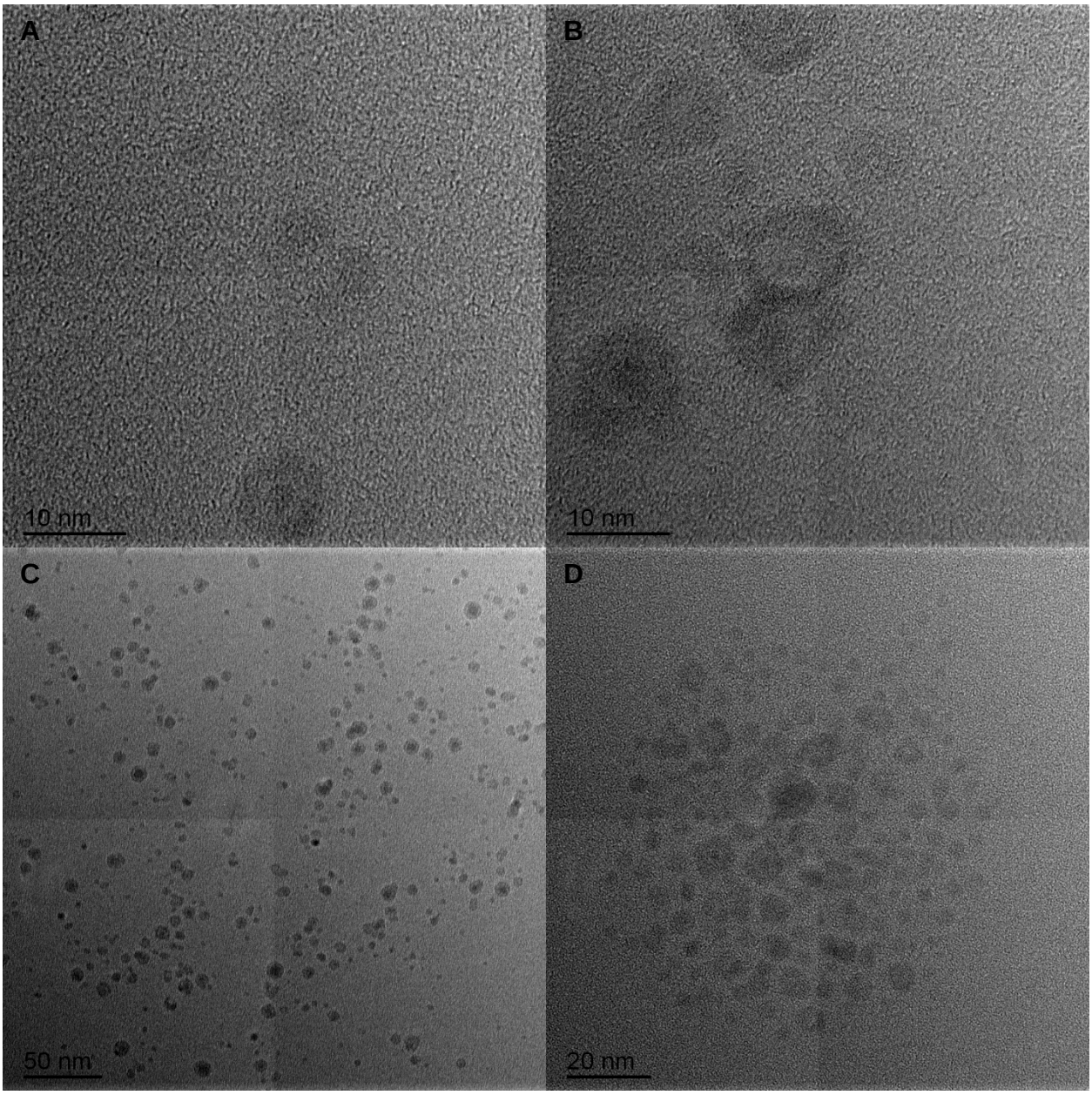



**Figure 64 TEM of JK027**

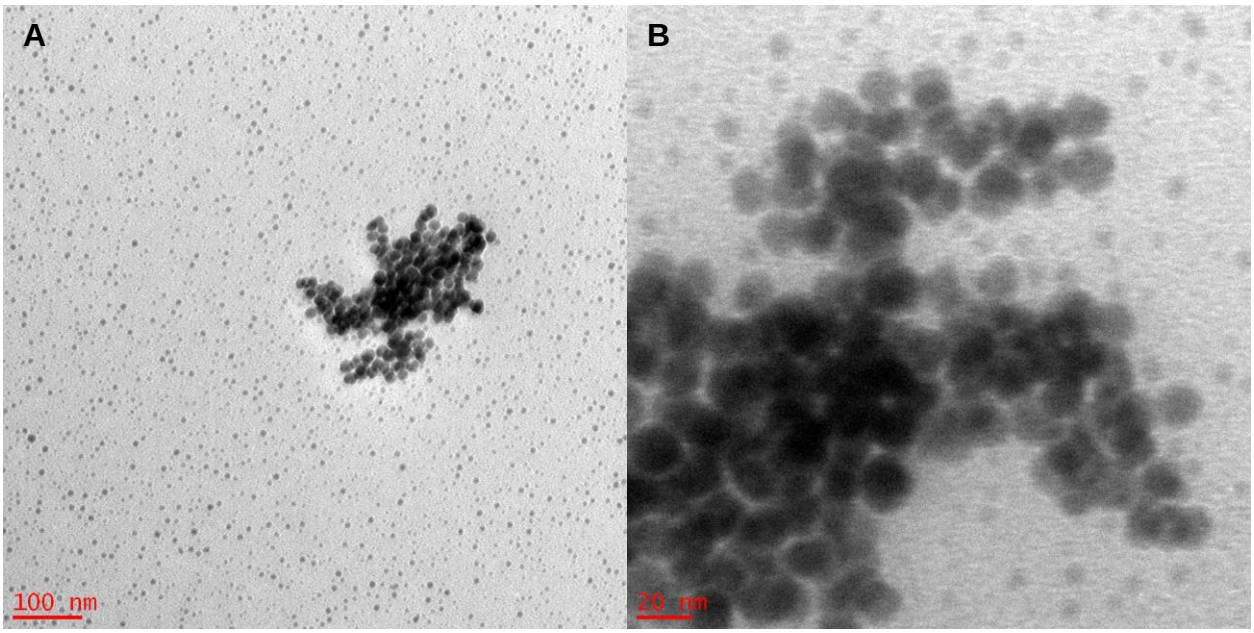



**Figure 65 TEM of JK028**

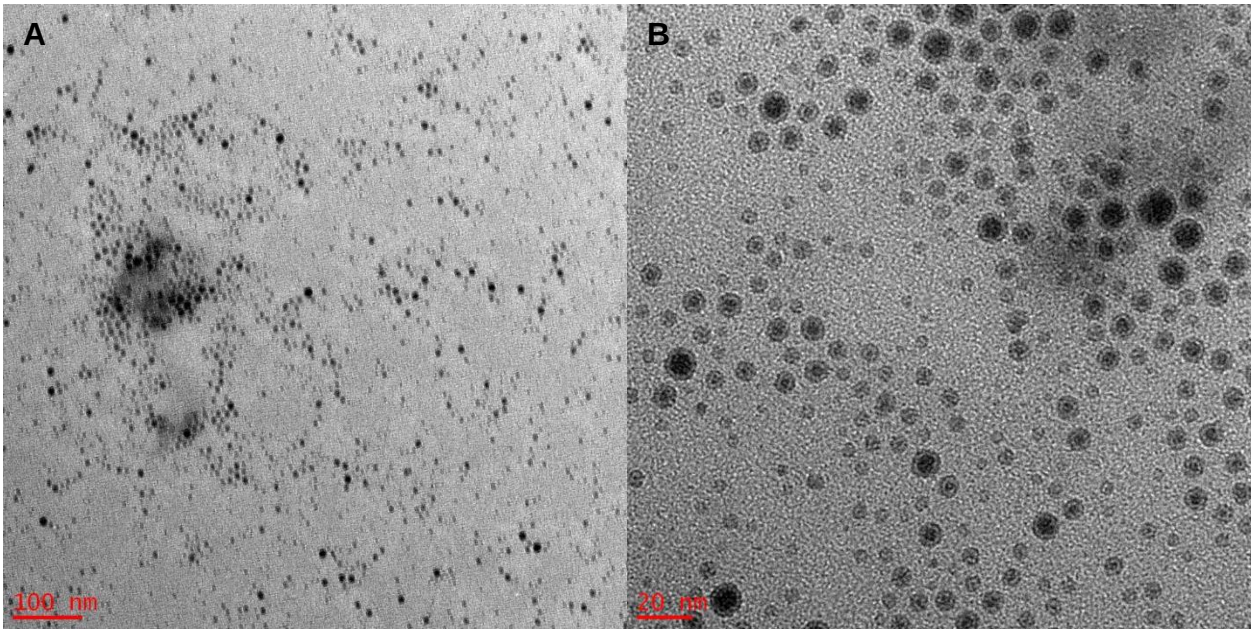



**Figure 66 TEM of JK029**

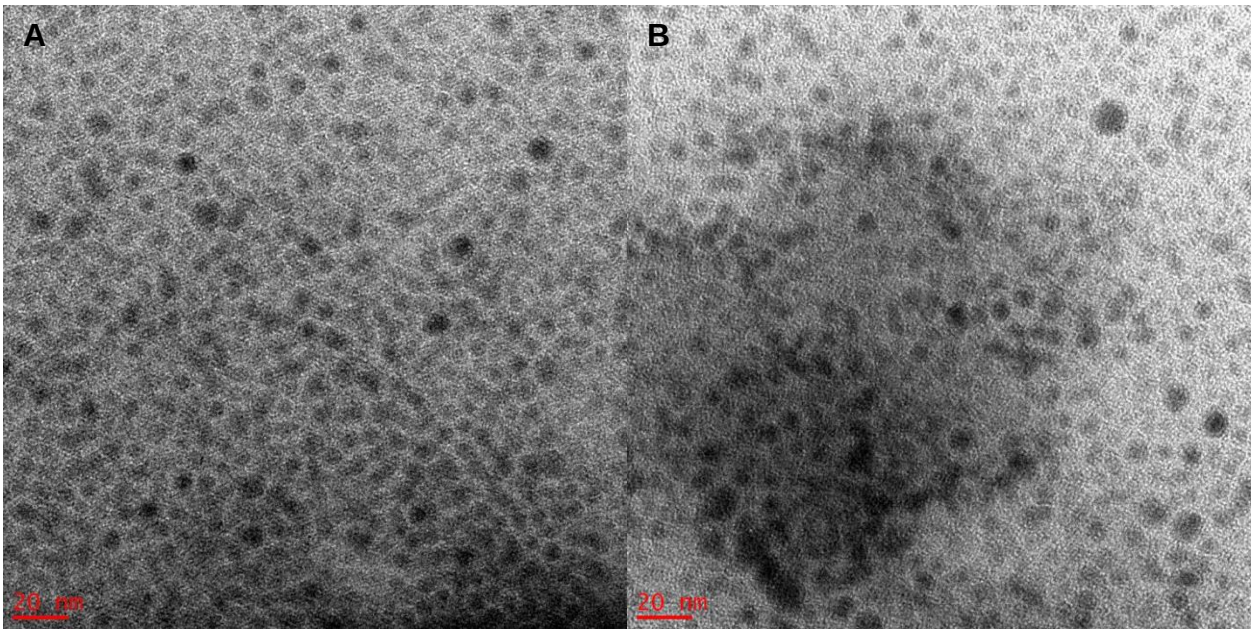



**Figure 67 TEM of JK30**

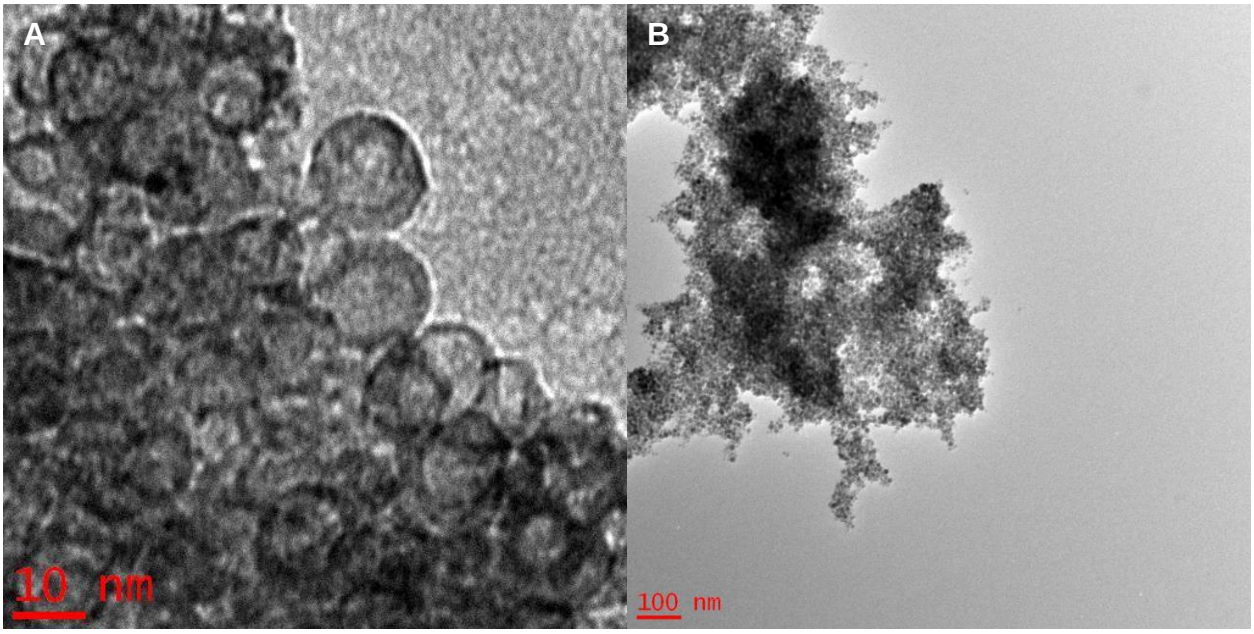



**Figure 68 TEM of JK038**

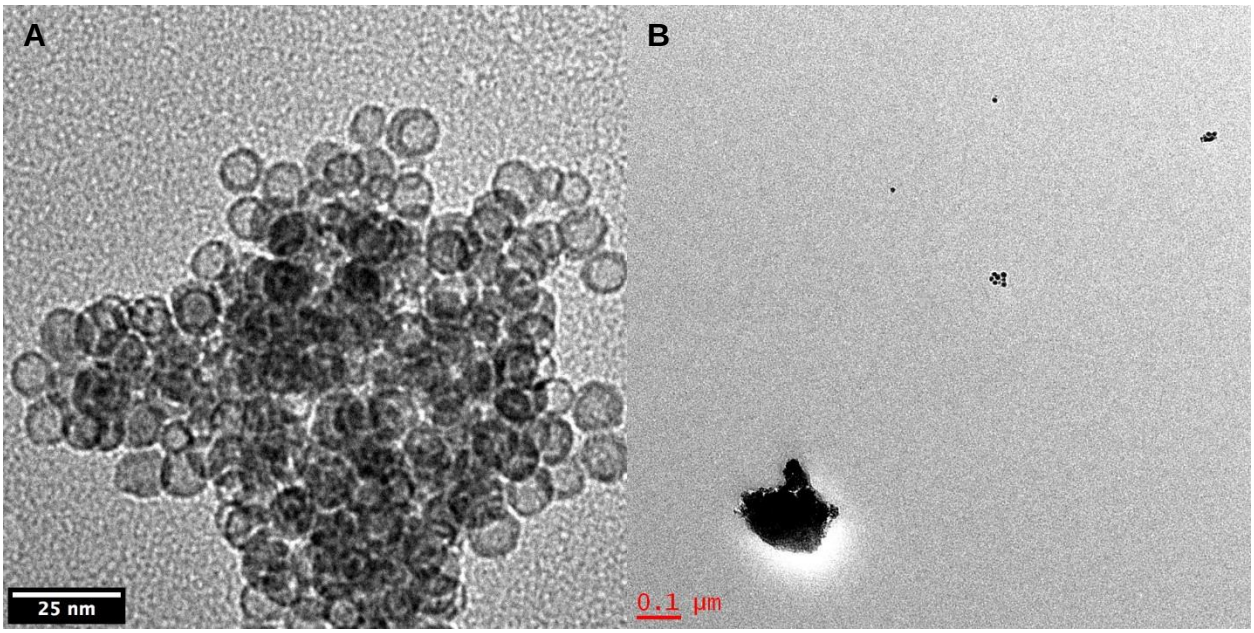



**Figure 69 TEM of JK039**

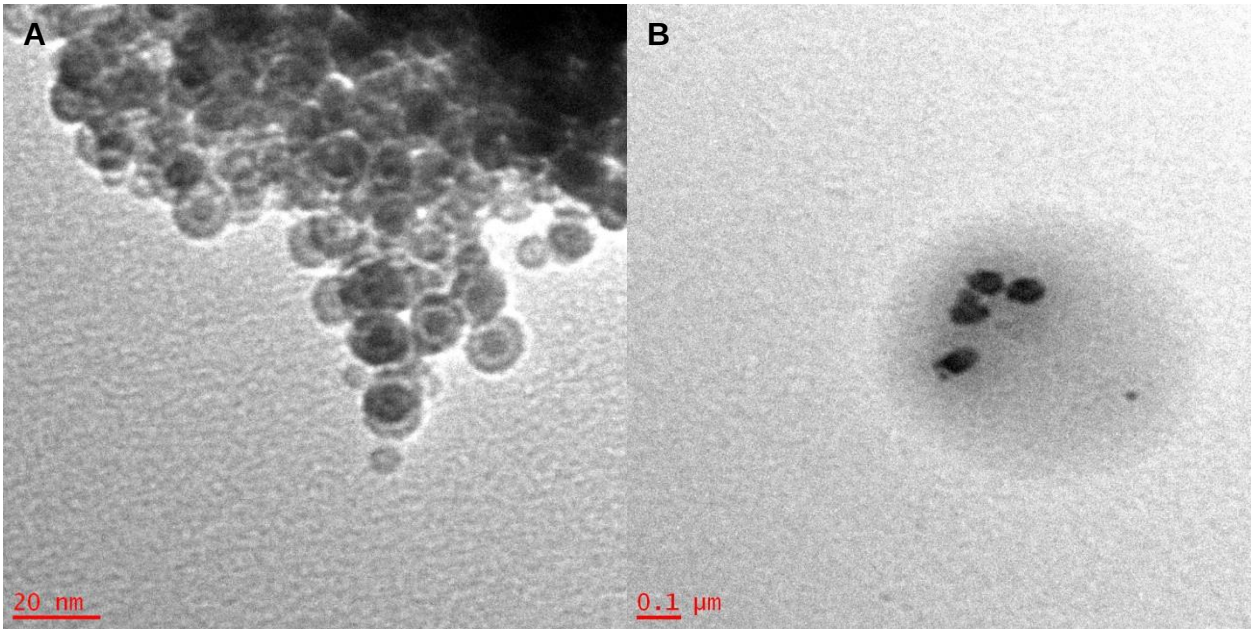



**Figure 70 TEM of JK041**

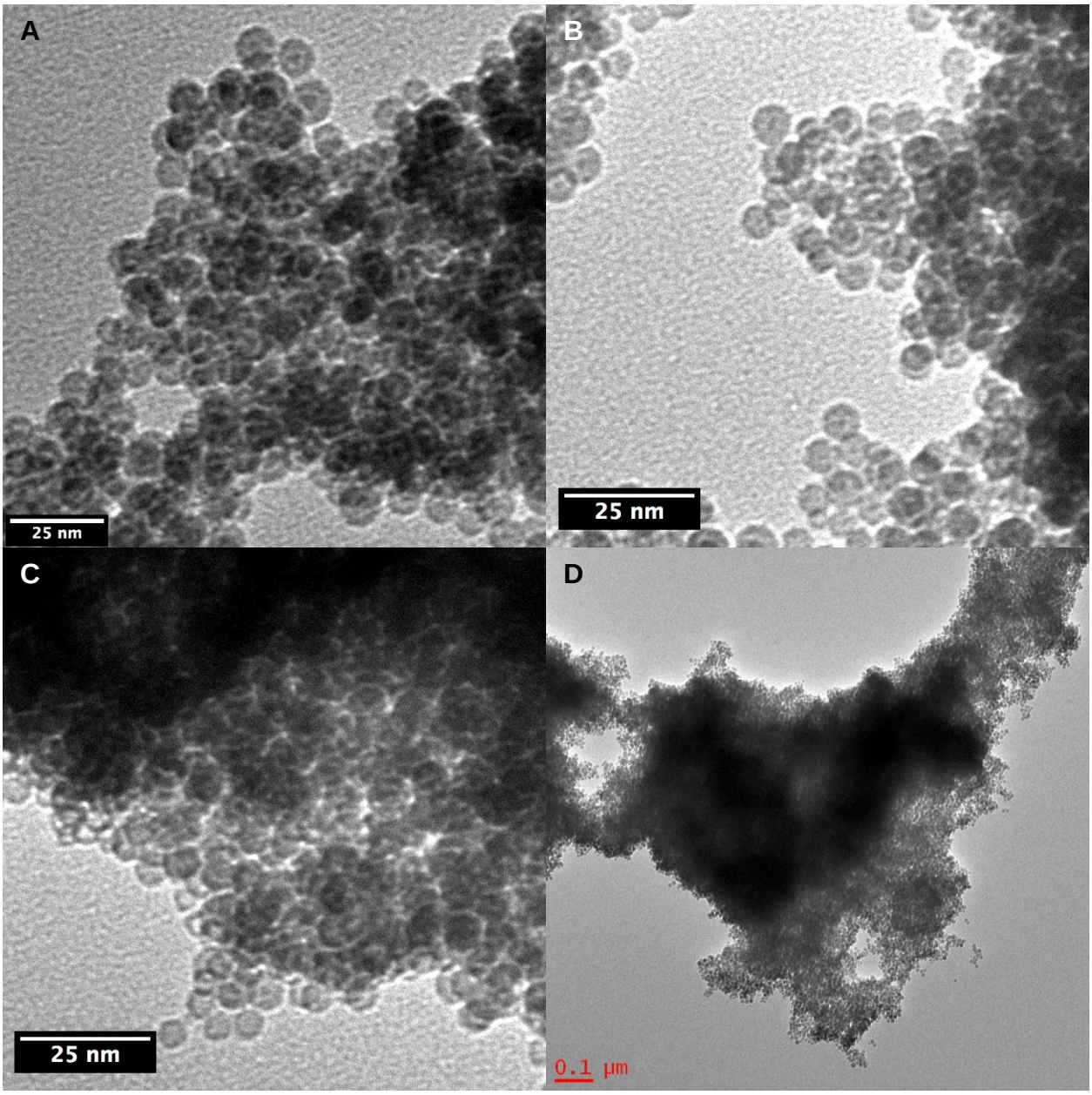



**Figure 71 TEM of JK042**

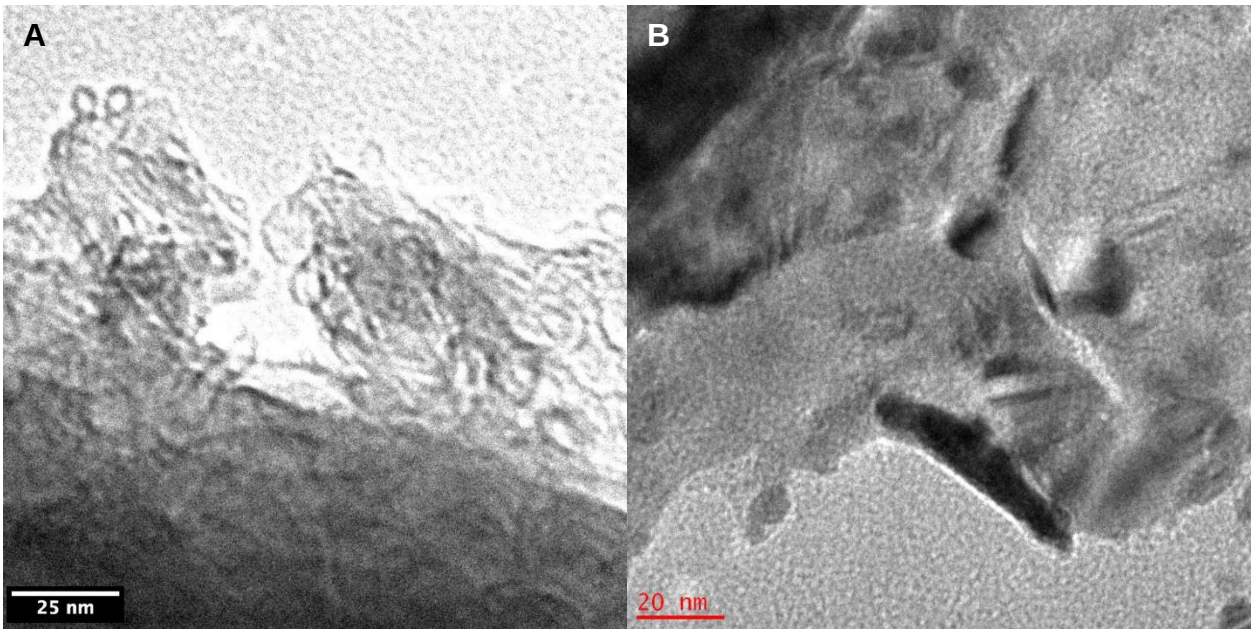



**Figure 72 TEM of A) JK040 and B) JK043**

B

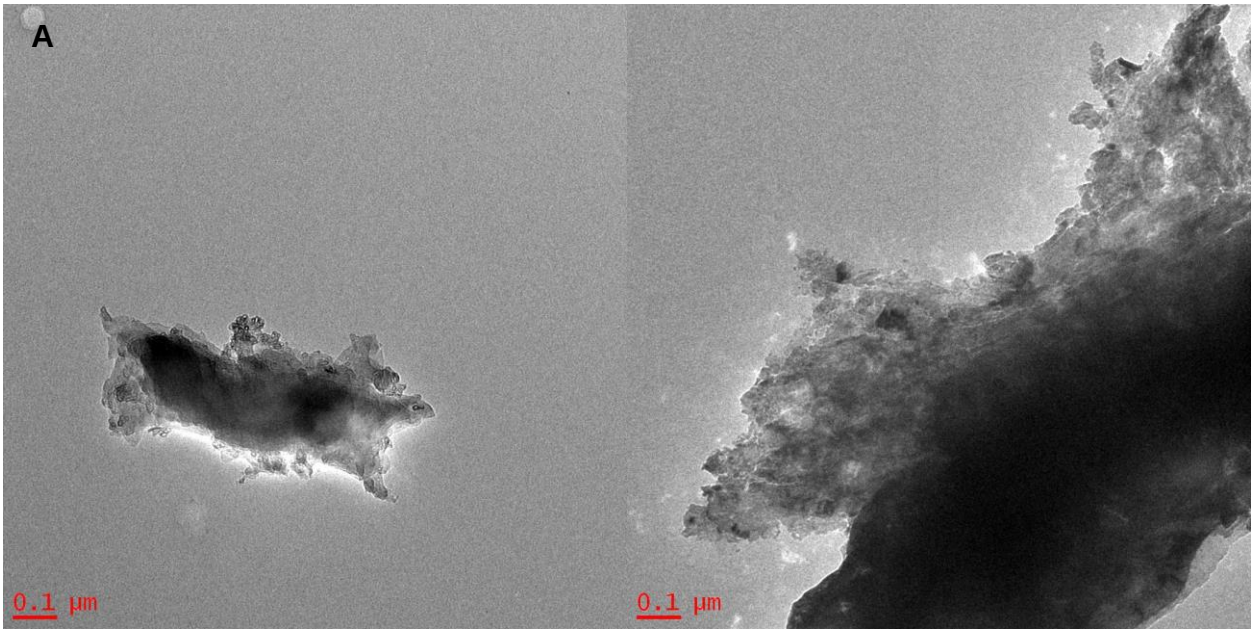



**Figure 73 TEM of A) JK040 B) JK043**

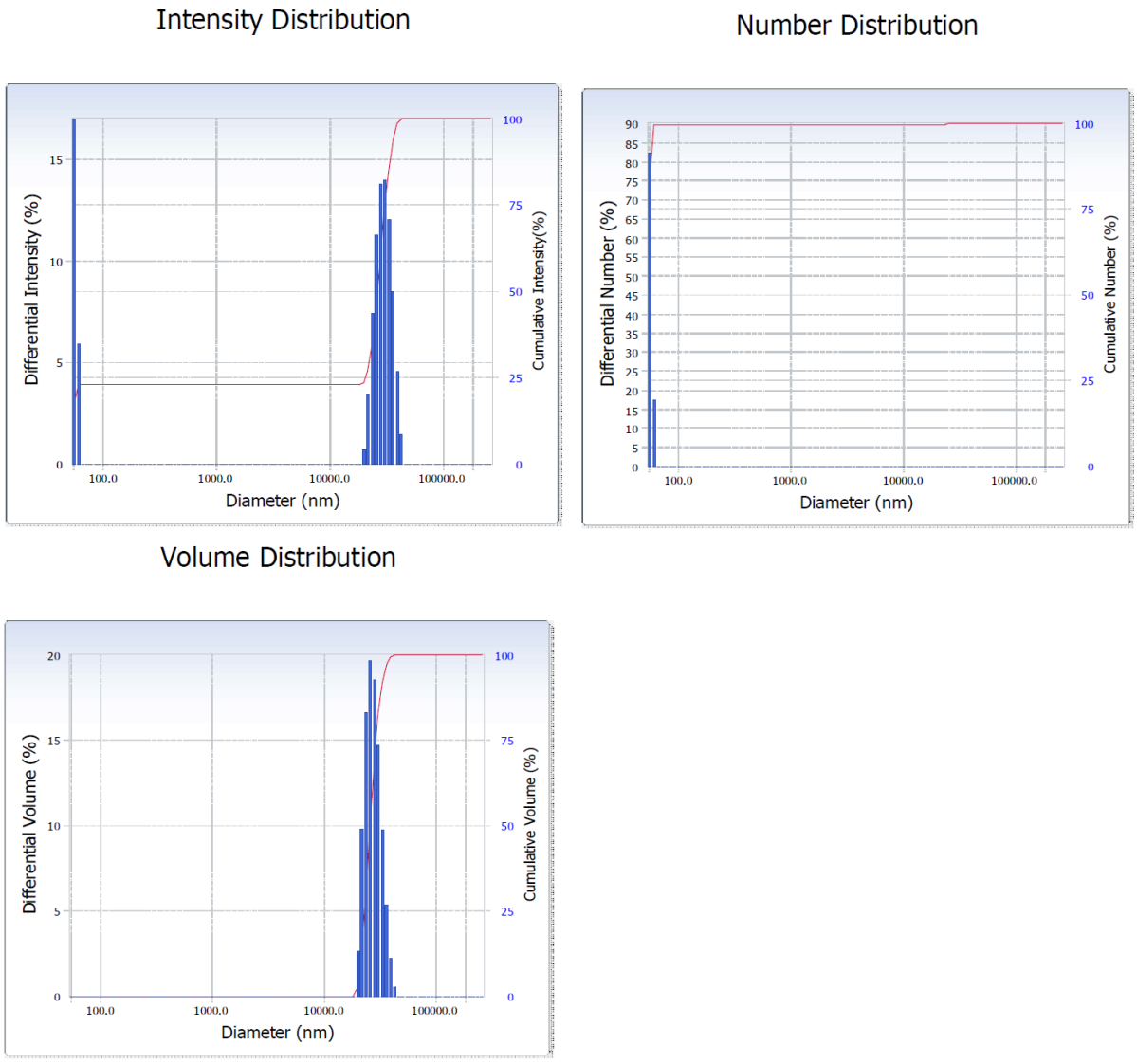



**Figure 74 DLS Distribution Results for JK020**

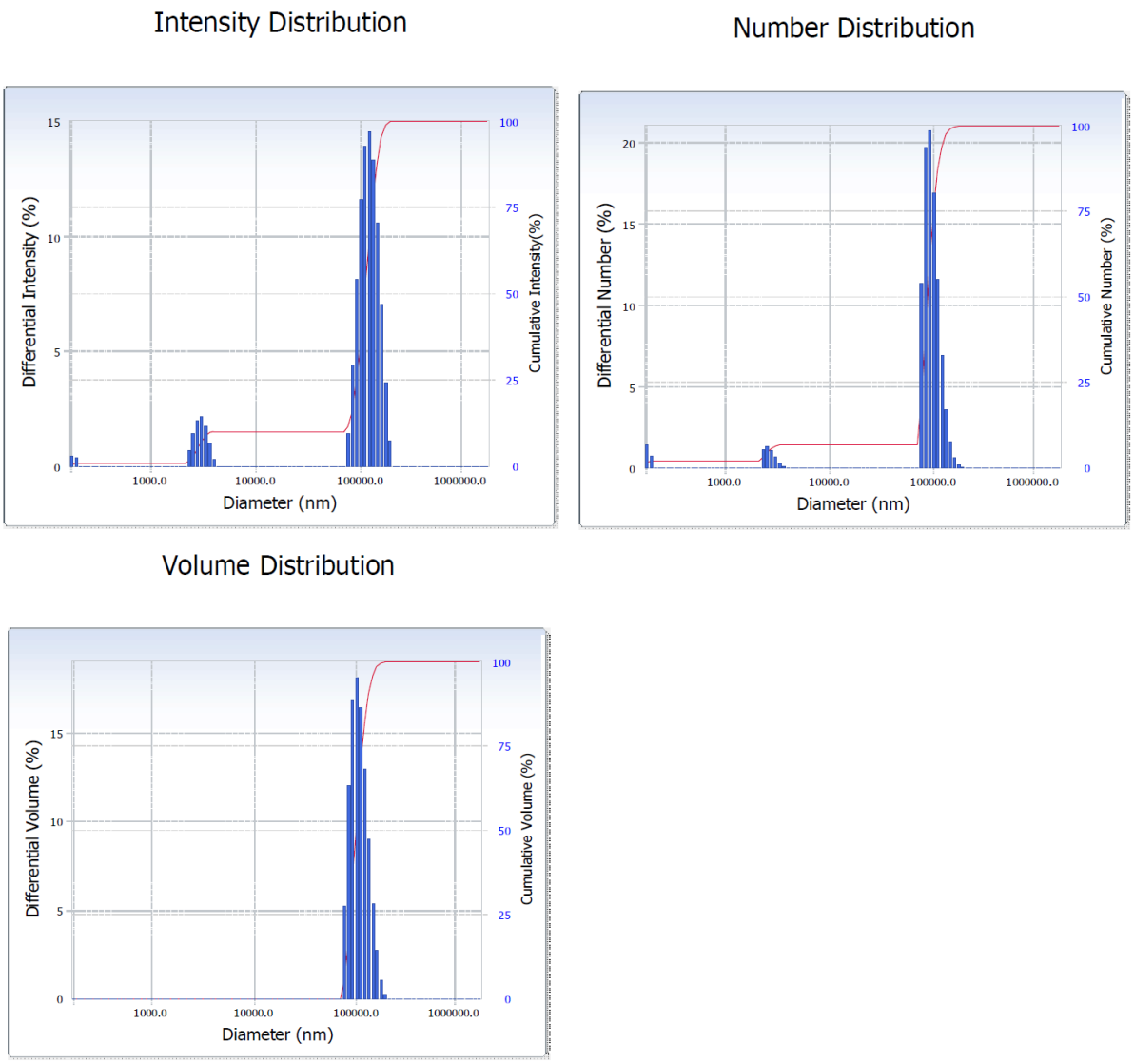



**Figure 75 DLS Distribution Results for JK021**

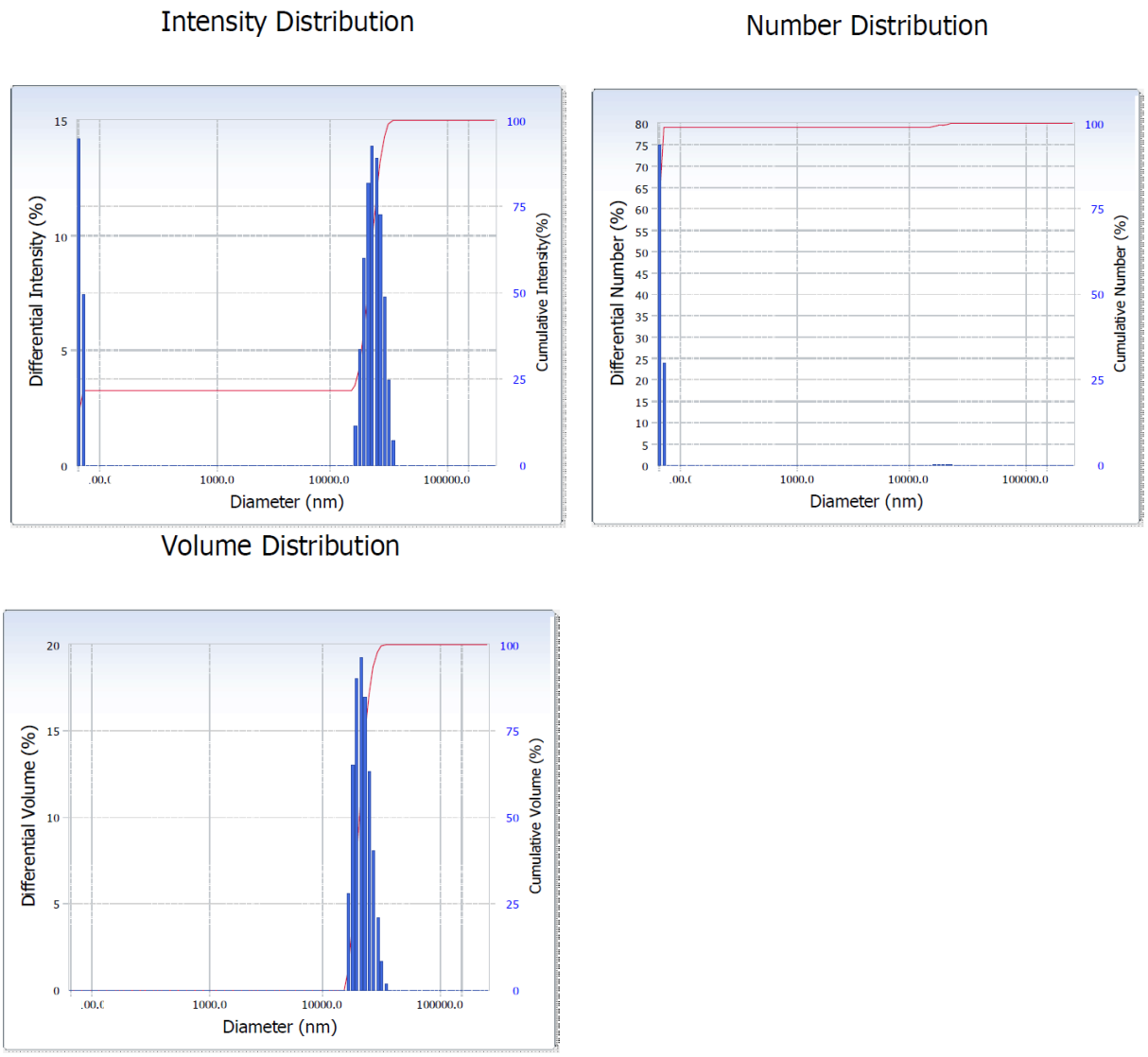



**Figure 76 DLS Distribution Results for JK022**

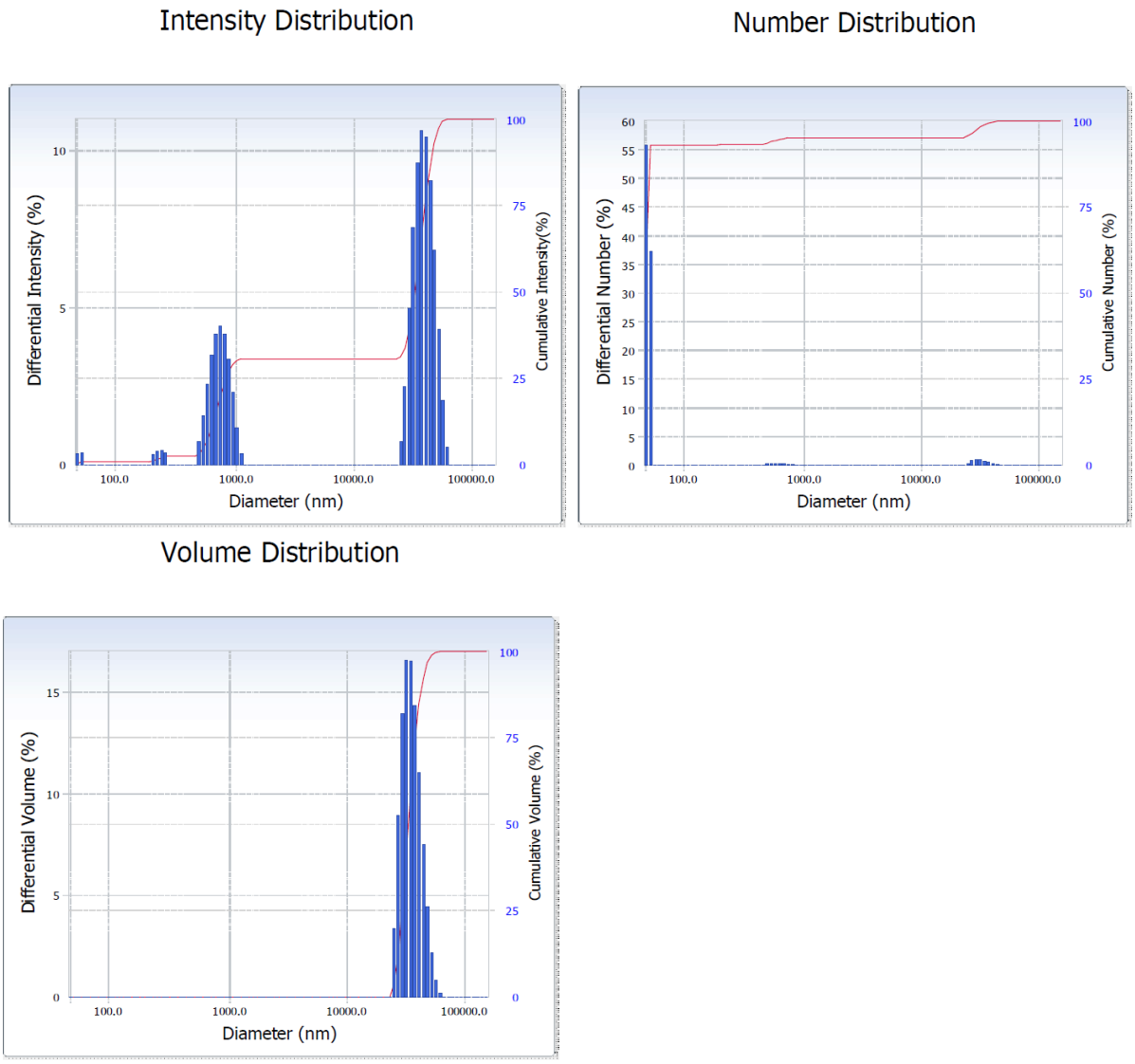



**Figure 77 DLS Distribution Results for JK023**

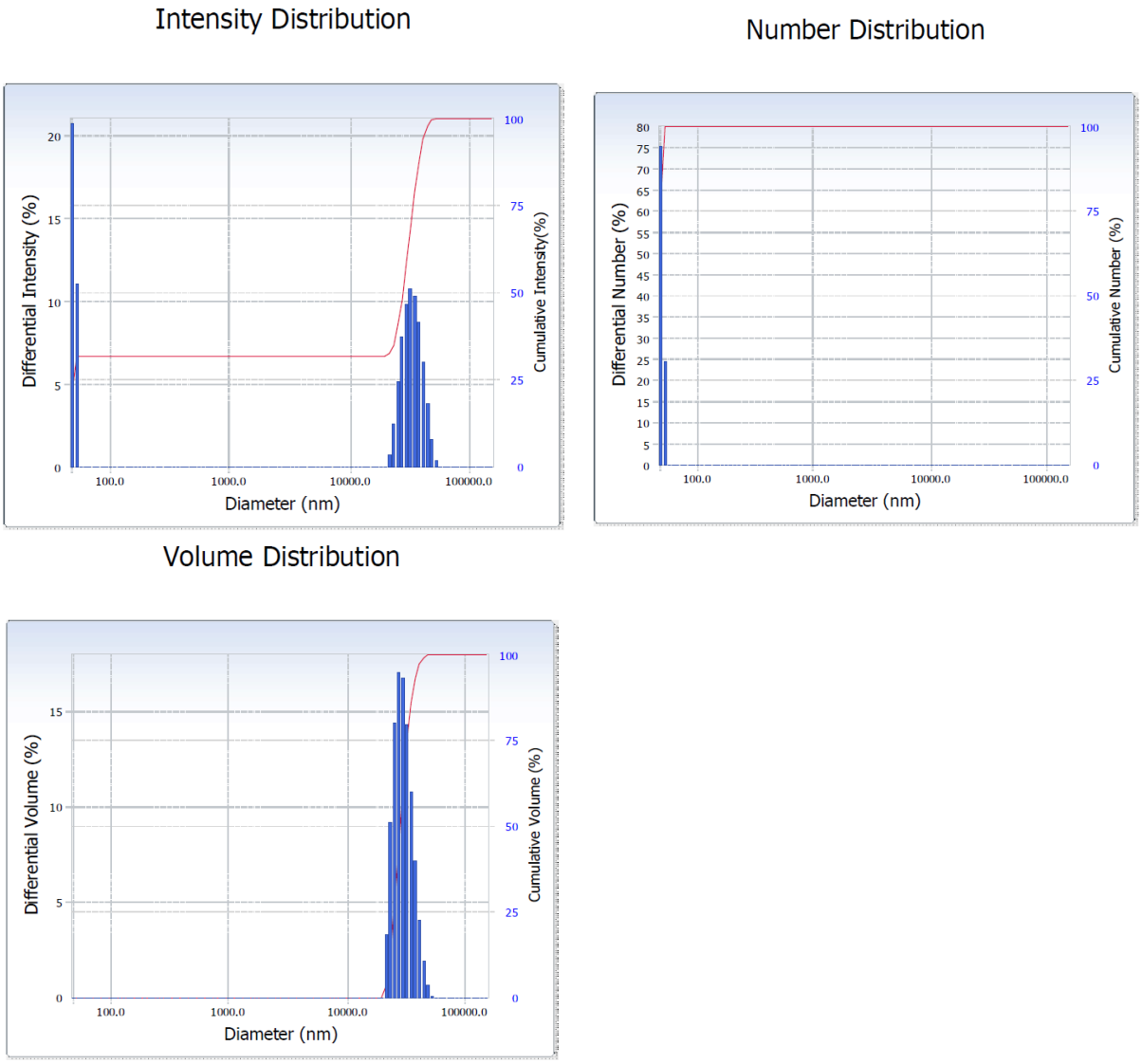



**Figure 78 DLS Distribution Results for JK024**

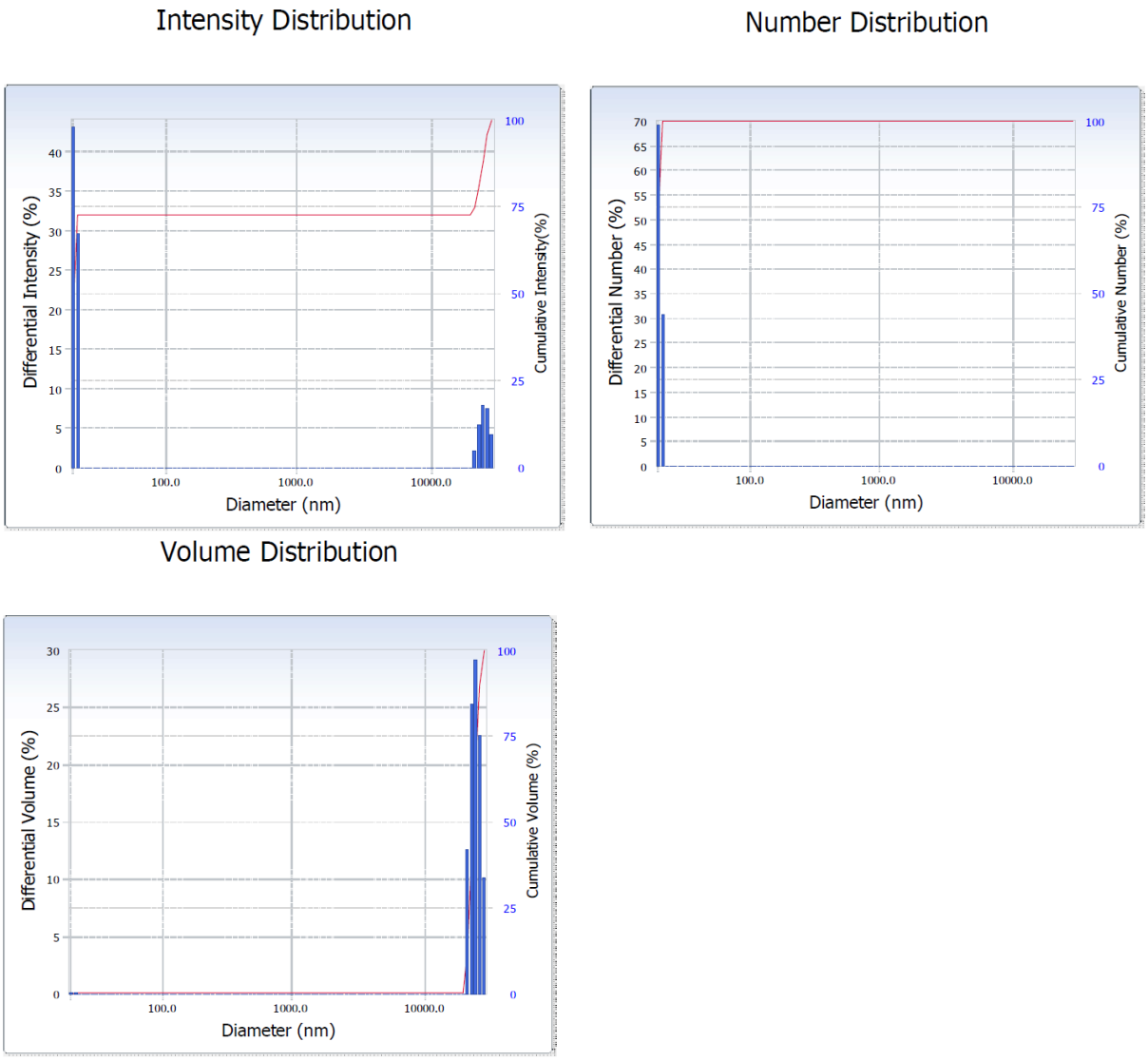
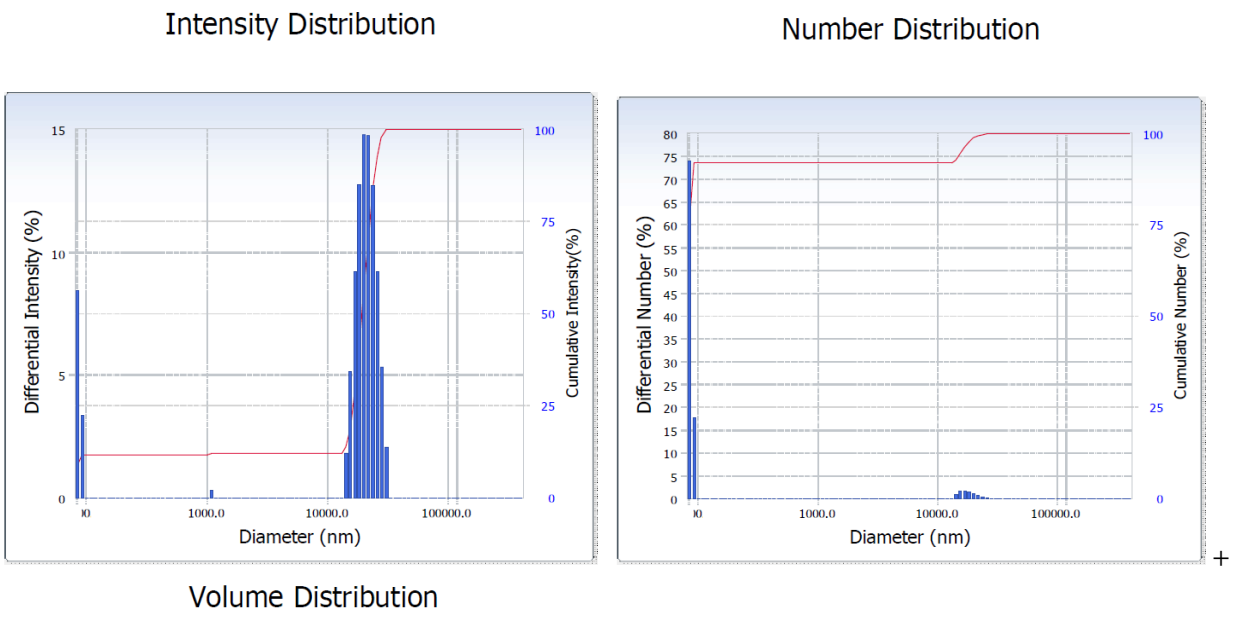



**Figure 79 DLS Distribution Results for JK025**



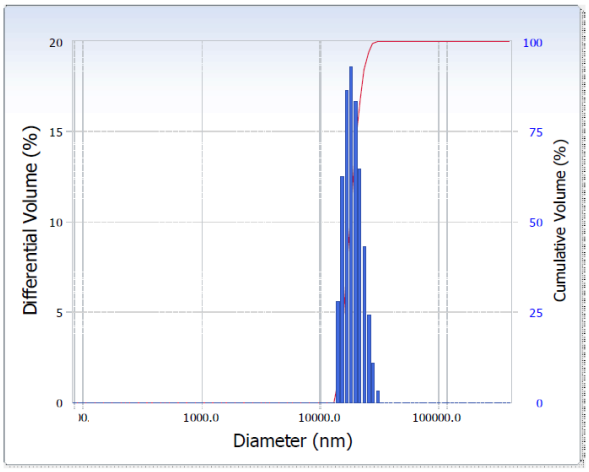




**Figure 80 DLS Distribution Results for JK026**

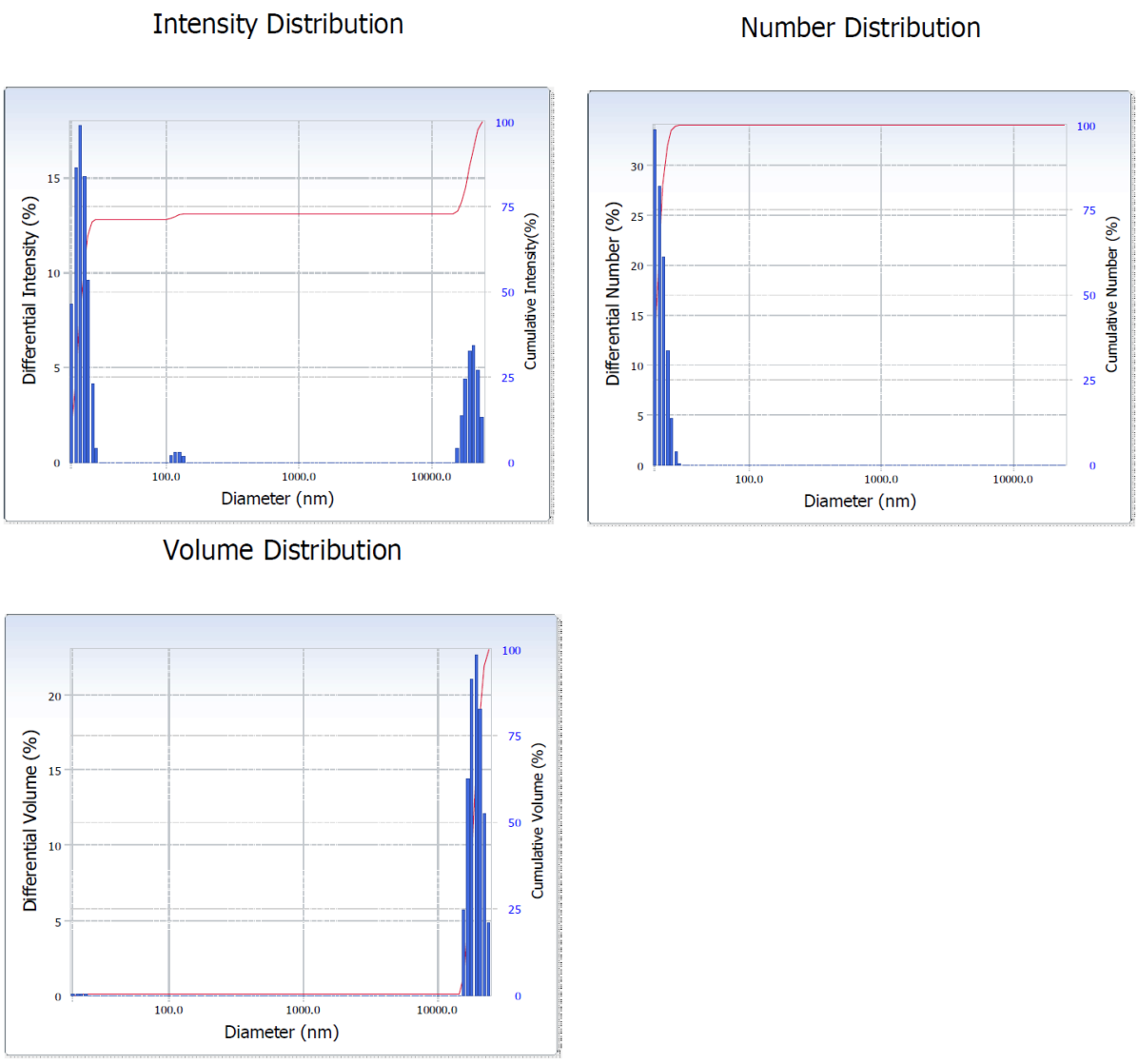



**Figure 81 DLS Distribution Results for JK027**

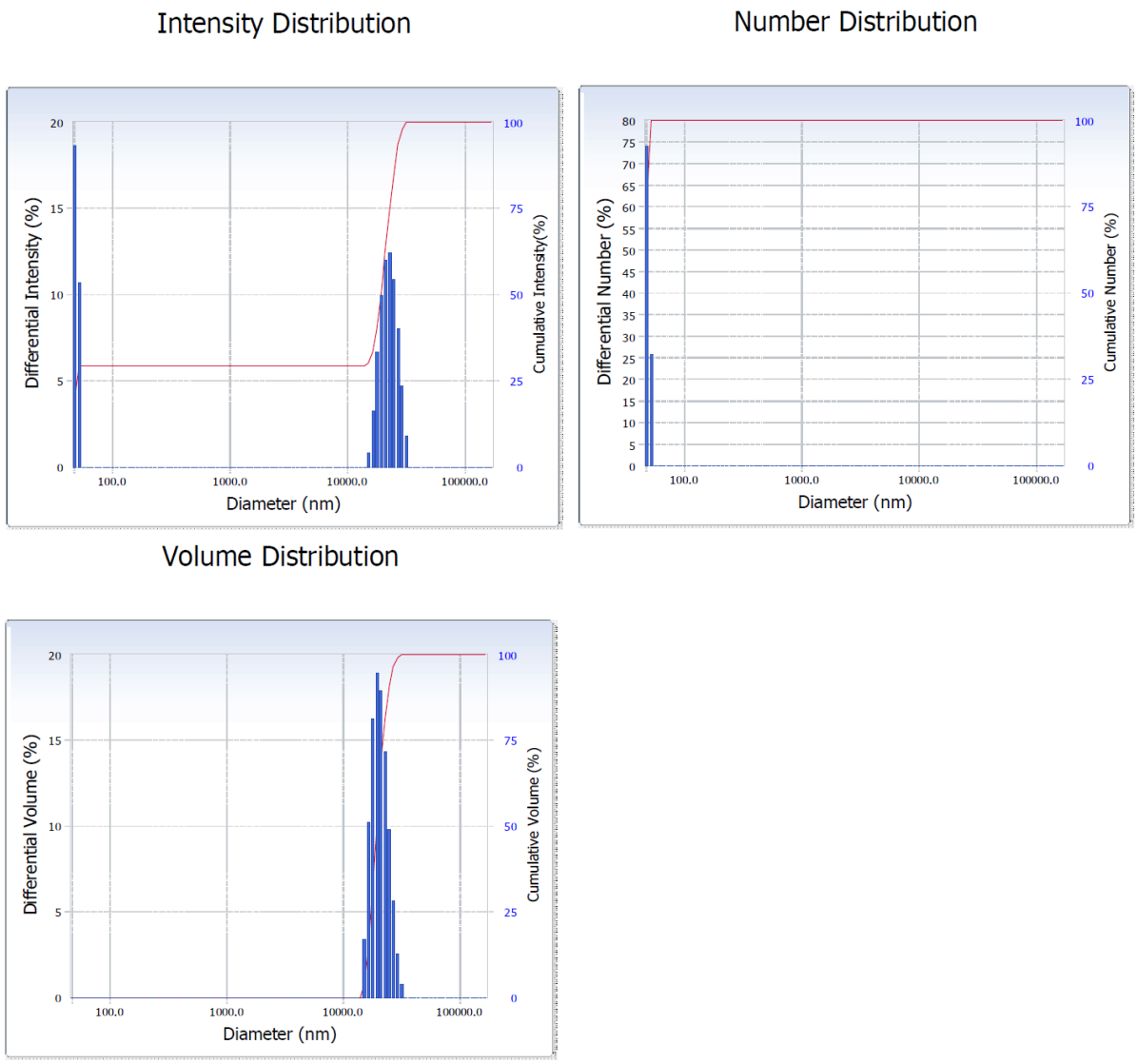



**Figure 82 DLS Distribution Results for JK028**

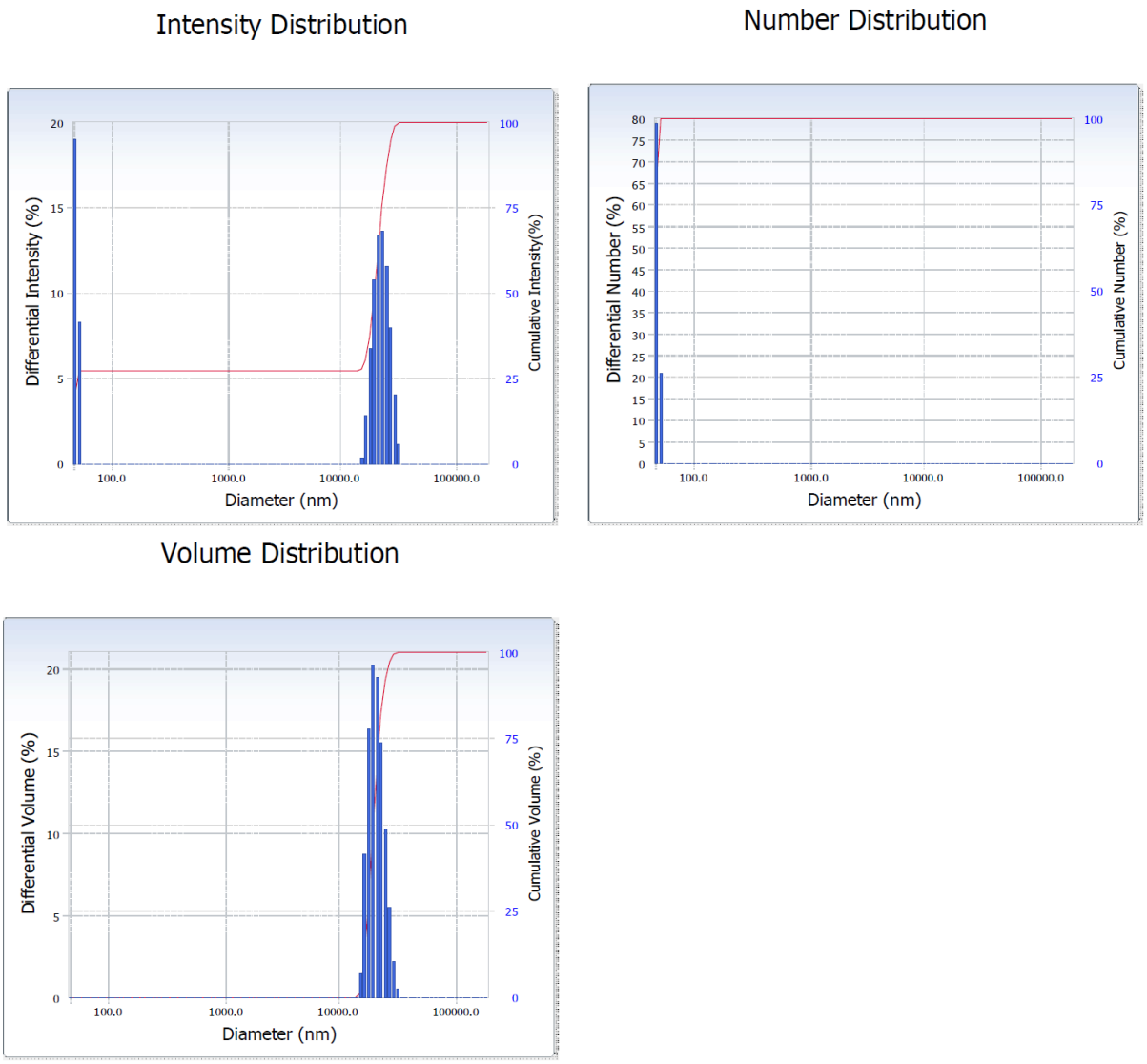



**Figure 83 DLS Distribution Results for JK029**

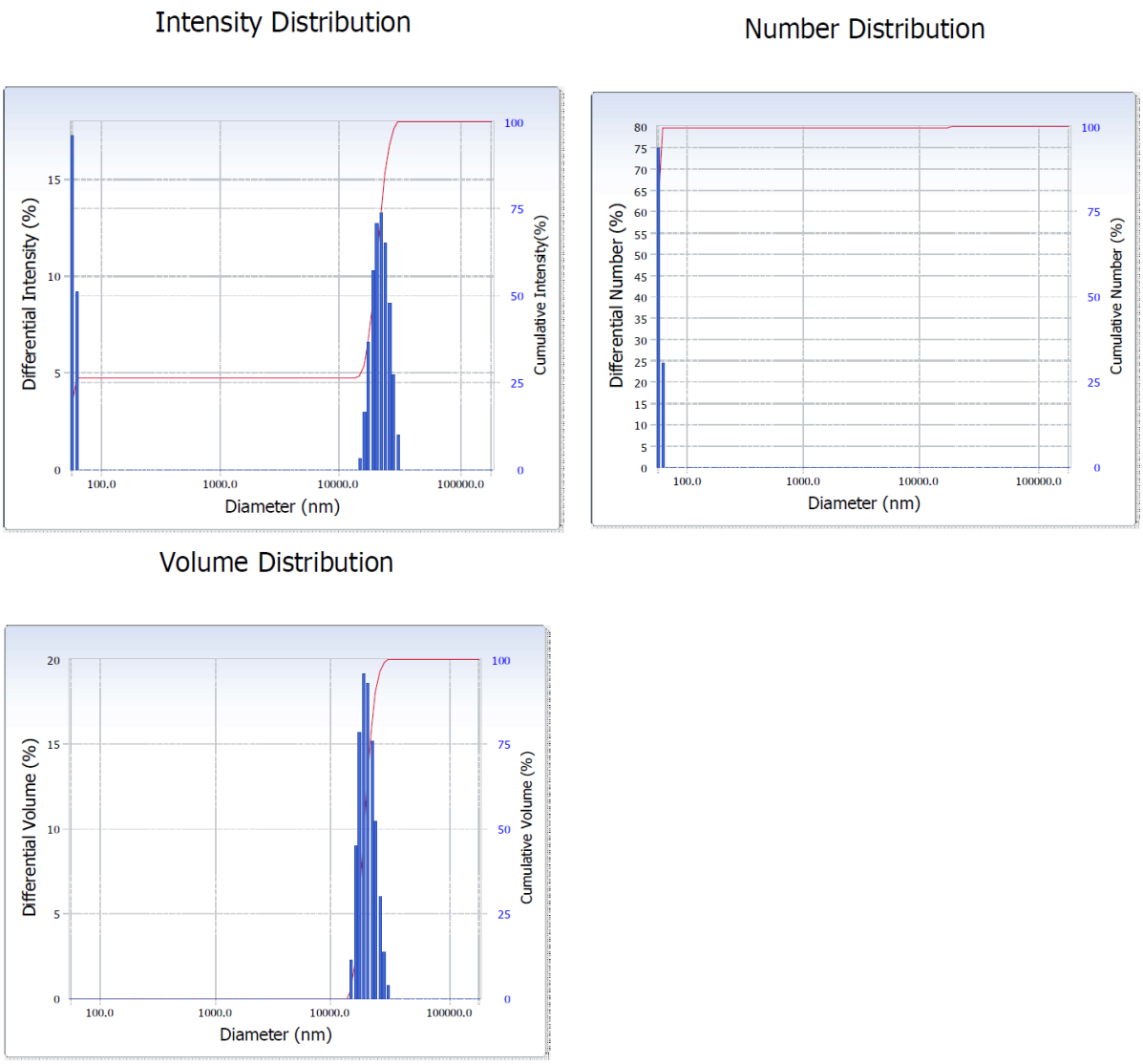



**Figure 84 DLS Distribution Results for JK030**

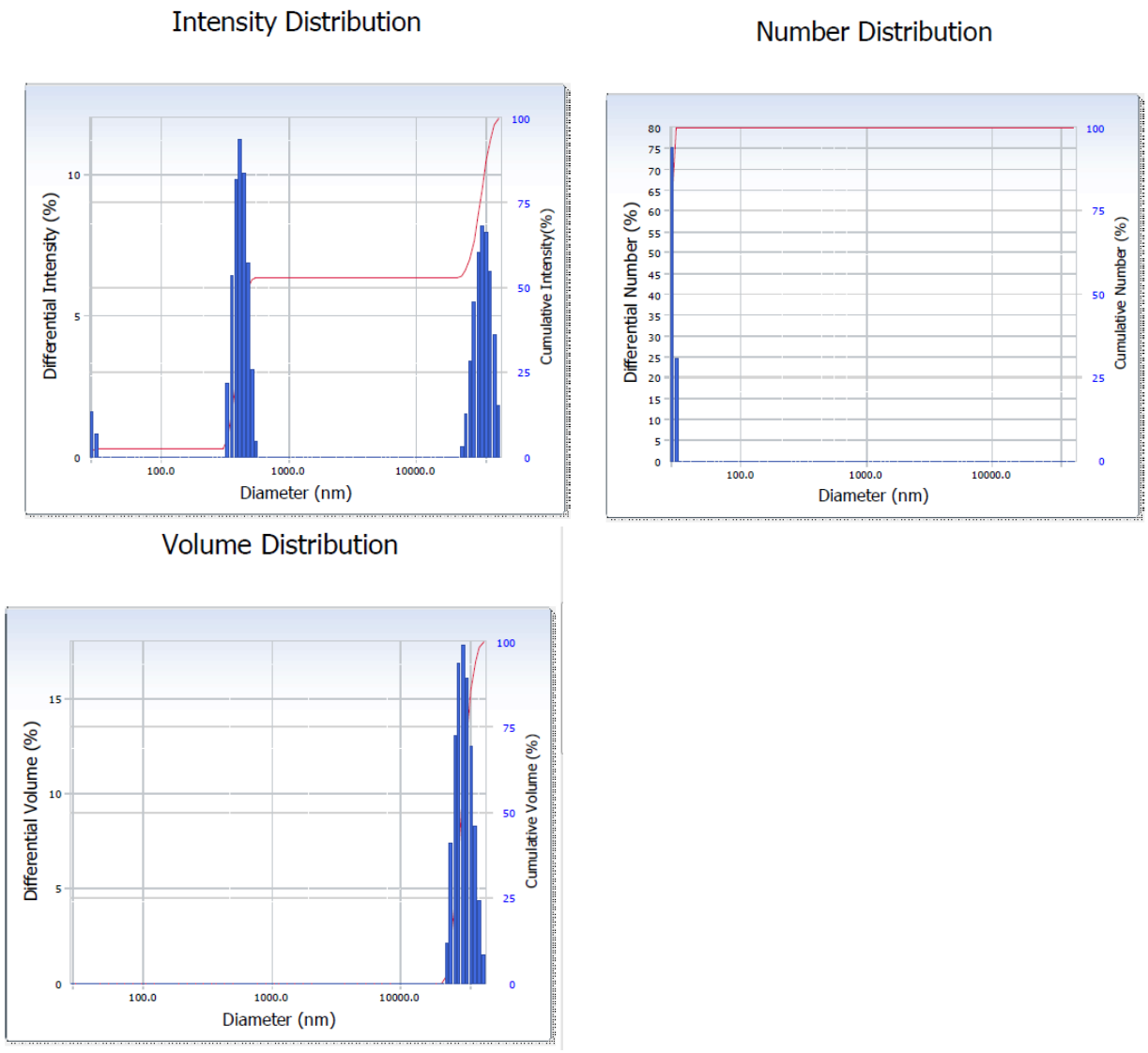



**Figure 85 DLS Distribution Results for JK031**

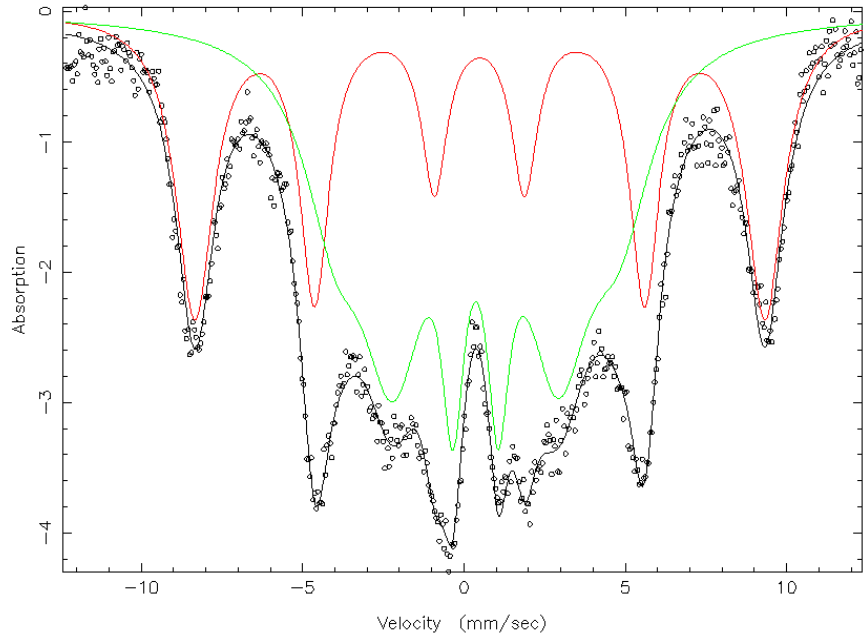



**Figure 86 Mössbauer Spectrum of JK020 at 6 K**

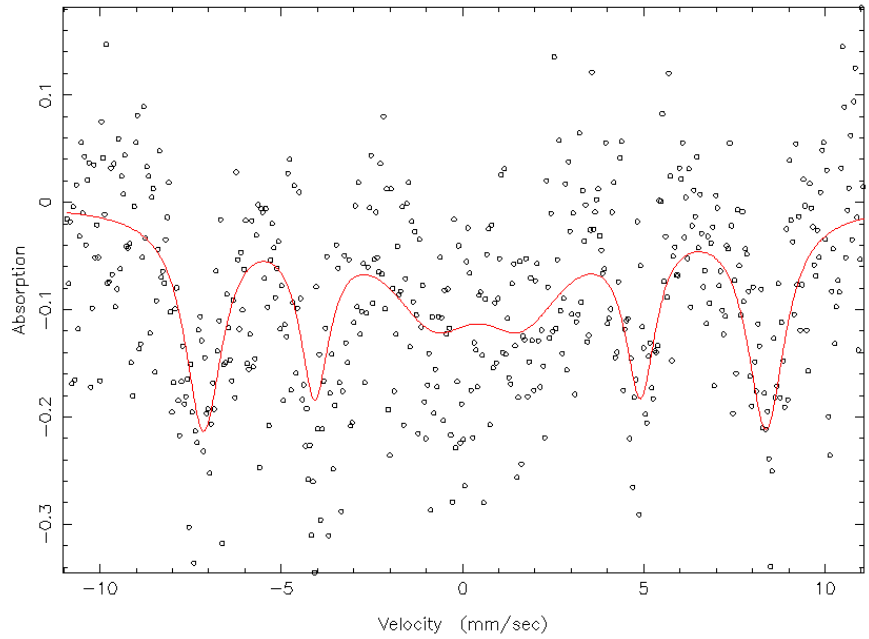



**Figure 87 Mössbauer Spectrum of JK021 at 6 K**

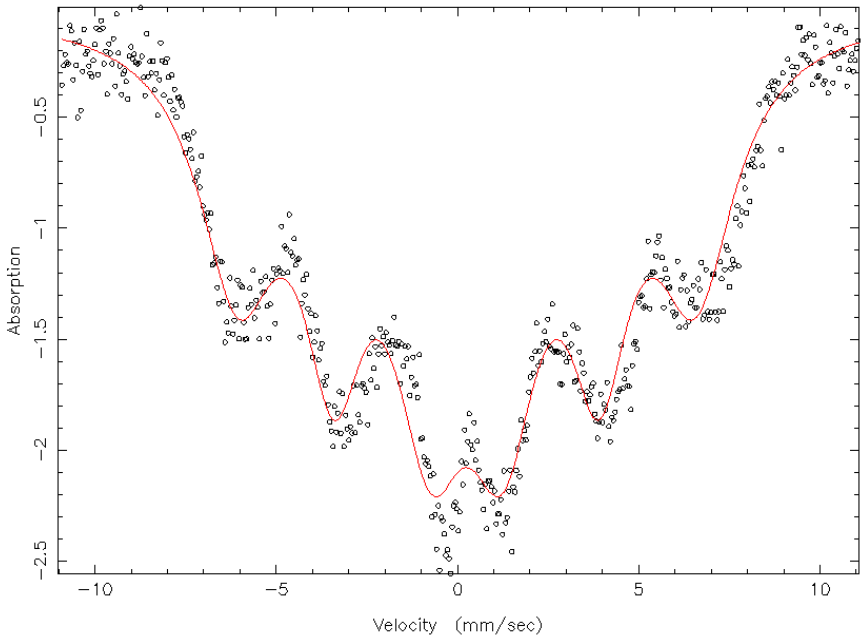



**Figure 88 Mössbauer Spectrum of JK023 at 6 K**

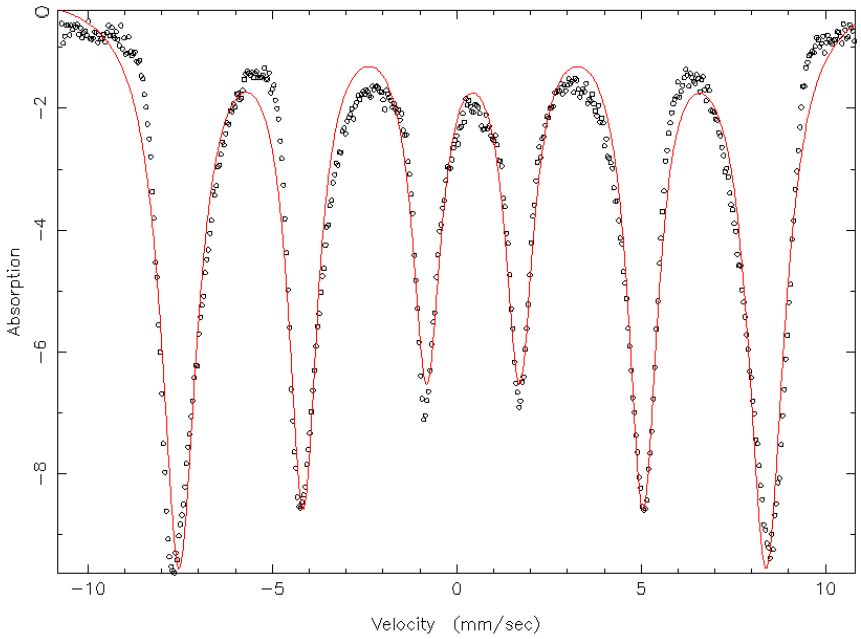



**Figure 89 Mössbauer Spectrum of JK025 at 6 K**

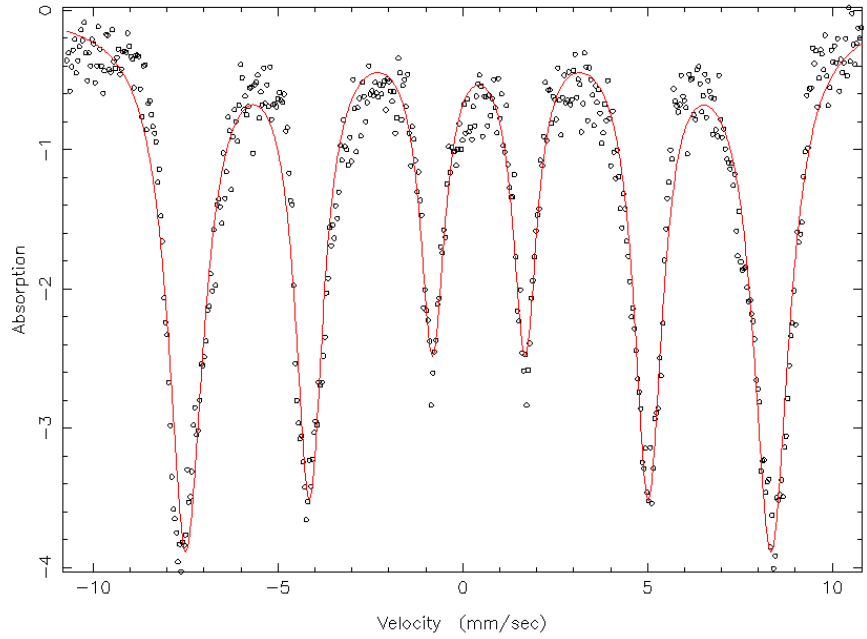



**Figure 90 Mössbauer Spectrum of JK026 at 6 K**

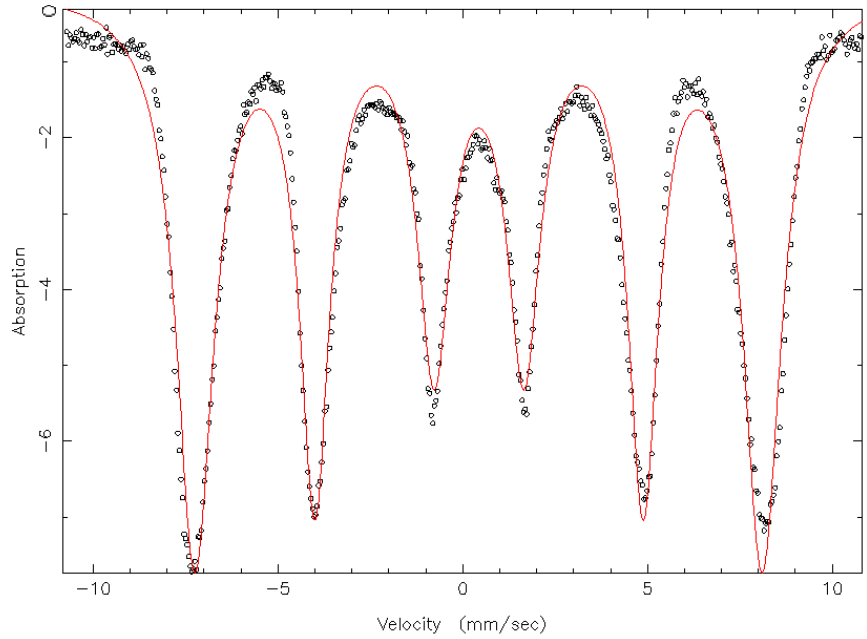



**Figure 91 Mössbauer Spectrum of JK027 at 6 K**

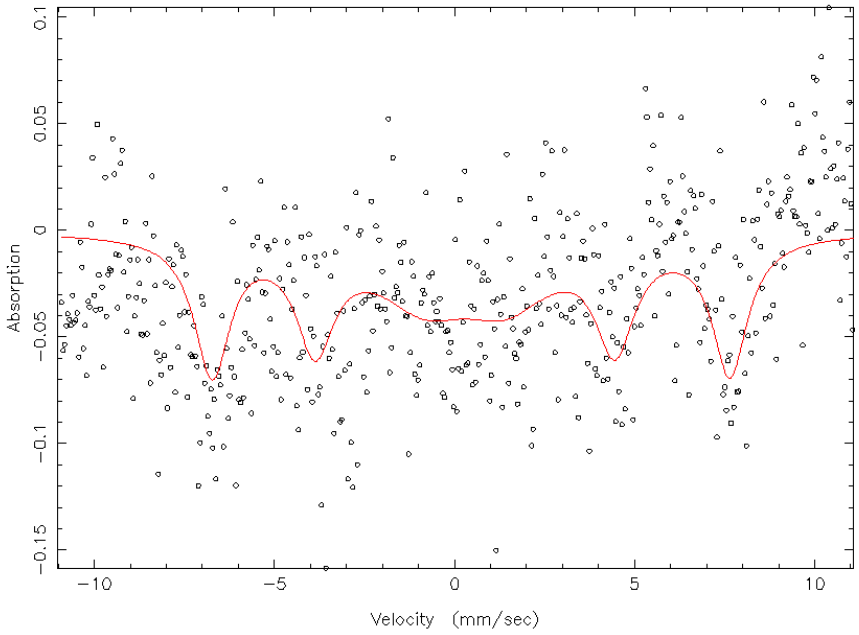



**Figure 92 Mössbauer Spectrum of JK028 at 6 K**

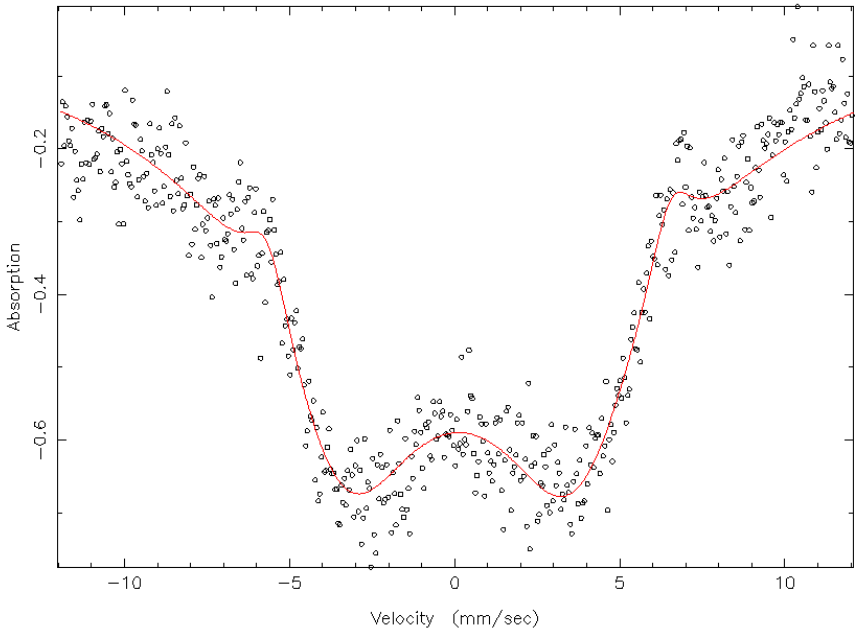



**Figure 93 Mössbauer Spectrum of JK029 at 6 K**

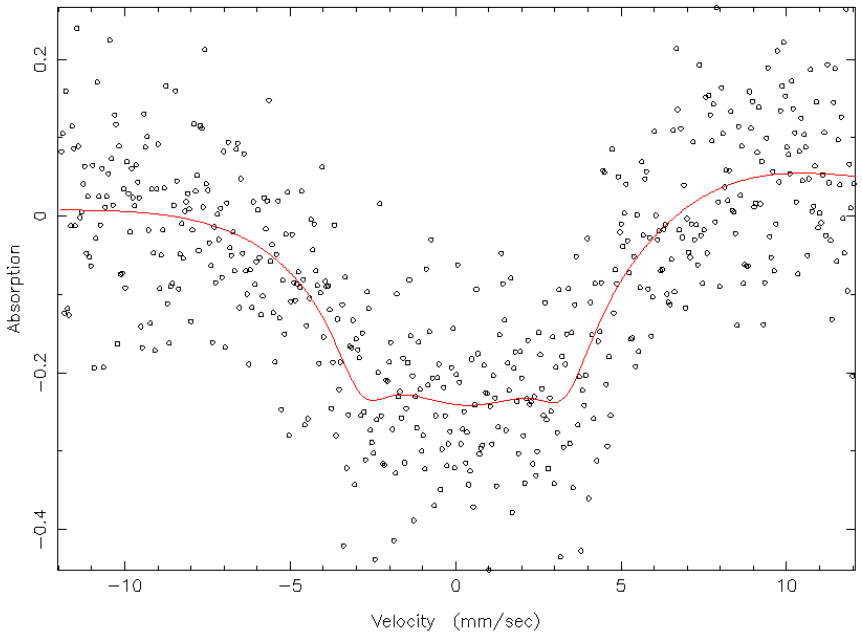



**Figure 94 Mössbauer Spectrum of JK029 at 290 K**

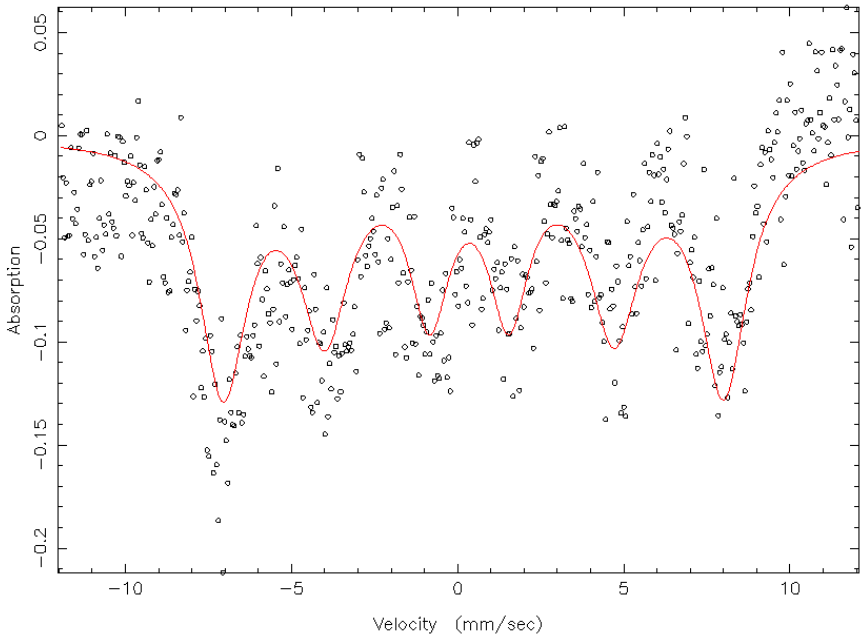



**Figure 95 Mössbauer Spectrum of JK030 at 6 K**

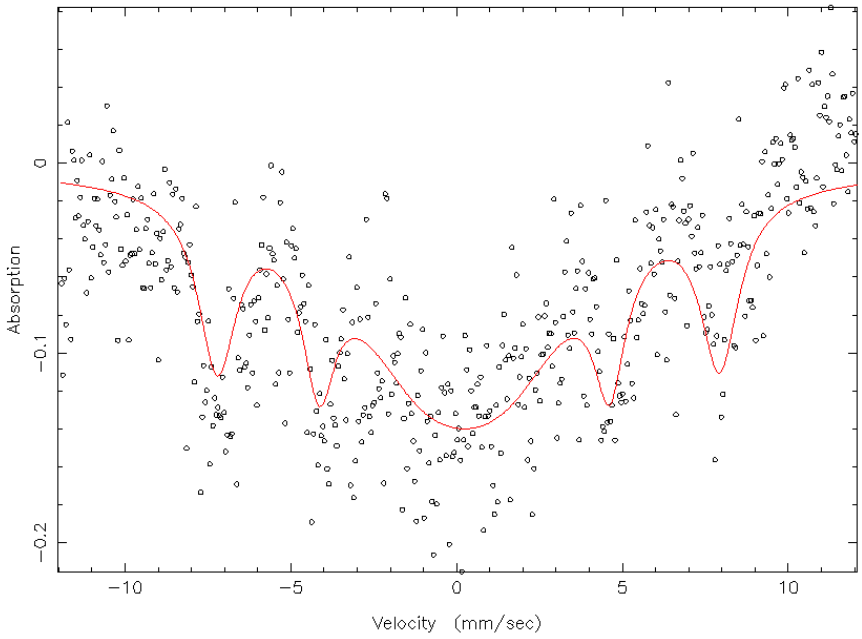



**Figure 96 Mössbauer Spectrum of JK031 at 6 K**

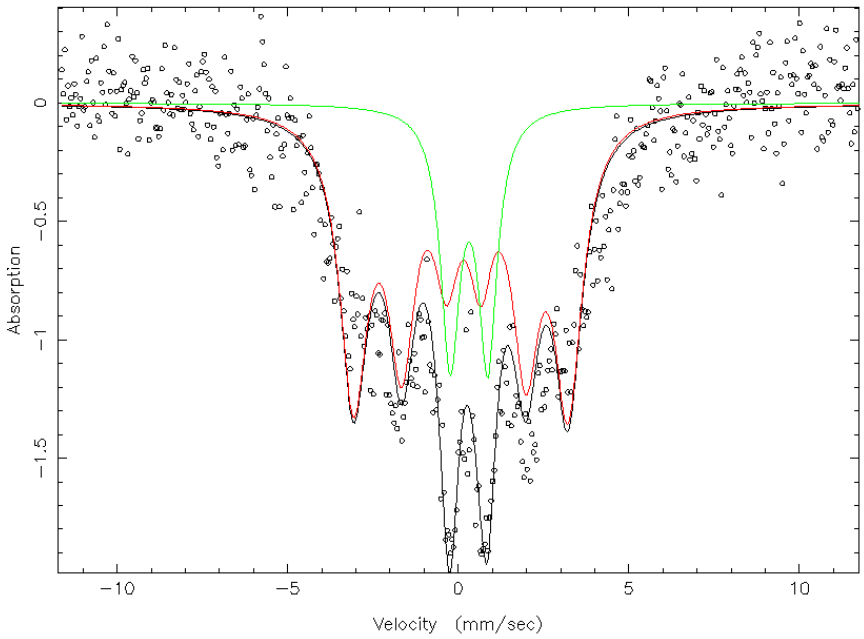



**Figure 97 Mössbauer Spectrum of JK032 at 290 K**

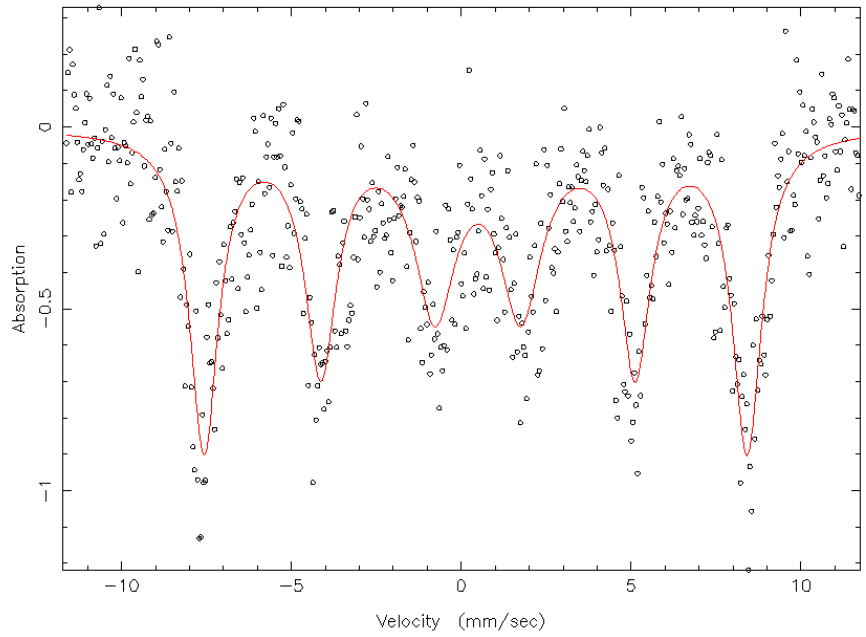



**Figure 98 Mössbauer Spectrum of JK033 at 6 K**

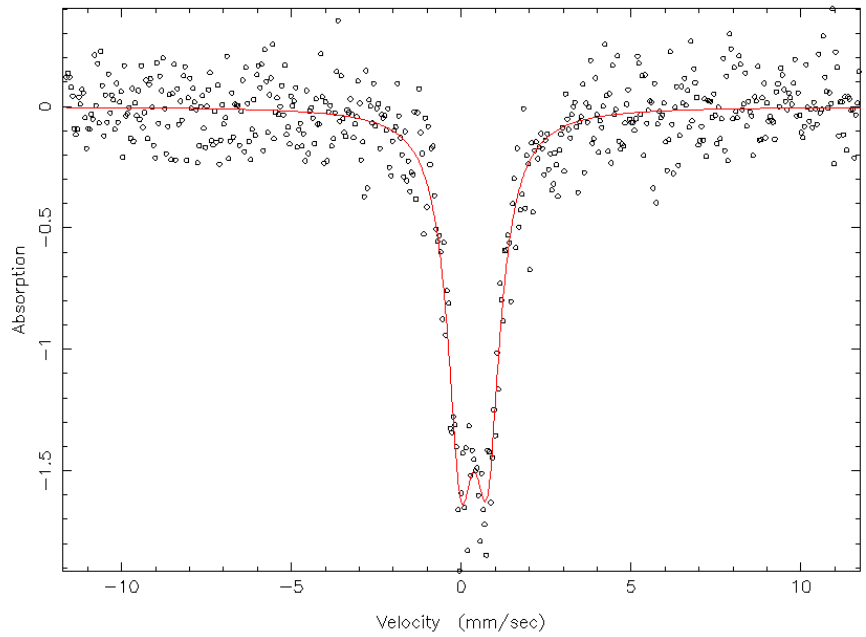



**Figure 99 Mössbauer Spectrum of JK033 at 290 K**

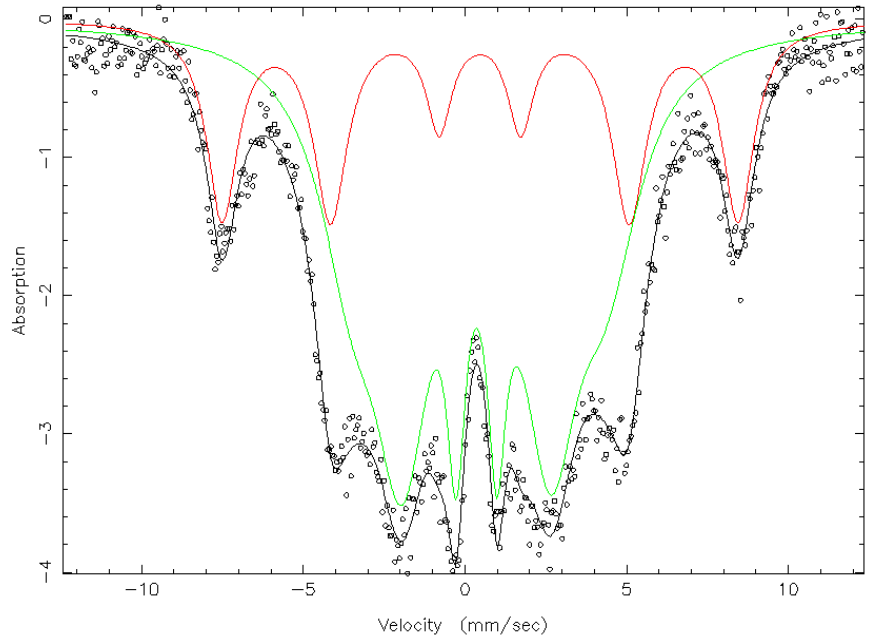



**Figure 100 Mössbauer Spectrum of JK034 at 6 K**

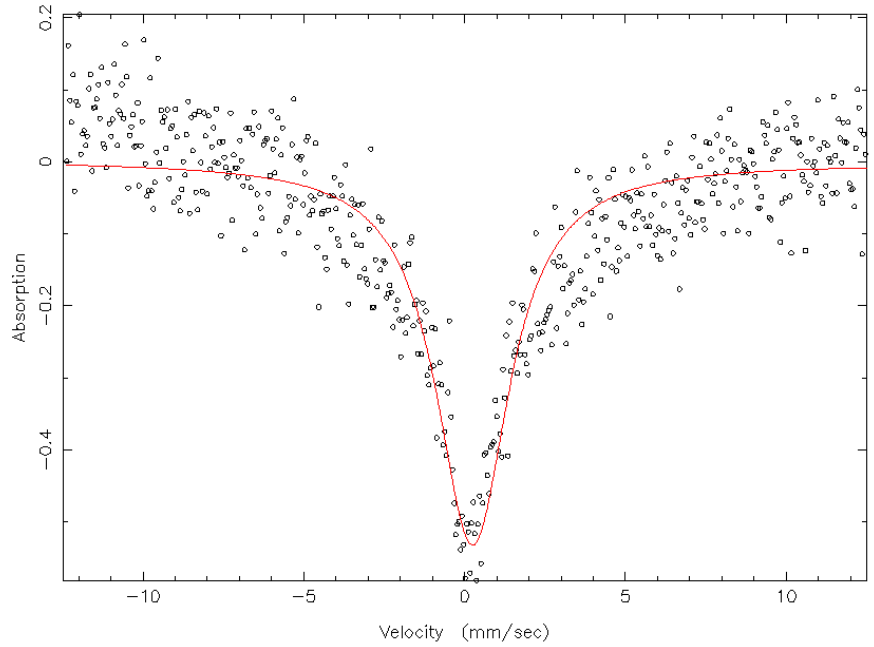



**Figure 101 Mössbauer Spectrum of JK034 at 293 K with a 10 kG Field**

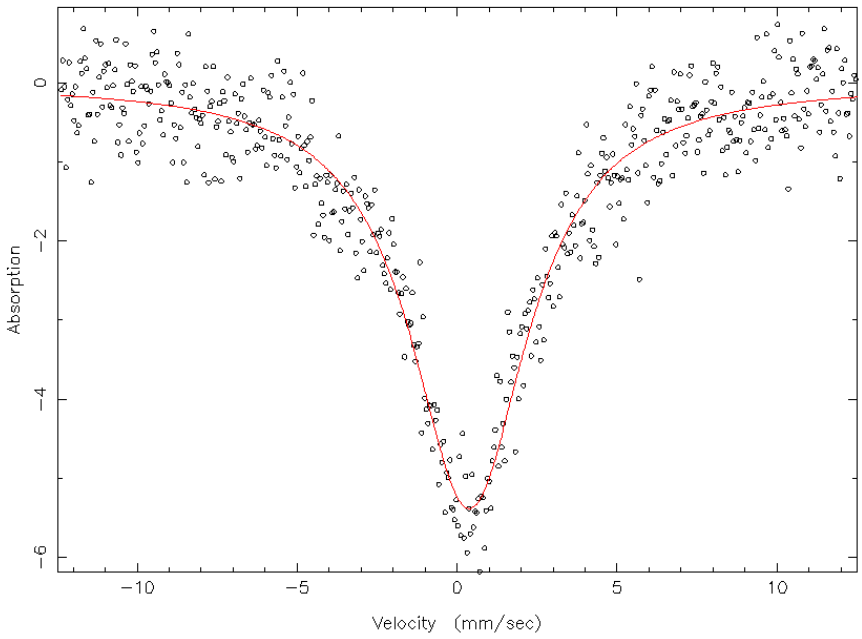



**Figure 102 Mössbauer Spectrum of JK034 at 300 K**

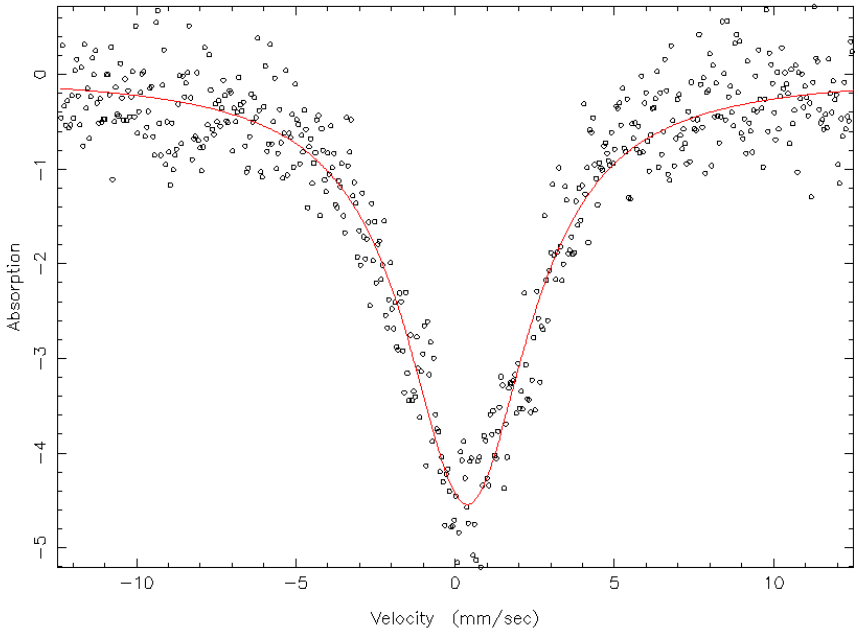



**Figure 103 Mössbauer Spectrum of JK034 at 300 K with a 0.078 T Field**

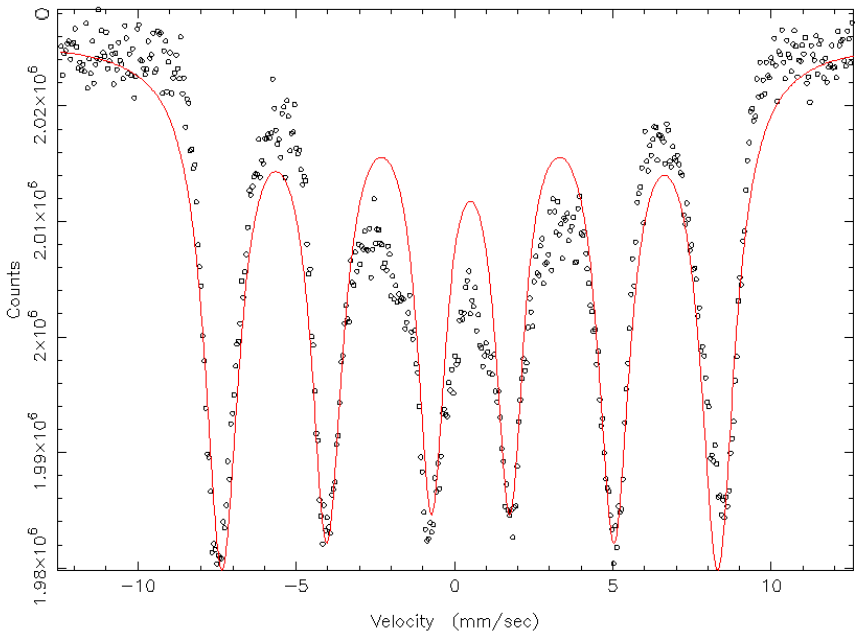



**Figure 104 Mössbauer spectrum of JK036 at 6 K**

# CHAPTER IV
# REDUCTION OF IRON SULFATE

# Introduction

In this chapter, iron nanoparticles were synthesized via a reduction of iron sulfate to further improve results produced in Chapter II (via reduction of iron chloride). Eleven samples were created in total. Polyethylene glycol was used as a biocompatible coating. The nanoparticles' size was characterized by Transmission Electron Microscopy (TEM) and Dynamic Light Scattering (DLS) and indicated small nanoparticles plus the presence of agglomerates. Composition was evaluated with Mössbauer Spectroscopy and appeared to show iron metal and amorphous iron present. Magnetic Resonance Relaxometry measurements were performed to determine viability as an MRI contrast agent; T2 relaxation was favored for the nanoparticles.

# Methods

### *Iron Nanoparticle Synthesis*

Samples were synthesized at the University of Tennessee Space Institute in Tullahoma, TN. Samples synthesis was similar to that detailed in Chapter 2 with the exception of the source of iron and lack of ethanol. Sample synthesis returned to a reduction method because oleic acid and organic solvents used in the thermal decomposition in Chapter 3 proved difficult, if not impossible, to completely remove from the particles and solution. This would prevent true biocompatibility and render the product unfeasible for clinical applications. Iron sulfate was chosen as a replacement for iron chloride used in Chapter 2.

Samples were prepared by reducing iron (ii) sulfate (Sigma Aldrich) in 30 mL deionized water with 2.4 g sodium borohydride (Sigma Aldrich) in 30 mL deionized water. Each solution was taken up into 30 mL syringes through tubing and placed in a dual syringe pump; the pump was set to a rate of 15 mL per minute. The nanoparticles formed by reacting down the side of a separatory funnel or condenser column and the neck of a round bottom flask into 20 mL of a coating mixture. The coating mixture was prepared by stirring 160 µL polyethylene glycol (PEG) 300 (Sigma Aldrich) and 20 mL deionized water. Deionized water was used to rinse the stir bar of any particles. A synthesis using the separatory funnel can be seen in Figure 105.

*Exceptions*

Two samples, JK050 and JK051, were made using a condenser column in place of the separatory funnel in an attempt to prevent irreversible agglomerates and oxidation possibly caused by particles that sometimes became trapped in the separatory funnel. Several modifications were made to the separatory funnel in an attempt to alleviate this problem which included drilling out larger openings in the stopcock and using cannulas to force material through the stem of the funnel. During this time the use of a separatory funnel was questioned. The purpose of the funnel was to provide a distance for the iron (ii) sulfate and sodium borohydride to react. The longer distance resulted in smaller particles in previous experiments (Chapter 2), so a 200 mm distillation column should provide the reaction distance necessary to synthesize small particles.

In addition to length, it was hypothesized the indentions throughout the column may help reduce agglomerates and the larger diameter would inhibit particles becoming trapped and thereby uncoated. The indentions helped disseminate agglomerates and the diameter of the column allowed for all material to react over the same amount of distance. A procedure where all particles were allowed to react over the same length could prevent coated agglomerates, improve size distribution, and avoid being trapped and possibly exposed to oxygen in a separatory funnel. This amended synthesis can be seen in Figure 106.

Sample JK051 was prepared using iron (iii) sulfate instead of iron (ii) sulfate. Unpublished results from Dr. Johnson's research group suggest the reduction of $Fe^{3+}$ resulted in a higher iron metal content. This sample was prepared using $Fe_2(SO_4)_3$ instead of $FeSO_4$ and a distillation column to lengthen the reaction time. This sample was coated in PEG 300 in a nitrogen environment.

*Washing and Sample Work-Up*

Samples were magnetically separated from the reaction solution. Ethanol was added to crash out the nanoparticles i.e. force a separation of coated nanoparticles from reaction/washing solution. The separated solution was pipeted from the sample jar and replaced with deionized water. The sample jar was left on a magnet to aid in particle separation. This was repeated three times. Following the third removal of washing solution from particles, some of the concentrated particles were pipeted out for preparation of Mössbauer Spectroscopy experiments. The remaining sample was resuspended in deionized water for storage and/or future characterization experiments.

***Transmission Electron Microscopy (TEM)***

Transmission electron microscopy (TEM) was performed using a FEI Tecnai Osiris TEM (Figure 107) at Vanderbilt Institute of Nanoscale Science and Engineering. Samples were prepared at The University of Tennessee Space Institute by diluting the nanoparticles with deionized water until the solution was barely tinted. A probe sonicator was used to break up agglomerates then a copper TEM grid was dipped into the solution and dried in air. The grid was mounted to a single-tilt sample holder (Figure 108) then loaded into the TEM. Samples JK044, JK045, JK045B, JK046, JK046B, JK047, JK047B, JK048, JK049, JK049B, JK050, and JK051 were characterized using this technique.

***Magnetic Resonance (NMR) Relaxometry***

Magnetic Resonance (MR) relaxometry analysis was performed at Vanderbilt University Institute of Imagining Science, Nashville, TN with the assistance of Dr. Dan Colvin. A Varian MR imaging system with a 4.7 Tesla field (Figure 109) was used for relaxometry measurements. Samples JK046, JK047, JK048, JK049 and JK050 were characterized using this technique.

Samples were prepared by extracting the sample after washing and pipetting into disposable NMR tubes. This step was repeated and each sample was slightly diluted before being added to NMR tubes. The concentrated and slightly diluted tubes can be seen in Figure 110. The tubes were stacked in a five by five pattern (Figure 111) before being placed in the scanner. Initial results deemed the samples too concentrated; the particles fell out of the solution causing false results. Samples were prepared a second time by diluting in four varying concentrations to the point where they are barely tinted (much like TEM or DLS). The diluted samples were subjected to 10 seconds of vortex mixing followed by 60 seconds of sonication using a Fisher Scientific model 100 Sonic Dismembrator at 7 Watts, seen in Figure 112, before being pipeted into disposable NMR tubes for analysis (Figure 113). The before and after pictures of these prepared samples can be seen in Figure 114.

***Mössbauer Spectroscopy***

Sample preparation and spectroscopy measurements took place at the, University of Tennessee Space Institute Center for Laser Applications. A $^{57}$Co source was used for the calibration and sample measurements. Low temperature measurements were made using a Janis cryostat system

in conjunction with a SEE Co Mössbauer Spectrometer in a helium environment (Figure 115). Concentrated samples were pipeted into Mössbauer sample cups after washing. The samples were dried under nitrogen gas flow then stored in an argon glovebox until characterization via Mössbauer Spectroscopy.

## Results

***Transmission Electron Microscopy (TEM)***

TEM was performed on samples JK044, JK045, JK045B, JK046, JK046B, JK047, JK047B, JK048, JK049, JK049B, JK050, and JK051. TEM results show that the diameter of the nanoparticles for Sample JK044 are 4-39 nm with 400 nm agglomerates (Figure 116). This samples appears to be completely oxidized and no core shell structure is discernable. This is expected since no coating was used to protect the nanoparticles from oxidation.

Sample JK045 has apparent core shell structures with cores ranging in size from 4-12 nm and shells from 11-28. The sample has agglomerates from 35 nm to 800 nm (Figure 117). The sample has fairly even size distribution.

Sample JK046 has a very even size distribution with agglomerates around 475 nm. It also has a core shell structure with cores of 2-4 nm and shells of 8-10 nm (Figure 118). Sample JK046B has a larger size distribution than its coated counterpart. JK046B has cores ranging from 2-8 nm and shells from 6-24 nm Figure 119. Agglomerates were noted from 218-1384 nm, so it has larger agglomerates than JK046 as well.

Sample JK047 had the largest size distribution of all samples produced via reduction of iron sulfate. JK047 had cores of 4-52 nm and shells of 8-68 nm. Agglomerates were observed from 218-1384 nm (Figure 120). Sample JK047B also had a core shell structure, but had a smaller size distribution and smaller agglomerates than JK047. JK047B had cores of 2-12 nm and shells of 5-20 nm Figure 121. Agglomerates found in JK047B were under 200 nm.

Sample JK048 had no core shell structures in TEM. The particle diameters ranged from 7-229 nm with agglomerate of 653-3600 nm (Figure 122). The lack of core shell structures could be due to particle oxidation after preparation on TEM grid. The grids were stored in air after preparation and

before characterization.

JK049 had discernable diffraction patterns and very small sample size. It also had noticeable core shell structures. Cores were measures as 1-2 nm with total diameters of 2-4 nm. The sample had agglomerates ranging from 103-874 nm Figure 123. JK049B had a larger sample size and greater size distribution than its coated counterpart. The core shell structure was observed with cores of 4-15 nm and shells of 5-21 nm. Agglomerates were slightly smaller than JK049 at 275-568 nm Figure 124.

JK050 had a very even size distribution and a core shell structure. Nanoparticles were very small. Cores were measures at 2-3 nm and total diameters at 3-5 nm (Figure 125). A large agglomerate was measures at 918 nm. The improved size distribution could be due to the use of a distillation column in place of a separatory funnel. The column prevented material from becoming trapped in the funnel, so all material traveled the same distance in roughly the same time.

JK051 also had good size distribution, but smaller agglomerates was the most notable feature. Agglomerates were measures at 76 nm. This was the smallest agglomerates of all the samples. Core shell structures were present: cores varied from 2-5 nm with shells at 5-14 nm. (Figure 126). A summary of these TEM results can be seen in **Error! Reference source not found.**.

***Magnetic Resonance Relaxometry***

As mentioned previously, the initial samples were too concentrated and resulted in the particles separating from the water solution. The relaxometry measurements demonstrating this can be seen in Figure 127. The second batch of samples prepared with a sonicator gave trustworthy results as seen in Figure 128.

Table 10 details the results for the first experiment and Table 11 presents results of the diluted and sonicated samples. Samples that were too concentrated and yielded no result are represented as n/a; this occurred to nearly every sample at the original concentration. In the second set of results no noticeable correlation of either concentration or iron content could be seen with the T2 or T1 relaxation times. The results do confirm the preference of T2 relaxation for these samples.

**Table 9 Summary of TEM Results**

| Sample | Core Diameter (nm) | Total Diameter (nm) | Agglomerates (nm) |
|---|---|---|---|
| JK044 | - | 4 - 39 | 400 |
| JK045 | 4 - 9 | 11 - 28 | 35 - 800 |
| JK046 | 2 - 4 | 8 - 10 | 475 |
| JK046B | 2 - 8 | 6 - 24 | 218 - 1384 |
| JK047 | 4 - 52 | 8 - 68 | 195 |
| JK047B | 2 - 12 | 5 - 20 | 430 |
| JK048 | - | 7 - 29 | 653 - 3600 |
| JK049 | 1 - 2 | 2 - 4 | 103 - 874 |
| JK049B | 4 - 15 | 8 - 21 | 275 - 568 |
| JK050 | 2 - 3 | 3 - 5 | 918 |
| JK051 | 2 - 5 | 5 - 14 | 76 |

**Table 10 Relaxometry Results of Concentrated Samples**

| Sample | Concentration | T2 (ms) | T1 (ms) | % Fe metal |
|---|---|---|---|---|
| JK046 | normal | 118.7 | 1388 | 59.84 |
| JK046 | dilute | 176.8 | 1386 | 59.48 |
| JK047 | normal | n/a | n/a | 45.53 |
| JK047 | dilute | 110.3 | 1242.6 | 45.53 |
| JK047B | normal | 70.3 | 1058.5 | 44.16 |
| JK047B | dilute | 73 | 1125.3 | 44.16 |
| JK048 | normal | n/a | n/a | 41.07 |
| JK048 | dilute | 162.7 | 1411.3 | 41.07 |
| JK049 | normal | 401.6 | 1527.2 | 50.98 |
| JK049 | dilute | 376.2 | 1496 | 50.98 |
| JK049B | normal | n/a | n/a | 22.70 |
| JK049B | dilute | 149 | 1225.3 | 22.70 |
| JK050 | normal | 365.2 | 1464.6 | 52.41 |
| JK050 | dilute | 587.7 | 1550.8 | 52.41 |
| DI water | normal | 985 | 1643.6 | 0.00 |

**Table 11 Relaxometry Value of Varying Concentrations**

| Sample | Concentration | T2 (ms) | T1 (ms) | % Fe metal |
|---|---|---|---|---|
| JK047 | conc 1 | 1173.6 | 2847.7 | 45.53 |
| JK047 | conc 2 | 1020.1 | 2848.3 | 45.53 |
| JK047 | conc 3 | 1119 | 2889.1 | 45.53 |
| JK047 | conc 4 | 1125.3 | 2917.4 | 45.53 |
| JK047B | conc 1 | 1175 | 2878.9 | 44.16 |
| JK047B | conc 2 | 1155.1 | 2873.2 | 44.16 |
| JK047B | conc 3 | 1180.9 | 2907.9 | 44.16 |
| JK047B | conc 4 | 1139.5 | 2888.9 | 44.16 |
| JK048 | conc 1 | 1101.5 | 2884.3 | 41.07 |
| JK048 | conc 2 | 1133.6 | 2882.9 | 41.07 |
| JK048 | conc 3 | 1107.7 | 2900.8 | 41.07 |
| JK048 | conc 4 | 1042.9 | 2848 | 41.07 |

***Mössbauer Spectroscopy***

Mössbauer spectroscopy was performed at varying temperatures. A field was applied to some samples. Analysis was performed using Mössbauer GenFit Software (R.S. Preston and D.E. Brown) to plot and fit spectra. Mössbauer spectroscopy consistently showed amorphous iron present throughout all samples made by reducing iron sulfate. Amorphous iron typically has a hyperfine field of 285 kG. This is consistent with spectra seen in Chapter IV Appendix.

Despite the presence of amorphous iron, all samples were composed of some percentage of metallic iron (Table 12). Metallic iron has a hyperfine field of 330 kG. This was seen in all spectra analyzed. Some samples did also contain iron oxide. The hyperfine field of iron oxide is around 520 kG; this was observed in JK044, JK047B, and JK049. The presence of oxide was expected in JK047B and JK044 since they have no coating. Sample JK044 was not synthesized in an inert environment and had the largest amount of oxide present.

**Table 12 Mossbauer Results of Iron Sulfate Reduction Samples**

| Sample | Temp | Field | Site 1 Percentage | Site 1 Hyperfine | Site 1 Isomer Shift | Site 2 Percentage | Site 2 Hyperfine | Site 2 Isomer Shift | Site 3 Percentage | Site 3 Hyperfine | Site 3 Isomer Shift |
|---|---|---|---|---|---|---|---|---|---|---|---|
| JK044 | 6 K | | 56.82% | 506.9 | 0.44 | 31.61% | 341.7 | 0.16 | 11.57% | 0.0 | 1.31 |
| JK044 | 293 K | | 31.89% | 443.8 | 0.55 | 30.04% | 330.7 | 0.00 | 19.45% | 0.0 | 1.16 |
| JK045 | 6 K | | 100.00% | 335.9 | 0.10 | | | | | | |
| JK045 | 293 K | | 100.00% | 308.6 | 0.08 | | | | | | |
| JK046 | 6 K | | 59.84% | 339.1 | 0.11 | 40.16% | 282.8 | 0.20 | | | |
| JK046 | 293 K | | 32.43% | 335.1 | 0.00 | 67.57% | 264.7 | 0.07 | | | |
| JK046 | 293 K | 10 kG | 28.02% | 326.3 | 0.00 | 71.98% | 253.1 | 0.07 | | | |
| JK047 | 6 K | | 45.53% | 341.9 | 0.16 | 54.47% | 289.6 | 0.19 | | | |
| JK047 | 293 K | | 28.89% | 266.1 | 0.08 | 71.11% | 332.56 | 0.00 | | | |
| JK047B | 6 K | | 44.16% | 342.1 | 0.11 | 55.84% | 284.85 | 0.18 | | | |
| JK047B | 293 K | | 25.64% | 334.8 | 0.00 | 74.36% | 249.9 | 0.00 | | | |
| JK048 | 6 K | | 41.07% | 342.0 | 0.11 | 58.93% | 284.4 | 0.18 | | | |
| JK048 | 293 K | | 27.94% | 332.3 | 0.00 | 72.06% | 263.5 | 0.04 | | | |
| JK049 | 6 K | | 50.98% | 341.4 | 0.11 | 30.31% | 286.9 | 0.22 | 18.71% | 499.5 | 0.45 |
| JK049 | 293 K | | 40.50% | 331.6 | 0.00 | 46.09% | 259.8 | 0.00 | 13.41% | 0.0 | 0.34 |
| JK049B | 6 K | | 35.04% | 341.3 | 0.11 | 50.67% | 277.9 | 0.20 | 14.29% | 493.6 | 0.54 |
| JK049B | 293 K | | 22.70% | 331.7 | 0.00 | 69.47% | 251.0 | 0.06 | 7.83% | 0.0 | 0.32 |
| JK050 | 6 K | | 52.41% | 342.3 | 0.11 | 45.90% | 285.9 | 0.21 | 1.69% | 500.0 | 0.00 |
| JK050 | 293 K | | 33.71% | 331.8 | 0.00 | 66.29% | 235.1 | 0.01 | | | |
| JK051 | 6 K | | 40.07% | 344.7 | 0.11 | 59.93% | 289.2 | 0.18 | | | |

## Discussion

These samples were made in a similar fashion as the samples in Chapter II. Iron sulfate was used instead of iron chloride. A distillation column was used to try and help break up agglomerates and encourage coating. Only polyethylene glycol was used as a coating in this chapter compared to several coatings in previous chapters, and only deionized water was used as a solvent (ethanol was used with deionized water in Chapter II).

The exchange of a separatory funnel for condenser column in sample synthesis did not appear to affect the composition of the nanoparticles. TEM of samples made with both the separatory funnel and distillation column showed similar size. The size distribution of samples made with the column were slightly better than those with the separatory funnel, and more coated material was produced using the column. It was common with the separatory funnel to have half of the reaction product not make it into the coating solution; these samples presented with more oxide than their coated counterparts. It can be concluded that the distillation column helped ensure every nanoparticle was coated resulting in more coated nanoparticles and possibly helped with size distribution by providing a consistent reaction length and time.

NMR results suggest this synthesis would be favored in applications of hyperthermia as the T2 was low. Mössbauer determined iron metal was present in all samples in addition to amorphous iron. Amorphous iron was not present in the reduction of iron chloride in Chapter II.

# Chapter IV Appendix

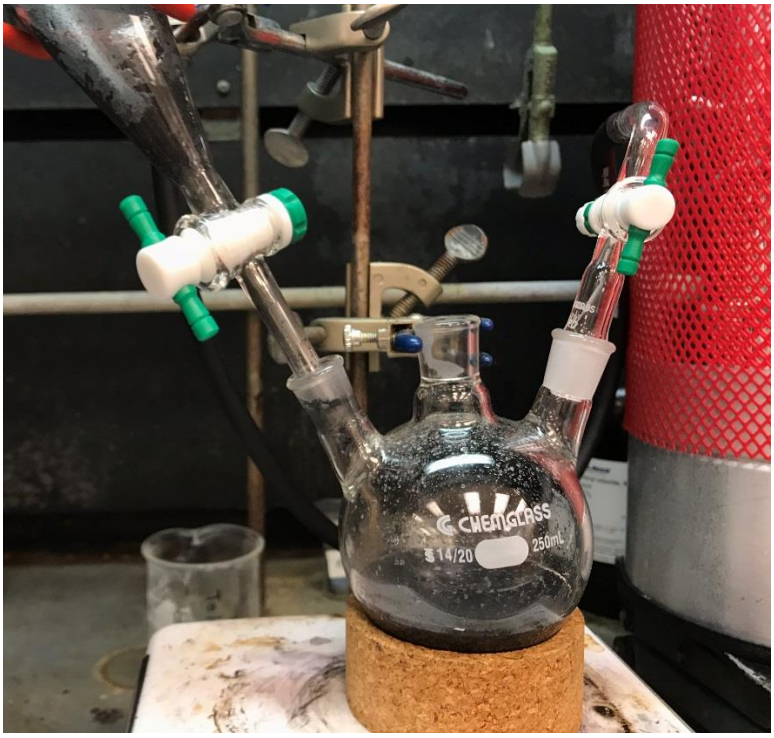



**Figure 105 Synthesis of iron nanoparticles with separatory funnel**




**Figure 106 Synthesis of iron nanoparticles with distillation column**

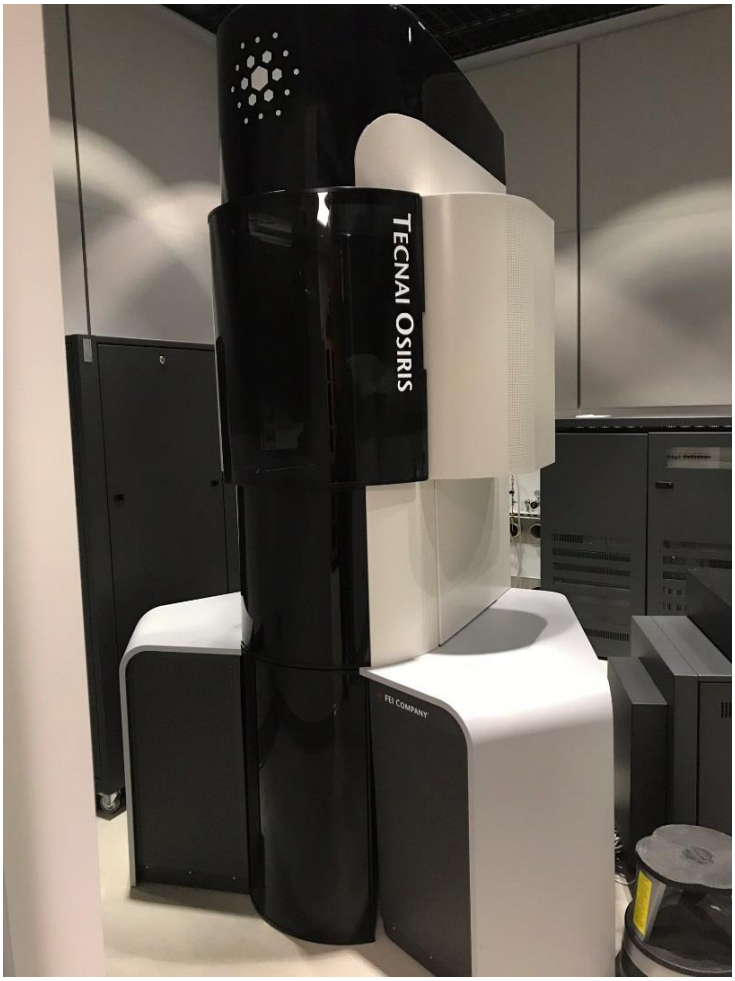



**Figure 107 FEI Tecnai Osiris TEM at VINSE**

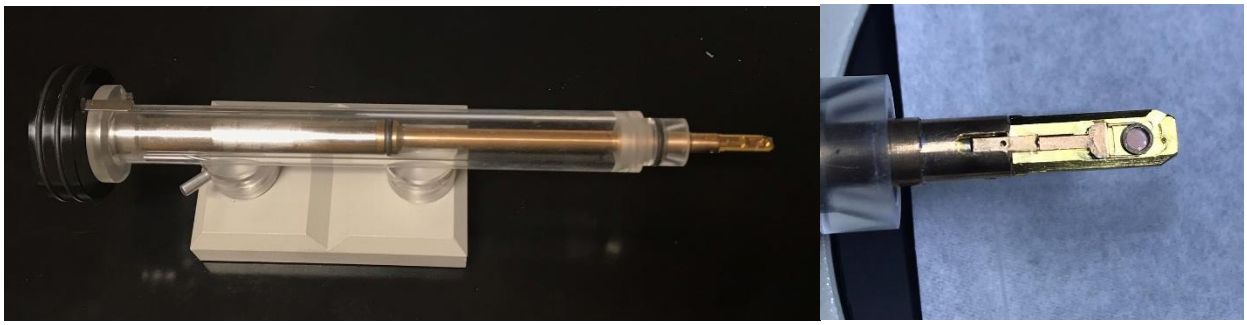


**Figure 108 TEM single tilt sample holder**




**Figure 109 Varian MR Imaging System**



**Figure 110 Concentrated samples in NMR tubes**



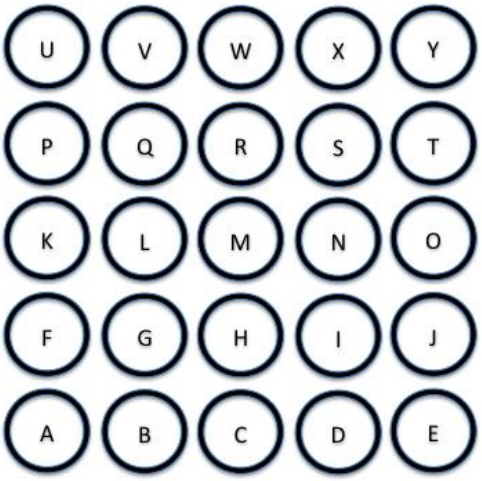




**Figure 111 Placement of NMR tubes**

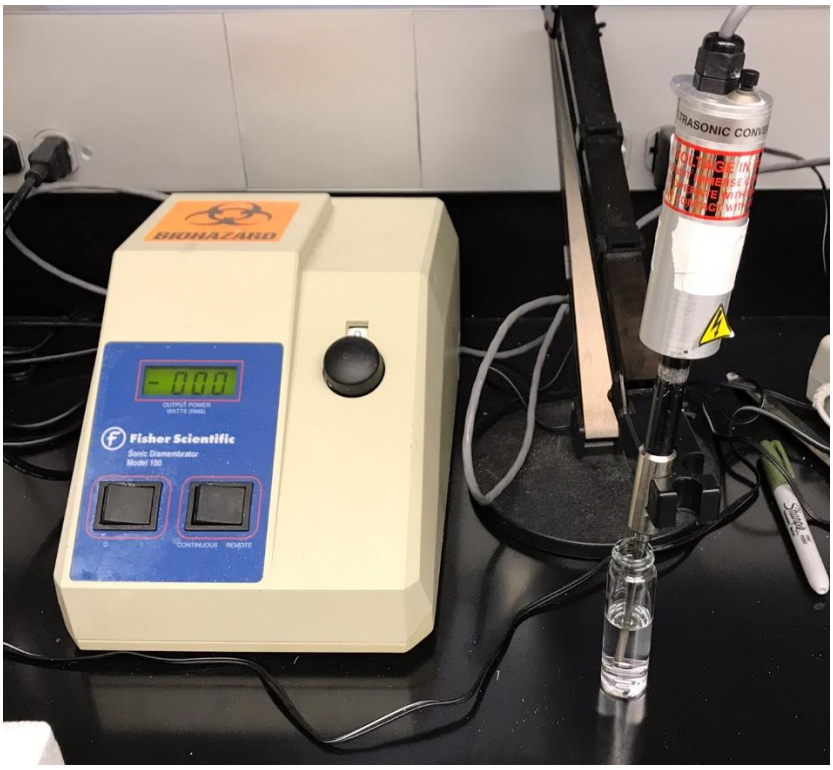



**Figure 112 Probe Sonicator at Vanderbilt University**



**Figure 113 Prepared NMR Tubes of Varying Concentrations**

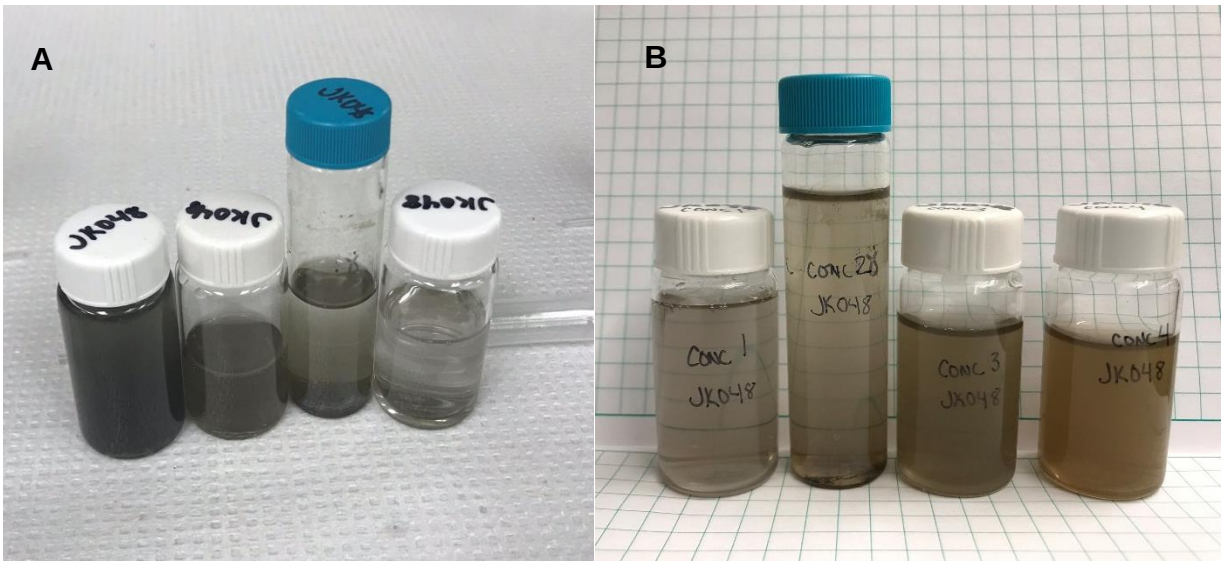



**Figure 114 A) Before and B) After Probe Sonication of Sample JK048**



**Figure 115 Mössbauer Spectrometer Setup**

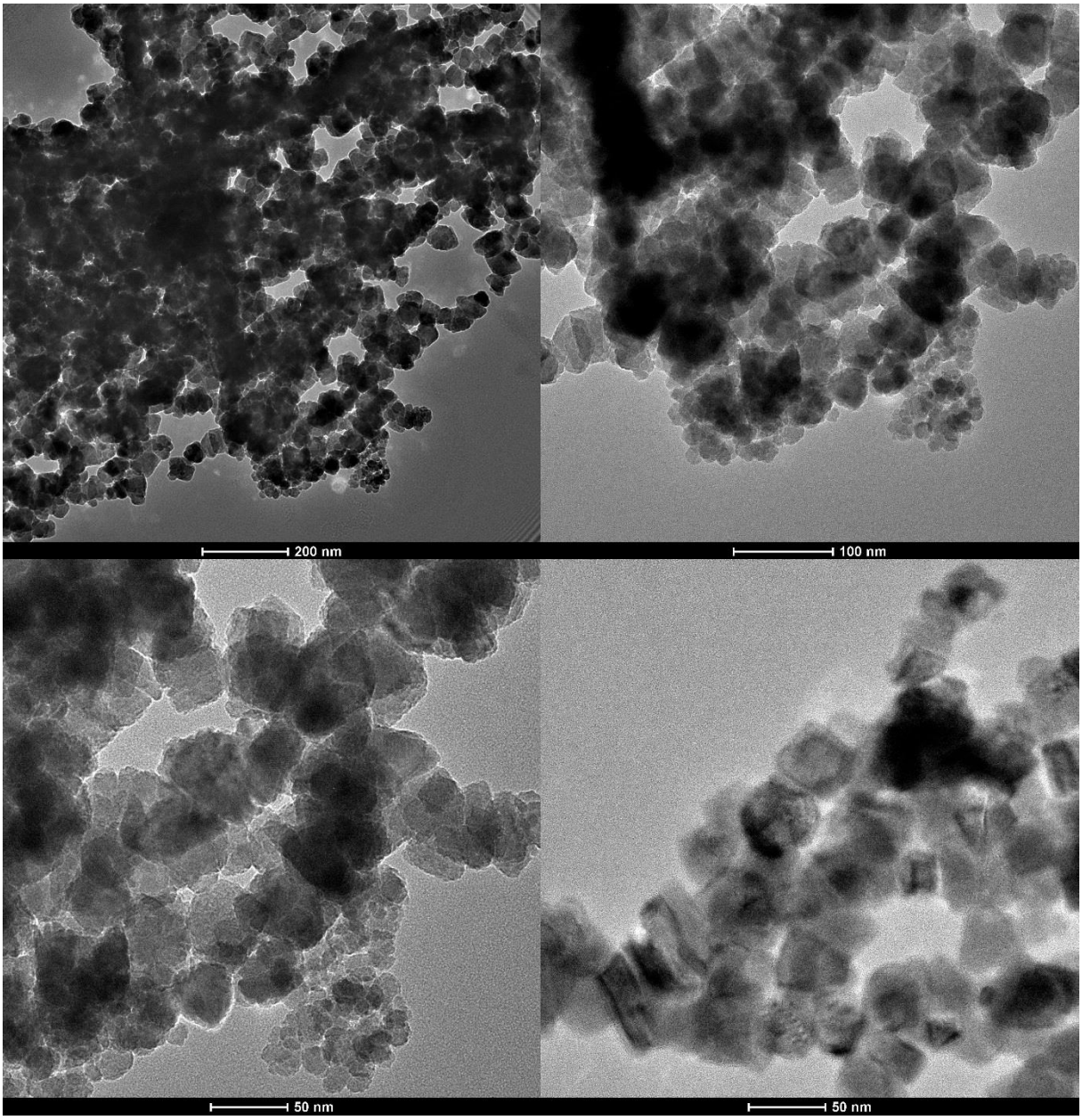



**Figure 116 TEM of JK044**

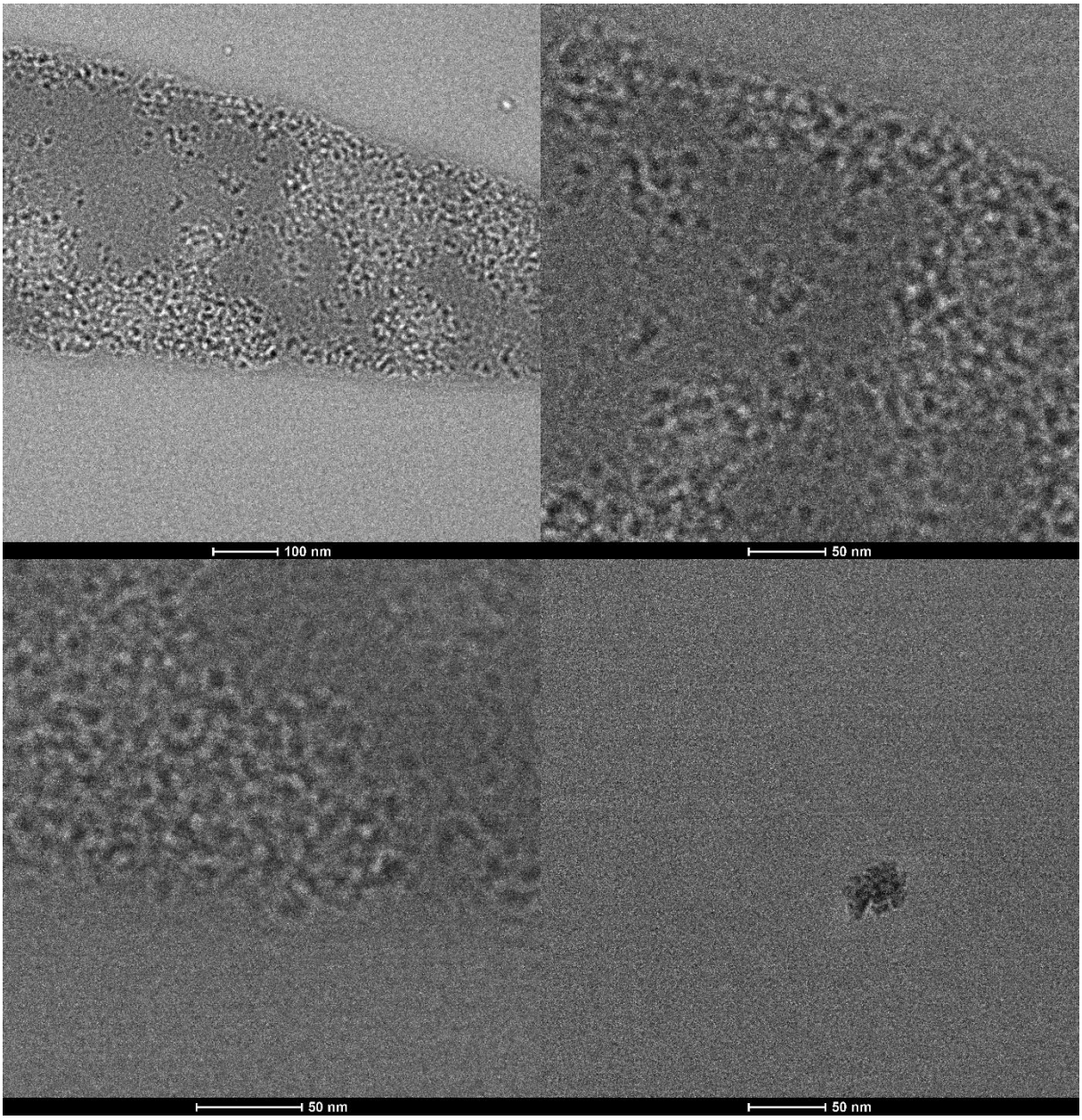



**Figure 117 TEM of JK045**

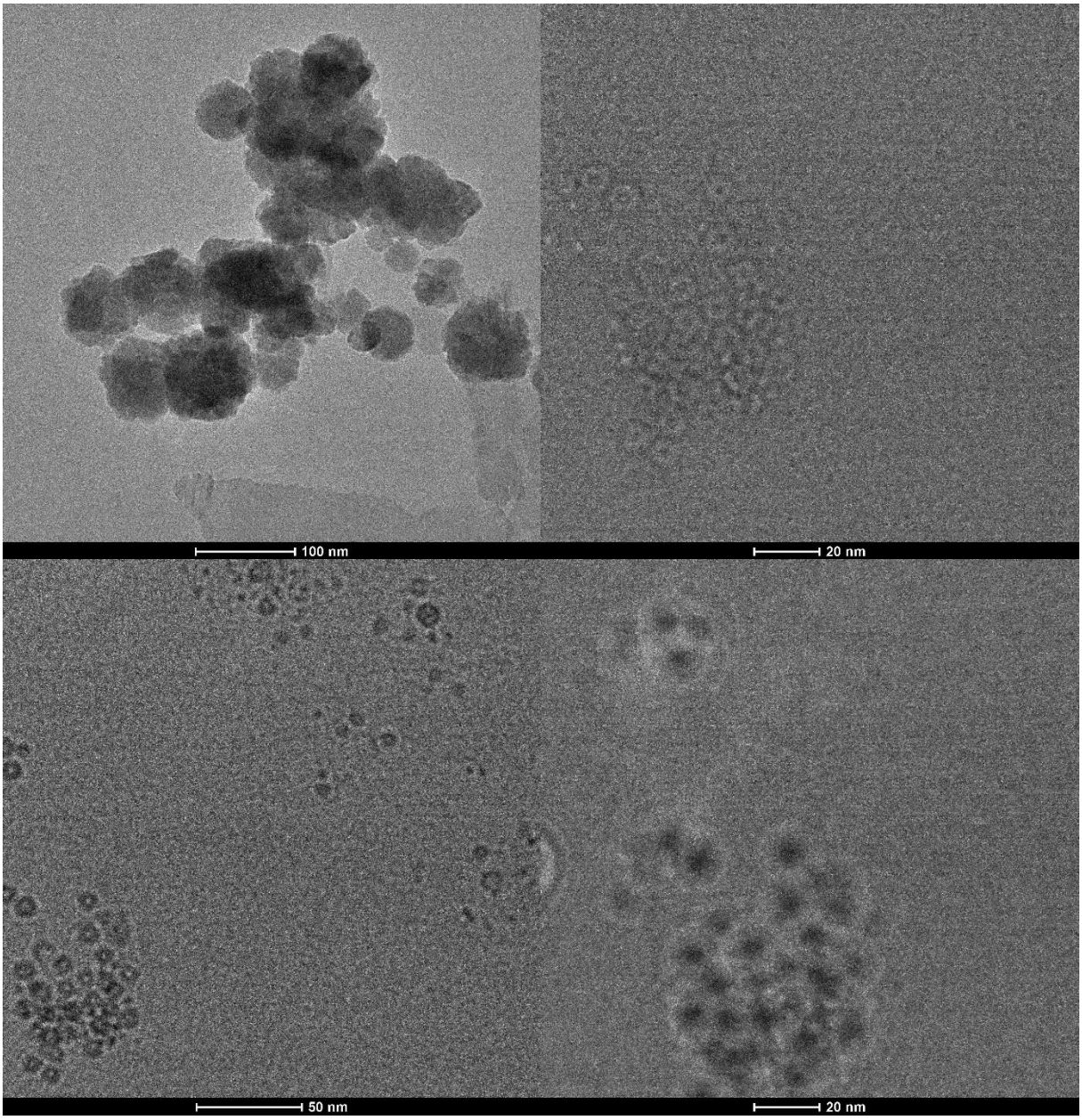



**Figure 118 TEM of JK046**

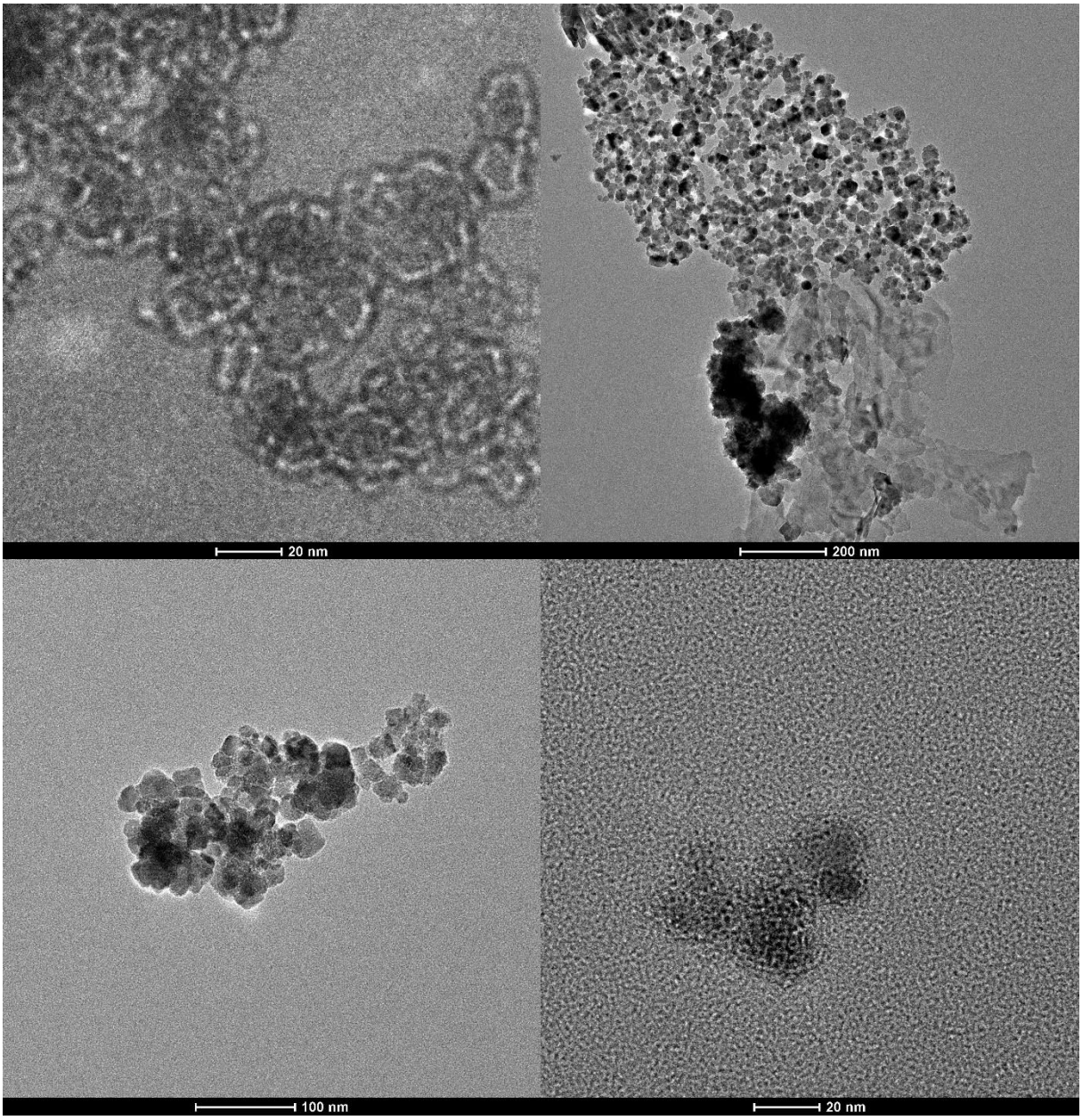



**Figure 119 TEM of JK046B**

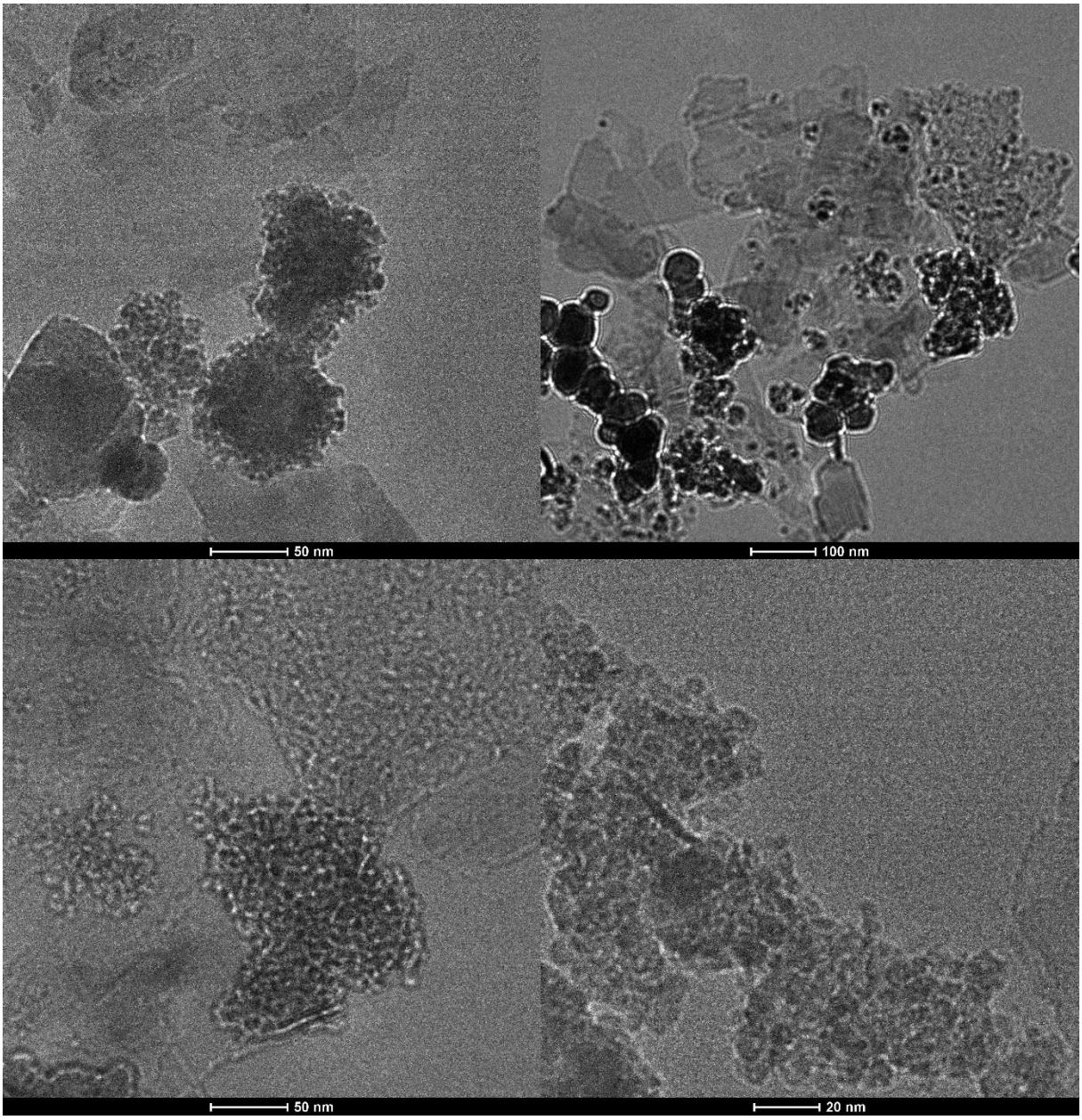



**Figure 120 TEM of JK047**

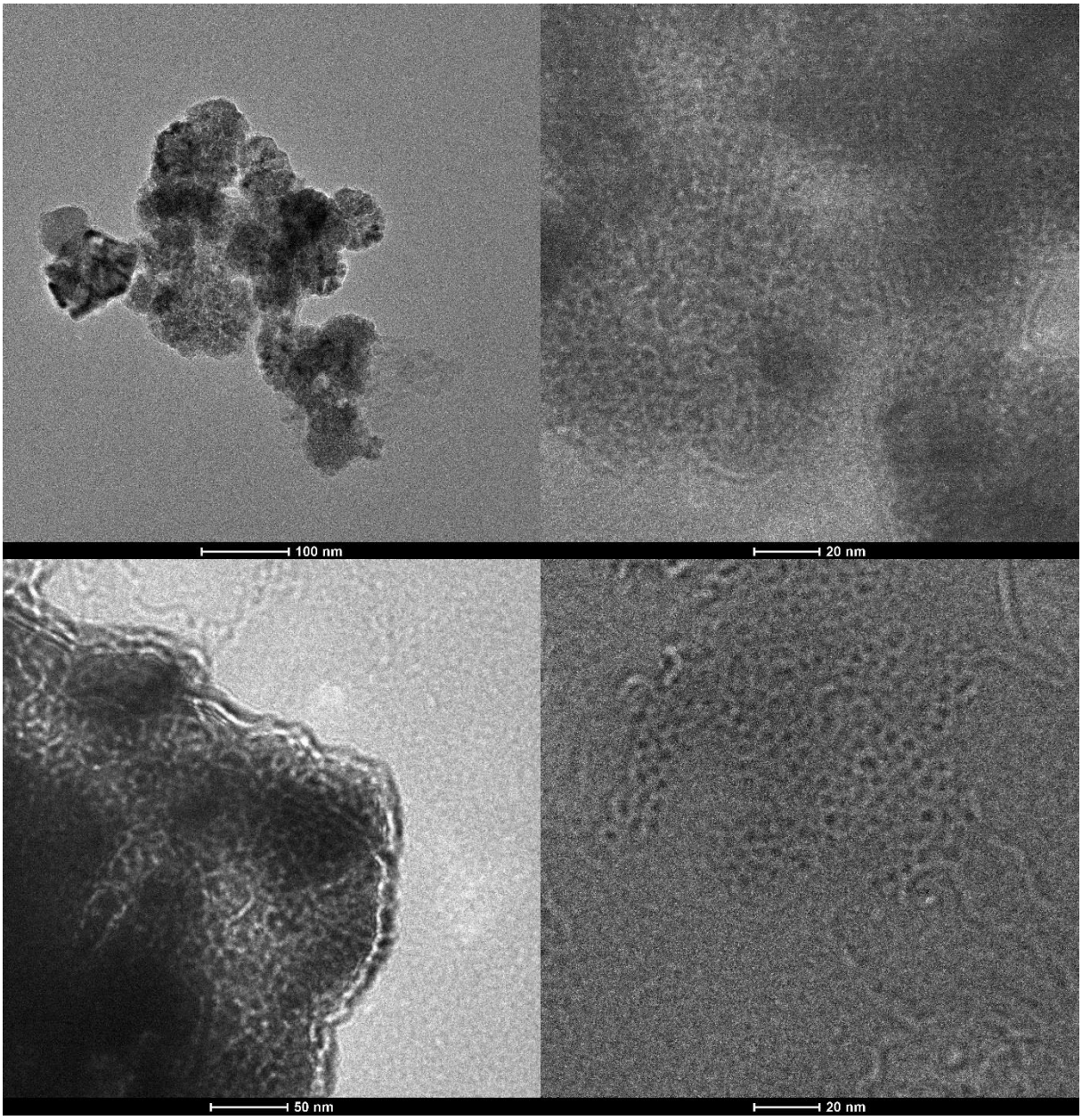



**Figure 121 TEM of JK047B**

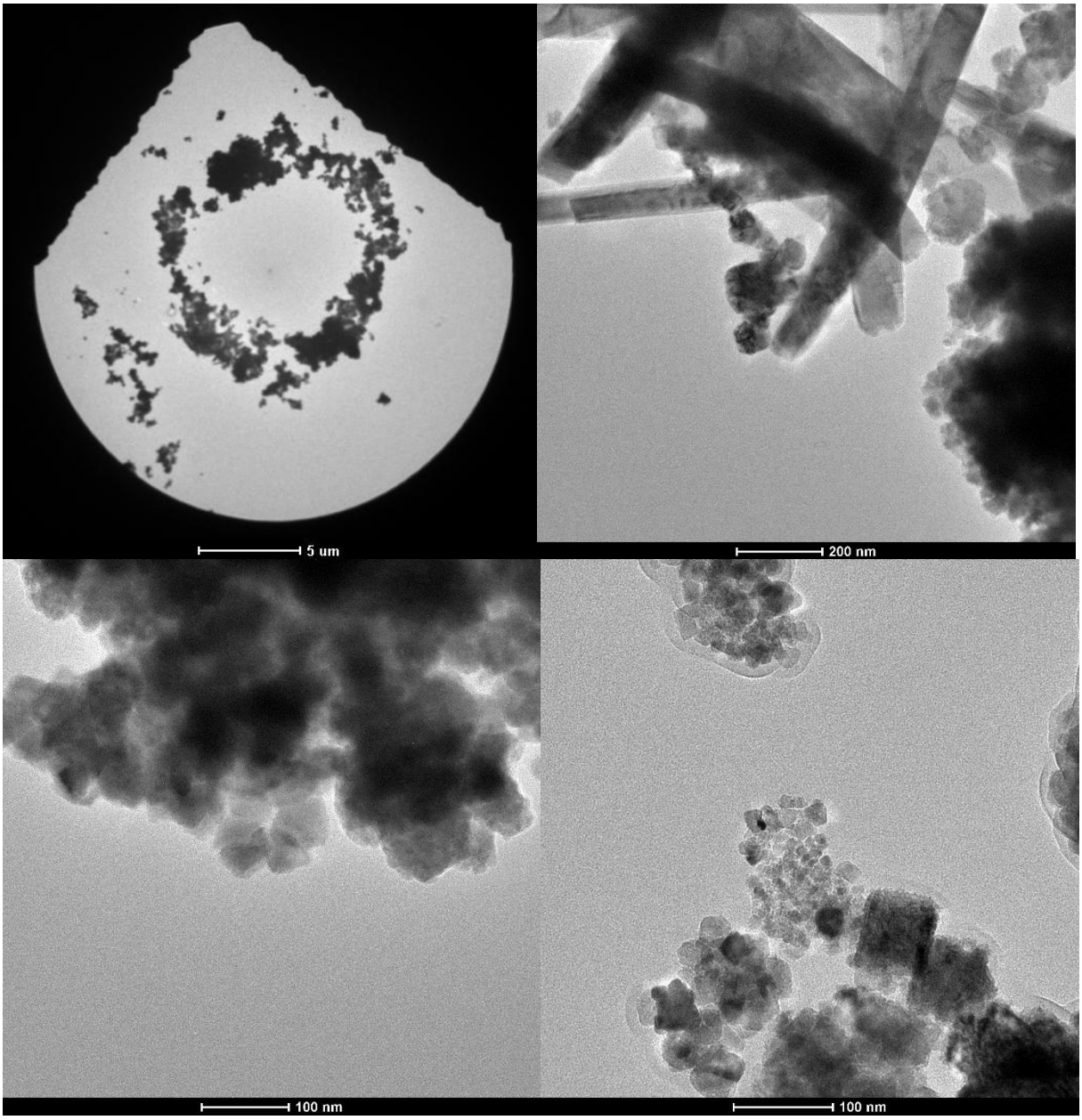



**Figure 122 TEM of JK048**

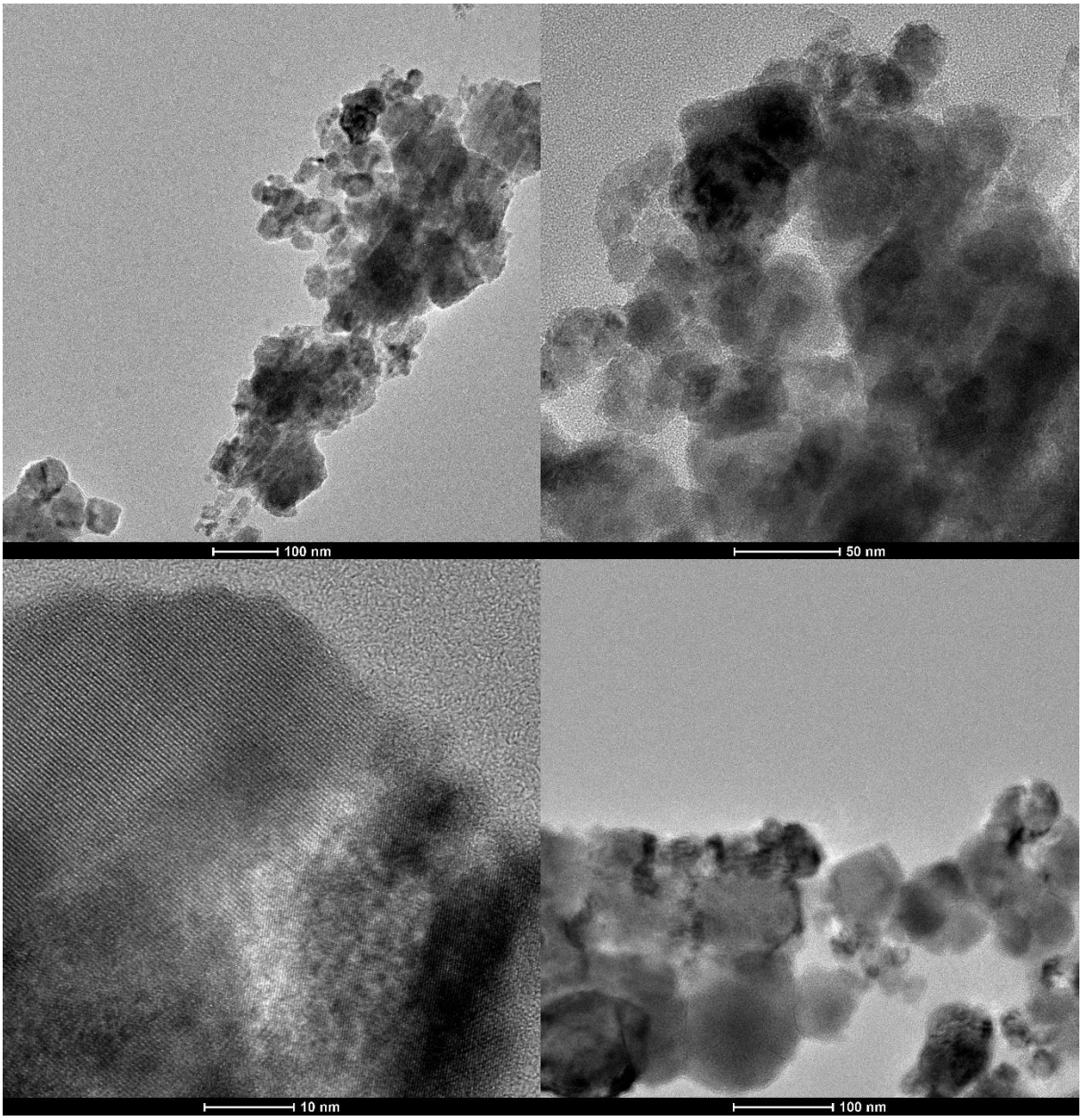



**Figure 123 TEM of JK049**

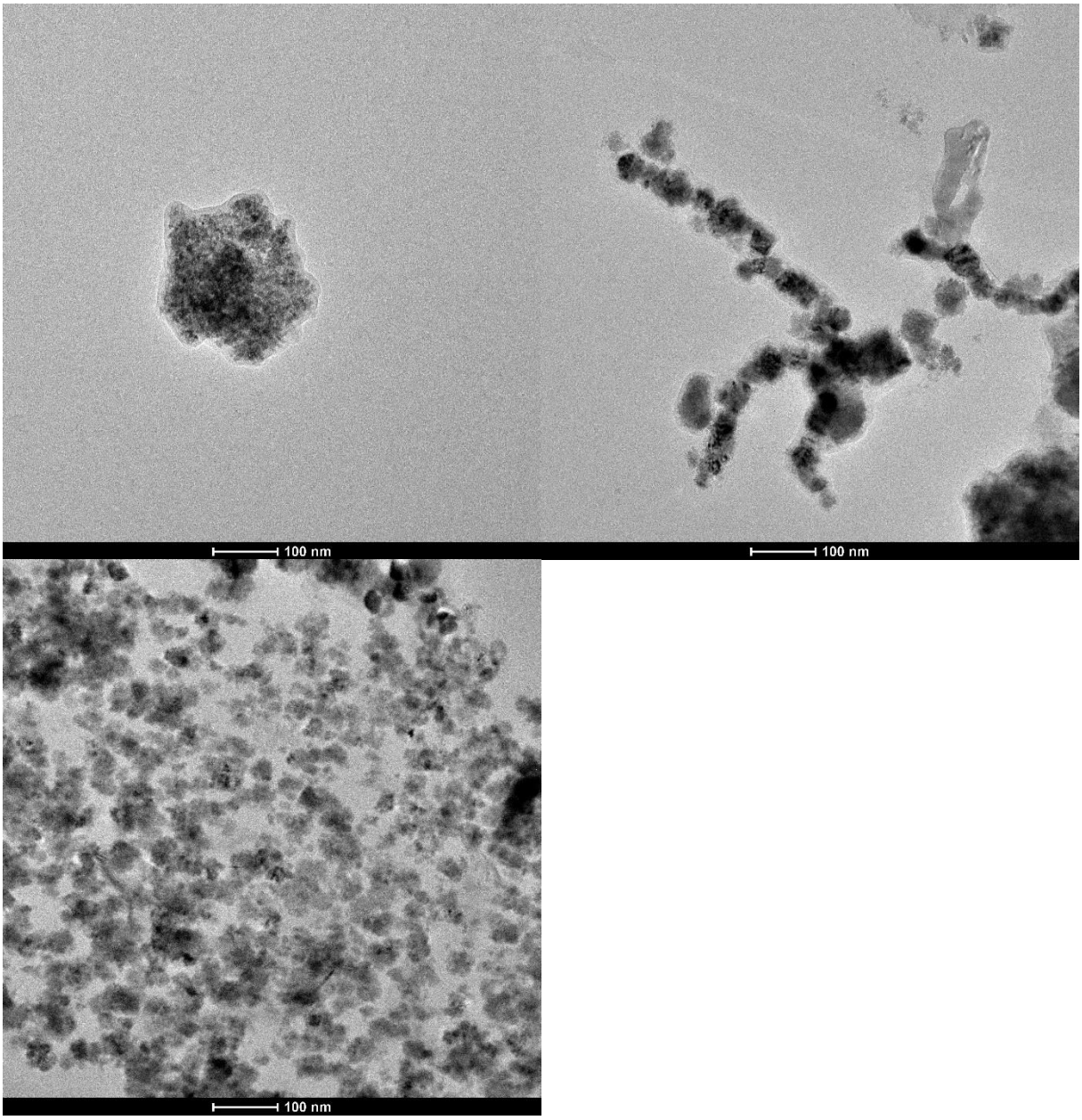



**Figure 124 TEM of JK049B**

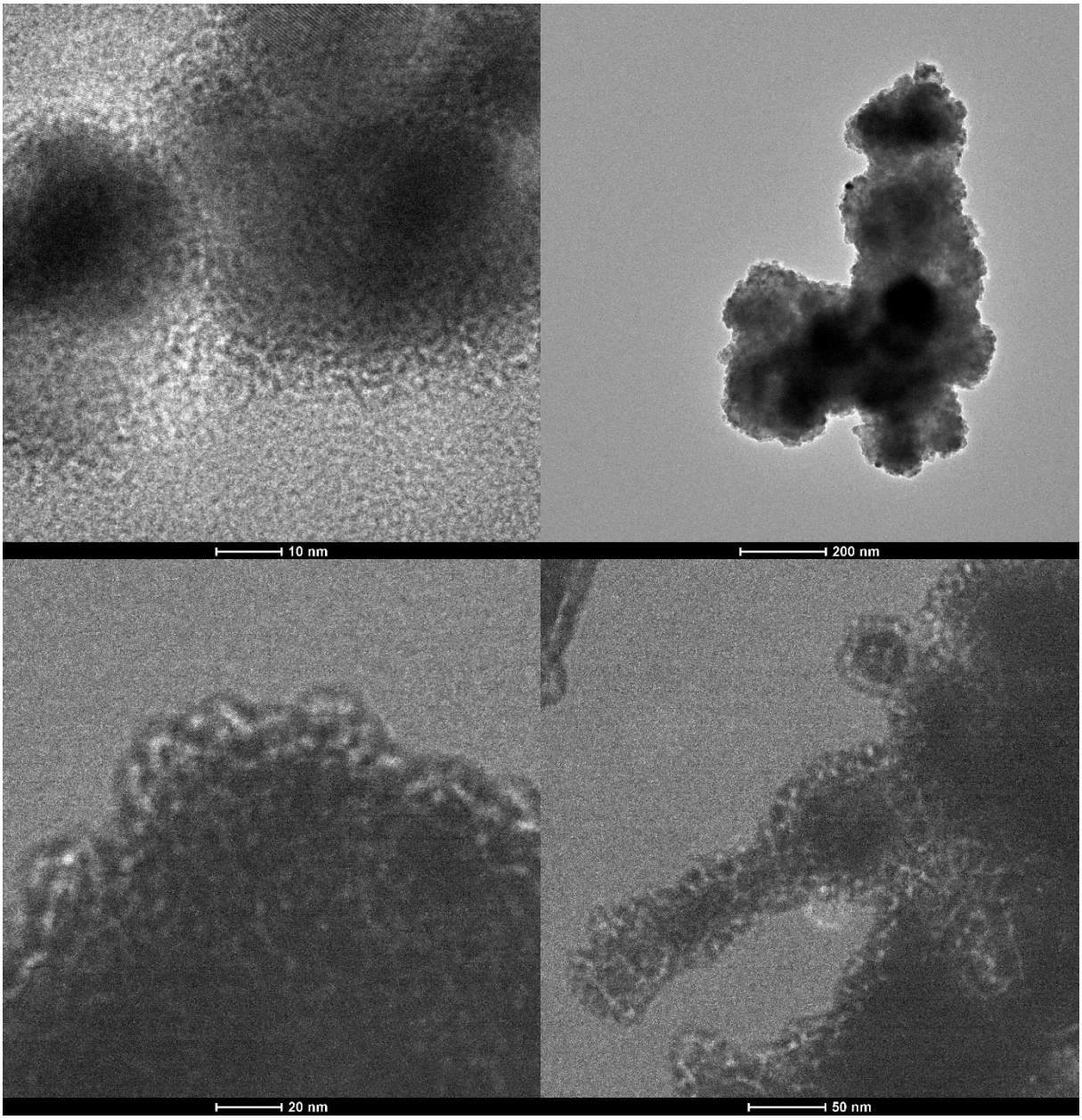



**Figure 125 TEM of JK050**

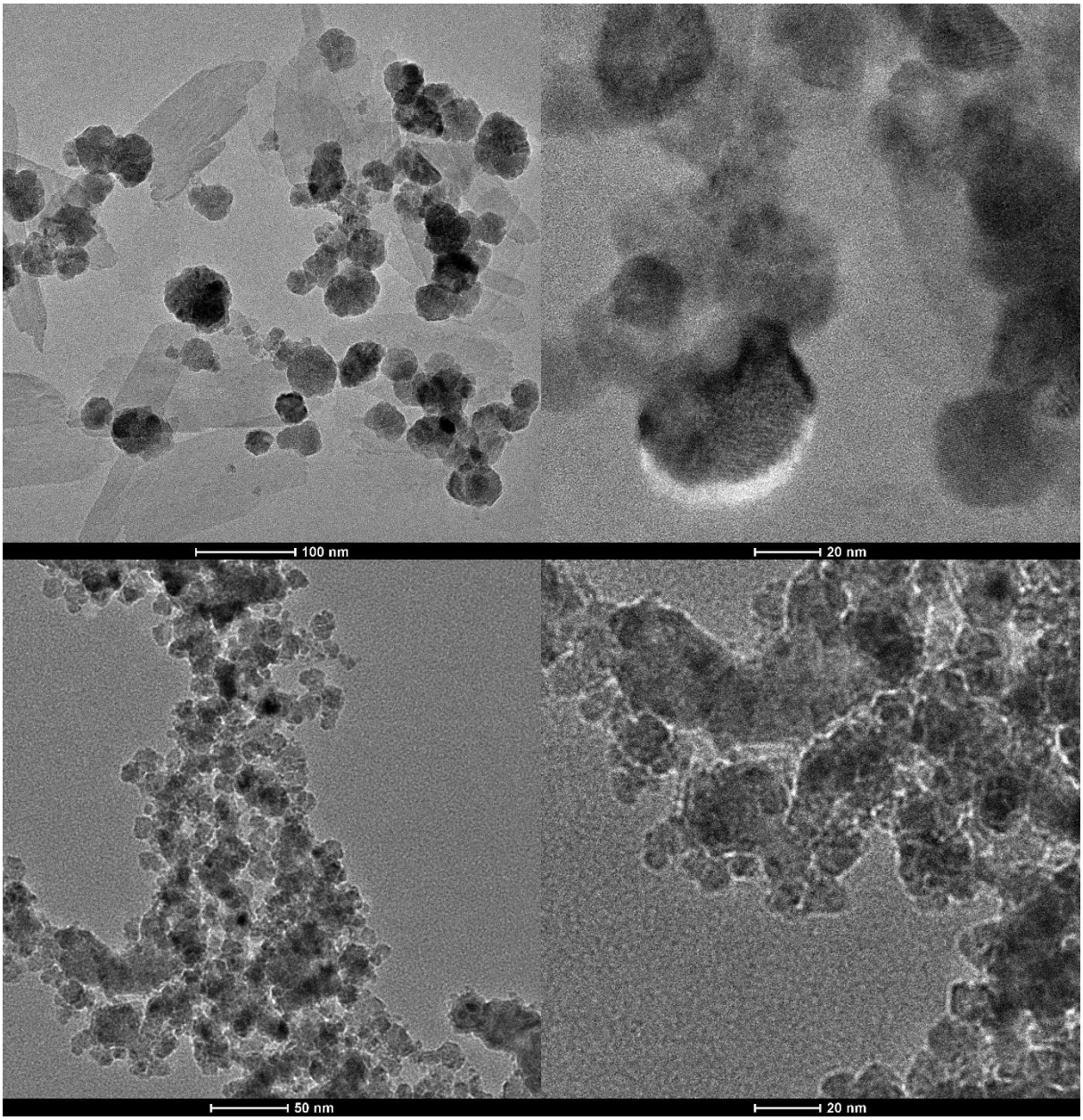



**Figure 126 TEM of JK051**

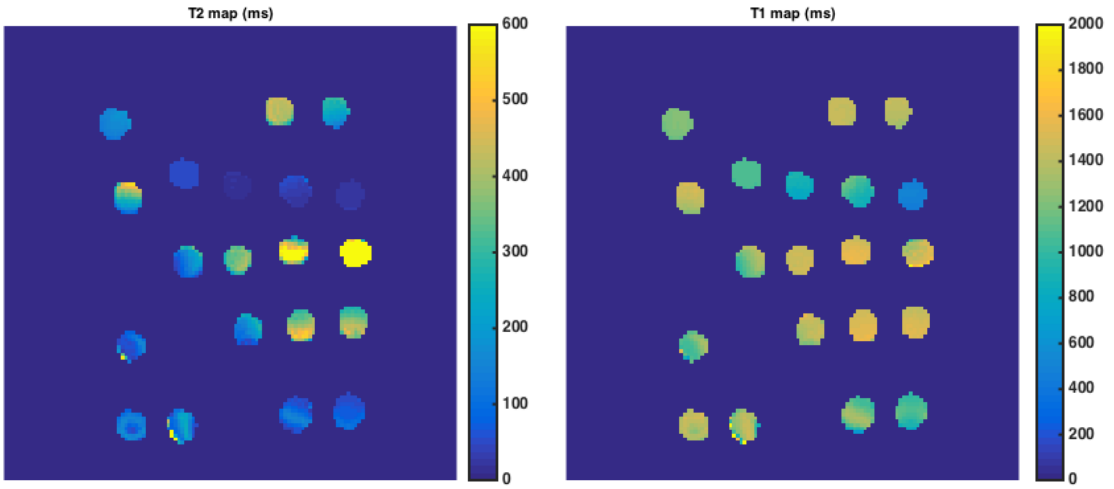



**Figure 127 Original T2 and T1 Map**

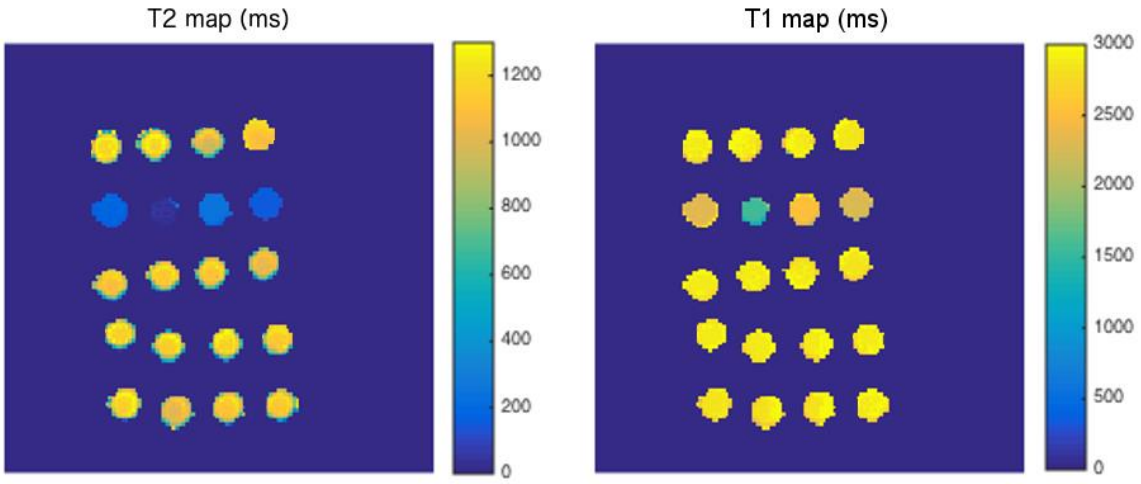



**Figure 128 T2 and T1 Map of Varying Concentrations**

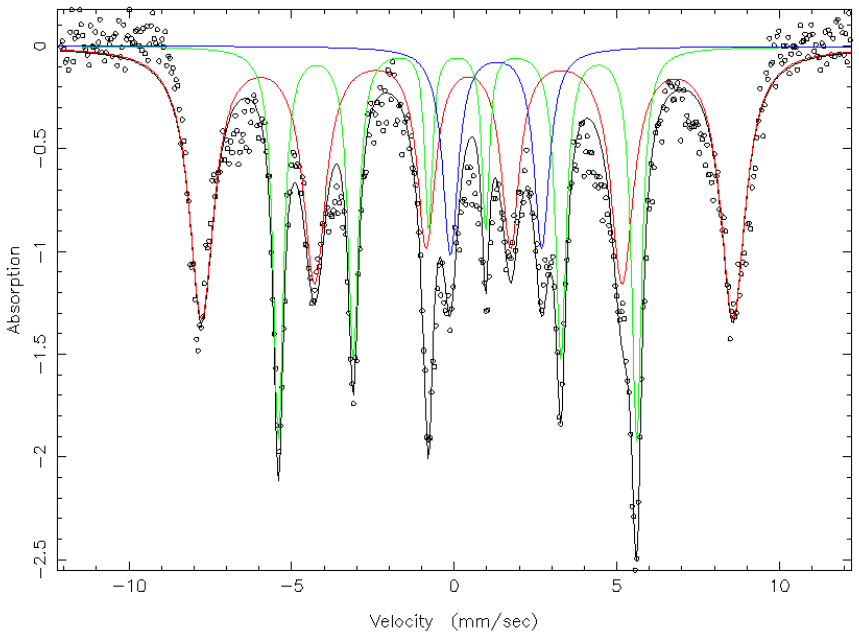



**Figure 129 Mössbauer Spectrum of JK044 at 5K**

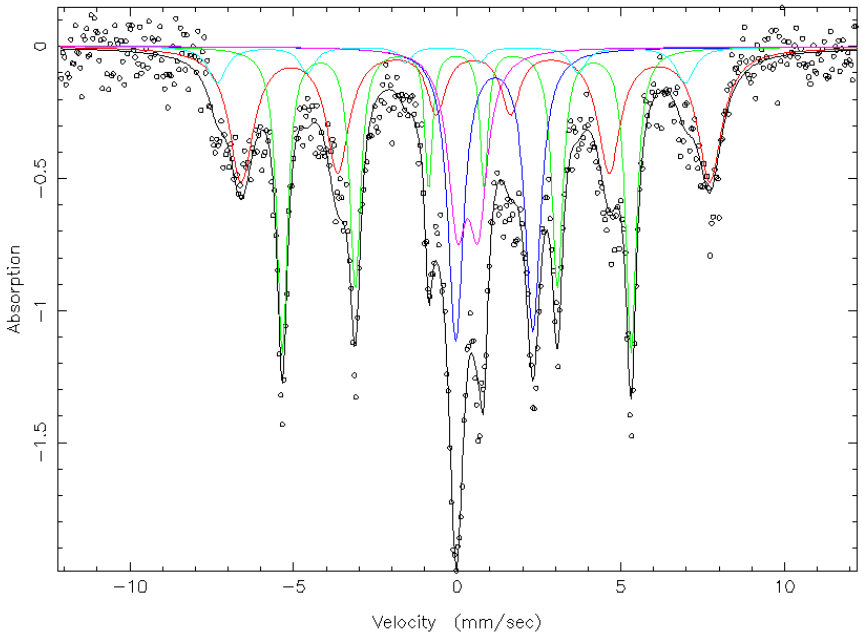



**Figure 130 Mössbauer Spectrum of JK044 at 293K**

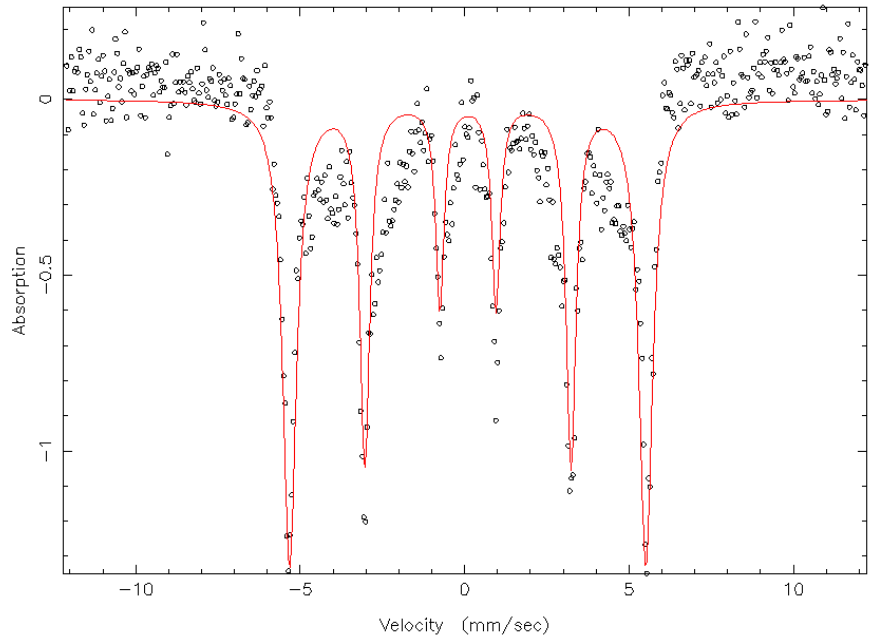



**Figure 131 Mössbauer Spectrum of JK045 at 5K**

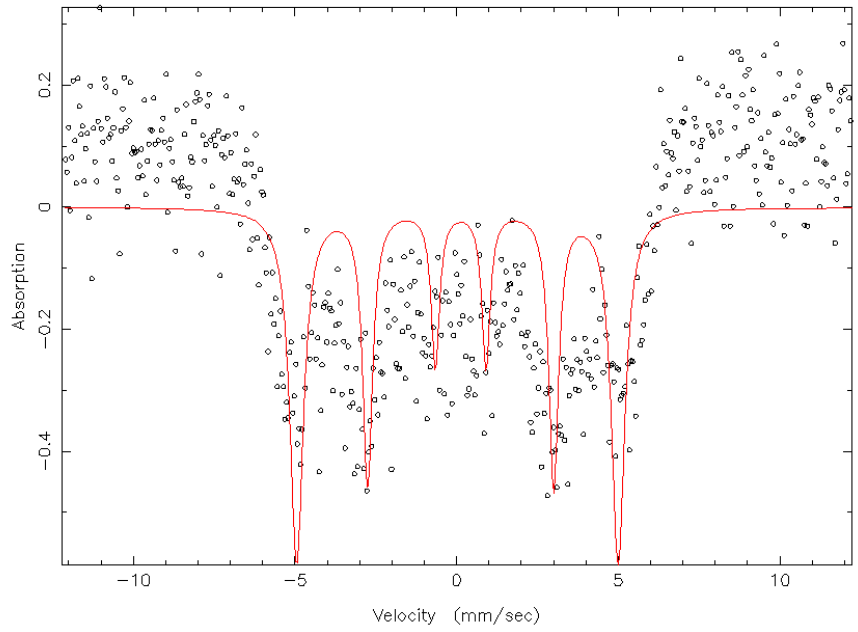



**Figure 132 Mössbauer Spectrum of JK045 at 293K**

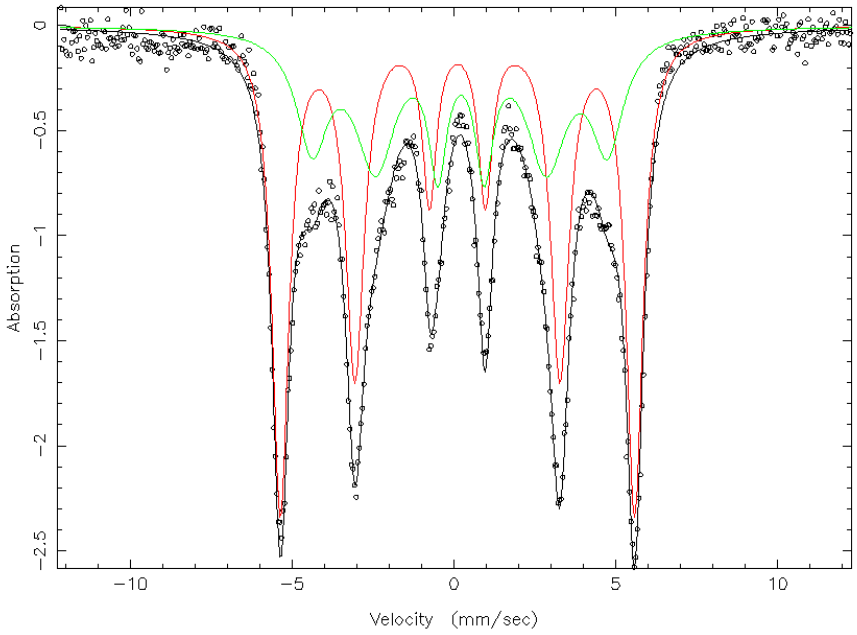



**Figure 133 Mössbauer Spectrum of JK046 at 5 K**

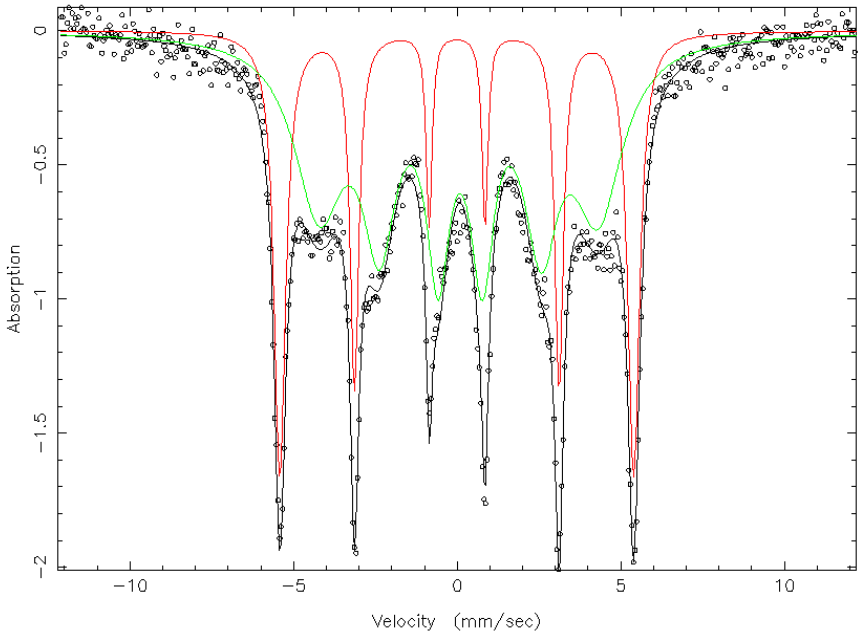



**Figure 134 Mössbauer Spectrum of JK046 at 293 K**

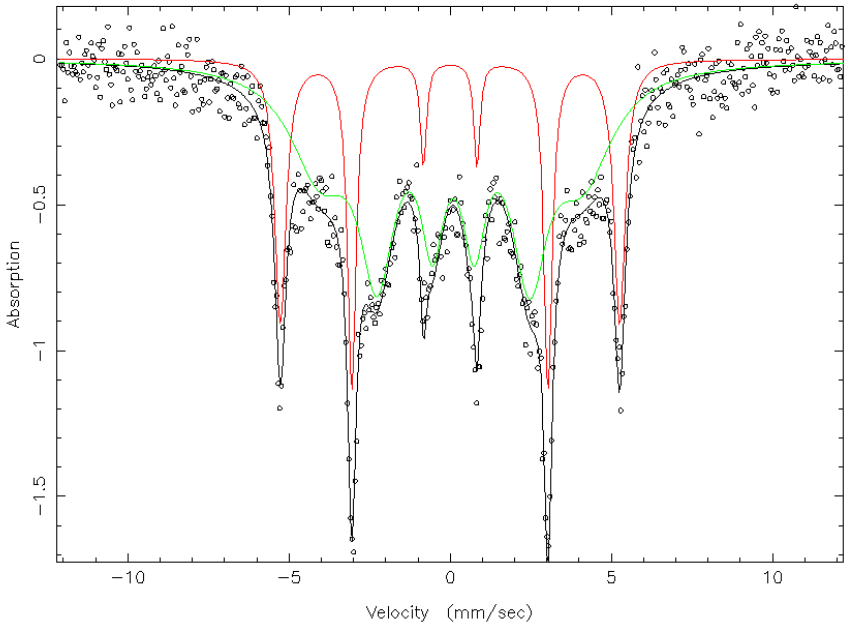



**Figure 135 Mössbauer Spectrum of JK046 at 293 K in 10 kG Field**

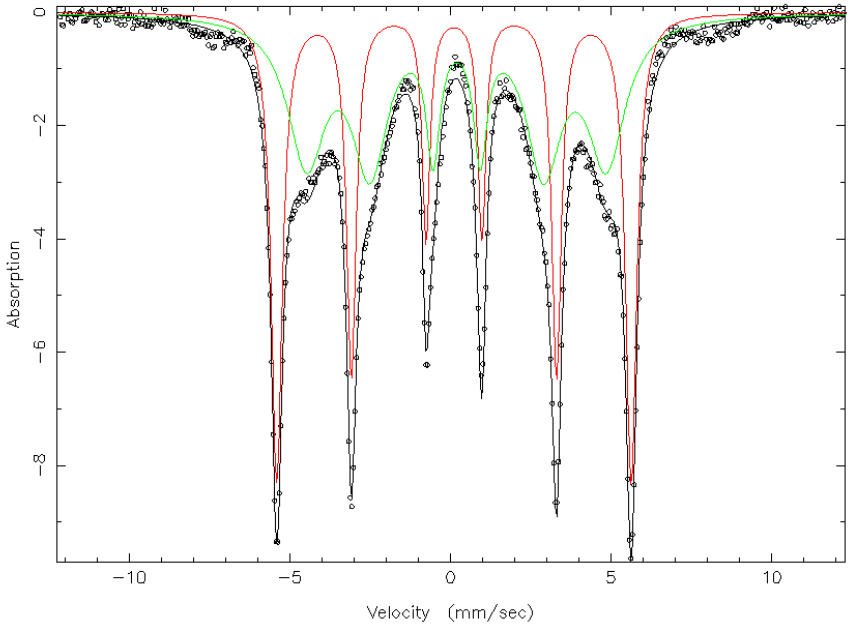



**Figure 136 Mössbauer Spectrum of JK047 at 5K**

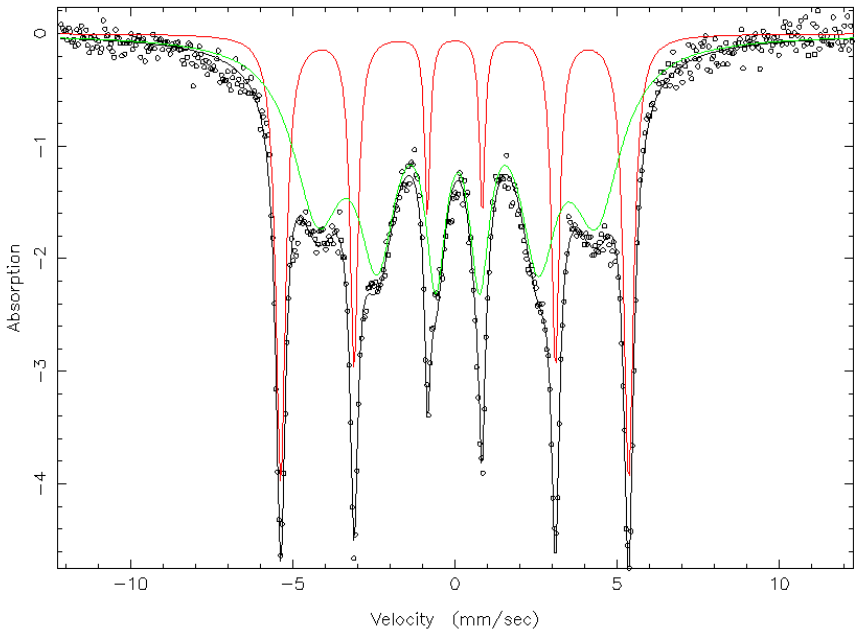



**Figure 137 Mössbauer Spectrum of JK047 at 293K**

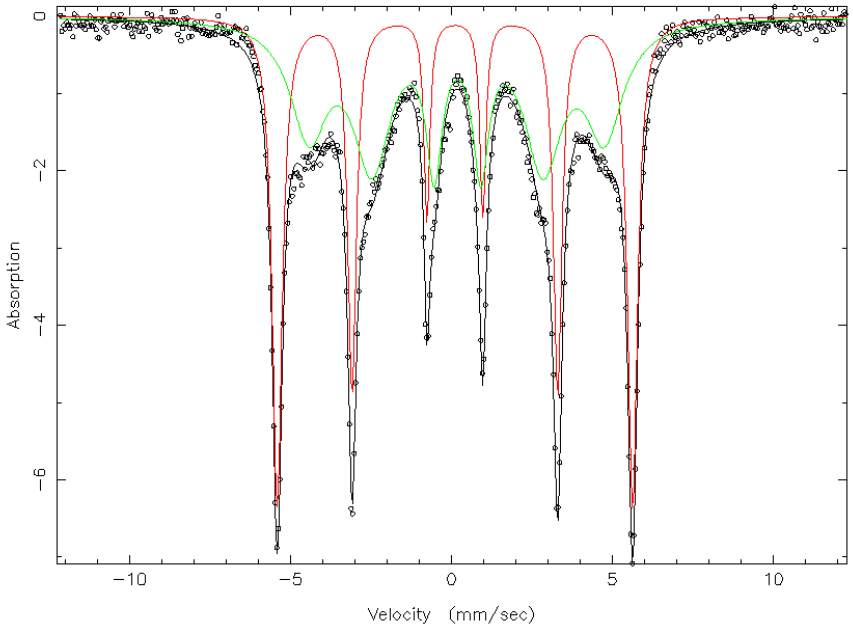



**Figure 138 Mössbauer Spectrum of JK047B at 5K**

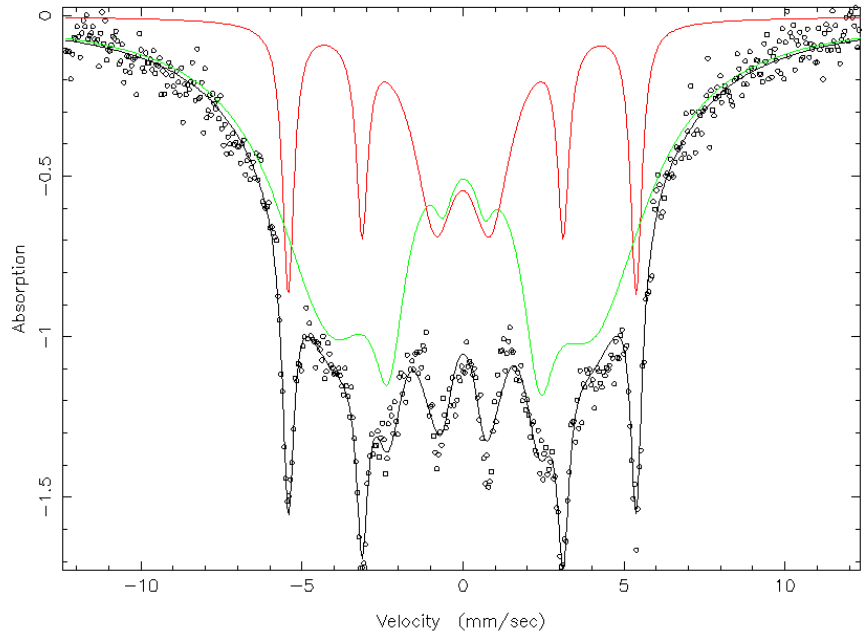



**Figure 139 Mössbauer Spectrum of JK047B at 293K**

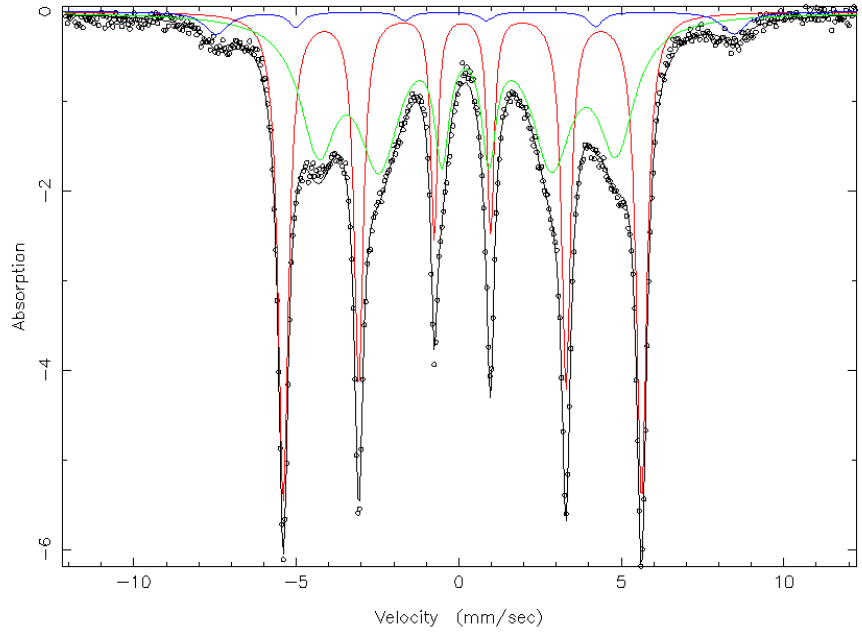



**Figure 140 Mössbauer Spectrum of JK047B at 5K after One Week in Air**

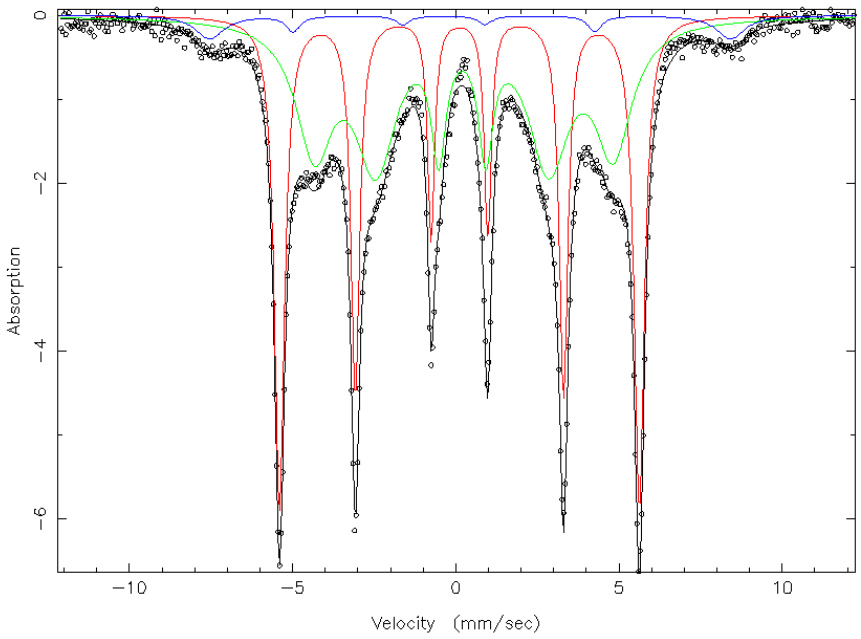



**Figure 141 Mössbauer Spectrum of JK047B after Two Weeks in Air**

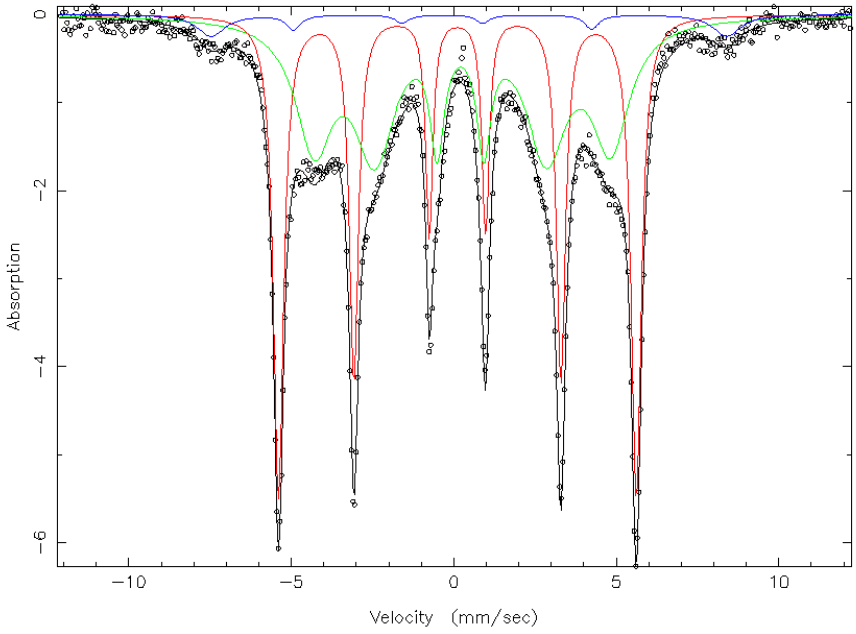



**Figure 142 Mössbauer Spectrum of JK047B at 6K after Three Weeks in Air**

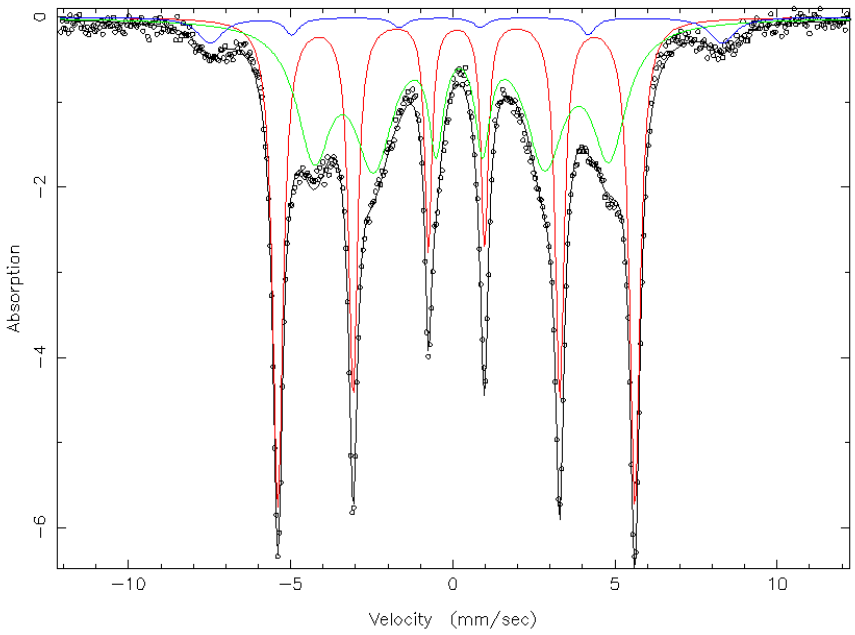



**Figure 143 Mössbauer Spectrum of JK047B at 6K after Four Weeks in Air**

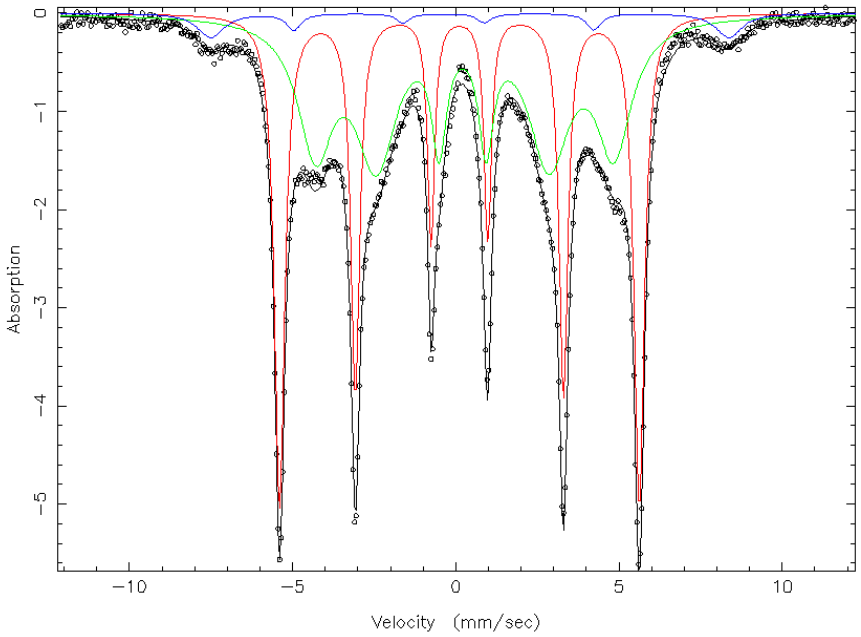



**Figure 144 Mössbauer Spectrum of JK047B at 6K after Five Weeks in Air**

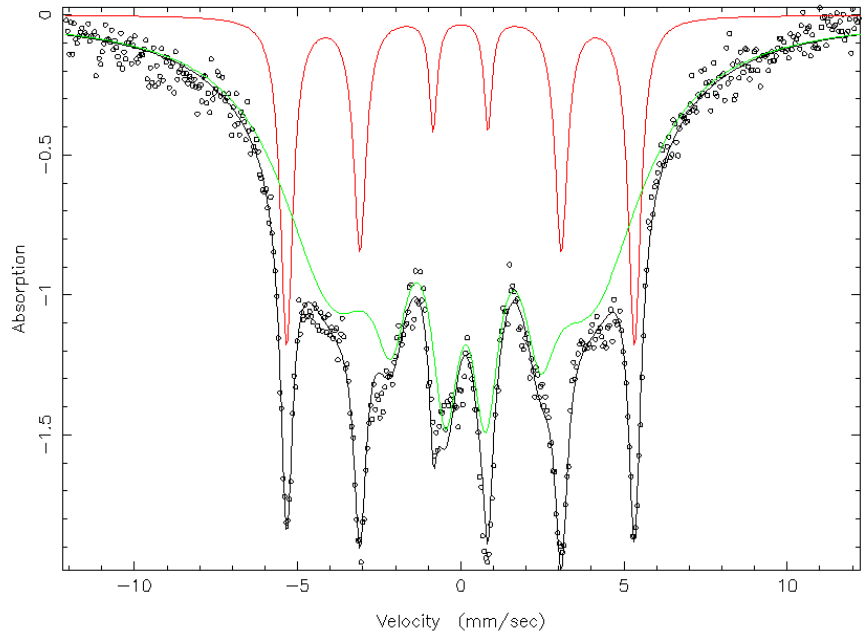



**Figure 145 Mössbauer Spectrum of JK047B at 293K after Five Weeks in Air**

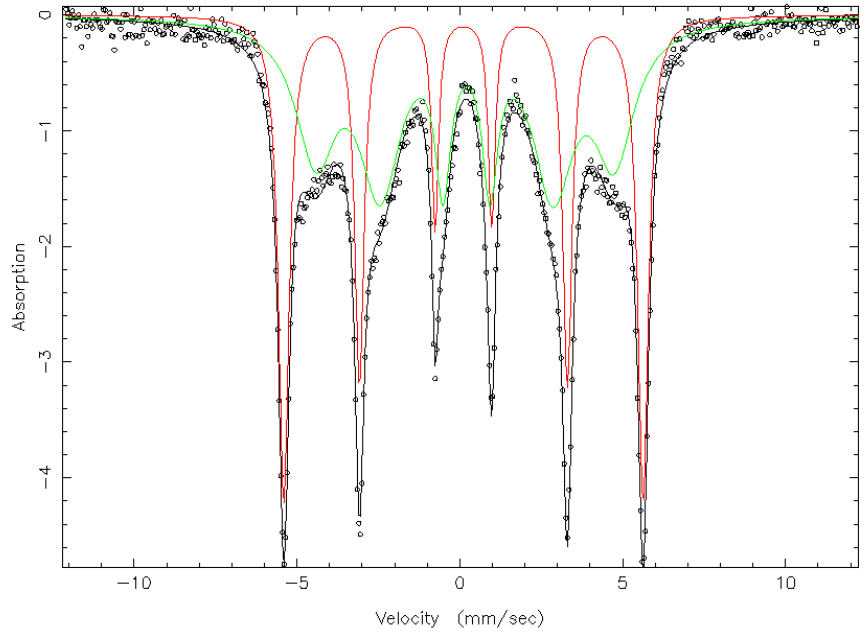



**Figure 146 Mössbauer Spectrum of JK048 at 5K**

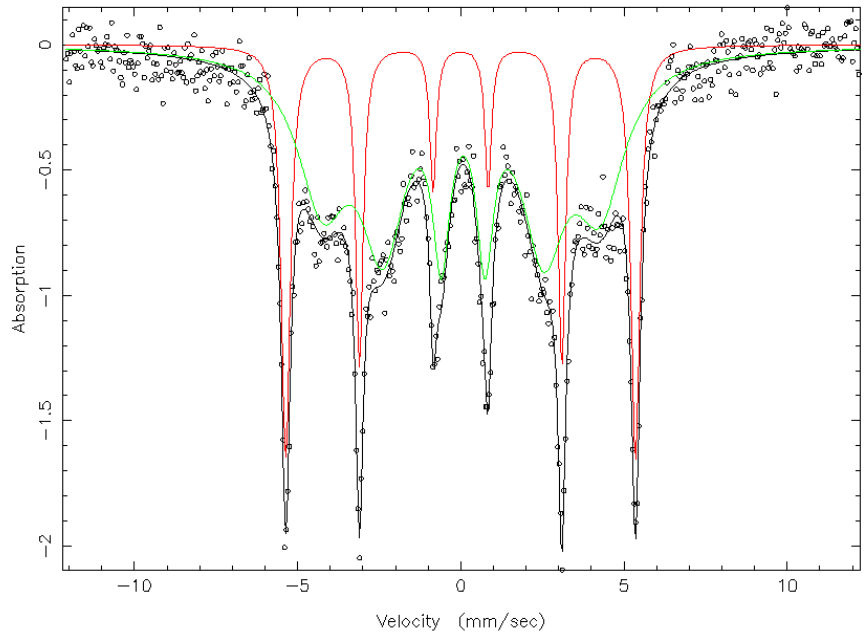



**Figure 147 Mössbauer Spectrum of JK048 at 293K**

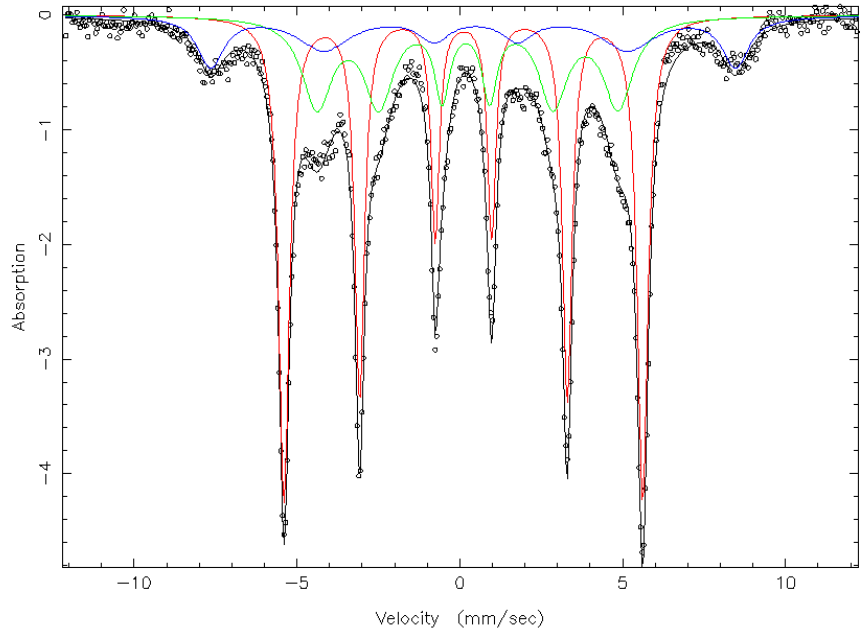



**Figure 148 Mössbauer Spectrum of JK049 at 6K**

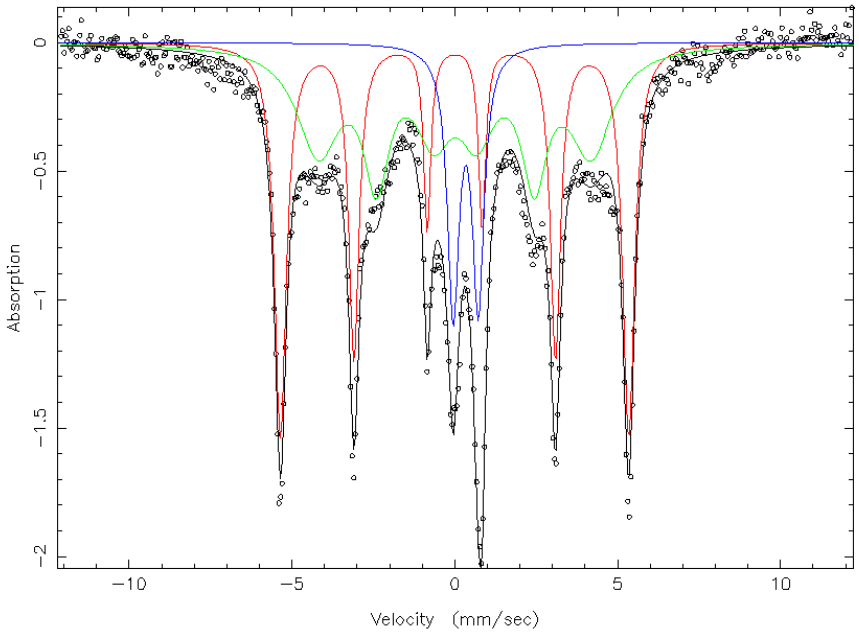



**Figure 149 Mössbauer Spectrum of JK049 at 293K**

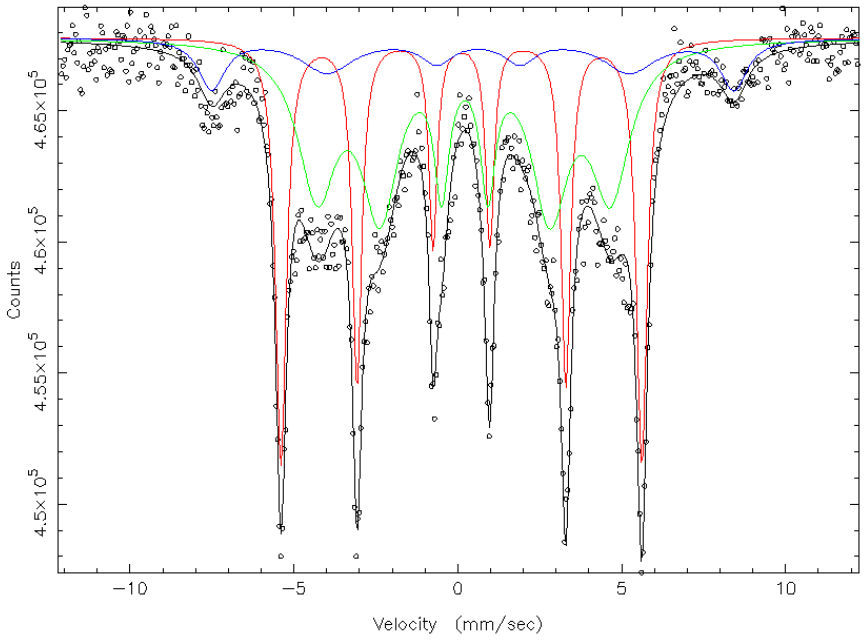



**Figure 150 Mössbauer Spectrum of JK049B at 6K**

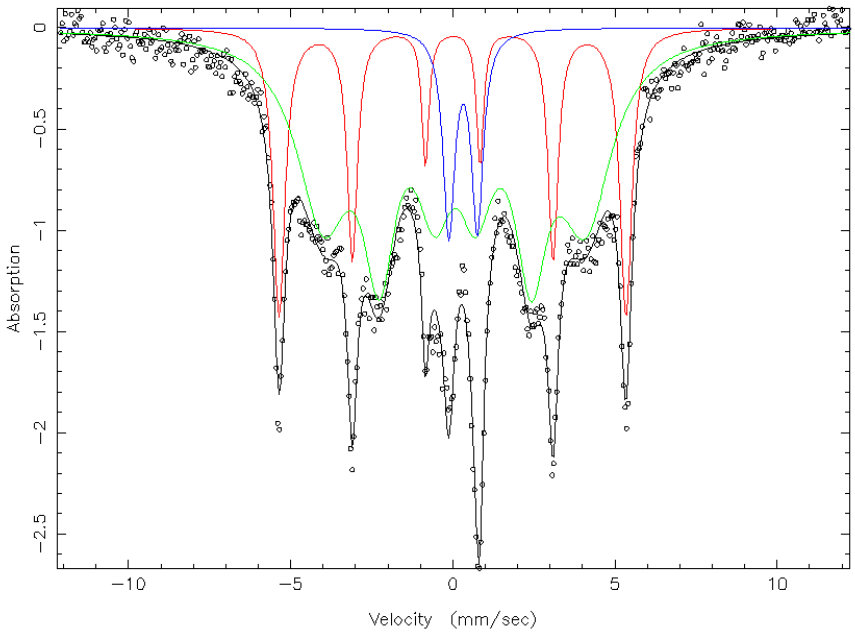



**Figure 151 Mössbauer Spectrum of JK049B at 293K**

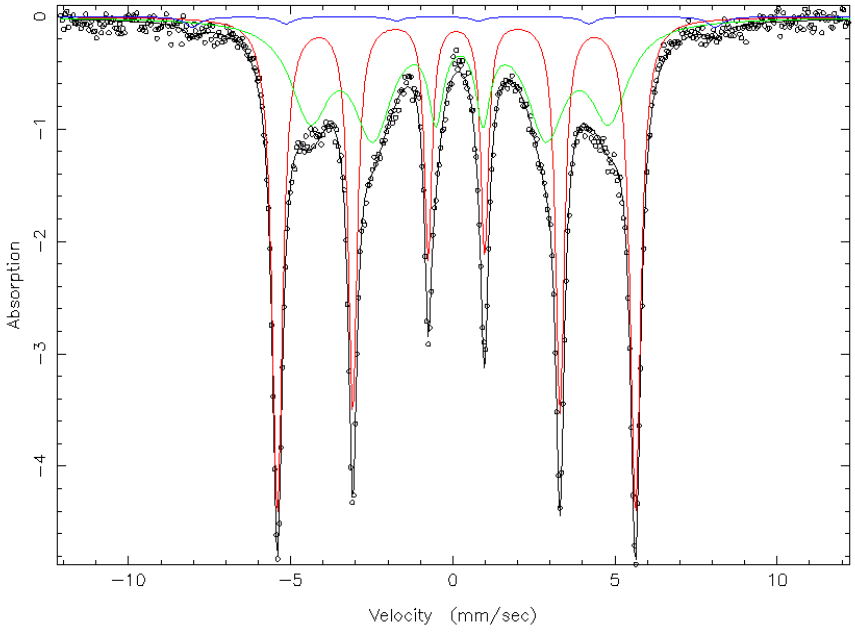



**Figure 152 Mössbauer Spectrum of JK050 at 6K**

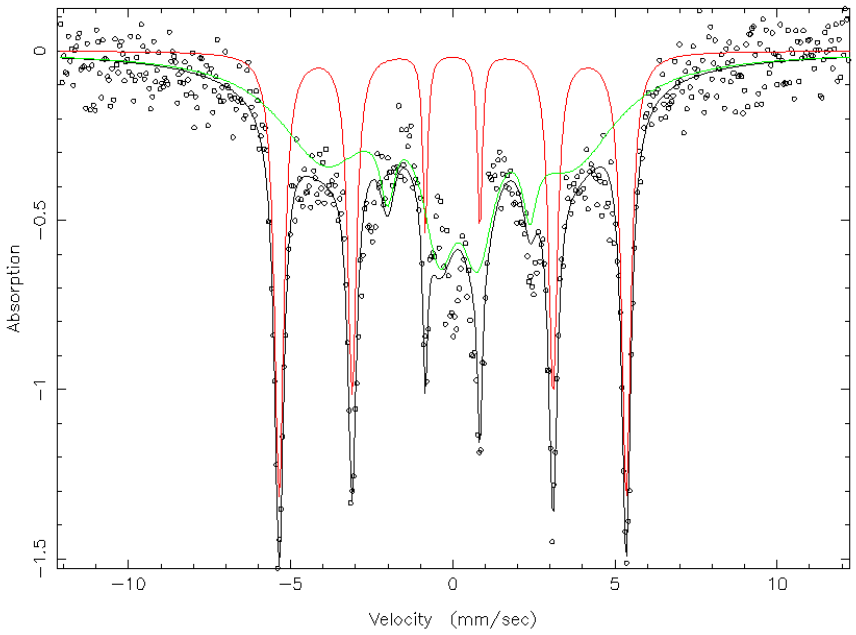



**Figure 153 Mössbauer Spectrum of JK050 at 293K**

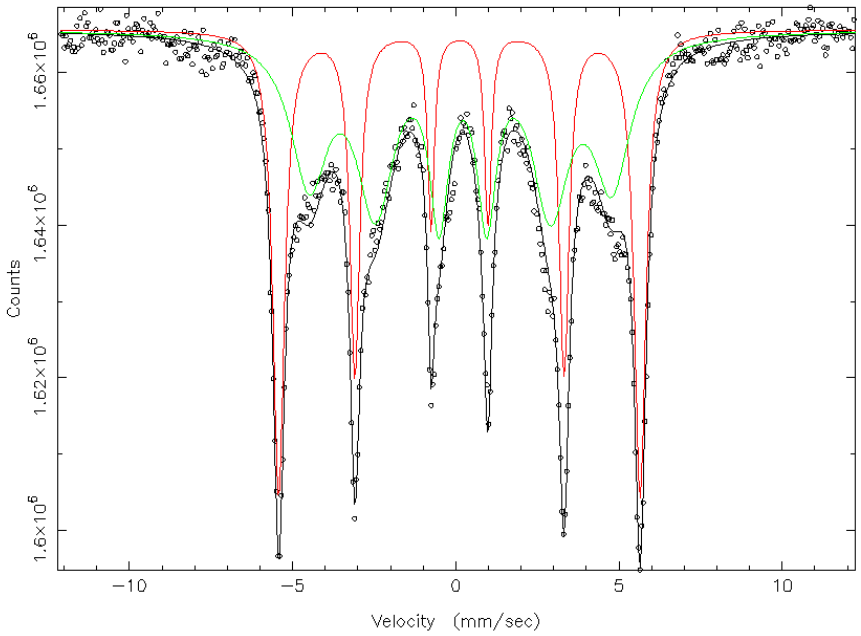



**Figure 154 Mössbauer Spectrum of JK051 at 6K**

# CHAPTER V
# CONCLUSIONS

The aim of this research is to develop iron nanoparticles suitable for use as MRI contrast agents, for enhancement of LITT, and to combine these capabilities for MRgLITT. Synthesis methods employed are reduction and thermal decomposition of varying iron reactants. Several biocompatible coatings were investigated to determine their performance as a protective layer. Characterization techniques used include DLS, TEM, Mössbauer Spectroscopy, NMR, and cytotoxicity. The main target of this biomedical application is to further the diagnosis and treatment of brain cancer, specifically glioblastoma multiforme.

## Iron Chloride Reduction

Reduction of iron (ii) chloride resulted in metal iron and iron oxide nanoparticles. Coatings attributed to agglomerates. Brij coated nanoparticles were deemed safe in cytotoxicity studies at low concentrations. A longer reaction length produced smaller nanoparticles. Iron metal nanoparticles had not oxidized completely after three years of storage in air.

## Iron Pentacarbonyl Thermal Decomposition

Thermal decomposition in organics produced iron oxide nanoparticles with an iron metal core. The reaction proved to be very reproducible. Both ferrite and polymer coatings were investigated. Polymer coatings, such as polyethylene glycol and Brij, protected the ore from further oxidation. Nanoparticles that had ferrite shells annealed had larger size distributions than those without; this is due to further growing the nanoparticles at high temperatures during the annealing process.

## Iron Sulfate Reduction

Iron sulfate reductions created metal and amorphous iron nanoparticles. Utilization of a probe sonicator drastically improved accuracy of characterization. The use of a distillation column provided the desired length to achieve small nanoparticles and reduced agglomerates during synthesis. The column improved size distribution and produced a larger yield of coated sample.

## Outlook

In the future, synthesis of iron nanoparticles using a reduction reaction could be improved by utilizing a probe sonicator during synthesis and coating. The addition of a sonicator during

synthesis could increase temperatures and cause oxidation, so temperature should be monitored throughout.

Examining the electrochemistry of the reaction could help minimize oxidation. The pH of nanoparticle samples should be evaluated. Utilizing a Pourbaix diagram for iron could improve the prevention of oxidation after synthesis by altering or maintaining pH.

# References

Christensen, P.H., Morup, S., & Niemantstverdriet, J.W. (1985). Particle size determination of superparamagnetic α-Fe in carbon-supported catalysts by in situ Mössbauer spectroscopy. Journal of Physical Chemistry.

Coey, J.M.D (2009). Magnetism and magnetic materials. Cambridge University Press.

Ding, Xuanfeng, at al. (2011). Development of iron-containing multiwalled carbon nanotubes for MR-guided laser-induced thermotherapy. Nanomedicine 6(8). doi:10.2217/nnm.11.37.

Elder, J. Bradley, Chiocca, E. Antonio (2013). Editorial: Glioblastoma multiforme and laser interstitial thermal therapy. J. Neurosurg 118(6):1199-1201. doi:10.3171/2012. 9.JNS121563.

Hafeli, U.O., Mahmoundi, M., Laurent, S., & Dutz, S. (2011). Magnetic fluid hyperthermia: Focus on superparamagnetic iron oxide nanoparticles. Advances in Colloid and Interface Science.

Hofmann, H. Hofmann, M. Von Rechenberg, B., Neugerger, & Schöpf. (2005). Superparamagnetic nanoparticles for biomedical applications: Possibilities and limitations of a new drug delivery system. Journal of Magnetism and Magnetic Materials.

Huang, H.S., & Hainfeld, J.F. (2013). Intravenous magnetic nanoparticle cancer hyperthermia. International Journal of Nanomedicine.

Huber, D. (2005). Synthesis, properties, and applications of iron nanoparticles. Small.

King, J.E. & Johnson, J.A. (2018). MRI-Guided Laser Induced Thermal Therapy of Glioblastoma. Michael Iv, M.D.**,** Max Wintermark, M.D. and Tarik F. Massoud, M.D., Ph.D. (Editors), Stanford, CA: Nova Science Publishers. Glioblastoma: State-of-the-Art Clinical Neuroimaging.

Lee, Ivan, Kalkanis, Steven, Hadjipanayis, Consttantinos G. (2016). Stereotactic Laser Interstitial Thermal Therapy for Recurrent High-Grade Gliomas. Neurosurgery 79. doi:10.1227/NEU.0000000000001443.

Leuthardt, E.C., Duan, C., Kim, M.J., Campain, J.L., Kim, A.H., Miller-Thomas, M.M., Shimony, J.S., & Tran, D.D. (2016). Hyperthermia laser ablation of recurrent glioblastoma leads to temporary disruption of the peritumoral blood brain barrier. PLoS ONE.

Lewin, J.S., Connell, C.F., Duerk, J.L., Chung, Y-C, Clampitt, M.E., Spisak, J., Gazelle, G.S., & Haaga, J.R. (2005). Interactive MRI-guided radiofrequency interstitial thermal ablation of abdominal tumors: Clinical trial for evaluation of safety and feasibililty. Journal of

Missios, Symeon, Bekelis, Kimon, Barnett, Gene H. (2015). Renaissance of laser interstitial thermal ablation. Neurosurgical Focus 38(3). doi:10.3171/2014.12.FOCUS14762.

Mørup, S., Topsøe, H., & Clausen, B.S. (1982). Magnetic properties of microcrystals studied by Mössbauer spectroscopy. Physica Scripta.

Naregalkar, R.R., Gupta, A.K., & Vaidya, V.D. (2007). Recent advances on surface engineering of magnetic iron oxide nanoparticles and their biomedical applications. Nanomedicine.

Noreed, Sarah E., Johnson, Jacqueline A. (2014). Magnetic Resonance-Guided Laser Induced Thermal Therapy for Glioblastoma Multiforme: A Review. BioMed Research International 2014. doi:10.1155/2014/761312.

Pinsanic, T.R., Shubayev, V.I., & Jin, S. (2009) Magnetic nanoparticles for theragnostics. Advanced Drug Delivery Reviews.

Rahmathulla, G., Recinos, P.F., Kamian, K., Mohammadi, A.M., Ahluwalia, M.S., & Barnett, G.H. (2013). MRI-guided laser interstitial thermal therapy in neuro-oncology: A review of its current clinical applications. Oncology.

Reddy, L.H., Arias, J.L., Nicolas, J., & Couvreur, P. (2012). Magnetic nanoparticles: Design and characterization, toxicity and biocompatibility, pharmaceutical and biomedical applications. Chemical Review.

Tucek, J., Sofer, Z., & et al. (2016). Air-stable superparamagnetic metal nanoparticles entrapped in graphene oxide matrix. Nature Communications.

Yu, K.N., Kim, B.G., Kim, H.W., Lee, K.H., Park, S.B., Lee, J.K., Cho, M.H., Kim, J.S., & Yoon, T.J. (2006). Toxicity and tissue distribution of magnetic nanoparticles in mice. Toxicological Sciences.

Shubayev VI, and et al. Magnetic nanoparticles for theragnostics. Advanced Drug Delivery Reviews, 2009.

Wu W, He Q, and et al. Magnetic iron oxide nanoparticles: Synthesis and surface functionalization strategies. Nanoscale Research Letters, 2008.

Carpentier A, Chauvet D, and et al. MR-guided laser-induced thermal therapy (LITT) for recurrent glioblastomas. Lasers in Surgery and Medicine, 2012.

Laurent S, Dutz S, and et al. Magnetic fluid hyperthermia: Focus on superparamagnetic iron oxide nanoparticles. Advances in Colloid and Interface Science, 2011.

Reddy LH, Arias JL, and et al. Magnetic nanoparticles: Design and characterization, toxicity, and biocompatibility, pharmaceutical and biomedical applications. Chemical Reviews, 2012.

Huber D, and et al. Synthesis, properties, and applications of iron nanoparticles. Small, 2005.

Gupta AK, Gupta M, and et al. Recent advances on surface engineering of magnetic iron oxide nanoparticles and their biomedical applications. Nanomedicine, 2007.

Illes D, Tombacz E, and et al. Novel carboxylated peg-coating on magnetite nanoparticles designed for biomedical applications. Journal of Magnetism and Magnetic Materials, 2015.

Yoon TJ, Lee H, and et al. Highly magnetic core-shell nanoparticles with unique magnetization mechanism. Angew Chem Int Ed Engl, 2011.

Park J, and et al. Ultra-large-scale syntheses of monodispersed nanocrystals. Nature Materials, 2004.

Peng S, Wang C, and et al. Synthesis and stabilization of monodisperse fe nanoparticles. Journal of American Chemical Society, 2006.

Bronstein LM, Huang X, and et al. Influence of iron oleate complex structure on iron oxide nanoparticle formation. Chemical Materials, 2007.

Christensen PH, Mørup S, and Niemantsverdriet JW. Particle size determination of superparamagnetic α-Fe in carbon-supported catalysts by in situ Mössbauer spectroscopy. Journal of Physical Chemistry, 1985.

Costa GM, Blanco-Andujar C, and et al. Magnetic nanoparticles for in vivo use: A critical assessment of their composition. Journal of Physical Chemistry, 2014.

# APPENDIX

**Table 13 Synthesis Method and Coating of All Samples**

| Sample | Synthesis Type | Coating(s) | Reaction Solvent |
|---|---|---|---|
| JK001 | $FeCl_2$ reduction with separatory funnel | Brij 30 | Ethanol |
| JK002 | $FeCl_2$ reduction | Brij 30 | Ethanol |
| JK003 | $FeCl_2$ reduction with separatory funnel | Brij 30 | Ethanol |
| JK004 | $FeCl_2$ reduction | Brij 30 | Ethanol |
| JK005 | $FeCl_2$ reduction | Brij 30 | Ethanol |
| JK006 | $FeCl_2$ reduction with separatory funnel | Brij 30 | Ethanol |
| JK007 | $FeCl_2$ reduction with separatory funnel | PEG 600 diacid | Ethanol |
| JK009 | $FeCl_2$ reduction with separatory funnel | none | Ethanol |
| JK010 | $FeCl_2$ reduction by pouring | Brij 30 | Ethanol |
| JK011 | $FeCl_2$ reduction with separatory funnel | PEG 600 diacid | Ethanol |
| JK012 | $FeCl_2$ reduction with separatory funnel | PEG 600 diacid | Ethanol |
| JK018 | Reduction with funnels into flask | Brij 30 | Ethanol |
| JK019 | Reduction with funnels into flask | Brij 30 | Ethanol |
| JK020 | Thermal decomposition 1.4 mL $Fe(CO)_5$ | none | ODE/OY |
| JK021 | Thermal decomposition 1.4 mL $Fe(CO)_5$ | 0.4 mL iron oleate | ODE/OY |
| JK022 | Thermal decomposition 1.4 mL $Fe(CO)_5$ | 0.4 mL iron oleate | ODE/OY |
| JK023 | Thermal decomposition 1.4 mL $Fe(CO)_5$ | none | ODE/OY |
| JK024 | Thermal decomposition 1.4 mL $Fe(CO)_5$ | none | ODE/OY |
| JK025 | Thermal decomposition 2.8 mL $Fe(CO)_5$ | 0.4 mL iron oleate | ODE/OY |
| JK026 | Thermal decomposition 2.8 mL $Fe(CO)_5$ | 0.4 mL iron oleate + Brij 30 | ODE/OY |
| JK027 | Thermal decomposition 2.4 mL $Fe(CO)_5$ | Brij 30 | ODE/OY |
| JK028 | Thermal decomposition 2.4 mL $Fe(CO)_5$ | 0.1 mL iron oleate + PEG 300 | ODE/OY |
| JK029 | Thermal decomposition 2.4 mL $Fe(CO)_5$ | 0.1 mL iron oleate | ODE/OY |
| JK030 | Thermal decomposition 2.4 mL $Fe(CO)_5$ | none | ODE/OY |
| JK031 | Thermal decomposition 2.4 mL $Fe(CO)_5$ | PEG 300 | ODE/OY |
| JK032 | Thermal decomposition 7.2 mL $Fe(CO)_5$ | 0.6 mL iron oleate | ODE/OY |
| JK033 | Thermal decomposition 7.2 mL $Fe(CO)_5$ | 0.3 mL iron oleate | ODE/OY |
| JK034 | Thermal decomposition 2.4 mL $Fe(CO)_5$ | 0.1 mL iron oleate | ODE/OY |
| JK035 | Thermal decomposition 2.4 mL $Fe(CO)_5$ | 0.1 mL iron oleate | ODE/OY |
| JK036 | Thermal decomposition 2.4 mL $Fe(CO)_5$ | 0.1 mL iron oleate | ODE/OY |
| JK038 | Thermal decomposition 2.4 mL $Fe(CO)_5$ | 0.1 mL iron oleate | ODE/OY |
| JK039 | Thermal decomposition 2.4 mL $Fe(CO)_5$ | 0.1 mL iron oleate | ODE/OY |
| JK040 | Thermal decomposition 2.4 mL $Fe(CO)_5$ | 0.1 mL iron oleate | ODE/OY |
| JK041 | Thermal decomposition 2.4 mL $Fe(CO)_5$ | 0.1 mL iron oleate | ODE/OY |
| JK042 | Thermal decomposition 2.4 mL $Fe(CO)_5$ | 0.1 mL iron oleate | ODE/OY |
| JK043 | Thermal decomposition 2.3 mL $Fe(CO)_5$ | 0.1 mL iron oleate | ODE/OY |

**Table 13 Continued**

| Sample | Synthesis Type | Coating | Reaction Solvent |
|---|---|---|---|
| JK044 | $FeSO_4$ reduction with separatory funnel | none | DI water |
| JK045 | $FeSO_4$ reduction with separatory funnel | PEG 300 | DI water |
| JK046/46B | $FeSO_4$ reduction with separatory funnel | PEG 300/none | DI water |
| JK047/47B | $FeSO_4$ reduction with separatory funnel | PEG 300/none | DI water |
| JK048 | $FeSO_4$ reduction with separatory funnel | PEG 300 | DI water |
| JK049/49B | $FeSO_4$ reduction with separatory funnel | PEG 300/none | DI water |
| JK050 | $FeSO_4$ reduction with distillation column | PEG 300 | DI water |
| JK051 | $FeSO_4$ reduction with distillation column | PEG 300 | DI water |

# VITA

Julie Elizabeth King was born in Mount Airy, North Carolina to Danny and Sandy King. She has one brother, Jason King, who is an officer in the United States Marine Corps. She obtained her Bachelor of Science Degrees at King University (known as King College at time of graduation) in 2012. She majored in Physics and Mathematics and minored in Biology and Chemistry. Julie obtained her Master of Science Degree from The University of Tennessee in Biomedical Engineering in 2015. She earned a Graduate Certificate in Engineering Management in 2017 from the University of Tennessee.